Title
Evolution in the Physical Conditions of Star-Forming Regions Throughout Cosmic History

Author
Sanders, Ryan Lee

Publication Date
2018

Peer reviewed|Thesis/dissertation

UNIVERSITY OF CALIFORNIA

Los Angeles

Evolution in the Physical Conditions of Star-Forming Regions Throughout Cosmic History

A dissertation submitted in partial satisfaction
of the requirements for the degree
Doctor of Philosophy in Astronomy

by

Ryan Lee Sanders

2018

ABSTRACT OF THE DISSERTATION

Evolution in the Physical Conditions
of Star-Forming Regions
Throughout Cosmic History

by

Ryan Lee Sanders
Doctor of Philosophy in Astronomy
University of California, Los Angeles, 2018
Professor Alice Eve Shapley, Chair

The gas-phase metallicity of the interstellar medium is a powerful probe of the cycle of baryons into and out of galaxies. Constraining the scaling of metallicity with global galaxy properties such as stellar mass (M_*) and star-formation rate (SFR) at multiple epochs provides insight into galaxy growth across cosmic history and the origin of the present-day galaxy population. In this dissertation, I investigate the evolution of the physical conditions of ionized gas in star-forming regions, including metallicity, over the past 12 billion years of cosmic history. This work is contained in five studies that collectively improve our knowledge of galaxy metallicities over the redshift range $z = 0 - 3$. I present measurements of the mass-metallicity relation at $z \sim 2.3$ using a novel high-redshift data set from the MOSFIRE Deep Evolution Field (MOSDEF) survey. I further show that there is a relation among M_*, SFR, and metallicity for $z \sim 2.3$ star-forming galaxies, unambiguously demonstrating the existence of this relation at $z > 1$ for the first time. Knowledge of the physical conditions of line-emitting gas, including the electron density and ionization state, is required for robust estimates of metallicity from strong optical emission lines. I show that the electron density of star-forming regions increases by an order of magnitude from $z \sim 0$ to $z \sim 2.3$, and place constraints on the evolution of ionization state. Obtaining unbiased galaxy metallicity estimates additionally requires proper treatment of the various line-emitting sources falling within spectroscopic apertures. I characterize systematic metallicity biases from $z \sim 0$ global

galaxy spectra using a model framework that treats galaxies as ensembles of H II and diffuse ionized gas regions of varying metallicities. The resulting corrections increase the accuracy of the $z \sim 0$ baseline for evolutionary studies. Finally, I present the first temperature-based metallicity determination at $z > 2$ from a detection of the auroral emission line [O III]λ4363. Measurements of auroral lines provide an independent estimate of metallicity that can be used to construct metallicity calibrations appropriate at high redshifts. Observational facilities coming online in the near-future will enable temperature-based metallicity measurements for large samples of high-redshift galaxies, providing unprecedented accuracy in metallicity measurements and a more complete understanding of gas flows and galaxy growth.

The dissertation of Ryan Lee Sanders is approved.

Edward Donald Young

Matthew A. Malkan

Tommaso L. Treu

Alice Eve Shapley, Committee Chair

University of California, Los Angeles

2018

To Amy

TABLE OF CONTENTS

LIST OF FIGURES

LIST OF TABLES

ACKNOWLEDGMENTS

There are many people who deserve thanks for getting me to where I am now. I would like to first thank my wife, Amy, for her love and support throughout my graduate career, for following me to California, and for joining me on the journey from this point onward. I would not be who I am today without her. I owe so much to my parents, Gary and Carol, who have been nothing but supportive throughout my life. They deserve much of the credit for this dissertation. Mom and dad, thank you for everything.

I cannot thank my advisor, Alice Shapley, enough for all that she has done over the past six years. She has molded me into the astronomer I am today. Her work ethic and commitment to her students have always amazed me. I hope to one day be even a fraction of the scientist and role model that she is. I am thankful and proud to have her as my Ph.D. advisor, mentor, and friend.

I would like to thank the UCLA Astronomy faculty, graduate students, postdocs, and staff for making my time at UCLA so enjoyable. A special thank you to the members of my cohort: Adam Greenberg, Emily Martin, Anson Lam, and Michelle Consiglio. I am very glad that my education path led me to UCLA and would have it no other way.

I am deeply indebted to my fellow members of the MOSFIRE Deep Evolution Field (MOSDEF) survey team, including PIs Alice Shapley, Naveen Reddy, Mariska Kriek, Brian Siana, Alison Coil, and Bahram Mobasher. I was very fortunate to begin graduate school and join the MOSDEF team just as science products from the first year of observations were coming out. I would like to thank and congratulate all of the MOSDEF PIs, fellow graduate students, and other team members for collecting an amazing data set that has enabled many interesting science investigations, with more to come. Thank you for your collegiality and support.

The MOSDEF survey makes use of data from the MOSFIRE spectrograph on the Keck I telescope at the W. M. Keck Observatory on Mauna Kea, Hawaii. I wish to acknowledge the cultural importance of this sacred mountain to the native Hawaiian community and those of Hawaiian ancestry. This work would not have been possible without their generous

hospitality. We are most privileged to observe the universe from atop their sacred mountain.

I would also like to thank Alice Shapley, Tommaso Treu, Matt Malkan, and Ed Young for serving on my dissertation committee.

Chapter 2 is a version of Sanders et al. (2015, ApJ, 799, 138, DOI:10.1088/0004-637X/799/2/138), and is reproduced with permission from the AAS. I would like to acknowledge my co-authors on this work: Alice Shapley, Mariska Kriek, Naveen Reddy, Bill Freeman, Alison Coil, Brian Siana, Bahram Mobasher, Irene Shivaei, Sedona Price, and Laura de Groot.

Chapter 3 is a version of Sanders et al. (2016a, ApJ, 816, 23, DOI:10.3847/0004-637X/816/1/23), and is reproduced with permission from the AAS. I would like to acknowledge my co-authors on this work: Alice Shapley, Mariska Kriek, Naveen Reddy, Bill Freeman, Alison Coil, Brian Siana, Bahram Mobasher, Irene Shivaei, Sedona Price, and Laura de Groot.

Chapter 4 is a version of Sanders et al. (2016b, ApJL, 825, L23, DOI:10.3847/2041-8205/825/2/L23), and is reproduced with permission from the AAS. I would like to acknowledge my co-authors on this work: Alice Shapley, Mariska Kriek, Naveen Reddy, Bill Freeman, Alison Coil, Brian Siana, Bahram Mobasher, Irene Shivaei, Sedona Price, and Laura de Groot. I would like to thank Tucker Jones, Dan Stark, and Ramesh Mainali for providing data used in this study.

Chapter 5 is a version of Sanders et al. (2017, ApJ, 850, 136, DOI:10.3847/1538-4357/aa93e4), and is reproduced with permission from the AAS. I would like to acknowledge my co-authors on this work: Alice Shapley, Kai Zhang, and Renbin Yan. This study makes use of data from SDSS-IV/Mapping Nearby Galaxies at APO (MaNGA) funded by the Alfred P. Sloan Foundation, the U.S. Department of Energy Office of Science, and the Participating Institutions.

Chapter 6 is a version of Sanders et al. (2018, ApJ, 858, 99, DOI:10.3847/1538-4357/aabcbd), and is reproduced with permission from the AAS. I would like to acknowledge my co-authors on this work: Alice Shapley, Mariska Kriek, Bill Freeman, Naveen Reddy, Brian Siana, Alison Coil, Bahram Mobasher, Romeel Davé, Irene Shivaei, Mojegan Azadi, Sedona Price, Gene Leung, Tara Fetherholf, Laura de Groot, Tom Zick, Francesca Fornasini, and

Guillermo Barro.

My work on these projects has been supported by the following funding sources: NSF AAG grants AST-1312780, AST-1312547, AST-1312764, and AST-1313171, grant AR-13907 provided by NASA through the Space Telescope Science Institute, and grant NNX16AF54G from the NASA ADAP program. I was supported by the Richard B. Kaplan Endowed Graduate Award in Astrophysics in 2013 and 2015. Support for the 2017-2018 academic year came from a UCLA Graduate Division Dissertation Year Fellowship. I have presented results from my dissertation work at domestic and international conferences thanks to support from Richard B. Kaplan, a Doctoral Student Travel Grant from the UCLA Graduate Division, and the AAS Rodger Doxsey Travel Prize.

VITA

2007	Graduated, St. Charles North High School, St. Charles, Illinois.
2012	B.S. (Physics) and B.M. (Jazz Performance), Summa Cum Laude, University of Louisville, Kentucky.
2014	M.S. (Astronomy), University of California, Los Angeles.
2017	Dissertation Year Fellowship, University of California, Los Angeles.

PUBLICATIONS

Sanders, R. L., Shapley, A. E., Kriek, M., Reddy, N. A., Freeman, W. R., Coil, A. L., Siana, B., Mobasher, B., Shivaei, I., Price, S. H., and de Groot, L. "The MOSDEF Survey: Mass, Metallicity, and Star-Formation Rate at $z \sim 2.3$." 2015, ApJ, 799, 138.

Shapley, A. E., Reddy, N. A., Kriek, M., Freeman, W. R., **Sanders, R. L.**, Siana, B., Coil, A. L., Mobasher, B., Shivaei, I., Price, S. H., and de Groot, L. "The MOSDEF Survey: Excitation Properties of $z \sim 2.3$ Star-Forming Galaxies." 2015, ApJ, 801, 88.

Kriek, M., Shapley, A. E., Reddy, N. A., Siana, B., Coil, A. L., Mobasher, B., Freeman, W. R., de Groot, L., Price, S. H., **Sanders, R. L.**, Shivaei, I., Brammer, G. B., Momcheva, I. G., Skelton, R. E., van Dokkum, P. G., Whitaker, K. E., Aird, J., Azadi, M., Kassis, M., Bullock, J. S., Conroy, C., Davé, R., Keres, D., and Krumholz, M. "The MOSFIRE Deep Evolution Field (MOSDEF) Survey: Rest-frame Optical Spectroscopy for 1500 H-selected Galaxies at $1.37 < z < 3.8$." 2015, ApJS, 218, 15.

Sanders, R. L., Shapley, A. E., Kriek, M., Reddy, N. A., Freeman, W. R., Coil, A. L., Siana, B., Mobasher, B., Shivaei, I., Price, S. H., and de Groot, L. "The MOSDEF Survey: Electron Density and Ionization Parameter at $z \sim 2.3$." 2016, ApJ, 816, 23.

Sanders, R. L., Shapley, A. E., Kriek, M., Reddy, N. A., Freeman, W. R., Coil, A. L., Siana, B., Mobasher, B., Shivaei, I., Price, S. H., and de Groot, L. "The MOSDEF Survey: Detection of [O III]λ4363 and the Direct-method Oxygen Abundance of a Star-Forming Galaxy at $z = 3.08$." 2016, ApJL, 825, L23.

Shapley, A. E., **Sanders, R. L.**, Reddy, N. A., Kriek, M., Freeman, W. R., Mobasher, B., Siana, B., Coil, A., Leung, G. C., de Groot, L., Shivaei, I., Price, S. H., Azadi, M., and Aird, J. "The MOSDEF Survey: First Measurement of Nebular Oxygen Abundance at $z > 4$." 2017, ApJL, 846, L30.

Sanders, R. L., Shapley, A. E., Zhang, K., and Yan, R. "Biases in Metallicity Measurements from Global Galaxy Spectra: The Effects of Flux Weighting and Diffuse Ionized Gas Contamination." 2017, ApJ, 850, 136.

Shivaei, I., Reddy, N. A., Shapley, A. E., Kriek, M., Mobasher, B., Freeman, W. R., **Sanders, R. L.**, Coil, A., Price, S. H., Fetherholf, T., Azadi, M., Leung, G., and Zick, T. "The MOSDEF Survey: Direct Observational Constraints on the Ionizing Photon Production Efficiency, $\xi_{\rm ion}$, at $z \sim 2$." 2018, ApJ, 855, 42.

Sanders, R. L., Shapley, A. E., Kriek, M., Freeman, W. R., Reddy, N. A., Siana, B., Coil, A. L., Mobasher, B., Davé, R., Shivaei, I., Azadi, M., Price, S. H., Leung, G., Fetherholf, T., de Groot, L., Zick, T., Fornasini, F. M., and Barro, G. "The MOSDEF Survey: A Stellar Mass-SFR-Metallicity Relation Exists at $z \sim 2.3$." 2018, ApJ, 858, 99.

CHAPTER 1

Introduction

A major goal of astronomy is to understand the formation and evolution of galaxies, that is, how galaxies first formed early in cosmic history and grew into the population of galaxies observed in the present-day universe. Galaxies contain two major components that make up their mass: dark matter that is non-luminous and only interacts gravitationally, and baryonic matter that primarily exists in the form of stars and gas. The growth of dark matter haloes in which galaxies reside is well established, but the assembly of the baryonic content of galaxies is not yet fully understood due to the complex nature of the physics of baryonic interactions.

There are three main processes that govern the growth of the baryonic content of galaxies: gas accretion, star formation, and feedback. There is significant interplay between these three processes. Gas from the intergalactic medium (IGM) and the circumgalactic medium (CGM) falls into the gravitational potential well of a galaxy, building up a gas reservoir in the interstellar medium (ISM) and providing fuel for star formation. Stars form from dense cold gas in the ISM. Energy is injected into the ISM by feedback processes including supernovae from recently formed massive stars, stellar winds and radiation pressure, and accreting supermassive black holes. This feedback can in turn drive galaxy-scale gas outflows, transporting material from the ISM to the CGM where it may be recycled back into the ISM over time or escape from the halo entirely into the IGM. The disruption of the ISM by feedback regulates star formation, while outflows can act preventatively to slow gas accretion rates. This complex processing and movement of gas into and out of galaxies is known as the cycle of baryons.

1.1 Metallicity as a probe of the cycle of baryons

The gas-phase metallicity (Z) of the ISM is a sensitive probe of the cycle of baryons. Metallicity is defined as the number density of metals relative to the number density of hydrogen, where metals are elements heavier than helium and are primarily produced through nucleosynthesis by stellar processes. Accretion of metal-poor gas from the IGM and CGM dilutes metals in the ISM, lowering the metallicity. The process of star formation leads to the production of additional metals through nucleosynthesis while consuming hydrogen, increasing the metallicity. Finally, outflows can remove both metals and hydrogen from the galaxy. In this way, the gas-phase metallicity of a galaxy is set by the cycle of baryons through an equilibrium between the accretion, star formation, and outflow rates (Finlator & Davé, 2008; Davé et al., 2012). The gas-phase oxygen abundance (12+log(O/H)) is a particularly useful tracer of ISM metallicity since oxygen is the most abundant element besides hydrogen and helium. In this dissertation, the term "metallicity" refers to the gas-phase oxygen abundance of the ISM unless specified otherwise.

Of particular interest is the scaling of galaxy metallicity with global galaxy properties, such as stellar mass (M_*) and star-formation rate (SFR). The shape and normalization of such metallicity scaling relations encodes information about key parameters of the cycle of baryons, including the global mass accretion and mass outflow rates (Finlator & Davé, 2008; Peeples & Shankar, 2011; Davé et al., 2012). The latter is often represented by the mass loading factor of galactic winds, defined as the ratio of the mass outflow and star-formation rates (e.g., Finlator & Davé, 2008). Observations of metallicity scaling relations can be combined with analytic galaxy chemical evolution models or compared to results from numerical simulations of galaxy formation to infer the values of these key parameters and the manner in which they scale with M_* (e.g., Davé et al., 2012; Lilly et al., 2013; Davé et al., 2017).

A tight relation between the M_* and metallicity of galaxies in the present-day universe (low-redshift; $z \sim 0$) has been observed, known as the mass-metallicity relation (MZR; e.g., Tremonti et al., 2004; Andrews & Martini, 2013). The shape of the mass-metallicity relation

encodes the scaling of outflow mass loading factor with M_*, which can distinguish between different wind-driving mechanisms (e.g., Finlator & Davé, 2008; Peeples & Shankar, 2011). A higher-order relation among M_*, SFR, and metallicity (the M_*-SFR-Z relation) has also been observed at $z \sim 0$ (Mannucci et al., 2010; Lara-López et al., 2010). The M_*-SFR-Z relation is thought to be a direct consequence of baryon cycling, where gas inflows decrease the ISM metallicity while increasing SFR (e.g., Davé et al., 2017). Characterizing these metallicity scaling relations at $z \sim 0$ has greatly expanded our knowledge of how galaxies grow their baryonic mass in the local universe.

Observational constraints on the nature of metallicity scaling relations are much weaker at high redshifts ($z > 1$, when the universe was less than 7 Gyr old). The MZR has been found to exist out to $z \sim 3$, and evolves such that metallicity decreases at fixed M_* with increasing redshift (e.g., Erb et al., 2006; Onodera et al., 2016). No consensus has been reached regarding the existence of the M_*-SFR-Z relation at $z \sim 1$ and whether it evolves with redshift (e.g., Stott et al., 2013; Zahid et al., 2014b; Salim et al., 2015). Progress at high redshifts has been limited by small sample sizes, unrepresentative or inhomogeneous samples of galaxies, and uncertain metallicity estimates due to large measurement and systematic uncertainties. Both a large, representative sample of high-redshift galaxies for which metallicities are available and a better understanding of the systematic biases affecting high-redshift metallicity estimates are required to gain a more complete understanding of galaxy growth in the early universe.

1.2 Metallicity measurements and ionized gas physical conditions

Galaxy metallicity is typically measured using ratios of emission lines produced in regions of fully-ionized gas surrounding hot, young, massive stars (H II or star-forming regions). A subset of the strong rest-frame optical emission lines [O II]$\lambda\lambda$3726,3729, Hβ, [O III]$\lambda\lambda$4959,5007, Hα, [N II]$\lambda\lambda$6548,6584, and [S II]$\lambda\lambda$6716,6731 are most commonly utilized to estimate metallicity. The intrinsic strength of these emission lines relative to one another is set by the physical conditions of the ionized gas, including the temperature (set by the metallicity),

electron density, ionization state (determined by the ionization parameter and the shape of the ionizing spectrum), and the abundance pattern of various chemical elements (e.g., N/O, the nitrogen-to-oxygen ratio).

The ionization state and N/O of gas in $z \sim 0$ H II regions are tightly correlated with metallicity. Accordingly, tight relations exist between metallicity and multiple rest-optical strong-line ratios in the local universe. Calibrations between strong-line ratios and metallicity have been empirically constructed based on measurements of strong emission lines and temperature-sensitive auroral emission lines (e.g., [O III]λ4363), where a determination of the gas temperature provides an independent estimate of metallicity (e.g., Pettini & Pagel, 2004; Curti et al., 2017). Because the physical conditions of $z \sim 0$ H II regions are well constrained, theoretical calibrations based on photoionization models have also been produced (e.g., Kewley & Dopita, 2002; Kobulnicky & Kewley, 2004). These metallicity calibrations have enabled detailed investigations of metallicity scaling relations for $\sim 100,000$ galaxies in the local universe (e.g., Tremonti et al., 2004; Mannucci et al., 2010).

At high redshifts, temperature measurements based on auroral lines such as [O III]λ4363 have not been available up to this point, such that no metallicity calibrations exist that are based on direct observations of high-redshift star-forming regions. Instead, metallicities of high-redshift galaxies are estimated using $z \sim 0$ metallicity calibrations under the assumption that these local calibrations are valid at $z > 1$. Initial measurements of emission-line ratios of galaxies at $z \sim 1 - 3$ suggest that at least some of the physical conditions of ionized gas in H II regions evolve with redshift (e.g., Shapley et al., 2005; Erb et al., 2006; Hainline et al., 2009). Consequently, the relations between metallicity and strong emission-line ratios may also evolve with redshift. In order to obtain robust metallicity measurements for high-redshift galaxies, we must place constraints on the physical conditions of ionized gas in high-redshift star-forming regions. Based on these constraints, we can significantly reduce systematic biases in current $z > 1$ metallicity estimates, leading to a more accurate picture of baryon cycling throughout cosmic history.

In this dissertation, I investigate the evolution of metallicity scaling relations over the past 12 Gyr of cosmic history, constrain the physical conditions of ionized gas in high-redshift

star-forming regions, make the first robust high-redshift measurement of metallicity independent of local calibrations, and characterize systematic uncertainties in galaxy metallicity estimates. This work is primarily based on data from the MOSFIRE Deep Evolution Field (MOSDEF) survey, a large observing program that obtained rest-frame optical spectra of $\sim$ 1500 representative galaxies at $1.4 \leq z \leq 3.8$, described in Kriek et al. (2015). The transformative MOSDEF data set provides robust measurements of the full suite of strong rest-optical emission lines, enabling determinations of SFR, metallicity, electron density, and ionization state for a sample that is an order of magnitude larger than those of previous studies of galaxy metallicities at high redshifts.

This dissertation is organized as follows. In Chapter 2, I present a preliminary study of the evolution of the MZR from $z \sim 0$ to $z \sim 2.3$ using the first year of data from the MOSDEF survey. I characterize the electron density and ionization state of $z \sim 2.3$ star-forming galaxies in Chapter 3. Chapter 4 presents the first detection of the temperature-sensitive auroral emission line [O III]λ4363 at $z > 2$, demonstrating the promise of constructing high-redshift metallicity calibrations using temperature-based metallicity measurements. In Chapter 5, I characterize systematic biases in $z \sim 0$ metallicity estimates from global galaxy spectra. Accounting for these biases carries important implications for metallicity evolution studies comparing high-redshift measurements to a $z \sim 0$ baseline. I present the first unambiguous detection of the M_*-SFR-Z relation at $z \sim 2$ in Chapter 6, and discuss implications of the evolution of the M_*-SFR-Z relation for the cycle of baryons. Finally, I summarize the results of these investigations and conclude in Chapter 7.

CHAPTER 2

The MOSDEF Survey: Mass, Metallicity, and Star-Formation Rate at $z \sim 2.3$

2.1 Introduction

The study of chemical abundances in galaxies at various epochs in cosmic history highlights key processes governing the growth and evolution of galaxies. In the local universe, there is a clear relationship between the stellar mass (M_*) of a galaxy and its gas-phase oxygen abundance, such that galaxies with lower stellar masses have lower metallicities than those with higher stellar masses. The $z \sim 0$ mass-metallicity relationship (MZR) has been confirmed by many studies (e.g., Tremonti et al., 2004; Kewley & Ellison, 2008; Andrews & Martini, 2013). Local galaxies follow this relationship with an intrinsic scatter of ~ 0.1 dex. The MZR has been confirmed at redshifts up to $z \sim 3.5$ and has been observed to evolve with redshift, such that galaxies of a given stellar mass have lower metallicities at higher redshifts (e.g., Erb et al., 2006; Maiolino et al., 2008; Henry et al., 2013; Maier et al., 2014; Maseda et al., 2014; Steidel et al., 2014). The MZR is most commonly understood in terms of the interplay between star formation and gas flows. As the stellar content of a galaxy grows over time, the chemical enrichment in the ISM increases due to the recycling of heavy elements produced in stars back into the ISM. This process of pure enrichment is modulated by gas inflows and outflows (e.g., Finlator & Davé, 2008; Mannucci et al., 2010; Davé et al., 2011, 2012) which may either increase or decrease the enrichment depending on the metallicity of the gas flow.

Much insight can be gained from the form and evolution of the MZR if the details of the underlying physical processes are understood. It has been suggested that the MZR arises

from the interaction of a galactic wind with the gravitational potential of a galaxy (Dekel & Silk, 1986; Tremonti et al., 2004). In this scenario, less massive galaxies are naturally less enriched as it is easier for winds to escape the gravitational potential well and remove metals in the process. At high stellar masses, winds are unable to escape and the galaxy retains all of the heavy elements injected into the ISM, naturally explaining the asymptotic behavior of the MZR assuming a constant stellar yield. Alternatively, in the equilibrium model of Finlator & Davé (2008) and Davé et al. (2011, 2012), outflows remove some metals, but have a more important effect of decreasing the fraction of inflowing gas from the intergalactic medium that is able to form stars and produce metals. In these models, the mass-loading factor quantifies the efficiency with which winds remove material from galaxies. Since the mass-loading factor of the momentum-driven winds in the equilibrium model scales inversely with M_*, the star-formation efficiency in low-M_* galaxies is drastically lowered and fewer metals are produced. In this context, the low-mass slope of the MZR can probe how the mass-loading factor scales with galaxy mass (Finlator & Davé, 2008). Other explanations attribute the MZR to variations in the star formation efficiency (Tassis et al., 2008) or the gas mass fraction (Zahid et al., 2014a) without referencing gas flows, although these processes are undoubtedly linked.

The local MZR has been observed to have a significant star-formation rate (SFR) dependence. Mannucci et al. (2010) found that local star-forming galaxies lie on a two-dimensional surface in M_*-SFR-metallicity space with a scatter of only 0.05 dex in metallicity. This surface is a strong function of SFR at low stellar masses such that galaxies of a given M_* with higher SFRs have lower metallicities, while only showing weak SFR dependence at high stellar masses. This relationship among M_*, SFR, and metallicity is referred to as the "fundamental metallicity relation" (FMR), and the MZR is a projection of the FMR in the M_*-metallicity plane. The existence of a local FMR has been confirmed by recent studies (Andrews & Martini, 2013; Lara-López et al., 2013). The connection between SFR and metallicity has been interpreted as a signature of infalling pristine gas which dilutes the metals in the ISM while simultaneously fueling additional star formation. If there is no inflow, the ISM enrichment increases while star formation naturally decreases as gas is used up. Mannucci et al. (2010)

find that high-redshift galaxies fall on the same FMR as local galaxies, naturally explaining redshift evolution in the MZR as a result of the SFR at fixed M_* increasing with redshift. More recently, Lilly et al. (2013) showed that a non-evolving FMR is a natural consequence of a physical model of galaxies in which the SFR is regulated by the mass of the gas reservoir if the dependence of the gas depletion timescale and the mass-loading factor on stellar mass is constant with redshift. However, the existence of the FMR has not been confirmed at redshifts above $z \sim 1$ as large and unbiased samples have been difficult to obtain up to this point and inconsistencies between different metallicity indicators and calibrations make comparisons difficult. Whether or not high-redshift galaxies lie on an extension of the local FMR, or follow an FMR at all, remains controversial (Belli et al., 2013; Stott et al., 2013; Cullen et al., 2014; Steidel et al., 2014; Troncoso et al., 2014).

In this work, we present early observations from the MOSFIRE Deep Evolution Field (MOSDEF) survey, which will contain rest-frame optical spectra of ∼1500 galaxies at $z \sim 1.5 - 3.5$ when completed. Here, we focus on an initial sample of 87 star-forming galaxies at $z \sim 2.3$ with estimates of stellar masses, gas-phase oxygen abundances, and Hα-based dust-corrected SFRs. We study the MZR at $z \sim 2.3$ with a representative sample of individual high-redshift measurements with a wide wavelength coverage and a large dynamic range in stellar mass and [N II]/Hα ratio. While this initial MOSDEF sample already surpasses nearly all samples in the literature used to study the MZR at this redshift, the full sample will provide a much larger dataset than has previously been available. In Section 2.2, we introduce and give a brief overview of the MOSDEF survey and describe our observations, measurements, and sample selection. In Section 2.3, we describe the metallicity calibrations, present the $z \sim 2.3$ MZR, and investigate dependence on SFR. Finally, we summarize and discuss our results in Section 4.5. We assume a standard ΛCDM cosmology throughout with $\Omega_m = 0.3$, $\Omega_\Lambda = 0.7$, and $H_0 = 70$ km s^{-1} Mpc^{-1}. Throughout this dissertation, the term metallicity refers to the gas-phase oxygen abundance ($12 + \log(O/H)$), which acts as a proxy for the true gas-phase metallicity.

2.2 Data

2.2.1 The MOSDEF Survey

The MOSDEF survey is a four-year project using the MOSFIRE spectrograph (McLean et al., 2012) on the 10 m Keck I telescope to survey the physical properties of galaxies at $1.4 \leq z \leq 3.8$. The full details of the survey are presented in Kriek et al. (2015), but here we describe its basic parameters. With MOSDEF, we target galaxies in the regions of the AEGIS, COSMOS, and GOODS-N extragalactic legacy fields with *Hubble Space Telescope* (*HST*) imaging coverage from the CANDELS survey (Grogin et al., 2011; Koekemoer et al., 2011), totaling 500 square arcminutes. All MOSDEF targets have extensive multi-wavelength ancillary data including *Chandra*, *Spitzer*, *Herschel*, *HST*, VLA, and ground-based optical and near-IR observations. The majority of this area is also covered by the 3D-HST grism survey (Brammer et al., 2012a).

When complete, the MOSDEF survey will consist of rest-frame optical spectra for ~ 1500 galaxies in three distinct redshift intervals (~ 750 galaxies at $2.09 \leq z \leq 2.61$, ~ 400 at $1.37 \leq z \leq 1.70$, and ~ 400 at $2.95 \leq z \leq 3.80$). Each range is dictated by the redshifts at which strong rest-frame optical emission features fall within windows of atmospheric transmission. Based on photometric catalogs compiled by the 3D-HST team (Skelton et al., 2014), galaxies are targeted down to limiting *HST*/WFC3 F160W magnitudes of 24.0, 24.5, and 25.0, respectively, at $z \sim 1.5, 2.3$, and 3.4. Target priorities are determined by both apparent brightness and existing redshift information, according to which brighter galaxies and those with more secure redshift information are assigned higher priority. We adopt photometric and grism redshifts from the 3D-HST survey, while additional redshift information is assembled in the form of ground-based spectroscopic redshifts from various sources. We note that only $\sim 40\%$ of MOSDEF targets observed to date had prior spectroscopic redshifts.

2.2.2 Observations, Data Reduction, and Measurements

As described in Kriek et al. (2015), MOSDEF observations are designed to maximize the number of strong rest-frame optical spectroscopic features covered at $3700 - 7000$ Å that are accessible from the ground. In this study, we focus on the $z \sim 2.3$ redshift interval, for which we obtain J, H, and K-band spectra. The nominal wavelength coverage in each of these bands is $1.153 - 1.352\mu$m (J-band), $1.468 - 1.804\mu$m (H-band), and $1.954 - 2.397\mu$m (K-band), but varies slightly depending on the horizontal slit location in the mask. The average exposure time for each mask is 2 hours per filter, reaching unobscured SFRs of ~ 1 $M_\odot$ yr^{-1} as traced by Balmer emission lines.

The data presented here are drawn from the first observing season of the MOSDEF survey, spanning five observing runs from 2012 December to 2013 May and comprising eight MOSFIRE masks.[1] Due to the range of field visibility, two of the masks observed during a pilot run in 2012 December target additional CANDELS legacy fields: one mask in GOODS-S and one in UDS. Each mask typically had ~ 30 $0\farcs7$ slits, yielding a resolution of, respectively, 3300 in J, 3650 in H, and 3600 in K. As motivated in Kriek et al. (2015), masks were generally observed using an ABA'B' dither sequence with $1\farcs5$ and $1\farcs2$ outer and inner nod amplitudes. However, during the first MOSDEF run in 2012 December, we experimented with an ABBA dither pattern. Individual exposure times within a dither sequence consisted of 180 seconds in K, and 120 seconds in J and H. The seeing as measured in individual exposures ranged from $0\farcs35$ to $1\farcs65$, with a median value of $0\farcs65$, and photometric conditions ranged from clear to variable. For galaxies at $z \sim 2.3$, the strongest features of interest are [O II]$\lambda\lambda$3726,3729 in the J band, Hβ and [O III]$\lambda\lambda$4959,5007 in the H band, and Hα, [N II]λ6584, and [S II]$\lambda\lambda$6717,6731 in the K band. Specifically, we use combinations of Hβ, [O III], Hα, and [N II] emission-line fluxes for metallicity estimates, Hα/Hβ line ratios for estimates of dust extinction, and dust-corrected Hα luminosities for estimates of SFRs.

The data were reduced using a custom IDL pipeline (see Kriek et al., 2015, for a full

[1]In addition to data collected on observing runs specifically scheduled for the MOSDEF project, H- and K-band observations were obtained by K. Kulas, I. McLean, and G. Mace in 2013 May for one MOSDEF mask in the GOODS-N field.

description). In brief, science frames were cut up into individual two-dimensional slits, flat-fielded, sky-subtracted, wavelength-calibrated, cleaned of cosmic rays, rectified, combined, and flux-calibrated. The relative spectral response was estimated using observations of B8 – A1 V standard stars matched in air mass to the science observations, while an initial absolute calibration was achieved by forcing the flux density in the spectrum of a reference star on the mask to match its cataloged photometry. Flux densities between different filters were verified to be consistent for those objects with detected continuum, confirming that the absolute calibration is valid across all filters. Two-dimensional error spectra were calculated including the effects of both Poisson counts from the sky and source as well as read noise. One-dimensional science and error spectra for the primary target in each slit were then optimally extracted (Horne, 1986), along with those of any serendipitous objects detected (Freeman et al., 2017). The initial absolute flux calibration for each spectrum was refined by estimating the amount of slit loss for each target relative to that for the reference star – a function of a two-dimensional elliptical Gaussian fit to the *HST* F160W image of the galaxy convolved with the average seeing profile estimated for each mask and filter. After slit loss correction, the flux densities of objects with detected continuum were consistent with broadband photometric measurements, and the systematic offset between spectroscopic and photometric flux densities was small compared to other sources of uncertainty.

Emission-line fluxes were measured by fitting Gaussian line profiles to the extracted, flux-calibrated one-dimensional spectra. Uncertainties on the emission-line fluxes were estimated by perturbing the one-dimensional spectrum many times according to the error spectrum, refitting the line profile, and measuring the width of the resulting distribution of fluxes. Redshifts were measured from the observed centroids of the highest signal-to-noise (S/N) emission lines, typically Hα or [O III]λ5007.

Stellar masses were estimated using the MOSDEF redshifts and pre-existing photometric data assembled by the 3D-HST team (Skelton et al., 2014). We modeled the photometric dataset for each galaxy with the SED-fitting program FAST (Kriek et al., 2009), assuming the stellar population synthesis models of Conroy et al. (2009) and a Chabrier (2003) IMF. Star-formation histories were parameterized using so-called delayed-τ models of the form

SFR(t)$\propto$ $te^{-t/\tau}$, where t is the stellar-population age, and τ is the e-folding timescale in the SFR. Dust extinction was described using the Calzetti et al. (2000) attenuation curve. For each galaxy, a grid in stellar population age, e-folding timescale, metallicity, and dust extinction was explored and χ^2 minimization was used to find the best-fitting model. The normalization of the best-fit model yielded the stellar mass. Confidence intervals in each stellar population parameter were determined using Monte Carlo simulations where the input SED was perturbed and refit 500 times. SFRs are based on dust-corrected Hα luminosities. Dust corrections are estimated from the ratio of Hα/Hβ, in which Hα and Hβ fluxes have been corrected for underlying Balmer absorption (Reddy et al., 2015). Balmer absorption equivalent widths for Hα and Hβ are measured from the best-fit SED model for each galaxy. $E(B\text{-}V)_{neb}$ is calculated assuming an intrinsic ratio of 2.86 and using the dust-attenuation curve of Calzetti et al. (2000). Dust-corrected Hα luminosities are translated into SFRs using the calibration of Kennicutt (1998), converted to a Chabrier (2003) IMF.

2.2.3 Sample Selection

We select a sample of $z \sim 2.3$ star-forming galaxies from early MOSDEF observations, requiring the following criteria:

1. Redshift in the range $2.08 \leq z \leq 2.61$ in order to have spectral coverage of Hα, Hβ, [O III]λ5007, and [N II]λ6584.

2. S/N ≥ 3 for Hα and Hβ to reliably measure the dust-corrected star formation rate.

3. Objects must not be flagged as an active galactic nucleus (AGN) in the MOSDEF catalog, identified by X-ray luminosity and infrared colors (Donley et al., 2012). Additionally, we require $\log([\text{N II}]\lambda6584/\text{H}\alpha) < -0.3$.

These criteria result in a sample of 88 $z \sim 2.3$ star-forming galaxies. One object is excluded from the sample because of a lack of wavelength coverage of [O III]λ5007 due to the location of the slit on the mask. Our final sample is therefore 87 galaxies with an average redshift of $\langle z \rangle = 2.296 \pm 0.126$. The sample redshift distribution is shown in the left panel of Figure 2.1.

The right panel of Figure 2.1 shows the specific SFR (SFR/M_*; sSFR) as a function of stellar mass for this sample, where sSFR values are based on dust-corrected Hα luminosities. The red dashed line shows the broken power-law fit to the star-forming sequence at $2.0 < z < 2.5$ by Whitaker et al. (2014), where SFR was determined using IR and UV luminosity. Our MOSDEF sample of $z \sim 2.3$ star-forming galaxies is consistent with this sequence and does not show any obvious bias towards high SFR at a given stellar mass. To better understand the biases of our sample, we divide the sample into four bins in stellar mass such that each bin contains approximately the same number of galaxies and take the median sSFR and M_* of each bin, shown as green stars. Our high-redshift sample is quite representative across the mass range $\log(M_*/M_\odot) \sim 9.4 - 10.5$, although there may be a very slight bias toward high-SFR galaxies at low stellar masses.

In order to study the evolution of the MZR from $z \sim 0$ to $z \sim 2.3$, we select a sample of local galaxies from the Sloan Digital Sky Survey (SDSS; York et al., 2000) Data Release 7 (DR7; Abazajian et al., 2009) catalog. Emission-line measurements and galaxy properties are taken from the MPA-JHU catalog of measurements for SDSS DR7.[2] We require the following criteria:

1. Minimum redshift restriction of $z \geq 0.04$ to avoid aperture effects.
2. Maximum redshift restriction of $z < 0.1$ to keep the sample local and avoid any redshift evolution in the MZR, observed at redshifts as low as $z \sim 0.3$ (Lara-López et al., 2013).
3. Measured stellar mass (Kauffmann et al., 2003a).
4. S/N ≥ 5 for Hα, Hβ, [O III]λ5007, and [N II]λ6584.

AGN are rejected using the criterion of Kauffmann et al. (2003b), producing a comparison sample of 70,321 local galaxies.

[2]Available at `http://www.mpa-garching.mpg.de/SDSS/DR7/`

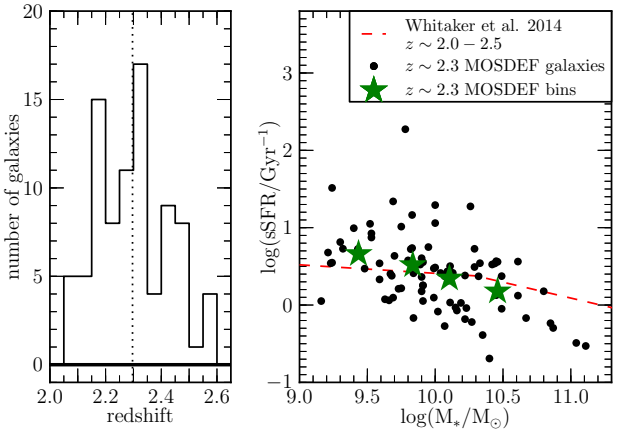

Figure 2.1: Properties of the $z \sim 2.3$ MOSDEF MZR sample, containing 87 star-forming galaxies. Left: Redshift distribution, in which the vertical dotted line shows the mean redshift of $\langle z \rangle = 2.296$ with a standard deviation of 0.126. Right: sSFR vs. M_* for the $z \sim 2.3$ sample. Black points show individual MOSDEF galaxies. The red dashed line shows the broken power-law fit to the $2.0 < z < 2.5$ star-forming sequence from Whitaker et al. (2014), with SFRs based on IR and UV luminosity. Green stars show the median sSFR and M_* after dividing the MOSDEF sample into four bins in stellar mass such that each bin contains ~ 22 galaxies.

2.3 Metallicity

We use the N2 ($\log$ ([N II]λ6584/Hα)) and O3N2 ($\log$ (([O III]λ5007/Hβ)/([N II]λ6584/Hα))) indicators to estimate oxygen abundances. For both indicators, we use the calibrations of Pettini & Pagel (2004) based on a sample of H II regions with direct electron temperature measurements. These calibrations are given by

$$12 + \log\,(\mathrm{O/H}) = 8.90 + 0.57 \times \mathrm{N2} \tag{2.1}$$

$$12 + \log\,(\mathrm{O/H}) = 8.73 - 0.32 \times \mathrm{O3N2} \tag{2.2}$$

where $12 + \log\,(\mathrm{O/H})$ is the oxygen abundance. The N2 and O3N2 calibrations have systematic uncertainties of 0.18 and 0.14 dex, respectively. Analyses were also performed using the N2 calibration of Maiolino et al. (2008), but these results are omitted from this study as they are very similar to those based on the Pettini & Pagel (2004) N2 calibration.

The MZR for $z \sim 2.3$ star-forming galaxies from the MOSDEF sample is shown in

Figure 2.2 with metallicities determined using the N2 indicator (left) and O3N2 indicator (right). We present 53 individual detections and 34 upper limits: the largest rest-frame optical selected sample of individual measurements for which the MZR has been observed at $z > 2$. Black points indicate $z \sim 2.3$ MOSDEF galaxies with detections of all lines, downward arrows indicate 3σ upper limits where [N II]λ6584 was not detected at 3σ significance or greater, and gray blocks show the density of local SDSS galaxies. The mean uncertainty on a single MOSDEF point, excluding the calibration uncertainty, is shown by the black error bar in the lower left-hand corner. We observe a progression in metallicity with increasing mass among the individual $z \sim 2.3$ galaxies, with the upper limits suggesting this trend continues to lower metallicities at low stellar masses. The scatter amongst individual points is large with respect to the range of parameter space covered, with smaller scatter in the O3N2 MZR than in the one based on N2. When we include only detections, the N2 and O3N2 MZRs have Spearman correlation coefficients of 0.31 and 0.53, respectively, corresponding to likelihoods of 0.022 and 4.0×10^{-5} that M_* and metallicity are uncorrelated.

There are three detections in the mass range $\log(M_*/\mathrm{M}_\odot) \sim 9.5 - 10$ with unusually large [N II]λ6584/Hα ratios for their stellar masses, causing these galaxies to appear as outliers with high metallicities in the N2 MZR. Of these three objects, two also have high [O III]λ5007/Hβ ratios and are offset in the [O III]/Hβ vs. [N II]/Hα diagnostic diagram (BPT diagram; Baldwin et al., 1981) into a region occupied by AGN in the local universe, lying slightly above both the Kewley et al. (2001) $z \sim 0$ "maximum- starburst" line and the "evolved" $z \sim 2$ line from Kewley et al. (2013a). Thus, we consider these two objects to be potential optical AGN candidates. However, given that high-redshift star-forming galaxies are offset from the local star-forming sequence in the BPT diagram (Shapley et al., 2005; Liu et al., 2008; Kewley et al., 2013b; Shapley et al., 2015; Steidel et al., 2014), local demarcations dividing star-forming galaxies and AGN in this parameter space likely need to be revised for application at high redshifts (see Coil et al., 2015). There is no indication based on X-ray properties and rest-frame near-IR colors that these two objects are AGN (Coil et al., 2015), although the X-ray upper limits on these objects are not very constraining, and furthermore none of the N2 outliers are offset in the O3N2 MZR. For these reasons, we retain these

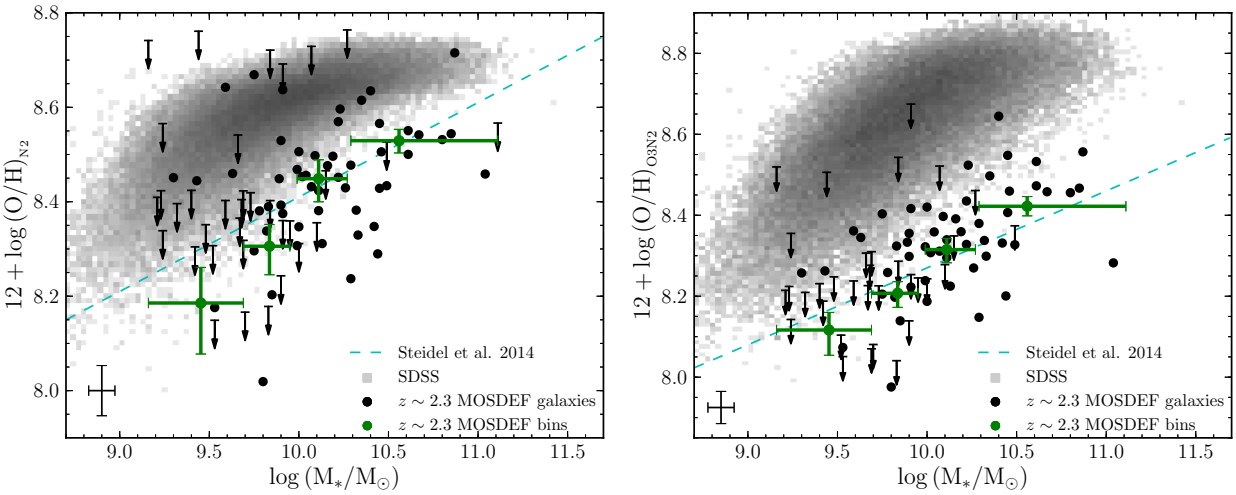

Figure 2.2: The MZR for $z \sim 2.3$ star-forming galaxies with metallicities determined using the N2 (left) and O3N2 (right) indicators. Black points indicate MOSDEF galaxies with 3σ or greater significance in Hα, [N II]λ6584, Hβ, and [O III]λ5007. Black arrows indicate 3σ upper limits where [N II]λ6584 was not detected. The black error bar in the lower left-hand corner shows the mean uncertainty in 12+log (O/H) and stellar mass for individual MOSDEF galaxies, excluding the calibration error. The gray two-dimensional histogram shows the density of local SDSS galaxies in this parameter space. Green points with error bars represent stacks of individual $z \sim 2.3$ galaxies containing ~ 22 galaxies each, in which the oxygen abundance was estimated from the emission-line measurements of composite spectra and the stellar mass is plotted at the mean $\log(M_*/\mathrm{M}_\odot)$. The vertical error bar indicates the uncertainty in oxygen abundance estimated from the uncertainty on composite emission-line fluxes, excluding the calibration error. The horizontal error bar shows the range of M_* for a given bin. The cyan dashed line shows the best-fit line to the $z \sim 2.3$ N2 and O3N2 MZR as observed by Steidel et al. (2014).

objects in the sample as star-forming galaxies, although removing them from the sample has a negligible effect on the results presented in Figure 2.2.

The cyan dashed line in Figure 2.2 shows the best fit to the $z \sim 2.3$ N2 and O3N2 MZR as observed by Steidel et al. (2014) based on independent datapoints. While generally consistent in normalization, the MOSDEF sample suggests a steeper slope of the MZR than the sample of Steidel et al. (2014). This inconsistency can be at least partially attributed to a difference in selection criteria. The sample of Steidel et al. (2014) is rest-frame ultraviolet selected, which results in biases against galaxies with low SFRs and low stellar masses, as well as abundantly dusty galaxies at all masses (Reddy et al., 2012). The MOSDEF sample is rest-frame optical selected and less susceptible to these biases, as shown in Figure 2.1. It is interesting to note that Steidel et al. (2014) observe higher metallicities at low M_* where their sample has higher typical SFRs than the MOSDEF sample. This offset is contrary to what one would expect based on the local FMR. Steidel et al. (2014) also use a lower detection threshold, considering lines with 2σ significance as detections, which could have an effect on the observed low-mass slope of the MZR where the [N II]λ6584 line is very weak.

To determine more clearly where the $z \sim 2.3$ MZR lies with respect to the local MZR, we separated the MOSDEF galaxies into four bins in stellar mass such that each mass bin had approximately the same number of galaxies and created a composite spectrum for each mass bin. Individual spectra were first shifted into the rest-frame, converted from flux density to luminosity density, and normalized by Hα luminosity in order to obtain mean line ratios of the galaxies in the bin, as well as prevent high-SFR galaxies from dominating the composite spectrum. The Hα-normalized spectra were interpolated on a grid with wavelength spacing equal to the rest-frame wavelength spacing of the average redshift of the sample. This yields wavelength spacings of 0.49 Å in the H-band and 0.66 Å in the K-band. At each wavelength increment, the median value of the normalized spectra in the bin was selected to create a normalized composite spectrum. The normalized composite spectrum was then multiplied by the average Hα luminosity in that bin to give the final composite spectrum in units of luminosity density (erg s^{-1} Å^{-1}). In order to create error spectra for the composite spectra, we first perturbed the stellar masses according to their uncertainties assuming a

log-normal distribution, then separated the objects into four stellar mass bins with the same mass ranges used to produce the original composite spectra. Within each bin, we bootstrap resampled to account for sample variance and perturbed the spectrum of each object in the bootstrap sample according to the error spectrum of that object to account for measurement uncertainty. The resulting perturbed spectra were combined to form a new composite spectrum. This process was repeated 2500 times to build up a well-sampled distribution of luminosities for each wavelength increment. The magnitude of the error spectrum at a given wavelength is half of the 68th-percentile width of this distribution. The composite spectra and composite error spectra of the four stellar mass bins for the $z \sim 2.3$ sample are shown in Figure 2.3.

Emission-line fluxes were measured by fitting Gaussian line profiles to emission lines in the composite spectra. As can be seen in the composite spectra, none of the lines of interest are blended, so lines were fit separately with single Gaussian profiles. We required [N II]λ6584 to have the same width as Hα. Uncertainties on the line fluxes were estimated using the 68th-percentile half-width of the distribution of line fluxes obtained by perturbing the composite spectrum according to the composite error spectrum and remeasuring the line fluxes 1000 times. Measured emission-line fluxes and uncertainties for the composite spectra were converted into metallicities using equations (6.7) and (6.8). Emission-line measurements and oxygen abundances from the composite spectra are presented in Table 2.1, as well as the average galaxy properties of the bins. We note that in the lowest stellar mass bin, [N II]λ6584 has a significance lower than 3σ with respect to the uncertainty on the emission-line flux. However, the significance is greater than 3σ when using the RMS scatter of a blank portion of the composite spectrum as the error spectrum. Past studies have used this technique to estimate uncertainties on emission-line fluxes from stacked spectra (Erb et al., 2006; Andrews & Martini, 2013). Given our very conservative process for estimating uncertainties, and in order to be comparable to other works, we treat all measurements of the composite spectra that have significance greater than 3σ when using the RMS scatter as detections, and as limits otherwise. This practice is adopted throughout this chapter. Plotted error bars still denote the uncertainty estimated by the process described above.

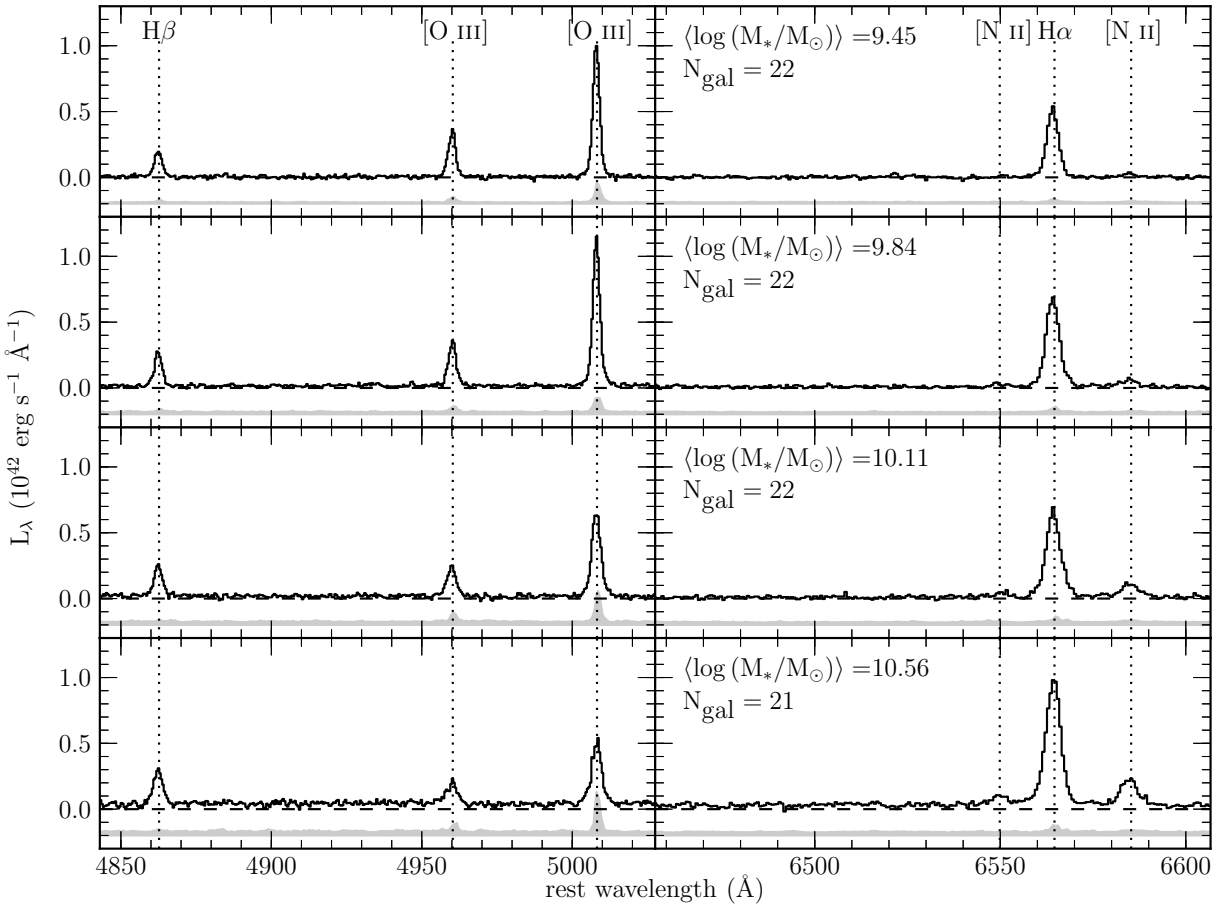

Figure 2.3: Composite spectra for the $z \sim 2.3$ sample separated into four stellar mass bins. Composite error spectra are shown as a gray band offset below the composite spectra for clarity. Each bin contains ~ 22 galaxies. The average $\log(M_*/\mathrm{M}_\odot)$ for each bin is shown, with mass increasing from top to bottom. Dotted vertical lines highlight strong rest-frame optical emission lines. From left to right, these lines are Hβ, [O III]λ4959, [O III]λ5007, [N II]λ6548, Hα, and [N II]λ6584.

Table 2.1: Galaxy properties and emission-line luminosities from $z \sim 2.3$ composite spectra

$\log(\frac{M_*}{M_\odot})^a$	$\langle\log(\frac{M_*}{M_\odot})\rangle^b$	N_{gal}^c	SFR_{med}^d ($M_\odot$ yr^{-1})	$L_{[N\ II]}^e$ (10^{42} erg s^{-1})	$L_{H\alpha}^e$ (10^{42} erg s^{-1})	$L_{[O\ III]}^e$ (10^{42} erg s^{-1})	$L_{H\beta}^e$ (10^{42} erg s^{-1})	$12+\log(O/H)$ N2[f]	$12+\log(O/H)$ O3N2[g]
Full sample									
9.15-9.68	9.45	22	11.6	0.11 ± 0.04	2.03 ± 0.05	2.78 ± 0.14	0.60 ± 0.03	$8.18^{+0.07}_{-0.10}$	$8.11^{+0.04}_{-0.06}$
9.68-9.94	9.84	22	23.4	0.27 ± 0.05	3.03 ± 0.08	3.21 ± 0.14	0.82 ± 0.05	$8.30^{+0.04}_{-0.05}$	$8.20^{+0.02}_{-0.03}$
9.99-10.27	10.11	22	26.8	0.49 ± 0.08	3.05 ± 0.10	2.44 ± 0.20	0.76 ± 0.06	$8.44^{+0.04}_{-0.04}$	$8.31^{+0.02}_{-0.03}$
10.29-11.11	10.56	21	53.8	1.07 ± 0.10	4.82 ± 0.12	2.01 ± 0.21	0.98 ± 0.08	$8.52^{+0.02}_{-0.02}$	$8.42^{+0.02}_{-0.02}$
High-SFR subsample									
9.23-9.89	9.70	11	37.1	0.26 ± 0.08	3.61 ± 0.05	4.35 ± 0.20	0.83 ± 0.08	$8.25^{+0.06}_{-0.08}$	$8.13^{+0.03}_{-0.05}$
9.90-10.11	10.02	11	30.5	0.58 ± 0.11	3.49 ± 0.08	2.72 ± 0.25	0.79 ± 0.09	$8.45^{+0.04}_{-0.05}$	$8.31^{+0.03}_{-0.03}$
10.13-10.45	10.33	11	74.2	0.80 ± 0.19	5.46 ± 0.10	2.92 ± 0.30	1.09 ± 0.14	$8.42^{+0.05}_{-0.06}$	$8.32^{+0.03}_{-0.04}$
10.46-11.11	10.73	11	41.2	1.09 ± 0.12	4.71 ± 0.12	1.88 ± 0.27	0.89 ± 0.11	$8.53^{+0.02}_{-0.02}$	$8.42^{+0.03}_{-0.03}$
Low-SFR subsample									
9.15-9.47	9.32	11	11.1	0.09 ± 0.04	1.83 ± 0.08	2.69 ± 0.22	0.57 ± 0.05	8.28^h	8.16^h
9.52-9.75	9.65	11	9.26	0.14 ± 0.08	1.82 ± 0.07	2.40 ± 0.10	0.50 ± 0.05	$8.27^{+0.12}_{-0.16}$	$8.16^{+0.07}_{-0.09}$
9.80-10.02	9.89	11	14.5	0.22 ± 0.08	2.59 ± 0.09	2.68 ± 0.30	0.76 ± 0.07	$8.29^{+0.07}_{-0.10}$	$8.21^{+0.04}_{-0.06}$
10.07-10.40	10.21	10	11.7	0.43 ± 0.09	2.19 ± 0.10	1.44 ± 0.13	0.62 ± 0.07	$8.50^{+0.05}_{-0.06}$	$8.38^{+0.03}_{-0.04}$

(a) Range of $\log(M_*/M_\odot)$ of galaxies in a bin.

(b) Average $\log(M_*/M_\odot)$ of galaxies in a bin.

(c) Number of galaxies in a bin.

(d) Median dust-corrected Hα SFR of galaxies in a bin.

(e) Emission-line luminosity and uncertainty on [N II]λ6584, Hα, [O III]λ5007, and Hβ, as measured from the composite spectra.

(f) Oxygen abundance and uncertainty determined with the N2 indicator using equation (6.7).

(g) Oxygen abundance and uncertainty determined with the O3N2 indicator using equation (6.8).

(h) 3σ upper limit on the oxygen abundance where [N II]λ6584 is not detected.

Measurements from the four mass bins are shown in green in Figure 2.2. Bin points are plotted at the average $\log(M_*/\mathrm{M}_\odot)$, the vertical error bar is the uncertainty in the oxygen abundance, and the horizontal error bar shows the range of stellar masses in that bin. The calibration uncertainty is not included in the metallicity uncertainty. Note that the calibration uncertainty should be reduced by a factor of $\sqrt{\mathrm{N}}$ when using stacked spectra, where N is the number of galaxies in the stack (Erb et al., 2006). The reduction in the calibration uncertainty is approximately a factor of $\sqrt{22} \approx 4.7$ for our mass bins, yielding binned calibration uncertainties of 0.038 and 0.030 dex respectively for the N2 and O3N2 calibrations.

After binning $z \sim 2.3$ MOSDEF galaxies according to stellar mass, we find a clear progression in which metallicity increases monotonically as stellar mass increases, in agreement with previous studies (Erb et al., 2006; Maiolino et al., 2008; Steidel et al., 2014). This progression is well described by a single power law when determining metallicities with the O3N2 indicator, while it appears to flatten at high stellar masses when metallicities are based on the N2 indicator. We note that the two indicators yield different values for the low-mass slope of the MZR, which is an important test of outflow models. This difference is further evidence that care must be taken interpreting results that are dependent on the metallicity calibration used (Kewley & Ellison, 2008; Andrews & Martini, 2013), and demonstrates that disagreement between metallicity indicators persists at high redshifts. We find that the $z \sim 2.3$ MZR is offset below the local MZR by $\sim 0.15 - 0.3$ dex and ~ 0.3 dex based on the N2 and O3N2 indicators, respectively. The offset observed with the N2 indicator is very similar to that found by Erb et al. (2006) using stacked spectra of $z \sim 2.2$ galaxies and the Pettini & Pagel (2004) N2 metallicity calibration. However, the N2 indicator must be used with caution at high redshifts due to secondary dependences on the ionization parameter, N/O abundance ratio, and hardness of the ionizing spectrum, some or all of which may evolve with redshift. In addition to these parameters, the N2 line ratio can be significantly affected by the presence of shock excitation which could be present in high-redshift galaxies due to large gas flows (Newman et al., 2014). It is likely that the true offset in the N2 MZR is larger than that shown in Figure 2.2 since the N2 indicator is believed to overestimate

the metallicity at high redshifts (Liu et al., 2008; Newman et al., 2014). While changes in parameters such as the N/O abundance ratio could also bias metallicity estimates of the O3N2 indicator, Liu et al. (2008) and Steidel et al. (2014) have found that O3N2 is significantly less biased than the N2 indicator. One aspect of the $z \sim 2.3$ MOSDEF sample is the requirement of both Hα and Hβ detections in order to estimate dust-corrected SFRs. We tested that the S/N requirement for Hβ does not bias the $z \sim 2.3$ sample against dusty metal-rich galaxies by including galaxies with Hβ upper limits in the composite spectra. Emission line measurements from such composite spectra agreed with those presented in Table 2.1 to better than 1σ and displayed no systematic offset.

In order to investigate the SFR dependence of the $z \sim 2.3$ MZR, we divide the sample into high-SFR and low-SFR subsamples at the median SFR, as shown in Figure 2.4. The median SFR of the total sample is 25.9 $M_\odot$ yr^{-1}, while the median SFRs of the high- and low-SFR subsamples are 41.1 $M_\odot$ yr^{-1} and 11.8 $M_\odot$ yr^{-1}, respectively. The abundance of upper limits, especially in the low-M_*, low-SFR regime, makes it difficult to determine if SFR dependence is present. There is only a narrow mass range of $\log(M_*/M_\odot) \sim 10.0 - 10.5$ that is populated by detections from both the high- and low-SFR subsample without a significant number of limits. Although this region may appear to suggest SFR dependence among individual $z \sim 2.3$ galaxies, a larger dynamic range in stellar mass is needed to confirm any trend. Additionally, much of the division seen between the high- and low-SFR subsamples in Figure 2.4 is a manifestation of the M_*-SFR relation for star-forming galaxies, according to which lower SFRs are more common among low-mass galaxies. Indeed, dividing a sample by SFR alone results in an offset between the average stellar masses for the two SFR subsamples (see Figure 2.4), with high-SFR objects characterized by higher stellar masses on average than those in the low-SFR subsample. In order to overcome the difficulty of interpreting upper limits in $12 + \log(O/H)$ and avoid stellar mass selection effects, we created composite spectra in four bins of stellar mass for each SFR subsample. Binning in both SFR and stellar mass is equivalent to selecting galaxies with a narrow range of sSFR, a property which has a weaker mass dependence than SFR. The median SFRs of the high-SFR bins range from $37.1 - 74.2$ $M_\odot$ yr^{-1}, while the median SFRs of the low-

SFR bins range from $9.3 - 14.5$ $M_\odot$ yr^{-1}. Composite spectra were produced by applying the same binning and stacking process outlined above to each subsample. Emission-line measurements and metallicity estimates were obtained in the same manner as before. Bin properties, emission-line measurements, and oxygen abundances for the high- and low-SFR subsamples are presented in Table 2.1.

In Figure 2.5, the high-SFR, low-SFR, and full sample bins are shown in blue, red, and green, respectively, with error bars as in Figure 2.2. Horizontal bars with downward arrows denote 3σ upper limits where [N II]λ6584 was not detected. For a comparison to the local universe, we use measurements from the stacked SDSS spectra of Andrews & Martini (2013). These stacks constitute a fair comparison to the $z \sim 2.3$ MOSDEF stacks as the galaxies are also binned according to M_* and SFR and the spectra are combined in a very similar manner to our method. We use published emission-line measurements for the Andrews & Martini (2013) stacks to estimate the metallicities using equations (6.7) and (6.8). The SDSS stacks are shown in Figure 2.5 as squares, where the color represents the SFR range of that bin. The SDSS stacks can be compared directly to the $z \sim 2.3$ stacks as they are produced using the same methods, same metallicity calibrations, and consistent SFR estimates.

We do not see evidence of significant SFR dependence in the $z \sim 2.3$ MZR. Bins of the high- and low-SFR subsamples do not follow a different MZR from that of the full sample bins within the uncertainties. Error bars of the high- and low-SFR subsample bins overlap with the full sample and each other, and the SFR subsamples appear to scatter about the full sample. While there may still be SFR dependence of the MZR at $z \sim 2.3$, our current sample lacks the size and possibly the dynamic range required to resolve it. By comparing the Andrews & Martini (2013) SDSS M_*-SFR bins to the $z \sim 2.3$ MOSDEF bins, we find that $z \sim 2.3$ galaxies have lower metallicities at a given M_* and SFR than is observed locally, with the high-redshift bins being offset $\sim$0.1 dex below the local bins. This result is confirmed using both the N2 and O3N2 indicators. According to the median SFRs of the MOSDEF bins, the low-SFR subsample matches the medium blue SDSS bins ($10 - 31.6$ $M_\odot$ yr^{-1}) and the high-SFR subsample matches the dark blue SDSS bins ($31.6 - 100$ $M_\odot$ yr^{-1}). Due to the increase with redshift of the typical sSFR at a given stellar mass, we can only compare the

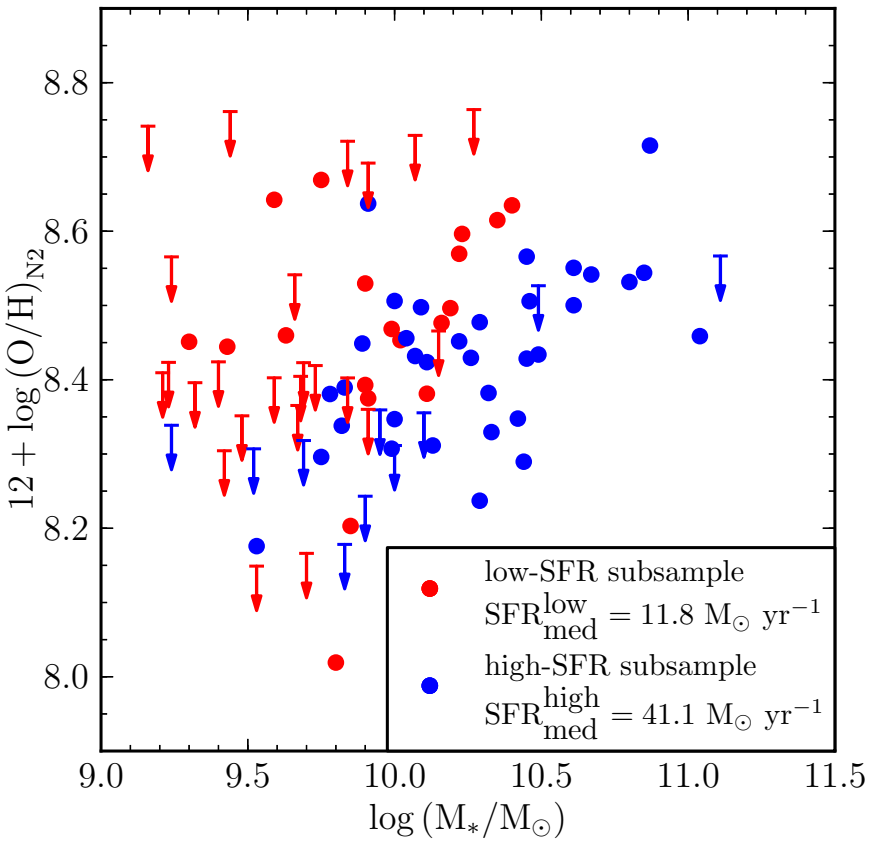

Figure 2.4: SFR dependence in the MZR at $z \sim 2.3$. Individual galaxies in the $z \sim 2.3$ sample are divided into high- and low-SFR subsamples at the median SFR of 25.9 $\mathrm{M_\odot\ yr^{-1}}$. The high- and low-SFR subsamples have median SFRs of 11.8 $\mathrm{M_\odot\ yr^{-1}}$ and 41.1 $\mathrm{M_\odot\ yr^{-1}}$, respectively.

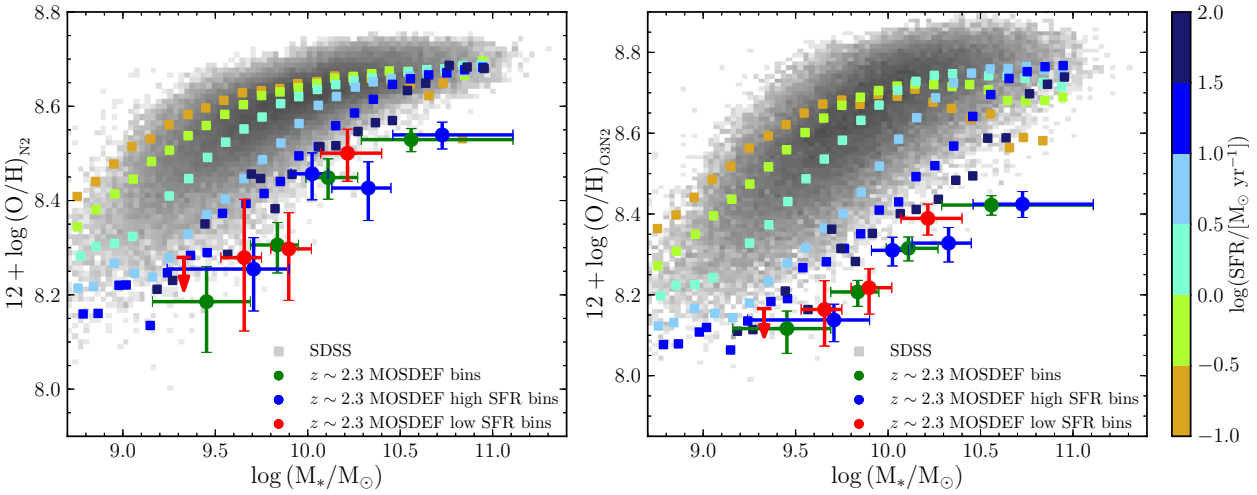

Figure 2.5: Comparison of M_*, metallicity, and SFR between $z \sim 2.3$ and local galaxies. The $z \sim 2.3$ high- and low-SFR subsamples are separated into four stellar mass bins, with metallicities determined using the N2 (left) and O3N2 (right) indicators. The blue and red points and error bars indicate bins of the high- and low-SFR subsamples, respectively. The green points with error bars indicate stellar mass bins from the full sample. Error bars for all binned points are the same as in Figure 2.2. The gray two-dimensional histogram shows the density of local SDSS galaxies in this parameter space. Colored squares are M_*-SFR bins of local SDSS star-forming galaxies from Andrews & Martini (2013), with the color indicating the range of SFRs in a bin (see colorbar). Red MOSDEF $z \sim 2.3$ bins are comparable to SDSS bins with $\log(\mathrm{SFR}) = 1.0 - 1.5$ (medium blue), while blue MOSDEF bins are comparable to those with $\log(\mathrm{SFR}) = 1.5 - 2.0$ (dark blue).

$z \sim 2.3$ MOSDEF sample with the high-SFR tail of the local distribution of star-forming galaxies. However, given the large size of the local sample, this high-SFR tail contains a sufficient number galaxies for a robust comparison ($\sim 10^4$).

Given that there are SDSS bins across the entire range of stellar masses probed by the MOSDEF sample, the MOSDEF bins should have the same metallicities as the SDSS bins with comparable M_* and SFR if the local FMR holds at this redshift. This is not the case. We conclude that $z \sim 2.3$ star-forming galaxies do not lie on the local FMR. An alternate explanation of this offset is that local metallicity calibrations do not hold at high redshifts, discussed further in Section 4.5. However, there is evidence that the N2 indicator may overestimate the oxygen abundance in high-redshift galaxies (Liu et al., 2008; Newman et al., 2014), in which case the true offset would be larger than the one displayed in Figure 2.5, strengthening the claim that $z \sim 2.3$ galaxies do not fall on the local FMR.

The O3N2 indicator is not expected to be significantly affected by redshift evolution (Steidel et al., 2014).

2.4 Summary and Discussion

In this chapter, we used early observations from the MOSDEF survey to investigate the $z \sim 2.3$ mass-metallicity relationship. Results were based on 87 galaxies with individual measurements from a rest-frame optical selected sample with coverage of all strong optical emission lines. We find a clear positive correlation between M_* and metallicity using composite spectra of galaxies binned by stellar mass. At this point, we defer measurements of the scatter and slope of the $z \sim 2.3$ MZR due to uncertainty regarding the reliability of local metallicity calibrations at high redshifts, discussed below.

We investigated the SFR dependence of the $z \sim 2.3$ MZR by dividing the sample at the median SFR and making composite spectra of galaxies binned according to stellar mass within the high- and low-SFR subsamples. We do not observe a significant dependence of metallicity on SFR at a given M_*. However, there is not strong SFR dependence of metallicity within local SDSS galaxies at comparable SFRs, as seen in the medium and dark blue squares in Figure 2.5. Given the uncertainties in oxygen abundance measurements for the $z \sim 2.3$ SFR bins, we are unable to resolve SFR dependence at the level that is observed in bins of local galaxies. Larger samples at $z \sim 2.3$ will be required to confirm or rule out such SFR dependence.

An outstanding question in galaxy evolution is whether or not high redshift galaxies fall on the local FMR. If the FMR is universal and redshift independent, then high- and low-redshift galaxies have similar metallicity equilibrium conditions for the balance between gas inflows and outflows, and star formation. To address this question, we compared the $z \sim 2.3$ MOSDEF stacks to composite spectra of local star-forming galaxies from Andrews & Martini (2013). We find $z \sim 2.3$ star-forming galaxies are ~ 0.1 dex lower in metallicity for a given M_* and SFR than the local FMR predicts, in agreement with some high redshift studies (Zahid et al., 2014b; Cullen et al., 2014; Troncoso et al., 2014; Wuyts et al., 2014).

Other studies have found agreement with the local FMR at these redshifts (e.g., Belli et al., 2013).

Of key importance to our study is the ability to directly compare SFR, stellar mass, and metallicity between the $z \sim 2.3$ MOSDEF sample and the local comparison sample. The SFRs used by Andrews & Martini (2013) were estimated following Brinchmann et al. (2004) which utilizes multiple emission lines simultaneously to estimate the SFR, but heavily weights Hα and Hβ, and is thus consistent with SFRs estimated using dust-corrected Hα. We have independently confirmed this consistency with SDSS DR7 measurements. Furthermore, both MOSDEF and SDSS SFRs are corrected to total galaxy SFRs, with estimates for slit losses in the case of MOSDEF, and fiber losses in the case of SDSS. Stellar masses for both MOSDEF and SDSS galaxies[3] are based on SED-fitting to broadband photometry. Finally, we use a stacking procedure nearly identical to that of Andrews & Martini (2013) and estimate metallicity using the same indicators and calibrations for each dataset. In summary, our comparison to the Andrews & Martini (2013) stacks constitutes a fair and direct FMR comparison because the two samples use the same metallicity calibrations and methods for stacking galaxy spectra, as well as consistent SFR and stellar mass estimates.

One difference between the $z \sim 2.3$ MODSEF sample and the local comparison sample is the method of obtaining spectra. MOSDEF data are obtained by placing a $0\farcs7$ slit on the target which typically contains a large fraction of the total light from the galaxy, while SDSS spectra are obtained by placing a 3"-diameter fiber on the centers of galaxies. Measured metallicities can be sensitive to the method of obtaining spectra if radial metallicity gradients are present. In the local universe, star-forming galaxies exhibit negative radial metallicity gradients such that the inner regions of galaxies (probed by SDSS fibers) are more metal-rich than the outer regions (e.g., Vila-Costas & Edmunds, 1992). At $z > 2$, observations have not yet confirmed the existence of ubiquitous metallicity gradients among star-forming galaxies, with various groups reporting negative, flat, or even positive (inverted) metallicity gradients

[3]Stellar mass estimates from the MPA-JHU SDSS DR7 spectroscopic catalog are based on fits to the photometry rather than spectral indices of stellar absorption features which were used for previous releases. See `http://www.mpa-garching.mpg.de/SDSS/DR7/mass_comp.html` for a comparison of SDSS stellar masses based on indices and photometry.

(Cresci et al., 2010; Jones et al., 2010, 2013; Queyrel et al., 2012; Stott et al., 2014). It is not currently possible to estimate how metallicity measurements at high redshifts may be biased because of metallicity gradients. However, due to the optimal extraction method we used, the line ratios measured for the MOSDEF sample are dominated by light from the inner regions of galaxies where the surface brightness is greatest. Thus, both MOSDEF and SDSS measure the metallicity of the innermost regions of star-forming galaxies.

An additional strength of our comparison is that it does not depend on any extrapolation of a parameterization of the local FMR and is thus free of the effects that the choice of extrapolation used can have on conclusions regarding the FMR, described in Maier et al. (2014). We emphasize that proper investigation of the universality of the FMR with redshift requires *both* checking for consistency with the local FMR or its projections *and* looking for SFR dependence within the high-redshift sample. Many previous studies have overlooked SFR dependence within the sample, or have been unable to investigate this aspect of the FMR due to small or incomplete samples. We have done both in this investigation, and additionally used dust-corrected Hα SFRs which are independent of the SED fitting used to determine stellar masses. A consistency of the bulk properties of a high-redshift sample with the local FMR is not sufficient proof that the relationship between SFR, M_*, and metallicity is the same at high redshifts.

If the observed $z \sim 2.3$ offset from the local FMR is real and not an artifact arising from unreliable metallicity calibrations at high redshifts, it may be evidence of the "gas accumulation phase" described by Davé et al. (2012). This phase occurs during galaxy growth when a galaxy cannot process inflowing gas and form stars as quickly as gas is accreted, building up the gas reservoir. In this case, metallicities are lower than expected at a given M_* and SFR because the ISM metallicity is diluted faster than metals are produced in stars. Large accretion rates can cause this imbalance, suggesting the possibility that the environments of $z \sim 2.3$ star-forming galaxies lead to high gas accretion rates. There is some evidence in the literature of extreme accretion rates at $z \gtrsim 2$, as suggested by gas mass fractions and sSFR (Tacconi et al., 2010, 2013; Reddy et al., 2012). However, the end of the gas accumulation phase is predicted to occur at $z \gtrsim 4$ (Davé et al., 2012), as has

been suggested by models of the star-formation histories of Lyman-break galaxies (Papovich et al., 2011).

We present these results with one very important caveat. Accurately determining metallicities at different redshifts is of key importance to studying the evolution of the MZR. In the local universe, relationships between strong emission line ratios and metallicity can be calibrated to "direct" electron temperature-determined metallicities from measuring auroral lines such as [O III]λ4363 (Pettini & Pagel, 2004; Pilyugin & Thuan, 2005) or photoionization models of star-forming regions (Zaritsky et al., 1994; Kewley & Dopita, 2002; Kobulnicky & Kewley, 2004; Tremonti et al., 2004). At redshifts above $z \sim 1$, it is nearly impossible to detect weak auroral lines for directly determining metallicity (but see Yuan & Kewley, 2009; Rigby et al., 2011; Brammer et al., 2012b; Christensen et al., 2012; Maseda et al., 2014). Creating photoionization models that suitably represent high-redshift star-forming regions requires knowledge of physical parameters which have been poorly constrained up to this point. Thus, it is unknown if local metallicity calibrations hold at high redshifts. Figure 2.6 shows a comparison between metallicities determined using the O3N2 indicator and the N2 indicator for both local SDSS galaxies (grey points) and MOSDEF $z \sim 2.3$ galaxies (black points). The black dashed line indicates a one-to-one relationship. If local calibrations do indeed hold at high redshifts, then the relationship between metallicities determined from different indicators should not evolve with redshift. It is clear that the $z \sim 2.3$ galaxies are offset below the local galaxies. The dotted line is the best-fit line of slope unity to the individual $z \sim 2.3$ galaxies, yielding an offset of -0.1 dex from a one-to-one correspondence, over twice that displayed by the SDSS sample. Steidel et al. (2014) found an offset slightly larger than this at $z \sim 2.3$. This offset demonstrates that the two metallicity indicators are not evolving in the same way with redshift, and shows the need of metallicity calibrations appropriate for high redshift galaxies.

There is mounting evidence in the literature that high-redshift star-forming galaxies have markedly different emission line ratios from those of local star-forming galaxies (Shapley et al., 2005; Liu et al., 2008; Hainline et al., 2009; Masters et al., 2014; Steidel et al., 2014). This has been observed as an offset of the star-forming sequence in the BPT diagram for

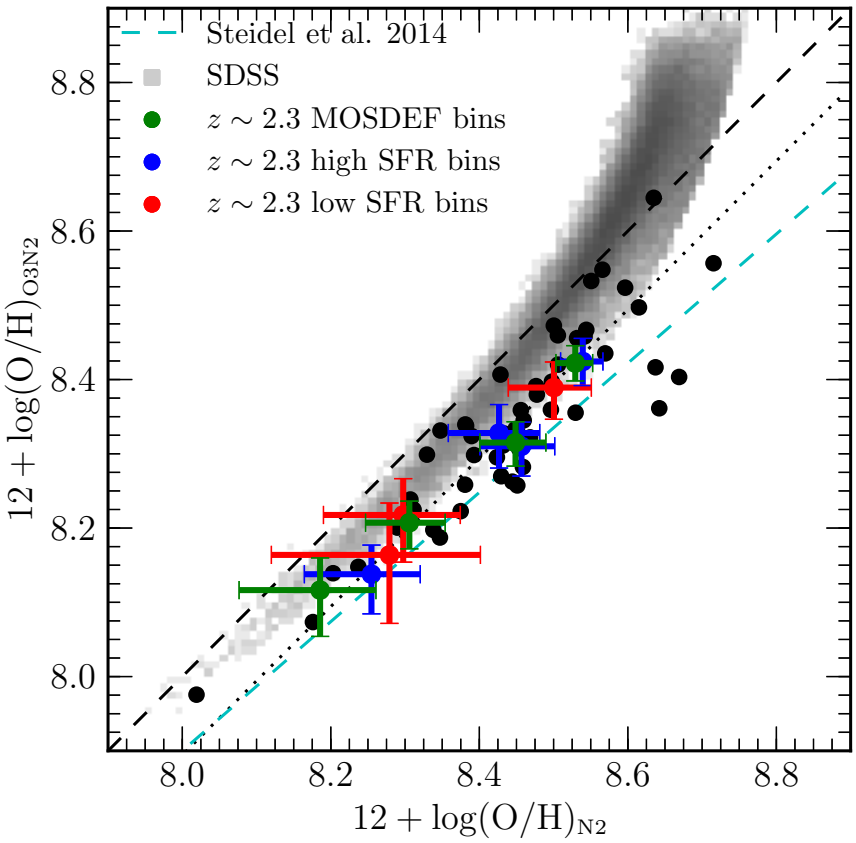

Figure 2.6: Comparison of metallicities estimated using the N2 and O3N2 indicators. The gray blocks show the density of local SDSS galaxies. Individual $z \sim 2.3$ galaxies with detections in Hβ, [O III]λ5007, Hα, and [N II]λ6584 are indicated by black points. Green points and error bars represent stellar mass bins of the full $z \sim 2.3$ sample, while blue and red points and error bars indicate the high- and low-SFR subsamples, respectively. The black dashed line indicates a one-to-one correspondence. The dotted line is the best-fit line of slope unity through the individual MOSDEF galaxies, offset 0.1 dex below the one-to-one line. The cyan dashed line indicates the best-fit line to $z \sim 2.3$ star-forming galaxies from Steidel et al. (2014).

high-redshift galaxies (Shapley et al., 2015). The difference in diagnostic emission line ratios suggests that the physical conditions of high-redshift star-forming regions are different from what is seen locally. If true, photoionization models of local H II regions are unsuitable to describe their high-redshift counterparts and one would expect the relationship between metallicity and strong emission line ratios to differ. One avenue forward is to use emission line ratios to constrain the physical conditions of high-redshift star-forming regions with a statistically significant sample and re-calibrate to photoionization models using these new constraints as input parameters. When complete, the MOSDEF survey will provide a sample of galaxies in three redshift bins spanning $z \sim 1.5 - 3.5$ with rest-frame optical spectra covering all strong optical emission lines that is an order of magnitude larger than similar existing samples. Using this dataset, we will constrain the physical conditions of high-redshift star-forming regions in order to provide input parameters for photoionization models that are appropriate for these redshifts. Predictions from these models can then be used to produce new metallicity calibrations that are suitable for high redshift galaxies that have more extreme interstellar media and star-forming regions than typically observed in the local universe. We will also consider additional line ratios used as metallicity indicators in order to more fully understand the bias of local metallicity calibrations at high redshifts, a critical step to estimating reliable abundances at these redshifts. Such robust metallicities are required to accurately measure the evolution, slope, and scatter of the MZR and investigate the existence of the FMR at high redshifts and, by extension, uncover the nature of gas flows at high redshifts.

CHAPTER 3

The MOSDEF Survey: Electron Density and Ionization Parameter at $z \sim 2.3$

3.1 Introduction

The star-formation rate density of the universe peaked at $z \sim 2$ (Hopkins & Beacom, 2006; Madau & Dickinson, 2014). Understanding the physical conditions in star-forming regions during this epoch is essential for a complete description of the evolution of the stellar and gaseous content of galaxies. One method of probing these conditions is observing recently formed stars embedded in ionized gas clouds. Rest-frame optical emission lines from HII regions encode a significant amount of information about the ionizing source and the physical conditions of the ionized gas. A small set of physical properties appears to determine the strong optical emission line fluxes produced in HII regions, including the chemical abundance, the shape and normalization of the ionizing spectrum, the ionization state of the gas, and the gas density (Dopita & Evans, 1986; Kewley & Dopita, 2002; Dopita et al., 2006a,b).

Over the past decade, a body of work has been produced showing that galaxies at $z \sim 1-2$ display certain emission line ratios that are atypical of local star-forming galaxies (e.g., Shapley et al., 2005; Erb et al., 2006; Liu et al., 2008; Hainline et al., 2009; Holden et al., 2016; Nakajima & Ouchi, 2014; Steidel et al., 2014; Shapley et al., 2015). These observations suggest that at least some of the physical conditions that influence emission line production in star-forming regions must be different in high-redshift galaxies. It is well-established that galaxies at $z > 1$ have lower metallicities than local galaxies at fixed stellar mass (Erb et al., 2006; Maiolino et al., 2008; Belli et al., 2013; Henry et al., 2013; Stott et al., 2013; Cullen et al., 2014; Steidel et al., 2014; Troncoso et al., 2014; Sanders et al., 2015). The electron

density and ionization state of the gas also affect emission line production, but are less well-constrained and have fewer measurements at $z > 1$.

Estimates of the electron density at $z \sim 2$ have suggested that densities in high-redshift star-forming regions are significantly higher than what is typically observed locally (Hainline et al., 2009; Lehnert et al., 2009; Bian et al., 2010; Shirazi et al., 2014). However, the small and heterogeneous galaxy samples used in these studies leave the electron density of typical star-forming regions at $z \sim 2$ poorly constrained. Electron density estimates in a large, representative sample of $z \sim 2$ galaxies are needed to obtain robust constraints on the typical electron densities at high redshift.

The typical ionization state of gas in $z \sim 2$ star-forming regions appears to differ from that of local star-forming regions. Galaxies at $z > 1$ display higher values of [O III]λ5007/Hβ and [O III]$\lambda\lambda$4959,5007/[O II]$\lambda\lambda$3726,3729 than are typical of local galaxies, leading to the conclusion that high-redshift galaxies have higher ionization parameters than local galaxies, on average (Brinchmann et al., 2008; Hainline et al., 2009; Holden et al., 2016; Nakajima & Ouchi, 2014; Shirazi et al., 2014). A systematic investigation of the variation of the ionization state with other galaxy properties at $z \sim 2$ is necessary to uncover the cause of these elevated ionization parameters.

In this chapter, we investigate the physical properties of star-forming regions at $z \sim 2.3$, specifically the electron density and ionization state, using a large, systematically-selected sample from the MOSFIRE Deep Evolution Field (MOSDEF) survey. Until recently, samples of rest-frame optical spectra of $z \sim 2$ galaxies were small, heterogeneous, and usually included only a subset of the strongest nebular emission lines. These samples reflected the difficulty of obtaining spectra of faint galaxies in the near-infrared, typically using long-slit spectrographs covering one near-infrared band at a time. With the development of sensitive near-infrared detectors and multi-object near-infrared spectrographs on 8-10 m class telescopes, large samples of $z \sim 2$ galaxies with rest-frame optical emission line measurements across multiple near-infrared bands are being assembled for the first time (Steidel et al., 2014; Kriek et al., 2015). These spectra contain a wealth of diagnostic information that probes the star-formation rate (SFR), dust attenuation, gas density, ionization state, chemical en-

richment, and more for $z \sim 2$ galaxies. Building on the work of Shapley et al. (2015), we utilize the full range of strong optical emission lines to investigate the physical properties of HII regions using various diagnostic line ratios. In combination with rich datasets at lower redshifts, such measurements make it possible to understand how conditions in star-forming regions have evolved over the past ~ 10 Gyr of cosmic history.

Changes in the physical conditions of star-forming gas are thought to be the cause of the offset of $z > 1$ galaxies from the local sequence of star-forming galaxies in the [O III]λ5007/Hβ vs. [N II]λ6584/Hα excitation diagram (Shapley et al., 2005; Liu et al., 2008; Hainline et al., 2009; Steidel et al., 2014; Shapley et al., 2015). It has been proposed that this offset is caused by higher gas density/pressure (Kewley et al., 2013a), systematically harder ionizing spectra (Steidel et al., 2014), higher ionization parameters (Brinchmann et al., 2008), or an enhancement in the N/O ratio (Masters et al., 2014; Shapley et al., 2015) in high-redshift galaxies in comparison to what is typically observed in the local universe. The offset could be caused by a combination of some or all of these parameters. By characterizing the differences in the density and ionization state of $z \sim 2$ and $z \sim 0$ star-forming galaxies, as we do here, we can gain a better understanding of which parameters drive the offset in the [O III]λ5007/Hβ vs. [N II]λ6584/Hα excitation diagram, and the relative importance of each. Determining the evolution of these properties with redshift also has implications for the applicability of local metallicity calibrations at $z \sim 1 - 2$.

This chapter is structured as follows. In Section 4.2, we briefly describe the MOSDEF survey, along with the observations, reduction, and measurements. We estimate the typical electron density in $z \sim 2.3$ star-forming regions and characterize the evolution of density with redshift in Section 3.3. In Section 3.4, we investigate the ionization state of $z \sim 2.3$ galaxies and its dependence on global galaxy properties and metallicity indicators. We propose a scenario in which galaxies at $z \sim 2.3$ have the same ionization parameter as galaxies at $z \sim 0$ at fixed metallicity. In Section 3.5, we provide evidence supporting our proposed scenario and discuss the implications for the interpretation of observed emission-line ratios of $z \sim 2.3$ galaxies, including the offset in the [O III]λ5007/Hβ vs. [N II]λ6584/Hα diagram. We conclude by summarizing our main results in Section 5.7.

We adopt the following shorthand abbreviations to refer to commonly used emission line ratios:

$$\mathrm{O_{32}} = [\mathrm{O\ III}]\lambda\lambda 4959, 5007 / [\mathrm{O\ II}]\lambda\lambda 3726, 3729 \tag{3.1}$$

$$\mathrm{R_{23}} = ([\mathrm{O\ III}]\lambda\lambda 4959, 5007 + [\mathrm{O\ II}]\lambda\lambda 3726, 3729) / \mathrm{H}\beta \tag{3.2}$$

$$\mathrm{O3N2} = ([\mathrm{O\ III}]\lambda 5007 / \mathrm{H}\beta) / ([\mathrm{N\ II}]\lambda 6584 / \mathrm{H}\alpha) \tag{3.3}$$

$$\mathrm{N2} = [\mathrm{N\ II}]\lambda 6584 / \mathrm{H}\alpha \tag{3.4}$$

Throughout this dissertation, the term "metallicity" is used synonymously with gas-phase oxygen abundance (O/H) unless otherwise mentioned. We adopt a Λ-CDM cosmology with $H_0 = 70$ km s^{-1} Mpc^{-1}, $\Omega_m = 0.3$, and $\Omega_\Lambda = 0.7$.

3.2 Observations

We use data taken during the first two years (2012B-2014A) of the MOSFIRE Deep Evolution Field survey. We briefly describe the MOSDEF survey, observations, reduction, and derived quantities here. Full technical details of the survey strategy, observations, reduction pipeline, and sample characteristics can be found in Kriek et al. (2015). We additionally use data from the Sloan Digital Sky Survey (SDSS; York et al., 2000) Data Release 7 (DR7; Abazajian et al., 2009) catalog to select local comparison samples for studying evolution with redshift. Emission-line measurements and galaxy properties are taken from the MPA-JHU catalog of measurements for SDSS DR7.[6]

3.2.1 The MOSDEF Survey

The MOSDEF survey is an ongoing multi-year project in which we are obtaining rest-frame optical spectra of galaxies at $z \sim 1.4-3.8$ with the goal of transforming the understanding of the gaseous, stellar, dust, and black hole content of galaxies at that epoch in cosmic history. This project utilizes the Multi-Object Spectrometer For Infra-Red Exploration (MOSFIRE;

[6]Available at `http://www.mpa-garching.mpg.de/SDSS/DR7/`

McLean et al., 2012) on the 10 m Keck I telescope. Potential for scientific gain from the MOSDEF dataset is maximized by targeting objects in the AEGIS, COSMOS, and GOODS-N extragalactic fields with extensive multi-wavelength ancillary data. These data include *Hubble Space Telescope* (*HST*) imaging from the Cosmic Assembly Near-infrared Deep Extragalactic Legacy Survey (CANDELS; Grogin et al., 2011; Koekemoer et al., 2011) and grism spectroscopy from the 3D-HST survey (Brammer et al., 2012a), as well as observations from *Chandra*, *Spitzer*, *Herschel*, VLA, and ground-based observatories in the optical and near-infrared.

In the MOSDEF survey, we target galaxies in the three redshift windows $1.37 \leq z \leq 1.70$, $2.09 \leq z \leq 2.61$, and $2.95 \leq z \leq 3.80$, where the redshift ranges are selected such that strong optical emission-line features fall within windows of atmospheric transmission in the Y, J, H, or K near-infrared bands. This targeting strategy leads to coverage of [OII]$\lambda\lambda$3726,3729, Hβ, and [O III]$\lambda\lambda$4959,5007 for all three redshift bins, as well as [N II]$\lambda\lambda$6548,6584, Hα, and [S II]$\lambda\lambda$6716,6731 for the $z \sim 1.5$ and $z \sim 2.3$ bins. These strong optical emission lines are powerful diagnostics for determining physical properties of galaxies including dust content (Reddy et al., 2015), star-formation rate (SFR) (Shivaei et al., 2015), chemical abundance (Sanders et al., 2015), gas density, ionization state, and black hole activity (Coil et al., 2015). Targets are selected from the 3D-HST photometric and spectroscopic catalogs (Skelton et al., 2014) based on their rest-frame optical (observed H-band) magnitudes and redshifts (grism or spectroscopic redshifts, if available, and photometric redshifts otherwise). Galaxies are targeted down to *HST*/WFC3 F160W AB magnitudes of 24.0 at $z \sim 1.5$, 24.5 at $z \sim 2.3$, and 25.0 at $z \sim 3.4$. Targets with pre-existing spectroscopic redshifts, including grism redshifts or ground-based spectroscopic redshifts, are given higher priority, as are galaxies with brighter F160W magnitudes. As described in Kriek et al. (2015), the MOSDEF survey will obtain spectra for ~ 1500 galaxies when complete, with ~ 750 at $z \sim 2.3$, and ~ 400 each at $z \sim 1.5$ and $z \sim 3.4$.

3.2.2 Observations and Reduction

We use data from the first two observing seasons of the MOSDEF survey. Observations were taken on ten observing runs from 2012 December to 2014 May, during which 21 MOSFIRE masks were observed. The first observing run, taking place in 2012 December, was a pilot program during which we observed one mask each in the GOODS-S and UDS CANDELS fields due to the limited visibility of the primary target fields. This work focuses on the $z \sim 2.3$ redshift bin, and, accordingly, we only describe the observations for this redshift interval. MOSDEF targets at $z \sim 2.3$ are observed in the J, H, and K near-infrared bands, with [O II]$\lambda\lambda$3726,3729 in J, Hβ and [O III]$\lambda\lambda$4959,5007 in H, and [N II]$\lambda\lambda$6548,6584, Hα, and [S II]$\lambda\lambda$6716,6731 in K. Observed MOSFIRE masks each contain ~ 30 slits with widths of $0\farcs7$, yielding a spectral resolution of 3300, 3650, and 3600 in J, H, and K bands, respectively. One slit on each mask was placed on a reference star used in the reduction. Masks were typically observed using an ABA'B' dither pattern, with individual exposure times at each dither position of 120 seconds in J and H, and 180 seconds in K. The total exposure time per filter per mask was typically 2 hours.

The raw data were reduced using a custom IDL pipeline developed by the MOSDEF team and described in detail in Kriek et al. (2015). The raw science frames were flatfielded and sky subtracted, cosmic rays were identified and masked, and the two-dimensional spectra were rectified. Individual exposures were combined and the resulting spectrum was flux calibrated. Shape correction due to varying spectral response with wavelength and telluric absorption features was achieved using observations of B8-A1 V standard stars matched to the typical air mass of science observations. Flux calibration was performed by requiring the flux density of the reference star on a mask to match its cataloged broadband photometry. For each slit, a two-dimensional error spectrum was produced accounting for Poisson counting uncertainty for the observed intensity per pixel and read noise. From the two-dimensional science and error spectra, one-dimensional spectra were produced using the optimal extraction technique. Spectra for any detected objects serendipitously falling on the slit were also extracted (Freeman et al., 2017). The final flux calibration was achieved by applying a slit-

loss correction term to the extracted science spectra on an individual basis. The fraction of light from an object falling outside of the slit was estimated using a two-dimensional Gaussian fit to the F160W image of a galaxy convolved with the seeing estimate for each mask and filter. The flux calibration was checked by verifying that objects with detected continuum had flux densities consistent with broadband photometry.

3.2.3 Measurements and Derived Quantities

Emission line fluxes were measured by fitting Gaussian profiles to emission lines in the one-dimensional spectra, while the uncertainty on the emission line flux was based on the 68th percentile width of the distribution of measured fluxes obtained by perturbing the spectrum according to the error spectrum and refitting the emission line 1,000 times (Reddy et al., 2015). All emission lines were fit with a single Gaussian profile except for the cases of [N II]$\lambda\lambda$6548,6584 and Hα, fit simultaneously with a triple Gaussian, and [O II]$\lambda\lambda$3726,3729, fit simultaneously with a double Gaussian and described in detail in Section 3.3.2. The highest signal-to-noise emission line of each object, typically Hα or [O III]λ5007, was used to constrain the centroid and width of the other emission lines and measure the redshift. Stellar masses were estimated by utilizing the stellar population synthesis models of Conroy et al. (2009) with the SED-fitting code FAST (Kriek et al., 2009) using the measured MOSDEF spectroscopic redshifts and broadband photometric catalogs assembled by the 3D-HST team (Skelton et al., 2014) spanning observed optical to mid-infrared. The Calzetti et al. (2000) attenuation curve and a Chabrier (2003) IMF were assumed. Uncertainties on the stellar masses were estimated using a Monte Carlo method where the input photometry was perturbed according to the errors and the SED was refit 500 times (Kriek et al., 2015). SFRs were estimated from dust-corrected Hα luminosities using the Kennicutt (1998) calibration converted to a Chabrier (2003) IMF (Shivaei et al., 2015). Balmer line fluxes were first corrected for stellar Balmer absorption using the best-fit SEDs (Reddy et al., 2015), and the dust correction was estimated using Hα/Hβ assuming an intrinsic ratio of 2.86 and the Cardelli et al. (1989) extinction curve.

Emission line fluxes are dust-corrected in line ratios involving lines significantly separated in wavelength (O_{32} and R_{23}), but are not dust-corrected in line ratios featuring lines with a close wavelength spacing (O3N2, N2, [O III]/Hβ, and [S II]/Hα). Uncertainties on emission line ratios are estimated using a monte carlo method by perturbing each individual line flux according to its uncertainty, recalculating the emission line ratio, and repeating the preceding steps 10,000 times to build up a distribution of perturbed line ratios. The uncertainty on the line ratio is determined from the 68th percentile width of this distribution. Error estimates on O_{32} and R_{23} values include uncertainty in the Balmer decrement by recalculating the dust correction for each realization.

After removing those objects identified as AGN based on their X-ray or IR properties (Coil et al., 2015), there are 225 star-forming galaxies confirmed to be in the $z \sim 2.3$ redshift interval spanning a stellar mass range of $10^{8.97} - 10^{11.64}$ $M_\odot$ with a median stellar mass of $10^{9.99}$ $M_\odot$. The subset of these galaxies with Hα and Hβ detected (67%) has SFRs spanning $1.61 - 323$ $M_\odot$/yr with a median SFR of 21.6 $M_\odot$/yr, and spans a range in stellar mass of $10^{8.97} - 10^{11.22}$ $M_\odot$ with a median stellar mass of $10^{10.0}$ $M_\odot$. Shivaei et al. (2015) have shown that the SFR-M_* relation of MOSDEF $z \sim 2.3$ star-forming galaxies is similar to what is observed in other studies that employ different SFR indicators (see their Figure 8). Accordingly, the $z \sim 2.3$ star-forming galaxy population recovered by the MOSDEF survey appears to be representative of the range of SFRs spanned by star-forming galaxies at these stellar masses and this redshift (Reddy et al., 2012; Whitaker et al., 2014; Shivaei et al., 2015).

3.3 Electron Densities

The electron density of star-forming regions affects the fluxes of collisionally excited lines and is thus an important quantity to measure as an input parameter to photoionization models.[7]

[7]The models described in Section 3.5 actually use the hydrogen gas density as an input parameter. In HII regions, the hydrogen gas is fully ionized such that the electron density is a good proxy for the hydrogen gas density.

The electron density can be estimated using the line fluxes of components of a doublet of a single species in which the two levels of the doublet have different collision strengths and radiative transition probabilities (Osterbrock & Ferland, 2006). The flux observed in each component of the doublet is dependent on the relative population in each energy level, which is sensitive to the density of electrons available for collisional excitation and de-excitation. Rest-frame optical spectra provide access to two strong emission line doublets useful for estimating the electron density, namely [O II]$\lambda\lambda 3726, 3729$ and [S II]$\lambda\lambda 6716, 6731$. We use the ratios of the components of these doublets to estimate densities for local SDSS galaxies and high-redshift galaxies from the MOSDEF sample.

3.3.1 Methods

We have written a python script that solves a 5-level atom approximation of the O II and S II ions for the relative populations in the second and third energy levels. Decays from these two energy levels produce the two components of the [O II]$\lambda\lambda 3726, 3729$ and [S II]$\lambda\lambda 6716, 6731$ doublets. We set up a detailed balance of transitions into and out of each of the five energy levels via radiative decay and collisional excitation and de-excitation, assuming the system is in thermal equilibrium. The detailed balance provides a system of equations that can be solved for the relative populations at a given density. Given n_2 and n_3, the relative populations in the second and third energy levels, the ratio of the line fluxes is given by

$$\frac{F_3}{F_2} = \frac{E_{31} n_3 A_{31}}{E_{21} n_2 A_{21}} \approx \frac{n_3 A_{31}}{n_2 A_{21}} \tag{3.5}$$

where F_i is the emission line intensity of decay from the ith level to the ground state, E_{i1} is the energy difference between the ith level and the ground state, and A_{i1} is the transition probability of the ith level to the ground state.

Calculating the proper emission line ratio corresponding to a given density requires accurate knowledge of the transition probabilities and collision strengths of each transition between the five energy levels. Recent investigations (Nicholls et al., 2013; Dopita et al., 2013) have suggested advantages in using the most up-to-date collision strength and tran-

sition probability atomic data instead of outdated values included in the IRAF routine *temden* (Shaw & Dufour, 1994). Motivated by these studies, we adopt the effective collision strengths from Tayal (2007) for O II and Tayal & Zatsarinny (2010) for S II, while the transition probabilities for both species are taken from the NIST MCHF database (Fischer & Tachiev, 2014). Using other estimates of the collision strengths and transition probabilities can change the calculated electron densities by up to $\sim 30\%$. We verified that our script can exactly match IRAF *temden* when using the same atomic data.

The effective collision strengths have some temperature dependence and have been calculated over a range of electron temperatures from 2000 K to 100,000 K for O II and 5000 K to 100,000 K for S II. We adopt the effective collision strengths calculated with an electron temperature of 10,000 K, a representative equilibrium temperature of HII regions that are neither metal-rich nor metal-poor. We note that the temperature dependence is not negligible. Assuming an electron temperature of 7,000 K yields electron densities that are $\sim 15-20\%$ lower at a fixed line ratio, while an electron temperature of 15,000 K gives densities that are higher by the same amount. Because we assume a fixed electron temperature of 10,000 K, we are likely overestimating the electron density in metal-rich galaxies, and underestimating the density in galaxies that are metal-poor. However, the uncertainty introduced by this assumption is smaller than the typical measurement uncertainty for individual $z \sim 2.3$ galaxies.

We calculate the line ratios [O II]λ3729/λ3726 and [S II]λ6716/λ6731 over a range of electron densities of $\log\left(\frac{\mathrm{n}_e}{\mathrm{cm}^{-3}}\right) = 0$ to 5 in 0.01 dex steps. The result is well fit by a function of the form

$$R(n_e) = a\frac{b+n_e}{c+n_e} \tag{3.6}$$

where R=[O II]λ3729/λ3726 or [S II]λ6716/λ6731 is the line flux ratio. The best-fit parameters using up-to-date atomic data are shown in Table 3.1 for [O II] and [S II]. Figure 3.1 shows this diagnostic relation for the new atomic data (black) and the relation from *IRAF temden* (red) for both [O II] (solid) and [S II] (dashed). It can be seen in Figure 3.1 that the line ratio asymptotically approaches a theoretical maximum value in the low-density limit

Table 3.1: Coefficients and limiting line ratios for [O II] and [S II] in equations 3.6 and 3.7

R	a	b	c	$R^{\rm a}_{\rm min}$	$R^{\rm b}_{\rm max}$
[O II]λ3729/λ3726	0.3771	2,468	638.4	0.3839	1.4558
[S II]λ6716/λ6731	0.4315	2,107	627.1	0.4375	1.4484

(a) Theoretical minimum line ratio calculated in the high-density limit of 100,000 cm^{-3}
(b) Theoretical maximum line ratio calculated in the low-density limit of 1 cm^{-3}

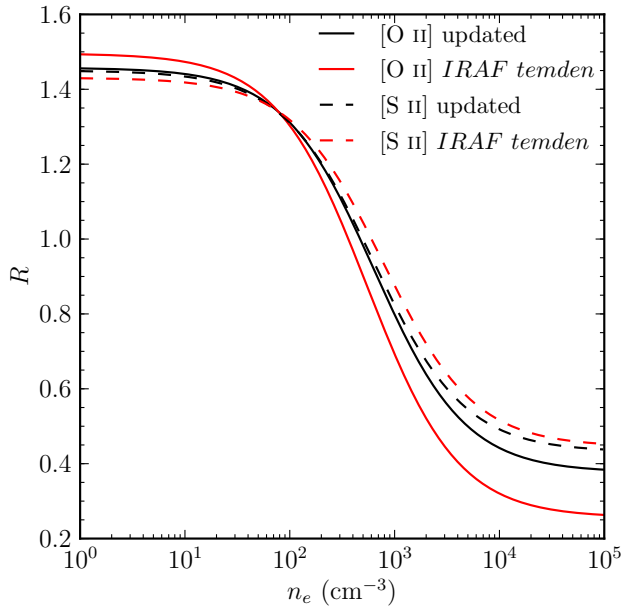

Figure 3.1: R vs. n_e curves (equation 3.6) from IRAF temden (red) and our five-level atom python script using new atomic data (black), where R =[O II]λ3729/λ3726 (solid) or [S II]λ6716/λ6731 (dashed).

and a theoretical minimum value in the high-density limit. We calculate the theoretical maximum and minimum line ratios at densities of 1 cm^{-3} and 100,000 cm^{-3}, respectively, and show these values in Table 3.1. Inverting equation 3.6 yields the density as a function of the line ratio

$$n_e(R) = \frac{cR - ab}{a - R} \tag{3.7}$$

which we use to calculate electron densities. Uncertainties on individual density measurements are estimated by converting the upper and lower 68th percentile uncertainties on the line ratio into electron densities, where the upper (lower) uncertainty in line ratio corresponds to the lower (upper) uncertainty in density.

3.3.2 Sample

For objects with electron densities in the range $\sim 100-1,000$ cm^{-3}, the line ratio will be fairly close to unity, as can be seen in Figure 3.1. In this regime, relatively small changes in the line flux can result in large changes to the inferred electron density. Therefore, it is imperative that the doublets used to infer electron densities be free of any contamination from skylines or poor line profile fitting. The [S II] doublet is well separated and the two components are fit separately with single Gaussian profiles. The [O II] doublet is well-resolved but the two components are blended and must be fit with two Gaussian profiles simultaneously. When fitting the [O II] doublet, we constrain the separation of the centroids of the two components to be within 0.5 Å of the nominal separation of 2.78 Å in the rest frame. We also require the widths of the two components to match each other exactly and to be no more than 10% larger than the velocity width inferred from the highest signal-to-noise line in the object's spectrum, typically Hα or [O III]λ5007. This method yields robust fits to [O II] doublets.

We select MOSDEF galaxies in the redshift range $2.0 < z < 2.6$ with S/N$\geq$3 in [O II]$\lambda\lambda$3726,3729 or [S II]$\lambda\lambda$6716,6731 which have not been flagged as AGN based on their IR and X-ray properties (Coil et al., 2015). This gives a sample of 97 [O II] doublets and 36 [S II] doublets at $z \sim 2.3$. We visually inspected each of these doublets and removed those with significant skyline contamination or spurious detections. One additional [S II] object with a very high value of $\log([\text{N II}\lambda6584/\text{H}\alpha) = -0.11$ indicating a probable AGN was also removed, giving a final density sample of 43 [O II] doublets and 26 [S II] doublets from 61 different targets at $\langle z \rangle = 2.24 \pm 0.12$. This sample spans a range of stellar mass from $10^{8.97} - 10^{11.22}$ M$_\odot$ with a median stellar mass of $10^{10.10}$ M$_\odot$. Of the 61 galaxies, 8 (13%) do not have measured SFRs, of which 3 galaxies do not have wavelength coverage of Hβ, 2 galaxies do not have wavelength coverage of Hα, and the remaining 3 galaxies show significant skyline contamination of the Hβ line. The other 53 objects have SFRs spanning $4.65 - 228$ M$_\odot$/yr with a median SFR of 29.7 M$_\odot$/yr. The density sample has only slightly higher median M_* and SFR than the parent sample of MOSDEF $z \sim 2.3$ star-forming galaxies (Section 3.2.3) and is still representative of the fairly massive $z \sim 2.3$ star-forming galaxy

population. The 8 galaxies without SFR measurements are included in all parts of the analysis for which SFR is not required. Examples of [O II] and [S II] doublets from six different objects in the MOSDEF $z \sim 2.3$ sample are shown in Figure 3.2, along with fits and inferred line ratios.

We use a local comparison sample from SDSS to investigate evolution in the typical densities of star-forming regions. We select galaxies from SDSS in the redshift range $0.04 < z < 0.1$ to attain a sample that is relatively free of aperture effects and limited to the local universe. We require galaxies to have S/N$\geq$3 in Hβ, [O III]λ5007, Hα, [N II]λ6585, [S II]λ6716, and [S II]λ6731. Detections in the first four of these lines are required to reject AGN using the empirical demarcation of Kauffmann et al. (2003b). We do not require detection of the [O II] doublet. The SDSS spectra have a spectral resolution of $\sim$ 2000, corresponding to a resolution element of $\sim$ 1.9 Å at 3727 Å. This resolution is insufficient to properly resolve and sample the [O II]$\lambda\lambda$3726,3729 doublet separated by 2.78 Å (see Section 3.3.3). Therefore, we only use the [S II] doublet to probe the electron density in the local comparison sample. The local comparison sample contains 99,291 galaxies with $\langle z \rangle = 0.0678$.

3.3.3 The consistency of [O II] and [S II] electron densities

Since our high-redshift electron density sample has a mixture of [O II] and [S II] doublet measurements while the local comparison sample only has reliable [S II] measurements, it is a useful exercise to evaluate the consistency of densities determined using these two ionic species to see if they can be directly compared. To this end, we have assembled a sample of local HII regions from the literature with high-resolution, high-signal-to-noise spectroscopic observations with sufficient wavelength coverage to span [O II]$\lambda\lambda$3726,3729 and [S II]$\lambda\lambda$6716,6731. We performed a literature search and identified 32 galactic and extragalactic HII regions observed at high spectral resolution ($R \sim 8,000 - 23,000$) with detections of both the [O II] and [S II] doublets (García-Rojas et al., 2005, 2006, 2007; López-Sánchez et al., 2007; Esteban et al., 2009, 2013, 2014).

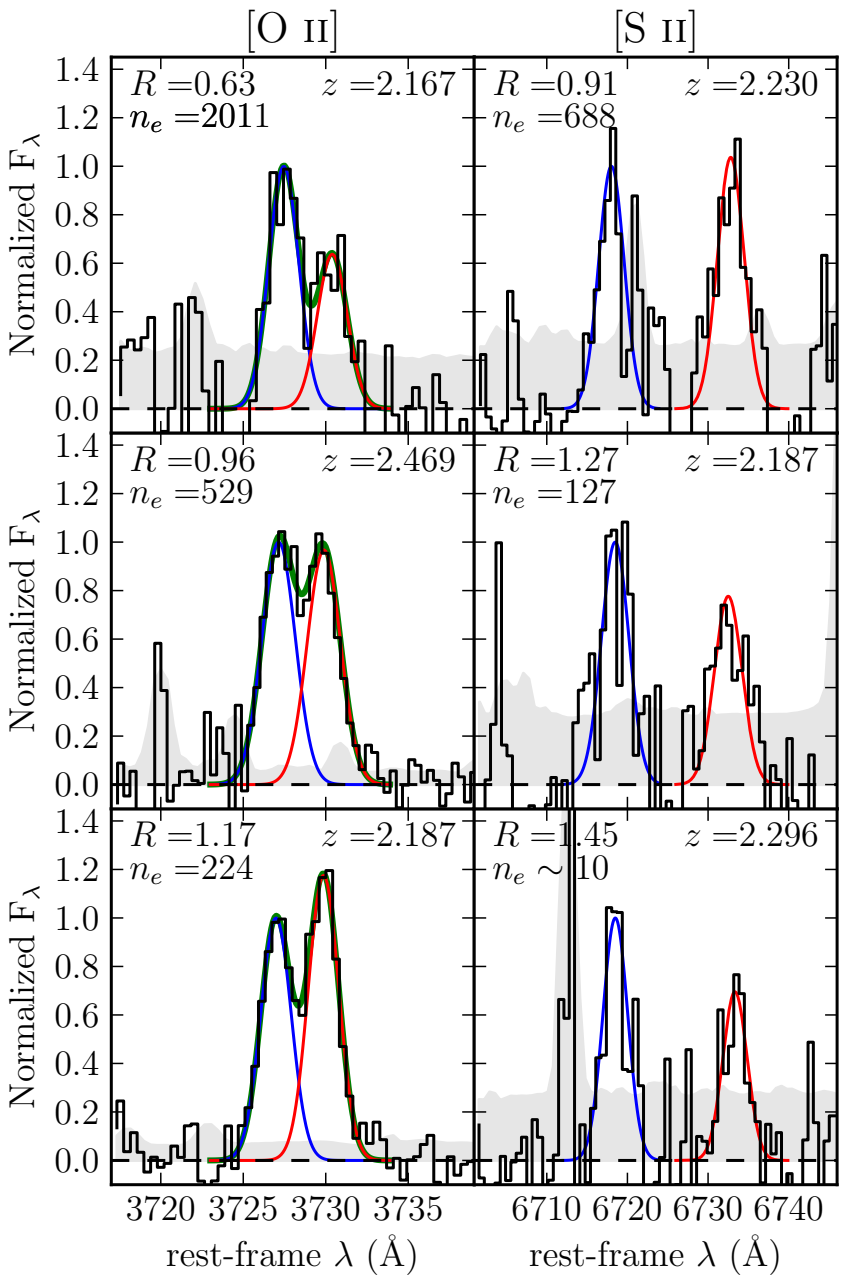

Figure 3.2: [O II]$\lambda\lambda$3726,3729 doublets (left column) and [S II]$\lambda\lambda$6716,6731 doublets (right column) from six different objects over a range of line ratios and densities. The black line shows the continuum subtracted spectrum for each object. The light gray band indicates the error spectrum for each object, while the blue and red lines show the Gaussian profile fits to the blueward and redward component of each doublet, respectively. The green line shows the total [O II] profile. In each panel, the spectrum has been normalized so that the blue component has a peak height of unity. The line ratio R, density (n_e) in cm^{-3}, and redshift is displayed for each object, with R =[O II]λ3729/λ3726 in the left column and R =[S II]λ6716/λ6731 in the right column.

Electron densities and uncertainties are calculated with the same method outlined above using the published line fluxes and errors. Densities and uncertainties are presented in Figure 3.3. Four of the 32 individual measurements have [S II]λ6716/λ6731 ratios that are higher than the theoretically allowed maximum in the low-density limit, and thus cannot be assigned a density. While these four objects have [S II]$\lambda\lambda$6716,6731 detected at greater than 3σ indicating they are in the low-density limit, we plot them as upper limits (red squares) where the data point is plotted at the [S II] density corresponding to the lower 1σ uncertainty on the [S II] line flux ratio. Fitting a line in logarithmic space yields the relationship

$$\log\left(\frac{[\text{S II}]\ n_e}{\text{cm}^{-3}}\right) = 1.00^{+0.29}_{-0.12} \times \log\left(\frac{[\text{O II}]\ n_e}{\text{cm}^{-3}}\right) - 0.01^{+0.32}_{-0.80} \tag{3.8}$$

where the 68th percentile confidence intervals are determined by perturbing the data points according to their uncertainties and refitting. This best-fit line is shown in Figure 3.3 as a solid blue line while the light blue shaded region shows the 68th percentile confidence region around the best-fit line. The relation between electron densities determined by [O II] and [S II] is completely consistent with a one-to-one relation (dashed black line). All four objects plotted as upper limits are also consistent with a one-to-one relation within the 1σ uncertainties. There are 8 objects in the $z \sim 2.3$ density sample that have density estimates from both the [O II] and [S II] doublets, but the number of galaxies is too small and measurement uncertainties are too large to perform a similar investigation at $z \sim 2.3$. We assume that the relationship between densities of star-forming regions determined using [S II] and [O II] does not change with redshift. Thus, we conclude that densities determined from either ionic species in the $z \sim 2.3$ sample can be directly compared with each other and with SDSS density measurements from [S II] doublets.

For this test, we specifically selected a sample with high S/N and very high spectral resolution so that each component of the doublets was well-detected and the [O II] doublet was well resolved. We note that repeating this exercise with medium-resolution spectra ($R \sim 1,000 - 2,000$) of local HII regions (Peimbert et al., 2012; García-Rojas et al., 2014; Berg et al., 2015) yields a relation in which [O II] electron densities are systematically over-

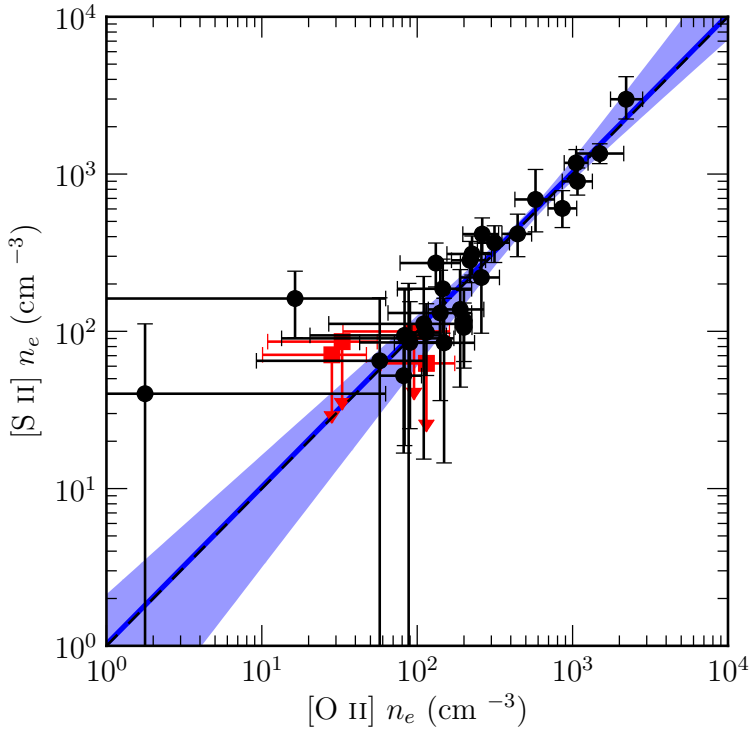

Figure 3.3: Comparison of density estimates from the [O II] and [S II] doublets for a sample of local HII regions with high-S/N, high-resolution spectra. Black points denote density measurements for individual HII regions. The four red squares show limits plotted at the upper 1σ uncertainty bound on the [S II] density for objects that have higher [S II]λ6716/λ6731 than the maximum theoretically allowed value. The black dashed line shows a one-to-one relationship. The blue line and shaded blue region show the best-fit line and 1σ confidence interval, respectively. Parameters of the best-fit line are shown in equation 3.8.

estimated with respect to [S II] electron densities. This effect is very similar to what is seen in the SDSS sample ($R \sim 2,000$). In order to have at least two resolution elements to sample the separation of the [O II] doublet components, a spectral resolution of $\Delta\lambda = 1.39$ Å at $\lambda = 3727$ Å is needed, corresponding to $R \sim 2,700$. MOSDEF observations adequately sample the [O II] doublet at $z \sim 2.3$ with $R \sim 3,300$ in the J band.

3.3.4 Typical electron density at $z \sim 2.3$ and $z \sim 0$

We would like to characterize the typical electron density in star-forming regions of $z \sim 2.3$ galaxies and $z \sim 0$ galaxies. However, given the shape of the function in equation 3.7 and Figure 3.1, a fairly symmetric distribution of line ratios leads to a very asymmetric distribution in electron densities. Furthermore, the diagnostic curve translating from line ratio to electron density is insensitive to the electron density at very low and very high densities, asymptotically approaching the theoretical maximum and minimum line ratio, respectively, in those two regimes. Measured line ratios that fall outside of the theoretically allowed region due to measurement uncertainty can only be assigned limits in the low- or high-density extremes. We consider the low-density limit to refer to a density below ~ 10 cm^{-3} and the high-density limit to denote density above $\sim 10,000$ cm^{-3}. For these reasons, we perform statistics on the line ratio distributions for each sample rather than the electron density distributions and infer typical electron densities based on the statistical properties of the line ratio distribution.

The distributions of line ratios of the $z \sim 2.3$ star-forming galaxies are shown in the top and bottom panels of Figure 3.4 for the [O II] and [S II] doublets, respectively. We determine the typical electron density from the median line ratio of a given sample. The uncertainty on the median is calculated using a bootstrap technique in which we randomly resample with replacement, perturb the emission line fluxes according to their uncertainties and recalculate the line ratio for each object in the new sample, take the median of the new perturbed sample, and repeat the preceding steps 1,000 times to build up a well-sampled distribution of median values. The reported lower and upper uncertainties on the median are determined to

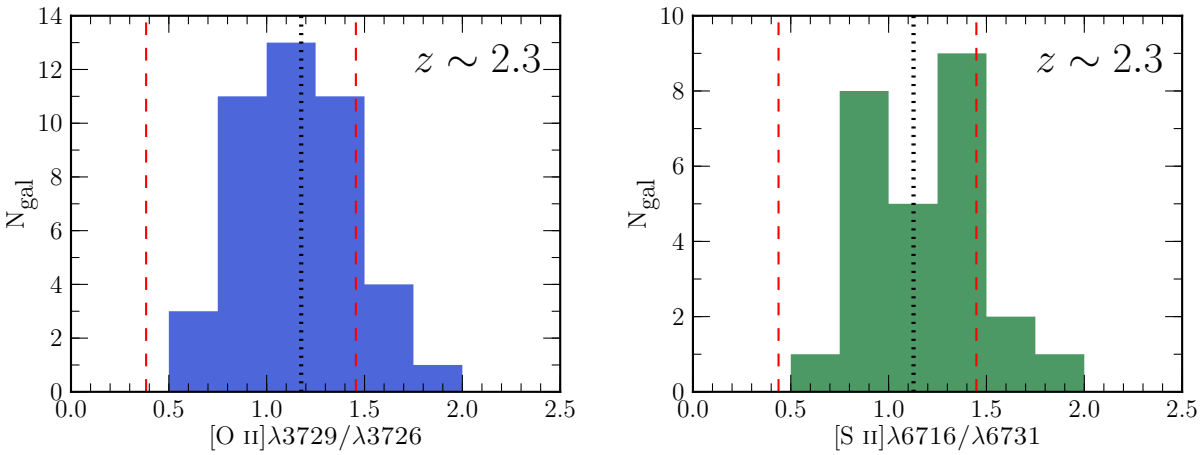

Figure 3.4: [O II]λ3729/λ3726 (top) and [S II]λ6716/λ6731 (bottom) line ratio distributions for 43 and 26 $z \sim 2.3$ star-forming galaxies, respectively. In each panel, the dotted black line shows the median line ratio (corresponding to an electron density of 225 cm^{-3} for [O II] and 290 cm^{-3} for [S II]), while the dashed red lines show the minimum and maximum theoretically-allowed line ratios from Table 3.1.

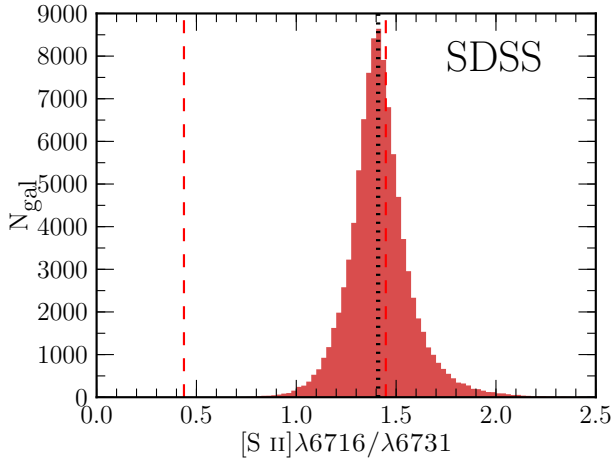

Figure 3.5: [S II]λ6716/λ6731 line ratio distribution for local star-forming galaxies from SDSS, with lines as in Figure 3.4. The median line ratio for local galaxies (corresponding to an electron density of 26 cm^{-3}) falls near the low-density limit.

be the 15.8-percentile and 84.2-percentile values, respectively, of the cumulative distribution function of the median. At $z \sim 2.3$, we find a median [O II]λ3729/λ3726 ratio of $1.18^{+0.01}_{-0.10}$ corresponding to an electron density of 225^{+119}_{-4} cm^{-3}. We find a median [S II]λ6716/λ6731 value of $1.13^{+0.16}_{-0.06}$ which gives an electron density of 290^{+88}_{-169} cm^{-3}, consistent within the uncertainties with the density determined using [O II]. We measure a range of individual electron densities from the low-density limit to 2,500 cm^{-3} and find that $z \sim 2.3$ star-forming regions have a typical electron density of ~ 250 cm^{-3}.

The typical density that we infer for high-redshift galaxies (~ 250 cm^{-3}) is in excellent agreement with what Steidel et al. (2014) observed by stacking J-band observations of 113 galaxies at $z \sim 2.3$, finding an average [O II]λ3729/λ3726 ratio of 1.16, corresponding to a density of 243 cm^{-3} using the atomic data adopted in this study. Shimakawa et al. (2015) found a median electron density of 291 cm^{-3} among 14 Hα emitters at $z \sim 2.5$ using the [O II] doublet. Previous observations of individual gravitationally lensed galaxies at $z \sim 2$ suggested electron densities of ~ 1000 cm^{-3} (Hainline et al., 2009; Bian et al., 2010), somewhat higher than the value we infer. Lehnert et al. (2009) presented electron densities in the range $400 - 1200$ cm^{-3} for 4 galaxies at $z \sim 2.3$ in the SINS survey (Förster Schreiber et al., 2009), also higher than our sample median. As noted in Section 3.3.1, different choices of atomic data can change the inferred densities by $\sim 30\%$ and can lead to differences of this magnitude in measured densities reported by different authors. In comparison to these previous estimates, except for that of Steidel et al. (2014), our sample is larger and selected in a more systematic way, and the galaxies in our sample display properties representative of the SFR-M_* relation at $z \sim 2$, as shown in Section 3.2.3. As such, the density estimate presented here should hold true for a population of typical star-forming galaxies at $z \sim 2.3$ with $M_* \gtrsim 10^{9.5}$ $M_\odot$.

For the local comparison sample, we find SDSS star-forming galaxies have a distribution with a median [S II]λ6716/λ6731 ratio of 1.41, shown in Figure 3.5, corresponding to an electron density of 26 cm^{-3}. The uncertainty on the SDSS median line ratio is less than 0.04% due to the large number of galaxies in the sample. We find that the typical electron density in star-forming regions increases by a factor of 10 from $z \sim 0$ to $z \sim 2.3$. The

local median [S II]λ6716/λ6731 ratio is close to the theoretical maximum ratio of 1.4484, suggesting that local star-forming galaxies typically fall close to the low-density limit. From the slope of the function in Figure 3.1, it is apparent that the line ratios of both [O II] and [S II] are almost completely insensitive to the density when the electron density is below ~ 10 cm^{-3}, and are only mildly sensitive to the density below ~ 50 cm^{-3}. Even if we assume a conservative upper limit of 50 cm^{-3} for the typical local density, we still observe a significant increase in electron density from $z \sim 0$ to $z \sim 2.3$.

The measurements above suggest that $z \sim 2.3$ star-forming regions are typically denser than local star-forming regions by an order of magnitude. We perform some tests to investigate the significance of the observed evolution in electron density. First, note that the SDSS line ratio distribution shown in Figure 3.5 is well-sampled and fairly narrow. We find that 89% of the SDSS sample has higher [S II] ratios (lower electron densities) than the median $z \sim 2.3$ [S II] ratio, while 64% of the $z \sim 2.3$ sample has lower [S II] ratios (higher electron densities) than the SDSS sample median. A two-sided Kolmogorov-Smirnov test on the $z \sim 0$ and $z \sim 2.3$ [S II] distributions yields a K-S statistic of 0.452 and a p-value (the probability that the two samples were drawn from the same underlying distribution) of 7.63×10^{-6}, indicating that the $z \sim 0$ and $z \sim 2.3$ density distributions are significantly different.

We are attempting to estimate the electron density in HII regions, but [S II] emission coming from other components of the ISM could contaminate measured [S II] ratios from integrated-light galaxy spectra. The S II ion has an ionization energy of 10.36 eV, somewhat lower than that of hydrogen. Because of its lower ionization energy, the S II zone can extend beyond the boundary of an HII region. Additionally, [S II]$\lambda\lambda$6716,6731 emission can be produced in diffuse ionized gas that is shock excited (Reynolds, 1985; Martin, 1997). To investigate the effects of contamination from a diffuse ionized ISM component, we used measurements of [S II] ratios of 44 HII regions in the star-forming spiral galaxy NGC 628 observed as part of the CHAOS survey (Berg et al., 2015). The spectra of these HII regions were attained by placing slits on top of individual HII regions and should contain very little light from the diffuse ISM. We find that the median [S II]λ6716/λ6731 ratio of these

HII regions is 1.39, corresponding to an electron density of 38 cm^{-3}. This ratio is nearly equivalent to the median [S II] ratio of 1.41 for the SDSS sample, suggesting that our estimate of the typical local HII region density from SDSS is not significantly biased by emission from diffuse ionized gas. However, all of these HII regions are from a single galaxy, and their median density may not be representative of the entire local HII region population. Currently, there is insufficient knowledge of the ISM structure of $z \sim 2$ galaxies to determine whether integrated-light spectra are significantly contaminated by emission from a diffuse component at that redshift.

3.3.5 Electron density vs. galaxy properties

We investigate whether the density of star-forming regions varies with other galaxy properties. As stated previously, the nature of the function converting between line ratio and electron density makes it difficult to work with distributions in density space, especially when some objects have measured line ratios that are outside of the theoretically allowed values. For this reason we will look for relationships between density and galaxy properties using the line ratio as a proxy for the density. We plot the line ratios against stellar mass (M_*), star-formation rate (SFR), and specific star-formation rate (sSFR; SFR/M_*) in Figure 3.6. The middle and right panels of Figure 3.6 only include the subset of the $z \sim 2.3$ density sample with Hα and Hβ detections. We note that the $z \sim 2.3$ sample has significant overlap with the SDSS sample in M_*, but the two are almost completely disjoint in SFR and sSFR. This difference is consistent with the evolution of the SFR-M_* relation with redshift (Shivaei et al., 2015). We do not see evidence for any significant trends in line ratio (electron density) as a function of stellar mass, SFR, or sSFR among the local SDSS sample or the MOSDEF $z \sim 2.3$ sample. This observation is confirmed by performing a Spearman correlation test on each sample in each parameter space. No correlations are more significant than $\sim 1\sigma$.

This result is in conflict with the recent work of Shimakawa et al. (2015), who found a correlation between electron density and sSFR at the 4σ level for 14 $z \sim 2.5$ Hα emitters, and observed this correlation when stacking the spectra in two density bins. We do not see

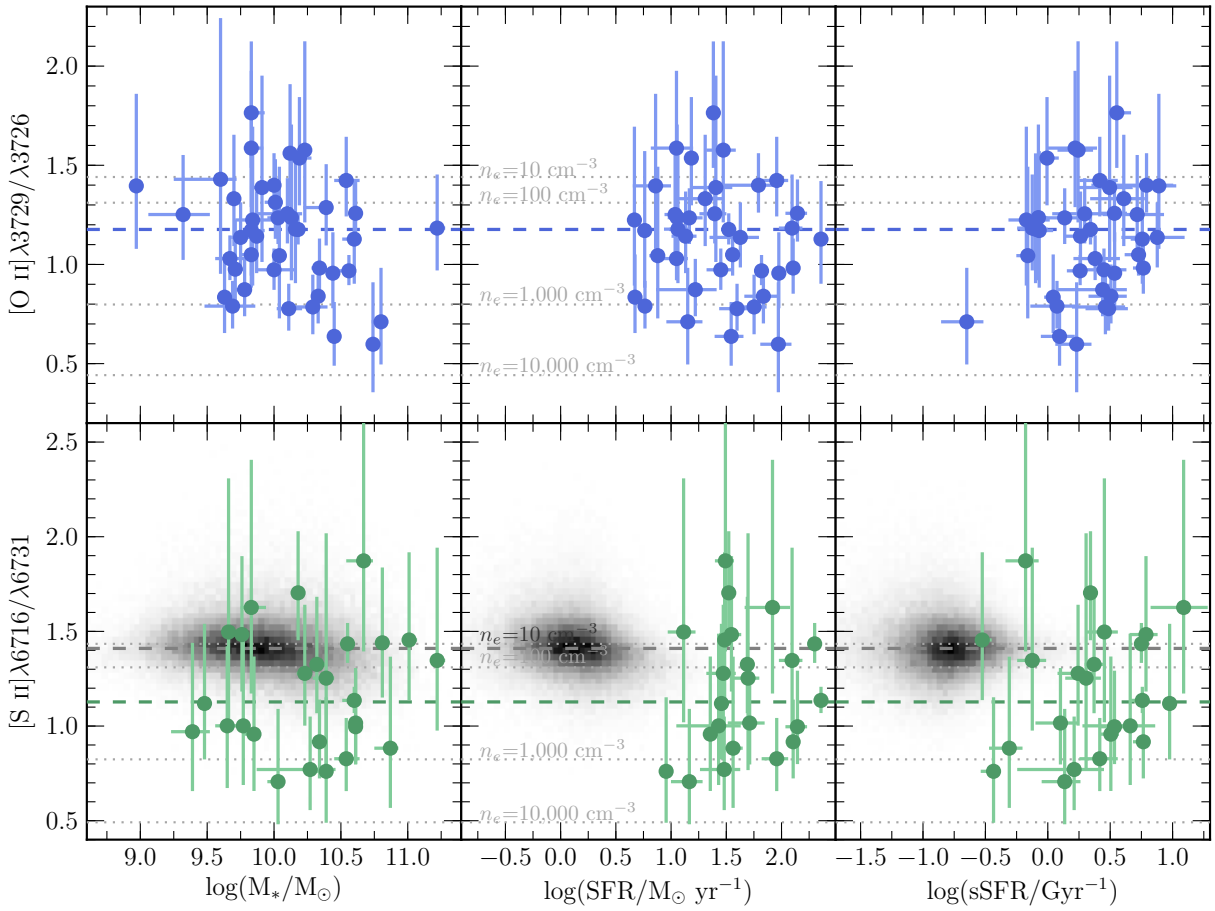

Figure 3.6: [S II]$\lambda\lambda$6716,6731 (bottom row) and [O II]$\lambda\lambda$3726,3729 (top row) as a function of stellar mass (left), SFR (middle), and sSFR (right). Blue and green points show the $z \sim 2.3$ [O II] and [S II] density samples, respectively. The gray two-dimensional histogram in the bottom row shows the distribution of the local comparison sample. Spectra from SDSS do not have a high enough spectral resolution to resolve the components of the [O II] doublet. The blue, green, and gray dashed lines show the median line ratios for the corresponding sample. Dotted lines show the line ratios corresponding to denities of 10, 100, 1,000, and 10,000 cm^{-3}.

evidence for correlation among these properties with a larger and more representative sample that is generally consistent with that of Shimakawa et al. (2015) in stellar mass and SFR. Shimakawa et al. (2015) found no correlation between electron density and stellar mass, in agreement with our results.

3.4 Ionization Parameter

The ionization state of ionized gas in star-forming regions refers to the interaction between the ionizing source and ionized gas. This interaction modulates the relative populations of different ionic species, which directly influence the observed emission line ratios. Multiple lines of evidence suggest that the ionization state in high-redshift star-forming regions may be systematically different from what is typically observed in the local universe in galaxies of similar masses (e.g., Holden et al., 2016; Nakajima & Ouchi, 2014; Steidel et al., 2014). The ionization parameter is useful for quantifying the ionization state, and encodes information about both the ionizing source and the surrounding ionized gas. In this section, we will use emission line measurements of $z \sim 2.3$ galaxies to investigate the relationship between ionization parameter and other galaxy properties in order to probe the ionization state of gas in $z \sim 2$ star-forming regions.

3.4.1 Definition of the ionization parameter

We begin with some useful definitions related to the ionization state. Ionic species in HII regions are in ionization equlibrium, where the rate of ionization is equal to the rate of recombination. The ionization equilibrium condition for ionic species i can be written as

$$n_i \frac{Q_i}{4\pi r^2} \bar{\sigma}_i = n_i^+ n_e \alpha_i \tag{3.9}$$

where n_i is the number density of the ionic species, Q_i is the rate of production of photons that can ionize species i, $\bar{\sigma}_i$ is the effective ionization cross-section, n_i^+ is the number density of the once-ionized state of n_i, n_e is the electron density, and α_i is the recombination coefficient.

If the ionization energy of n_i is close to that of hydrogen, which is the case for many of the ions that produce strong optical emission lines, then we can rearrange this expression and approximate the ratio of the relative populations in the higher and lower ionized states.

$$\frac{n_i^+}{n_i} \approx \frac{\bar{\sigma}_i}{\alpha_i} \frac{Q_0}{4\pi r^2 n_e} \tag{3.10}$$

Here, Q_0 is the rate of production of hydrogen-ionizing photons ($h\nu \geq 13.6$ eV). The first term ($\bar{\sigma}_i/\alpha_i$) on the right hand side of this expression is a constant that will change for each ionic species. The second term ($Q_0/4\pi r^2 n_e$) contains only properties of the ionizing source and the gas, and is not dependent on the specific ionic species. The dimensionless ionization parameter $\mathcal{U}$ is defined as the second term on the right-hand side of equation 3.10 divided by the speed of light, c.

$$\mathcal{U} = \frac{Q_0}{4\pi r^2 c n_e} \tag{3.11}$$

Accordingly, the ratio of the relative population in an upper ionization state to that in a lower ionization state scales directly with the ionization parameter. Since the electron density is approximately the hydrogen gas density in a fully-ionized plasma, the ionization parameter can be thought of as the ratio of the number density of hydrogen-ionizing photons to the number density of the hydrogen gas. When working with HII regions it is convenient to define the dimensionless ionization parameter using the radius of a canonical Strömgren sphere, R_S, as the distance between the gas and the ionizing source.

$$\mathcal{U} = \frac{Q_0}{4\pi R_S^2 c n_e} \tag{3.12}$$

Often, the dimensional ionization parameter, $q = c \times \mathcal{U}$, is used instead, which is the ratio of the flux of ionizing photons at the Strömgren radius to the hydrogen number density. The definition of the Strömgren radius, based on a balance between ioniziation and recombination rates assuming case B recombination, is

$$R_S = \left(\frac{3Q_0}{4\pi \alpha_B \epsilon n_H^2} \right)^{1/3} \approx \left(\frac{3Q_0}{4\pi \alpha_B \epsilon n_e^2} \right)^{1/3} \tag{3.13}$$

where ϵ is the volume filling factor of the gas. The volume filling factor can be defined by assuming that the gas is structured in dense clumps that are surrounded by a lower-density medium. In this case, the volume filling factor is defined as

$$\epsilon = \frac{\langle n_e \rangle^2}{n_{e,c}^2} \tag{3.14}$$

where $\langle n_e \rangle$ is the global average electron density and $n_{e,c}$ is the electron density of the clumps. The volume filling factor is equal to unity for a homogeneous constant-density gas, while its value decreases as the density of the clumps increases relative to the average density. We note that the density estimates from [S II] and [O II] are based on luminosity-weighted measurements of emission line strengths. Since emission strength scales as the square of the density, we are effectively measuring the clump density if a clumpy gas geometry exists, not the global average density (Kennicutt, 1984). Using the definition of the Strömgren sphere radius, we can simplify the ionization parameter and resolve its dependence on only the rate of ionizing photon production, the electron density, and the volume filling factor.

$$\mathcal{U} \propto Q_0^{1/3} n_e^{1/3} \epsilon^{2/3} \tag{3.15}$$

The ionization parameter has a weak dependence on both the rate of ionizing photon production and the gas density, and is somewhat more sensitive to the volume filling factor, through which this definition of the ionization parameter contains information about the geometry of the gas.

Defining the ionization parameter assuming the geometry of a Strömgren sphere is convenient, but likely does not hold for real HII regions. The Strömgren geometry assumes a sphere of constant density gas that immediately surrounds the central ionizing source. In local HII regions, feedback from stellar winds can clear out a cavity around the ionizing star cluster such that the ionized gas is a shell instead of a filled sphere (e.g., Watson et al., 2008). Accordingly, the Strömgren radius is not necessarily a good representative radius for the separation of the illuminated gas and the ionizing source. It is possible that the wind-blown bubble geometry exists at high redshifts where the intensity of star formation is

concentrated, or some entirely different geometry such as intersecting bubbles. The scalings presented in equation 3.15 should then be used with caution because of the breakdown of the Strömgren approximation. Real HII regions show a variety of complicated substructure and geometry (e.g., Pellegrini et al., 2011). The Strömgren sphere definition of the ionization parameter also assumes that the nebula is radiation-bounded (i.e. no hydrogen-ionizing photons escape) instead of density-bounded (Nakajima & Ouchi, 2014), which may not hold true at high redshifts. Additionally, in an integrated spectrum the measured ionization parameter is a luminosity-weighted average of all of the sources of emission inside the aperture, which includes multiple HII regions and emission from other ISM components.

While the ionization parameter carries interesting information about the ionizing source and gas geometry, it can be difficult to determine because it is not directly observable, but can only be estimated using calibrations derived from physically motivated models. The ionization parameter is often estimated using measurements of sets of emission line ratios that have some sensitivity to the ionization state of the gas (e.g., lower- and higher-ionization states), in conjunction with the predictions of a suite of photoionization models (Díaz et al., 2000; Kewley & Dopita, 2002; Dors et al., 2011; Levesque & Richardson, 2014; Shirazi et al., 2014). Because of differences in the translation between observables and ionization parameter for different photoionization models, it is convenient to instead use an empirical emission line ratio as a proxy for the ionization parameter. Line ratios featuring both higher and lower ionization state transitions from the same element can be used to estimate the ionization parameter because of the relation between the ionization parameter and the relative populations in the two ionization states. Here, we use O_{32}=[O III]$\lambda\lambda$5007,4959/[O II]$\lambda\lambda$3726,3729 as a proxy for the ionization parameter. Systematic uncertainties in this approach result from the way in which a given ionization parameter-sensitive line ratio depends also on the shape of the ionization spectrum and the metallicity of the gas, unless these two properties can be independently constrained.

Table 3.2: Properties of the full ionization parameter sample, and [N II] and [S II] subsamples

	$\langle z \rangle^{a}$	σ_z^{b}	$\log\left(\frac{M_*}{M_\odot}\right)^{c}$	$\log\left(\frac{M_*}{M_\odot}\right)^{d}_{med}$	SFR^{e}	SFR$^{f}_{med}$
Full sample	2.29	0.11	$8.97 - 11.22$	10.0	$1.61 - 228$	23.8
[N II] subsample	2.28	0.11	$9.3 - 11.22$	10.22	$4.71 - 228$	33.2
[S II] subsample	2.29	0.11	$9.3 - 11.22$	10.26	$5.77 - 228$	33.3

(a) Average redshift of galaxies in the sample.
(b) Standard deviation of the redshift distribution.
(c) Range of $\log(M_*/M_\odot)$ of galaxies in the sample.
(d) Median $\log(M_*/M_\odot)$ of galaxies in the sample.
(e) Range of SFR in $M_\odot/yr^{-1}$ of galaxies in the sample, determined from dust-corrected Hα luminosity.
(f) Median SFR in $M_\odot/yr^{-1}$ of galaxies in the sample, determined from dust-corrected Hα luminosity.

3.4.2 Sample selection

In order to study the ionization state of high-redshift galaxies, we selected a sample of star-forming galaxies from the MOSDEF parent spectroscopic sample requiring objects to fall in the redshift range $2.0 < z < 2.6$ and have S/N$\geq$ 3 in [O II]$\lambda\lambda$3726,3729, Hβ, [O III]λ5007, and Hα. The flux of [O III]λ4959 is taken to be 1/2.98 of the [O III]λ5007 flux (Storey & Zeippen, 2000). Hα and Hβ detections were necessary in order to correct line fluxes for dust attenuation, which is important for O_{32} because of the large wavelength separation of the emission lines. Objects with Hα and Hβ detections also have robust dust-corrected SFRs based on Hα luminosities. AGN were identified and removed based on their X-ray and IR properties (Coil et al., 2015) and objects with [N II]λ6584 detected at 3σ or greater were removed if $\log([\text{N II}]\lambda6584/\text{H}\alpha) > -0.3$. Any AGN not removed by these selection criteria would introduce a bias in emission line ratio diagrams. We discuss reasons why we are confident that our sample does not contain any AGN in Sections 3.4.4 and 3.5.4. Six additional objects were removed because of significant skyline contamination in the relevant emission lines. These criteria yield an ionization parameter sample of 103 MOSDEF galaxies and the properties of the sample are shown in Table 3.2. This sample has properties that are nearly identical to those of the parent MOSDEF spectroscopic sample at $z \sim 2.3$, and is representative of star-forming galaxies with similar stellar masses at this redshift.

In the discussion that follows, we will examine multiple line ratio diagrams, some of which involve additional emission lines along with oxygen and hydrogen Balmer-series strong lines. Therefore, we selected subsamples of the ionization parameter sample that have additional line detection criteria to plot in these spaces. We selected a subsample of 61 galaxies that additionally have S/N$\geq$ 3 in [N II]λ6585. We also selected a subset of 53 galaxies with S/N$\geq$ 3 in both [N II]λ6585 and [S II]$\lambda\lambda$6716,6731. The sample properties of the [N II] and [S II] subsamples are presented in Table 3.2. These stringent emission line cuts, requiring all or nearly all of the optical strong lines to be detected, introduce a bias against low-mass, low-SFR galaxies. However, the typical galaxy properties of the subsamples are not significantly different from those of the full ionization parameter sample or the MOSDEF parent $z \sim 2.3$ spectroscopic sample. While the [N II] and [S II] subsamples have slightly higher M_* and SFR than the full sample, the median values are still consistent with these galaxies falling on or near the $z \sim 2$ SFR-M_* relation (Whitaker et al., 2014; Shivaei et al., 2015).

We select a sample of typical star-forming galaxies in the local universe from SDSS DR7. We require $0.04 < z < 0.1$ and S/N$\geq$3 in [O II]$\lambda\lambda$3726,3729, Hβ, [O III]λ5007, Hα, and [N II]λ6585. Once again, the flux of [O III]λ4959 is assumed to be equal to 1/2.98 of the [O III]λ5007 flux (Storey & Zeippen, 2000). A detection in [N II] is required because AGN are rejected using the demarcation of Kauffmann et al. (2003b) in the [O III]/Hβ vs. [N II]/Hα diagram. These criteria yield a local sample of 68,453 star-forming galaxies at $z \sim 0.07$. We also selected a subsample of 65,000 local galaxies that additionally have S/N$\geq$ 3 in [S II]$\lambda\lambda$6716,6731.

3.4.3 O_{32} and global galaxy properties

Many studies have suggested that $z \gtrsim 2$ galaxies have systematically higher ionization parameters than are typical for local galaxies (Holden et al., 2016; Nakajima et al., 2013; Nakajima & Ouchi, 2014; Shirazi et al., 2014; Steidel et al., 2014). However, it is imperative to consider the evolution in global galaxy properties with redshift when interpreting the apparently high ionization parameters observed at high redshifts. To this end, we investigate

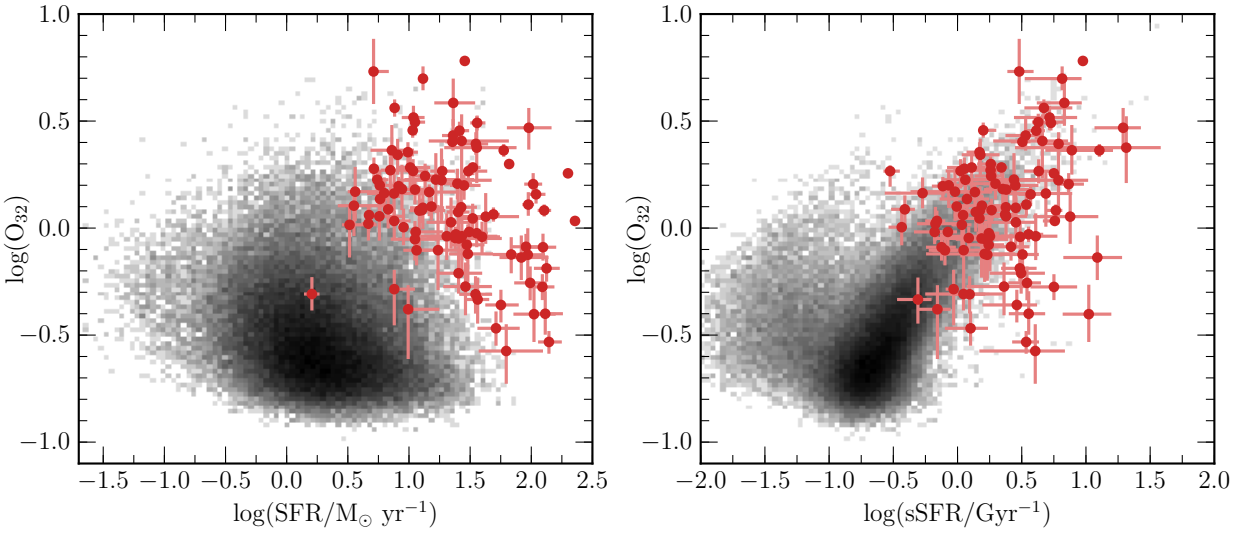

Figure 3.7: O_{32} vs. SFR (top) and sSFR (bottom) for local star-forming galaxies from SDSS (gray histogram) and $z \sim 2.3$ star-forming galaxies from MOSDEF (red circles).

the dependence of the ionization parameter on global galaxy properties through the proxy of O_{32}, motivated by the comparisons performed in Nakajima & Ouchi (2014). Figure 3.7 presents O_{32} vs. SFR and sSFR for local star-forming galaxies (gray histogram) and the $z \sim 2.3$ ionization parameter sample (red circles), while Figure 3.8 shows the dependence of O_{32} on stellar mass for the same samples. As described in Section 3.3.5, the $z \sim 2.3$ galaxies span a similar range in M_* as local SDSS galaxies, but have significantly higher SFR and sSFR at a given stellar mass, consistent with the evolution of the SFR-M_* relation with redshift (Reddy et al., 2012; Whitaker et al., 2014; Shivaei et al., 2015).

Figure 3.7, top panel, shows that there is a weak anti-correlation between O_{32} and SFR for local galaxies, although there is significant scatter in O_{32} at fixed SFR. Performing a Spearman correlation test yields a correlation coefficient of -0.19, indicating a weak anti-correlation, with a p-value[8] that is essentially zero due to the large sample size from SDSS. It is known that there is an anti-correlation between metallicity and ionization parameter in the local universe (Dopita & Evans, 1986; Dopita et al., 2006a,b; Pérez-Montero, 2014; Sánchez et al., 2015), while SFR and metallicity are correlated with large scatter (Mannucci

[8]In the Spearman correlation test, the p-value represents the probability of the dataset being drawn from an uncorrelated underlying distribution. A correlation or anti-correlation with a p-value less than 0.003 has a significange greater than 3σ.

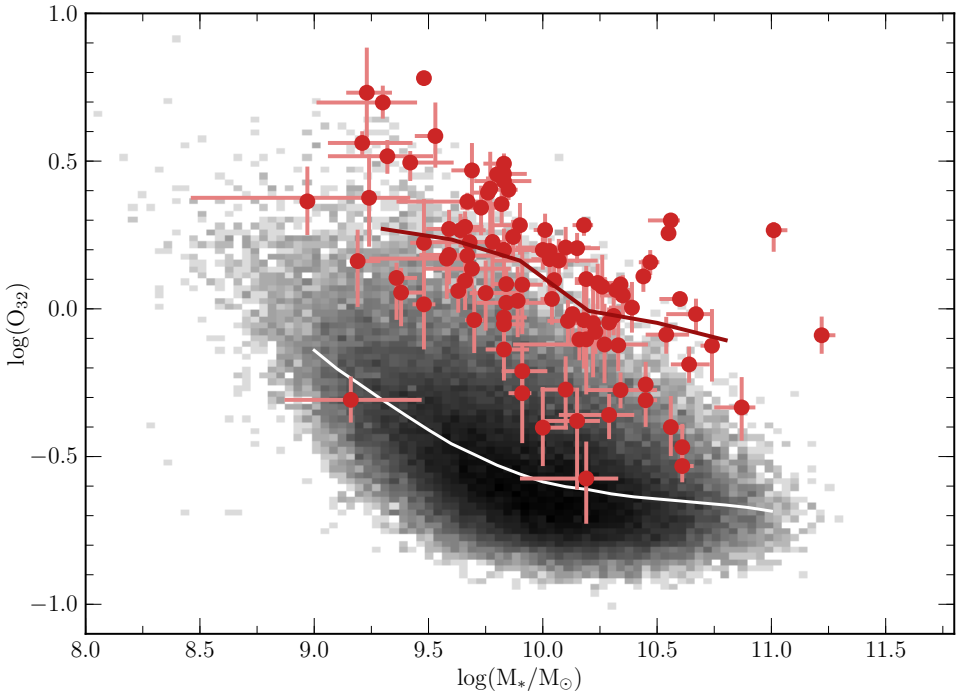

Figure 3.8: O_{32} vs. stellar mass for local star-forming galaxies from SDSS (gray histogram) and $z \sim 2.3$ star-forming galaxies from MOSDEF (red circles). The solid white line shows the running median O_{32} in bins of stellar mass for local galaxies. The solid dark red line shows the running median of $z \sim 2.3$ galaxies.

et al., 2010; Lara-López et al., 2013). Therefore, SFR and ionization parameter are anti-correlated (with large scatter) and the top panel of Figure 3.7 confirms that O_{32} acts as a proxy for the ionization parameter. The $z \sim 2.3$ galaxies also show a weak anti-correlation between O_{32} and SFR, with a Spearman correlation coefficient of -0.30 and a p-value of 0.002.

In the bottom panel of Figure 3.7, there is a tight correlation between sSFR and O_{32} for $z \sim 0$ galaxies, with a Spearman correlation coefficient of 0.42. The bulk of local star-forming galaxies lie on this relation, while a small fraction of local galaxies with the least star formation ($\log(\mathrm{sSFR}) \lesssim -1.0$) do not show any correlation. It is possible that these low-sSFR galaxies have a very low level of ongoing star formation and are transitioning to the red sequence via secular evolution or some other mechanism associated with the cessation of star formation. The ISM conditions in these low-sSFR galaxies may be different from those in typical local star-forming galaxies and would not be expected to follow the same trends. While $z \sim 2.3$ galaxies inhabit much of the same parameter space as highly star-forming local galaxies, they do not exhibit the same tight correlation between sSFR and O_{32}. Performing a Spearman correlation test yields a correlation coefficient of 0.28 with a p-value of 0.004, indicating a weak but significant correlation. There is significant scatter in O_{32} at fixed sSFR, and a non-negligible fraction of the high-redshift sample has high sSFR and low O_{32}, a region of the parameter space where essentially no local galaxies are found. The difference between $z \sim 0$ and $z \sim 2.3$ galaxies in this space is interesting, but outside of the scope of this investigation.

The most intriguing of these diagrams is that of O_{32} vs. M_*, shown in Figure 3.8. Local galaxies show a clear anti-correlation between O_{32} and M_* that is fairly tight, with a Spearman correlation coefficient of -0.52. In order to make the local trend more clear, Figure 3.8 shows the running median O_{32} at a given M_* as a white line. This anti-correlation is consistent with the existence of a tight correlation between M_* and metallicity, known as the mass-metallicity relation (MZR; Lequeux et al., 1979; Tremonti et al., 2004; Kewley & Ellison, 2008; Mannucci et al., 2010; Andrews & Martini, 2013), and an anti-correlation between metallicity and ionization parameter (Pérez-Montero, 2014; Sánchez et al., 2015).

In fact, O_{32} has been shown to be a metallicity indicator for objects up to $z \sim 0.8$ (Maiolino et al., 2008; Jones et al., 2015). The relation between O_{32} and M_* appears to flatten out at high stellar masses, consistent with the observed behavior of the local MZR.

The $z \sim 2.3$ sample also displays a fairly tight relation between O_{32} and M_*such that higher M_* corresponds to lower O_{32}, with a Spearman correlation coefficient of -0.57 and a p-value of 3.7×10^{-10}. We show the running median O_{32} of the high-redshift galaxies at a given M_* as a dark red line in Figure 3.8. The high-redshift anti-correlation shows nearly the same slope as that of the local relation, only offset towards higher O_{32} at fixed M_*. We find that $z \sim 2.3$ galaxies have O_{32} values ~ 0.6 dex higher at a given M_*, suggesting that high-redshift galaxies have significantly higher ionization parameters than local galaxies of the same stellar mass if the translation between O_{32} and ionization parameter is the same at both redshifts. Stellar mass and metallicity are correlated at $z \sim 2.3$ as well (e.g., Erb et al., 2006; Maiolino et al., 2008; Steidel et al., 2014; Sanders et al., 2015), but the MZR evolves such that galaxies at a given M_* have lower metallicities than are observed locally. The existence of a clear O_{32} vs. M_* anti-correlation at $z \sim 2.3$ is suggestive of an anti-correlation between metallicity and ionization parameter existing at high redshifts as well.

The striking similarity of the shape of the O_{32} vs. M_* relation for local and $z \sim 2.3$ galaxies suggests that a similar mechanism may set the observed ionization parameter at both redshifts, but must evolve with redshift such that high-redshift galaxies have higher ionization parameters at a given stellar mass. The evolution of the MZR from $z \sim 0$ to $z \sim 2.3$ provides a natural explanation for the apparent change in ionization parameter at fixed stellar mass. We further investigate the interplay of O_{32}, M_*, and metallicity by employing the use of emission line ratio diagrams.

3.4.4 O_{32} and metallicity

We have shown that there is a relation between O_{32} and M_*, the shape of which is similar for local and $z \sim 2.3$ galaxies, that has a higher normalization in O_{32} at high redshift. However, stellar mass is a global property that is not directly related to the production of emission lines

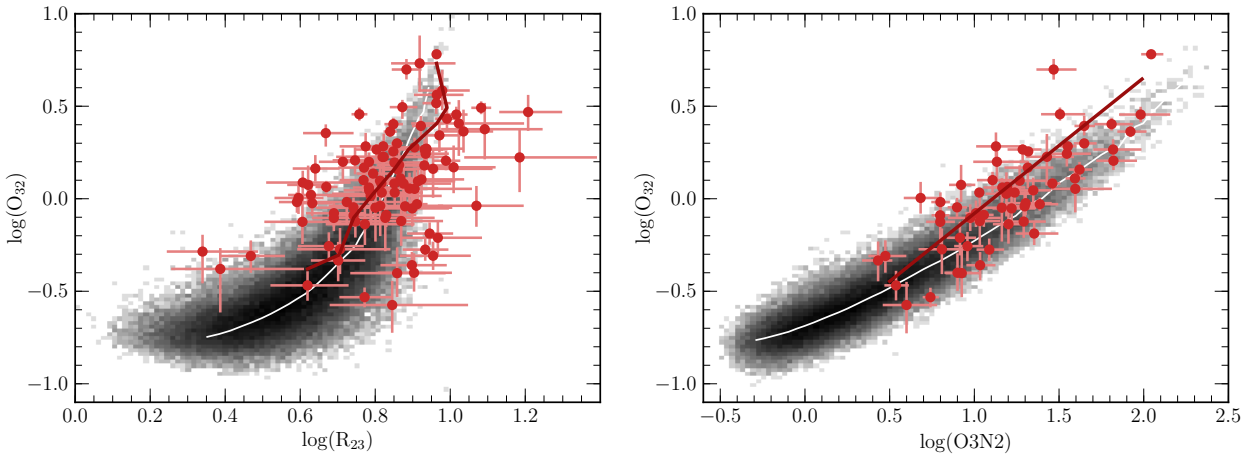

Figure 3.9: O_{32} vs. R_{23} (left panel) and O3N2 (right panel). The gray histogram shows the distribution of local star-forming galaxies from SDSS. The red points and error bars denote $z \sim 2.3$ star-forming galaxies from the MOSDEF survey. In both panels, the white line shows the running median of the local sample. The dark red line shows the running median of the $z \sim 2.3$ in the left panel, and the best-fit linear relation to the $z \sim 2.3$ galaxies in the right panel. The right panel only includes galaxies in the [N II] subsample.

in individual star-forming regions that are an observable probe of the ionization parameter. The metallicity of the gas in star-forming regions, on the other hand, has a direct impact on both the ionizing spectrum, assuming the gas-phase metallicity is related to the stellar metallicity of the ionizing cluster, and the intrinsic emission line fluxes. Therefore, comparing O_{32} values at fixed metallicity rather than fixed M_* utilizes a property that directly influences the physical conditions in star-forming regions, including ionization parameter, and removes systematic effects introduced by the evolution of galaxy scaling relations with M_*.

Figure 3.9 shows the dependence of O_{32} on R_{23} (left) and O3N2 (right) for local SDSS galaxies (gray histogram) and the $z \sim 2.3$ ionization parameter sample. Note that the right-hand panel only includes high-redshift galaxies in the [N II] subsample since the O3N2 ratio requires [N II]λ6584. Figure 3.9 demonstrates that the $z \sim 2.3$ sample is likely free from AGN contamination. AGN are found at low O3N2, high R_{23}, and high O_{32}. No galaxies in the $z \sim 2.3$ sample fall on the AGN sequence in the O3N2 diagram. In the R_{23} diagram, there are several $z \sim 2.3$ galaxies in the same region of parameter space as the AGN sequence ($\log(R_{23}) > 0.95$), but these galaxies fall below the Kauffmann et al. (2003b) line in the [O III]/Hβ vs. [N II]/Hα diagram and tend to have large uncertainties in R_{23}.

The R_{23} index is sensitive to metallicity, but is double-valued (Kewley & Dopita, 2002). This problem can be overcome by using a second excitation-sensitive line ratio in tandem with R_{23}. Shapley et al. (2015) used direct-method abundances of stacks of local galaxies (Andrews & Martini, 2013) to show that the local sequence in the O_{32} vs. R_{23} diagram is a sequence in monotonically increasing metallicity from the high-O_{32}, high-R_{23}, high-excitation tail towards the low-O_{32}, low-R_{23}, low-excitation region. The O3N2 index is also a metallicity indicator, reflecting the fact that the narrow sequence of star-forming galaxies in the BPT diagram is also a sequence in metallicity, and has been used as such in empirical metallicity calibrations (e.g., Pettini & Pagel, 2004). The position on either of these diagrams reflects the ionization parameter at a given oxygen abundance.

Using a smaller sample from the early MOSDEF dataset, Shapley et al. (2015) showed that $z \sim 2.3$ star-forming galaxies seem to follow the same distribution as local galaxies in the low-metallicity, high-excitation tail of the O_{32} vs. R_{23} diagram. We confirm this finding with the current MOSDEF $z \sim 2.3$ sample. The $z \sim 2.3$ galaxies display no systematic offset with respect to the local galaxies, and the bulk of the high-redshift sample inhabits the region in which $12+\log(O/H) \lesssim 8.6$ for local galaxies. The running median of the $z \sim 2.3$ sample (dark red line) closely follows that of $z \sim 0$ galaxies (white line) in the O_{32} vs. R_{23} diagram.[9] We also find that $z \sim 2.3$ galaxies closely follow the subsolar abundance tale of the local distribution in the O_{32} vs. O3N2 diagram, although there is a slight systematic offset towards lower O3N2 at fixed O_{32}. By comparing the best-fit linear relation of the $z \sim 2.3$ sample (dark red line) to the running median of the $z \sim 0$ sample (white line), we find the mean value of this offset to be 0.23 dex in O3N2 at fixed O_{32}. We will discuss the offset in the O3N2 diagram further in Section 3.5.2.

We propose the following scenario to explain the observed position of high-redshift galaxies in the O_{32} vs. R_{23}, O_{32} vs. O3N2, and O_{32} vs. M_* diagrams. Taken together, the two

[9]A running median creates a smooth representation of the local sequence of star-forming galaxies because of the large number of galaxies in the local sample. The small number of galaxies in the $z \sim 2.3$ sample and subsamples can cause the running median to be uneven and erratic. A linear fit better represents the $z \sim 2.3$ subsample distributions in the O3N2 diagram, while a running median is still used in the R_{23} diagram because the O_{32} vs. R_{23} sequence displays curvature.

plots in Figure 3.9 suggest that the ionization parameter at fixed metallicity is the same for galaxies at $z \sim 2.3$ and $z \sim 0$. Galaxies at high redshift must then follow the same anti-correlation between oxygen abundance and ionization parameter that is observed locally. This $\mathcal{U}$ vs. O/H relation shows little to no redshift evolution between $z \sim 0$ and $z \sim 2.3$. The nearly constant offset towards higher O_{32} at fixed M_* observed in Figure 3.8 is then simply a consequence of the evolution of the MZR with redshift. In Sanders et al. (2015), we found $z \sim 2.3$ galaxies have metallicities ~ 0.3 dex lower than local galaxies at fixed M_* using the O3N2 calibration of Pettini & Pagel (2004). If $z \sim 0$ and $z \sim 2.3$ galaxies follow the same metallicity-ionization parameter relation, then the decrease in metallicity at fixed M_* leads to an increase in O_{32}, as observed in Figure 3.8.

Earlier results suggesting that high-redshift galaxies have higher ionization parameters than are seen locally were based on either a comparison at fixed stellar mass (e.g., Holden et al., 2016) or a comparison of the average ionization parameter of the entire local star-forming population to that of high-redshift galaxies (e.g., Hainline et al., 2009). At fixed metallicity, which is more directly related to the ionization state of the gas, we find that $z \sim 2.3$ galaxies have roughly the same ionization parameters compared to local galaxies. The ionization state of star-forming regions in galaxies in our high-redshift sample must then be similar to what is observed in metal-poor local galaxies.

In Section 3.3, we found that the density of star-forming regions increases significantly from $z \sim 0$ to $z \sim 2.3$. Here, we are suggesting that galaxies at $z \sim 0$ and $z \sim 2.3$ have the same ionization parameter at fixed metallicity despite the difference in density. This initially seems to be at odds with the scaling of ionization parameter with density presented in equation 3.15. An increase in density of an order of magnitude would correspond to an increase in the ionization parameter of more than a factor of two. Shirazi et al. (2014) used the relation between ionization parameter and electron density to explain the high ionization parameters observed at $z \sim 2 - 3$ by an increase in the density of star-forming regions. If the scalings in equation 3.15 hold at $z \sim 0$ and $z \sim 2.3$, then an increase in density does not guarantee an increase in the ionization parameter unless the volume filling factor is the same at both redshifts. If high-redshift HII regions are clumpier, the volume filling factor

would decrease with redshift and could offset the effect of an increase in density. However, the scalings presented in equation 3.15 are derived assuming the Strömgren approximation, which does not apply to many local HII regions and likely does not hold at $z \sim 2.3$. Thus, an increase of a factor of 10 in density from $z \sim 0$ to $z \sim 2.3$ does not necessitate higher ionization parameters at fixed metallicity.

Our proposed scenario is only valid if some assumptions hold true. A location in O_{32} vs. R_{23} space must correspond to the same metallicity regardless of redshift. The relation between O3N2 and metallicity must not evolve significantly with redshift. Finally, the translation between ionization parameter and O_{32} must not evolve significantly from $z \sim 0$ to $z \sim 2.3$. We investigate the validity of these assumptions in the following section.

3.5 Discussion

In this section, we present evidence in support of our proposed scenario that $z \sim 2.3$ star-forming galaxies have roughly the same ionization parameter as $z \sim 0$ galaxies when comparing at fixed metallicity. In Section 3.5.1, we investigate whether the translation between O_{32} and ionization parameter evolves with redshift using a set of simple photoionization models in combination with the observed position of $z \sim 2.3$ galaxies in emission line ratio diagnostic diagrams. We explore whether or not there is evidence that the metallicity dependence of R_{23} and O3N2 changes significantly from $z \sim 0$ to $z \sim 2.3$ in Section 3.5.2. In Section 3.5.3, we discuss additional evidence for the existence of an anti-correlation between O/H and $\mathcal{U}$ and how the existence of this anti-correlation affects the interpretation of photoionization model grids. In Section 3.5.4, we use our results to explore the cause of the well-known offset of $z \sim 2$ galaxies in the [N II] BPT diagram compared to local galaxies. Finally, we discuss the uncertainty that diffuse ionized gas introduces in the interpretation of emission line ratios from integrated-light galaxy spectra in Section 3.5.5.

3.5.1 Is the ionization parameter-O_{32} relation redshift invariant?

We first address whether or not the relationship between ionization parameter and O_{32} is the same at $z \sim 0$ and $z \sim 2.3$. We describe the simple photoionization models used for this analysis, discuss the interdependence of the shape of the ionizing spectrum, ionization parameter, and O_{32}, and estimate the typical ionization parameter of $z \sim 2.3$ and local galaxies based on the models.

3.5.1.1 Description of the Cloudy photoionization models

As previously mentioned, the chief difficulty in determing the ionization parameter is that it can only be done with reference to a specific set of photoionization models. The extent to which the value of the estimated ionization parameter can be trusted depends on how well the models represent the observed objects and can produce self-consistent predictions in multiple line ratio spaces. Given the uncertainty of photoionization models both locally and at high-redshift where the physical properties are less constrained, we use a suite of simple photoionization models to understand qualitatively the trends in emission line ratios when changing the different input parameters of the models. We do not, however, use these models to place tight constraints on the metallicity or ionization parameter of any local or high-redshift galaxies.

We use the photoionization code Cloudy[10] to model emission line ratios from star-forming regions with a range of physical conditions. These models are very similar to those used by Steidel et al. (2014) to investigate the position of $z \sim 2.3$ galaxies in the [O III]/Hβ vs. [N II]/Hα diagram. There are five main input parameters that determine the location of a grid point in various emission line ratio diagrams: hydrogen gas density, gas-phase metallicity, ionization parameter, shape of the ionizing spectrum, and N/O abundance ratio.

In Section 3.3, we presented a robust characterization of the typical electron density in local and $z \sim 2.3$ galaxies, finding densities of ~ 25 cm^{-3} and ~ 250 cm^{-3}, respectively. In

[10]Calculations were performed with version 13.02 of Cloudy, last described by Ferland et al. (2013).

HII regions, the gas is fully ionized and the electron density provides a good estimate of the hydrogen gas density. Since we have measured the typical density at $z \sim 0$ and $z \sim 2.3$, we only allow the density to be either 25 cm^{-3} or 250 cm^{-3} in the models. The metallicity sets the global abundance scale of the gas, which is assumed to follow a solar abundance pattern with the exception of nitrogen. We vary the metallicity between 0.2 $Z_\odot$ and 1.0 $Z_\odot$ ($12 + \log(O/H) = 8.0 - 8.69$) in 0.2 $Z_\odot$ steps with solar metallicity corresponding to $12 + \log(O/H)_\odot = 8.69$ (Asplund et al., 2009). The ionization parameter sets the ionization state of the gas and is allowed to vary between $\log(\mathcal{U}) = -3.6$ and -1.5 ($\log(\frac{q}{\mathrm{cm/s}}) = 6.9-9.0$) in 0.1 dex steps.

As described in Section 3.4.1, the shape of the ionizing spectrum affects the relative populations of an element in different ionized states. A harder ionizing spectrum results in a larger fraction of oxygen in O III compared to O II, for example. We use a blackbody spectrum with an effective temperature of 40,000 K, 50,000 K, or 60,000 K as the input ionizing spectrum. Steidel et al. (2014) showed that, when properly normalized, a blackbody spectrum is a good approximation of the spectrum of massive stars bluewards of 912 Å using BPASS stellar models that include effects from binarity (Eldridge et al., 2011; Eldridge & Stanway, 2012). We have found this observation to hold true when using Starburst99 (SB99) stellar models that include effects of rotation in massive stars (Leitherer et al., 2014). We note that the effective temperature of the blackbody is not the same as the effective temperature of a star. It is simply a parameter that allows us to specify the shape of the input spectrum. When referring to a "harder" ionizing spectrum, we are referring to an increase in the blackbody effective temperature of the input spectrum. We additionally utilize input spectra produced by SB99 using the Geneva 2012/13 tracks (Ekström et al., 2012; Georgy et al., 2013) that include the effects of rotation in massive stars (Leitherer et al., 2014). We create two input spectra from SB99 that create bracketing cases of a very hard ionizing spectrum, which we refer to as "*SB99 hard*", and a softer ionizing spectrum, which we refer to as "*SB99 soft*." *SB99 hard* is produced assuming a single burst of star-formation that formed 0.5 Myr ago with stellar metallicity of 1/7 $Z_\odot$. *SB99 soft* instead assumes a 10 Myr-old population with solar metallicity formed with a continuous SFR of 1 $M_\odot$/yr. An age of 10 Myr was

chosen to ensure that the ionizing spectrum of the stellar population had reached a steady state, occuring after $\sim$ 5 Myr (Kewley et al., 2001). In both cases, a Salpeter (1955) IMF slope is assumed above 0.5 $M_{\odot}$. These two cases roughly bracket the range of ionizing spectra appropriate for HII regions contributing significantly to integrated-light galaxy spectra.

In reality, the shape of the ionizing spectrum should be related to the gas-phase metallicity, which traces the stellar metallicity since recently formed massive stars are ionizing the remnants of their birth cloud. In lower metallicity stars, there is less metal line blanketing and opacity in the stellar atmospheres, leading to hotter effective temperatures and harder ionizing spectra. However, we allow the shape of the ionizing spectrum to vary separately from the metallicity to accomodate the possibility that the hardness of the ionizing spectrum at fixed metallicity evolves with redshift.

A solar abundance pattern is assumed for all elements except nitrogen. In the local universe, the N/O abundance ratio is observed to have a dependence on O/H, such that N/O is a constant value at low abundance but begins to rise roughly linearly with O/H at higher abundance (Pérez-Montero & Contini, 2009; Pilyugin et al., 2012b; Andrews & Martini, 2013; Pérez-Montero, 2014). At low metallicity, nitrogen is a primary nucleosynthetic product of hydrogen and helium burning. At high metallicity, nitrogen is produced as a secondary product through the CNO cycle where the yield of nitogren depends on the amount of pre-existing C and O, which leads to the dependence of N/O on O/H (van Zee & Haynes, 2006). There is disagreement about the shape of the N/O vs. O/H relation (see Fig. 12 in Steidel et al., 2014). We assume the relation found by Pérez-Montero & Contini (2009), which is a simple linear relation over the range of metallicities considered in the models. We note that the assumed N/O ratio can strongly affect those line ratios involving [N II]λ6584, but has negligible effects on other line ratios.

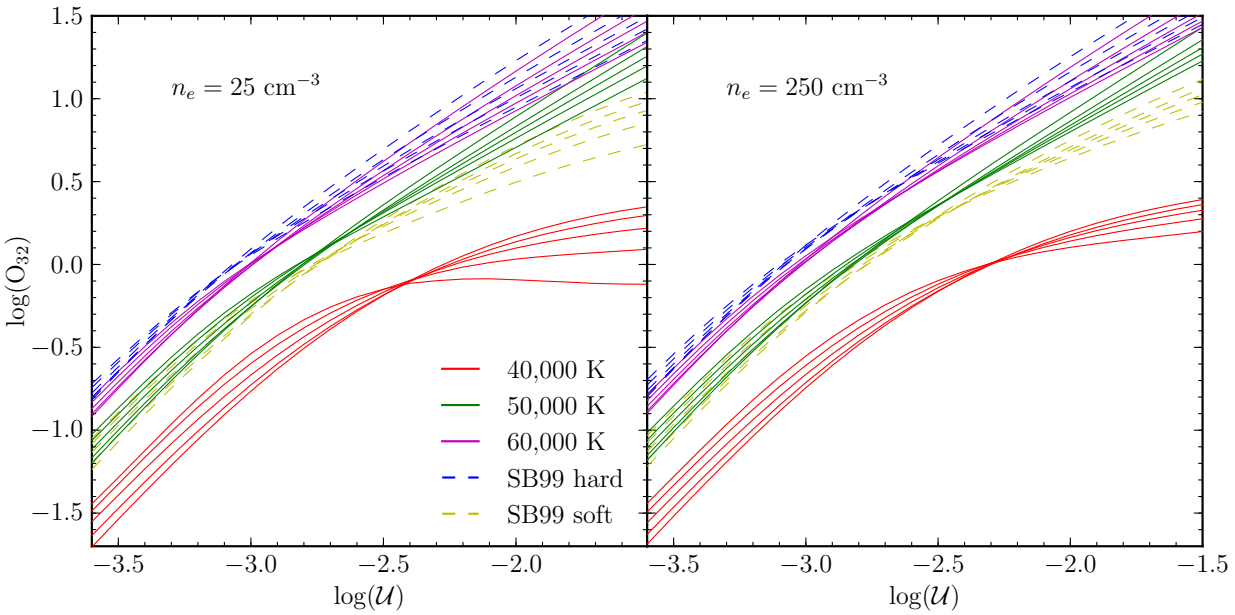

Figure 3.10: O_{32} vs. ionization parameter, $\mathcal{U}$, from simple photoionization models of HII regions assuming a gas density of 25 cm^{-3} (top panel) and 250 cm^{-3} (bottom panel). The dependence of O_{32} on $\mathcal{U}$ is extracted from a set of models assuming different ionizing spectra, denoted by the color of the line, and different gas-phase metallicities. Input ionizing spectra are assumed to be either a blackbody spectrum with an effective temperature of 40,000-60,000 K or one of two spectra produced by Starburst99 (*SB99 hard* and *SB99 soft*). Each line of a single color connects models with the same gas-phase metallicity, from 0.2 $Z_\odot$ to 1.0 $Z_\odot$.

3.5.1.2 Ionization parameter and the hardness of the ionizing spectrum at $z \sim 0$ to $z \sim 2.3$

From the set of models with density, gas-phase metallicity, ionization parameter, ionizing spectrum, and N/O ratio defined as above, we extract the relationship between O_{32} and ionization parameter to resolve its dependence on the various input parameters. Figure 3.10 shows O_{32} vs. $\log(\mathcal{U})$ for models with electron density of 25 cm^{-3} (top panel) and 250 cm^{-3} (bottom panel). The line color denotes the input spectrum, while the different lines of a single color connect grid points with the same metallicity. We note that the *SB99 hard* models behave very similarly to the 60,000 K blackbody models. The *SB99 soft* spectrum appears to be slightly softer than a 50,000 K blackbody based on the position of the model grids. Variation in N/O has no effect on the relationship between O_{32} and $\mathcal{U}$. In addition, Figure 3.10 shows that this relation has very little dependence on the gas density. Lines of constant metallicity show that the relation between O_{32} and $\mathcal{U}$ has only a small dependence on gas-phase metallicity *when the shape of the input spectrum is fixed*. The one exception is for a soft ionizing spectrum with high ionization parameter and low gas density ($T_{\rm eff} = 40,000$ K, $\log(\mathcal{U}) > -2.5$, $n_e = 25$ cm^{-3}), a region in which real objects are unlikely to be found. Calibrations of O_{32} and the ionization parameter typically show significant dependence on metallicity because the ionizing spectrum is tied to the metallicity (e.g., Kewley & Dopita, 2002). On the other hand, the hardness of the ionizing spectrum has a significant effect on the O_{32} vs. $\log(\mathcal{U})$ relation, such that a harder ionizing spectrum produces a larger O_{32} value at fixed ionization parameter. Therefore, the translation between O_{32} and ionization parameter will only show significant evolution if the hardness of the ionizing spectrum at a given metallicity evolves with redshift.

We investigate the possibility of the shape of the ionizing spectrum evolving with redshift by combining the observed line ratios for our $z \sim 2.3$ sample with grids from the Cloudy models in emission line ratio diagrams. It has been proposed that the position of high-redshift galaxies in the [O III]/Hβ vs. [N II]/Hα diagram can be explained by a systematically harder ionizing spectrum compared to that of local galaxies with similar metallicity (Kewley et al.,

2013a; Steidel et al., 2014). If true, this explanation would lead to evolution of the ionization parameter-O_{32} relation.

Figure 3.11 shows the [O III]/Hβ vs. [N II]/Hα ([N II] BPT) diagram (left column) and the [O III]/Hβ vs. [S II]/Hα ([S II] BPT) diagram (right column). The local distribution of star-forming galaxies is shown as the gray histogram in all panels. The top row presents the observed line ratios for the $z \sim 2.3$ [N II] subsample (top left) and [S II] subsample (top right). The middle and bottom rows show the Cloudy model grid points as circles. The size of the circle indicates the metallicity, with the largest size indicating solar metallicity and the smallest size indicating 0.2 $Z_{\odot}$. The color indicates the input ionizing spectrum, with the effective temperature listed for blackbodies in the middle row and the bracketing SB99 models shown in the bottom row. Solid lines connect points of constant ionization parameter, with ionization parameter increasing to the upper left. The model grids are only shown for a density of 250 cm^{-3}. Displaying models at a single density will suffice since we are only interested in discerning trends in line ratio with the model input parameters instead of making quantitative predictions. While the absolute line ratios change, the trends with metallicity, ionization parameter, and hardness of the ionizing spectrum are the same regardless of the assumed density. Qualitatively, increasing the electron density while keeping all other parameters fixed increases [O III]/Hβ, [N II]/Hα, and [S II]/Hα.

In the top right panel of Figure 3.11, we observe the well-documented offset of $z \sim 2.3$ galaxies towards higher [O III]/Hβ and/or [N II]/Hα compared to the local star-forming sequence. The magnitude of this offset can be observed by comparing the running median of the $z \sim 2.3$ sample (dark red line) to that of the $z \sim 0$ sample (white line). However, we do not observe a significant offset between $z \sim 0$ and $z \sim 2.3$ galaxies in the [S II] BPT diagram (top left panel), in agreement with results from early MOSDEF data (Shapley et al., 2015). Masters et al. (2014) found a similar result using a composite spectrum of 24 $z \sim 2$ emission-line galaxies from the WISP survey. In the [S II] BPT diagram, the running median of the $z \sim 2.3$ sample is marginally offset to lower [O III]/Hβ and/or [S II]/Hα, although this offset is not significant given the sample size and measurement uncertainty. In the middle and lower left panels, it can be seen that an increase in the hardness of the ionizing spectrum

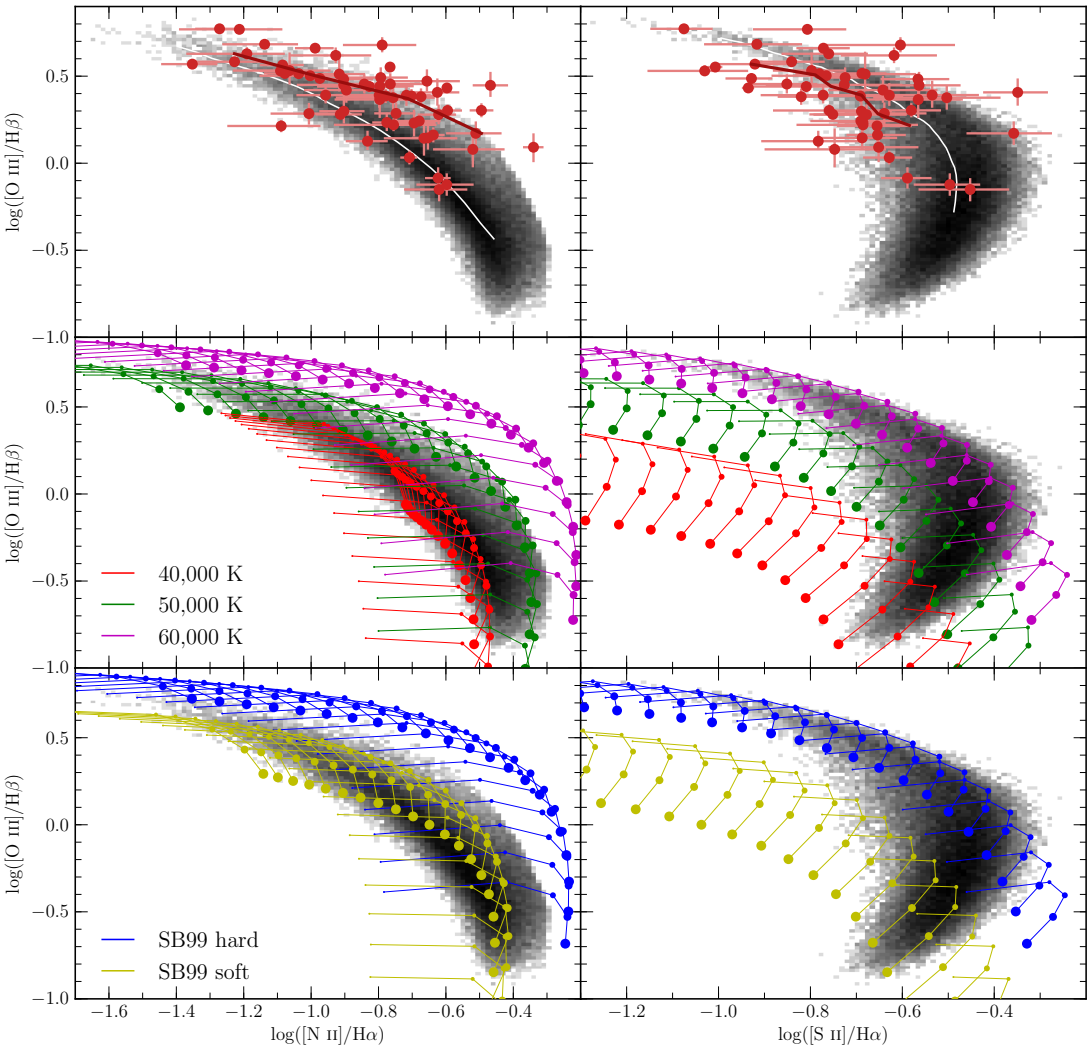

Figure 3.11: [N II] (left column) and [S II] (right column) BPT diagrams. The local sequence of star-forming galaxies from SDSS is shown as the gray histogram in all panels. The top row shows the position of $z \sim 2.3$ star-forming galaxies in the [N II] and [S II] BPT diagrams as red points with error bars. The white and dark red lines show the running median of the local and $z \sim 2.3$ samples, respectively. The bottom two rows show grids from simple photoionization models of HII regions produced using Cloudy. Different colors represent different input ionizing spectra. In the middle row, the input ionizing spectrum is assumed to be a blackbody spectrum and the effective temperature is listed, representing the hardness of the ionizing spectrum. In the bottom row, the input ionizing spectrum is assumed to be one of two spectra produced by the stellar population synthesis code Starburst99 (*SB99 hard* and *SB99 soft*). Colored circles show the model grid points, where the size of the circle represents the gas-phase metallicity, from 0.2 $Z_{\odot}$(smallest circles) to solar metallicity (largest circles). Grid points of constant ionization parameter with the same input ionizing spectrum are connected with solid lines. All model grids shown are calculated assuming a hydrogen gas density of 250 cm^{-3}.

generally moves grid points to higher [O III]/Hβ and [N II]/Hα at fixed metallicity and ionization parameter, which could potentially explain the $z \sim 2.3$ offset. In the [S II] BPT diagram (middle and lower right), the models show that an increase in the hardness of the ionizing spectrum increases [O III]/Hβ at fixed [S II]/Hα. We emphasize that we are using these models to demonstrate how predicted line ratios change qualitatively as the hardness of the ionizing spectrum varies. We are less concerned with a match between a specific blackbody or SB99 spectrum and either the local or high-redshift excitation sequences.

In both BPT diagrams, an increase in the hardness of the ionizing spectrum leads to a significant increase in [O III]/Hβ at fixed [N II]/Hα or [S II]/Hα for the same ionization parameter and metallicity. If a harder ionizing spectrum was the cause of the offset of high-redshift galaxies in the [N II] BPT diagram, simple photoionization models predict that there should also be an offset of similar magnitude towards higher [O III]/Hβ in the [S II] BPT diagram. We observe no significant offset between the $z \sim 2.3$ and $z \sim 0$ galaxies in the [S II] BPT diagram. We note that in the [N II] BPT diagram, the 60,000 K and 50,000 K blackbody models approximately match the position of the $z \sim 2.3$ and local galaxies, respectively. The same 60,000 K and 50,000 K blackbody models are offset from one another in the [S II] BPT diagram, and yet no offset is observed in the corresponding observations of $z \sim 2.3$ and local galaxies. We conclude that there is not a systematically harder ionizing spectrum in high-redshift star-forming regions compared to local star-forming regions of similar metallicity. We will revisit the cause of the [N II] BPT diagram offset in Section 3.5.4. Having established that the relation between ionization parameter and O_{32} is only significantly sensitive to changes in the hardness of the ionizing spectrum, we further conclude that the $\mathcal{U}$-O_{32} relation does not strongly evolve with redshift.

3.5.1.3 Estimating the typical ionization parameter at $z \sim 2.3$

Having shown that the translation between O_{32} and ionization parameter does not appear to evolve significantly with redshift, we will now estimate the range of ionization parameters that would be inferred from the local and $z \sim 2.3$ galaxy samples. We advise caution when

using these ionization parameter estimates because a different ionizing spectrum should be used for the low- and high-metallicity galaxy populations and the use of different stellar models will change these estimates. Matching the appropriate stellar models to a given object is further complicated by uncertainty in the metallicity estimates used to tie the observed metallicity to the absolute metallicity built into the stellar models. Since we do not know which input ionizing spectrum is appropriate for each sample, we provide estimates of the ionization parameter assuming each of the five ionizing spectra considered in the models. The median $\log(O_{32})$ value of the $z \sim 2.3$ sample is 0.10 and the middle 68% span $\log(O_{32}) = -0.11$ to 0.37. The local SDSS sample has a median $\log(O_{32})$ value of -0.53 and the middle 68% span $\log(O_{32}) = -0.71$ to -0.24. Estimates of the corresponding values of $\log(\mathcal{U})$ are presented in Table 3.3 using the curves in Figure 3.10. We note that the median ionization parameter is approximately the same for $z \sim 0$ and $z \sim 2.3$ galaxies if the ionizing spectrum of local galaxies is well-described by a 40,000 K blackbody and that of $z \sim 2.3$ galaxies is described by a 60,000 K blackbody. However, we have shown that $z \sim 0$ and $z \sim 2.3$ galaxies have similar ionizing spectra at fixed metallicity. While the ionizing spectrum at the median metallicity of each sample will be different, it is unlikely that the magnitude of that difference is as large as the difference between a 40,000 K and 60,000 K blackbody spectrum. Therefore, $z \sim 2.3$ galaxies have a higher median ionization parameter than local galaxies.

3.5.2 Is the dependence of R_{23} and O3N2 on metallicity redshift invariant?

We proposed that the relationship between metallicity and ionization parameter is the same locally and at $z \sim 2.3$. In Figures 3.10 and 3.11, we have shown evidence that the relationship between ionization parameter and O_{32} does not significantly change with redshift. In order for the proposed scenario to hold in concordance with Figure 3.9, we must also show that the dependence of R_{23} and O3N2 on metallicity does not significantly evolve with redshift. In Figure 3.12, we show the local star-forming sample (gray histogram) and the $z \sim 2.3$ [N II] subsample (red circles) in the spaces of O_{32} vs. R_{23} (left), O3N2 (middle), and N2 (right).

Table 3.3: Ionization parameter estimates of local SDSS and $z \sim 2.3$ star-forming galaxies based on O_{32} for each of the five input ionizing spectra assumed in our photoionization models.

		$\log(O_{32})$	$\log(\mathcal{U})$ assuming an ionizing spectrum of:				
			40,000 K	50,000 K	60,000 K	SB99 soft	SB99 hard
SDSS	median	-0.53	-2.90	-3.20	-3.40	-3.20	-3.45
	lower 68%[a]	-0.71	-3.05	-3.35	-3.50	-3.35	-3.60
	upper 68%[b]	-0.24	-2.60	-3.05	-3.20	-3.00	-3.25
$z \sim 2.3$	median	0.10	-2.10	-2.75	-2.95	-2.70	-3.00
	lower 68%[a]	-0.11	-2.45	-2.95	-3.10	-2.90	-3.15
	upper 68%[b]	0.37	$\gtrsim -1.5$[c]	-2.50	-2.70	-2.40	-2.75

(a) The lower bound on the middle 68% of the distribution of $\log(O_{32})$

(b) The upper bound on the middle 68% of the distribution of $\log(O_{32})$

(c) The range of ionization parameters considered in this set of models did not extend high enough to give $\log(O_{32}) = 0.37$ for a 40,000 K blackbody input spectrum, so a lower limit is assigned.

As previously mentioned, no systematic offset is observed between $z \sim 0$ and $z \sim 2.3$ galaxies in the O_{32} vs. R_{23} diagram, although $z \sim 2.3$ objects only occupy the low-metallicity tail of the local distribution. We also pointed out the 0.23 dex offset $z \sim 2.3$ galaxies show towards low O3N2 at fixed O_{32} in Section 3.4.4. We find a larger systematic offset between local and high-redshift galaxies in the O_{32} vs. N2 diagram of 0.33 dex higher N2 at fixed O_{32}. There is an assymetric scatter towards high N2, such that no $z \sim 2.3$ galaxies scatter below the local sequence. We additionally observed no significant offset in the [S II] BPT diagram (Fig. 3.11). These results collectively suggest that, on average, high-redshift galaxies have higher [N II]λ6584 flux compared to the strength of other strong optical emission lines than typical local galaxies with the same ionization parameter. Outside of line ratios involving nitrogen, high-redshift galaxies appear to behave similarly to the low-metallicity tail of the local distribution. We have measurements constraining the evolution of density with redshift, and have found no evidence suggesting the ionization parameter or hardness of the ionizing spectrum evolve significantly at fixed metallicity. Therefore, we conclude that metallicity indicators involving nitrogen will evolve with redshift, but the relation between metallicity and location in the O_{32} vs. R_{23} diagram is likely the same at $z \sim 0$ and $z \sim 2.3$. Jones et al. (2015) recently found that the relationship between R_{23}, O_{32}, and direct-method metallicity

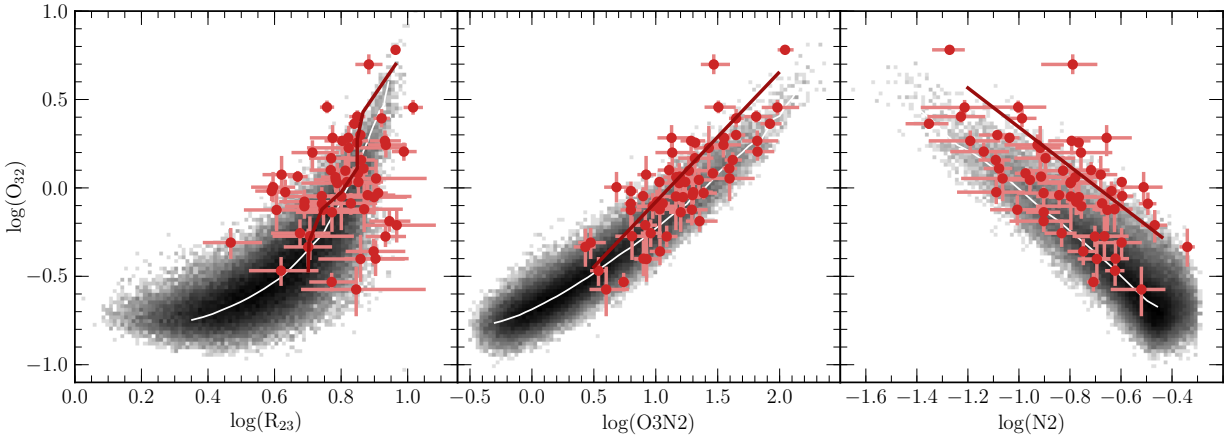

Figure 3.12: O_{32} vs. R_{23} (left), O3N2 (middle) and N2 (right) for local star-forming galaxies (gray histogram) and the $z \sim 2.3$ [N II] subsample (red points). In all panels, the white line shows the running median of the local sequence of star-forming galaxies. The dark red line shows the running median of the $z \sim 2.3$ sample in the left panel, and the best-fit linear relation in the middle and right panels.

does not evolve out to $z \sim 0.8$. Liu et al. (2008) and Steidel et al. (2014) concluded that the N2 indicator significantly over-estimates the metallicity of objects offset from the local star-forming sequence, while the O3N2 indicator has a much smaller bias. In conjunction with the arguments presented in Section 3.5.1, these results support our proposed scenario that galaxies at fixed metallicity have the same ionization parameter locally and at $z \sim 2.3$.

3.5.3 Additional evidence for the existence of the metallicity-ionization parameter anti-correlation

The argument for an anti-correlation between O/H and ionization parameter arises from the fact that low-metallicity stars produce more ionizing photons in total and have harder ionizing spectrum (Leitherer et al., 2014). Observational evidence for this anti-correlation comes from finding that O_{32} and [O III]/Hβ increase with decreasing metallicity (Maiolino et al., 2008; Jones et al., 2015). However, in Figure 3.10 it can be seen that harder ionizing spectra give higher values of O_{32} at fixed ionization parameter. We must then consider the possibility that high- and low-metallicity star-forming regions have similar ionization parameters while having higher O_{32} values because of the change in the hardness of the ionizing spectrum with metallicity. At fixed $\mathcal{U}$, the range of ionizing spectra considered in

the models spans ~ 0.9 dex in O_{32}. Local star-forming galaxies from SDSS span a range of ~ 1.9 dex in O_{32} from $\log(O_{32}) \sim -1.0$ to 0.9 (see Fig. 3.9). Based on physically-motivated input spectra, it is not possible for the models to span a range that large in O_{32} at fixed $\mathcal{U}$. It would require spectra that are harder or softer than what is reasonably expected from models of the young stellar populations responsible for ionizing HII regions. Because the hardness of the ionizing spectrum increases with decreasing metallicity and low-metallicity objects are observed to have higher O_{32} values on average, the only way to produce the dynamic range in O_{32} observed among the SDSS sample is for high-metallicity objects to have low ionization parameters, and vice versa. The relation between O/H and ionization parameter must exist in the local universe, along with a changing ionizing spectrum with metallicity, to reproduce the observed range in O_{32}.

Once established, the existence of an anti-correlation between O/H and ionization parameter lends insight into the interpretation of the simple models presented in Figure 3.11. Using similar photionization models to those presented above, Steidel et al. (2014) argued that the sequence of galaxies in the [N II] BPT diagram at low or high redshift is primarily a sequence in ionization parameter because increasing ionization parameter with all other inputs fixed moves grid points along the star-forming sequence. Given the dependence of the ionization parameter and hardness of the ionizing spectrum on O/H, many of the grid points shown in Figure 3.11 are not descriptions of real objects. We do not expect to see galaxies with high metallicities, high ionization parameters, and hard ionizing spectra. Likewise, galaxies with low metallicities, low ionization parameters, and soft ionizing spectra are not likely to be observed. In fact, it has been previously observed that local HII regions and star-forming galaxies only occupy a narrow subset of the parameter space in photoionization model grids (e.g., Dopita & Evans, 1986; Dopita et al., 2006a,b). While individual HII regions can simultaneously demonstrate low metallicity and low ionization parameter, as in the sample discussed in van Zee & Haynes (2006), such objects would contribute negligibly to a luminosity-weighted galaxy-averaged spectrum for galaxies that are actively star-forming.

The star-forming sequence in the [N II] BPT diagram can be understood as a sequence in both ionization parameter and metallicity because the two are fundamentally linked (Bresolin

et al., 2012; Sánchez et al., 2015). Steidel et al. (2014) did mention the relations between ionization parameter, metallicity, and ionizing spectrum as a way to reconcile the utility of strong-line metallicity indicators in the *local universe* with the apparent lack of dependence of the star-forming sequence on metallicity in photoionization models. Our results suggest that these relations hold in similar form at $z \sim 2.3$ as well. We note that these relations are traced by the *typical* properties of the galaxy population, and do not preclude the existence of a small number of galaxies in unexpected regions of the parameter space due to scatter in the relations or significantly different conditions caused by some rare process or event, such as a major merger.

3.5.4 Nitrogen abundance and the cause of the [N II] BPT diagram offset

A significant amount of effort has been put forth to find the cause of the offset high-redshift galaxies display in the [N II] BPT diagram (Kewley et al., 2013a,b; Masters et al., 2014; Steidel et al., 2014; Shapley et al., 2015). Proposed causes include systematically higher ionization parameters (Brinchmann et al., 2008), systematically harder ionizing spectra (Steidel et al., 2014), elevated nitrogen abundance at fixed metallicity (Masters et al., 2014; Shapley et al., 2015), and higher gas density/ISM pressure (Kewley et al., 2013a). It has additionally been proposed that the offset in the BPT diagram is an artifact arising from widespread, weak AGN in the high-redshift galaxy population (Wright et al., 2010). Coil et al. (2015) have shown that such global AGN contamination does not appear to be present among $z \sim 2.3$ galaxies from the MOSDEF survey.

In this chapter, we have sought to characterize the physical properties influencing the ionization state of high-redshift galaxies, and can now use the results presented herein to investigate the cause of the [N II] BPT diagram offset. Figure 3.13 shows the [N II] and [S II] BPT diagrams (Fig. 3.11) and the O_{32} vs. R_{23}, O3N2, and N2 diagrams (Fig. 3.12) with the $z \sim 2.3$ galaxies color-coded according to the magnitude of the offset in the [N II] BPT diagram. We divided the $z \sim 2.3$ sample in the [N II] BPT diagram at the running median [O III]/Hβ in bins of [N II]/Hα, shown by the solid purple line in the top right panel.

Galaxies above and to the right of this line in the [N II] BPT diagram are shown in blue, while those galaxies that show a smaller offset and overlap the local sequence are shown in red. We have verified that our results do not change if other dividing lines in the [N II] BPT diagram are used, including a linear fit and the best-fit line to the $z \sim 2.3$ star-forming sequence from Shapley et al. (2015) (red dashed line).

We find that the blue and red data points are well mixed and are not systematically offset from the local distribution in the O_{32} vs. R_{23} diagram. The running median of the three samples follow a very similar sequence where there is overlap at $\log(O_{32}) \sim -0.1$ to 0.4. Similarly, the blue data points do not appear to follow a different distribution from that of the red data points or the low-metallicity local sequence in the [S II] BPT diagram. There is some separation in the two subsamples in the [S II] BPT diagram because the blue data points have higher [O III]/Hβ a priori due to the selection. In the O3N2 diagram, the red points fall close to the local distribution, while the blue points appear to be slightly more offset towards lower O3N2 at fixed O_{32}. The blue data points display less overlap with the red data points in the N2 diagram and a larger offset compared to local galaxies. We use the best-fit linear relations to the blue and red datapoints, respectively, to quantify the mean offsets and make the offsets clearer. The red line has a mean offset of -0.11 dex in O3N2 at fixed O_{32} compared to the local median, while the blue line is offset -0.30 dex on average. In the N2 diagram, the red and blue lines are offset 0.08 and 0.40 dex, respectively, towards higher N2 at fixed O_{32}.

To summarize, we find that, as a whole, the $z \sim 2.3$ sample shows no significant offset in line ratio diagrams that do not include nitrogen ([S II] BPT and O_{32} vs. R_{23} diagrams). We find a slight offset in a diagram that utilizes a line ratio including nitrogen as well as oxygen (O_{32} vs. O3N2 diagram). This offset increases in the N2 diagram, in which nitrogen is the only metal species in the line ratio. Additionally, we find that galaxies showing the largest offset in the [N II] BPT diagram do not distinguish themselves from galaxies showing a smaller offset when plotted in diagrams that do not include nitrogen. The most-offset galaxies in the [N II] BPT diagram display systematically lower O3N2 values at fixed O_{32} than galaxies showing a small offset in the [N II] BPT diagram. This effect increases in

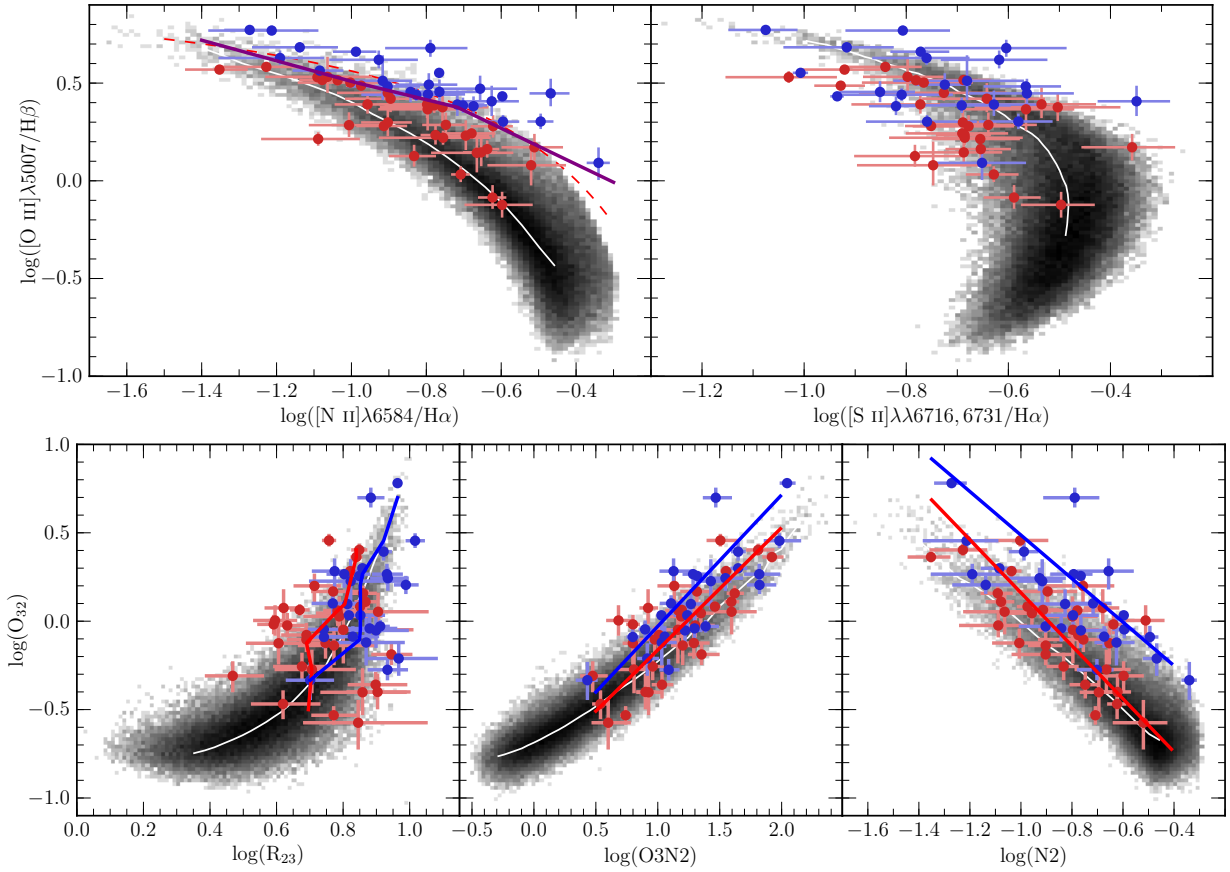

Figure 3.13: Emission line ratio diagrams with $z \sim 2.3$ galaxies color-coded by the offset in the [N II] BPT diagram. In each panel, the gray histogram shows the distribution of local star-forming galaxies from SDSS. The top row shows the [N II] (top left) and [S II] (top right) BPT diagrams. The O_{32} vs. R_{23}, O3N2, and N2 diagrams are shown in the left, middle, and right panels, respectively, of the bottom row. In each panel, the white line shows the running median of the $z \sim 0$ sample. In the top left panel, the solid purple line shows the running median of the $z \sim 2.3$ star-forming galaxies, while the dashed red line shows the fit to the MOSDEF $z \sim 2.3$ star-forming sequence from Shapley et al. (2015). In all panels, $z \sim 2.3$ galaxies falling above and to the right of the dashed red line are color-coded blue, while $z \sim 2.3$ galaxies falling below and to the left of this line are color-coded red. In the lower left panel, the red and blue curves show the median R_{23} in bins of O_{32} for the red and blue data points, respectively. The solid red and blue lines in the lower middle and right panels show the best linear fit to the red and blue data points, respectively. See Footnote 9 regarding the use of running medians and best-fit lines.

magnitude in the O_{32} vs. N2 diagram, in which those galaxies showing a large offset in the [N II] BPT diagram display significantly larger N2 values at fixed O_{32} than the less-offset subsample of the $z \sim 2.3$ galaxies. A simple way to change the [N II]λ6584 flux without affecting the flux of the other strong optical emission lines is to change the nitrogen abundance. Our observations suggest that the N/O ratio at fixed O/H is higher on average in $z \sim 2.3$ star-forming galaxies compared to local star-forming galaxies. The high-redshift galaxies showing the largest offset in the [N II] BPT diagram appear to have higher N/O ratios than less offset $z \sim 2.3$ galaxies of the same metallicity.

In Sections 3.5.1 and 3.5.2, we showed that our data are inconsistent with a systematically harder ionizing spectrum or higher ionization parameter in high-redshift galaxies at fixed metallicity. An increase in the gas density or ISM pressure can also move galaxies in the direction of the observed offset. We utilize Cloudy photoionization models to quantify the magnitude of this effect using the characteristic densities obtained in Section 3.3. Figure 3.14 shows the local star-forming sequence for reference, along with two photoionization model grids produced with the same ionizing spectrum (blackbody with $T_{\rm eff} = 50,000$ K) while varying the electron density between 25 cm^{-3} and 250 cm^{-3}. The grids are shown over the metallicity range 0.2-0.6 $Z_\odot$ in which the typical metallicity at $z \sim 2.3$ is expected to fall. The lowest metallicity grid points show negligible change in line ratios with density, while the dependence on density increases with metallicity. With an increase of a factor of 10 in density, [O III]/Hβ and [N II]/Hα are increased by $\lesssim 0.1$ dex at fixed ionization parameter and metallicity. This is not a large enough shift to account for the observed offset in the [N II] BPT diagram. If our density estimate for local star-forming regions is underestimated, then the magnitude of the line ratio shift caused by density will be even smaller. Thus, the increase in density from $z \sim 0$ to $z \sim 2.3$ plays only a minor role in the [N II] BPT diagram offset.

We conclude that the observed offset of $z \sim 2.3$ galaxies from the local star-forming sequence in the [N II] BPT diagram is mostly caused by elevated N/O at fixed O/H compared to local galaxies, while an increase in density/pressure of the star-forming regions plays a minor role. We do not find evidence that a change in the ionizing spectrum or ionization

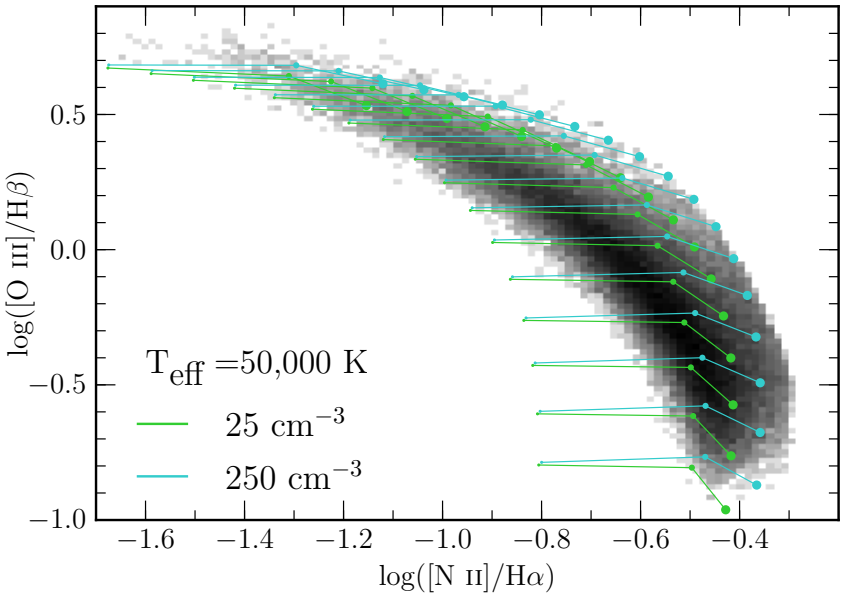

Figure 3.14: Model grids assuming a gas density of 25 cm^{-3} (light green) and 250 cm^{-3} (cyan) with gas-phase metallicity spanning 0.2-0.6 $Z_{\odot}$ and an input ionizing spectrum of a 50,000 K blackbody. Grid points are displayed as in Figure 3.11.

parameter at fixed metallicity plays a part in the offset. This finding is consistent with earlier MOSDEF results from Shapley et al. (2015) attributing the offset in the BPT diagram to higher N/O in high-redshift galaxies with $M_* < 10^{10}$ $M_{\odot}$. Our results are also in agreement with the interpretation of Masters et al. (2014), in which anamolous nitrogen abundance was first proposed as a cause of the offset. Steidel et al. (2014) also found an elevated N/O among their $z \sim 2.3$ sample, but argued that the primary cause of the offset lies in harder ionizing spectra and higher ionization parameters in comparison to what is observed locally.

The cause of the higher N/O ratios observed at high-redshift is not yet clear. Masters et al. (2014) speculated that a larger-than-normal population of Wolf-Rayet stars could produce a nitrogen enhancement, although a mechanism to produce such a population exclusively at high redshifts was not proposed. If the nitrogen enhancement is due to a significant difference in the stellar population at a given metallicity, there would likely be a difference in the overall ionizing spectrum that population produces, for which we do not see evidence. Another possibility is that gas flows lead to a larger nitrogen abundance at fixed O/H. If a large amount of unenriched gas is accreted and mixed into the star-forming re-

gions before intermediate-mass stars enrich the ISM with nitrogen, O/H will decrease. The intermediate-mass stars will then release an amount of nitrogen that is larger than what is expected at that O/H because the gas is now less enriched than the stars. This scenario, or another mechanism involving gas inflows and outflows, is perhaps more likely in high-redshift galaxies which are known to have large gas fractions and concentrated star formation that could correspond to active accretion of metal-poor gas (Tacconi et al., 2013). We found evidence consistent with an accumulation of unenriched gas in $z \sim 2.3$ galaxies through the mass-metallicity relation in Sanders et al. (2015). Observations of the rest-frame UV could determine if exotic stellar populations are present, while more observations of the cold gas content of high-redshift galaxies with, e.g., ALMA could help uncover the role of gas flows.

The presence of AGN within the $z \sim 2.3$ sample could significantly bias conclusions drawn from excitation diagrams. We did not use a locally-determined demarcation to separate star-forming galaxies from AGN in the [N II] BPT diagram (e.g., Kewley et al., 2001; Kauffmann et al., 2003b) because such a selection would introduce a bias against objects with high N/O at fixed [O III]/Hβ. While some of the galaxies in the $z \sim 2.3$ sample fall in the local AGN region of the [N II] BPT diagram, we do not see any $z \sim 2.3$ galaxies present where the AGN sequence would fall in the other four panels of Figure 3.13. Therefore, we are confident that our $z \sim 2.3$ sample is free of AGN.

3.5.5 Diffuse ionized gas and the interpretation of global galaxy spectra

The observed positions of local and $z \sim 2.3$ galaxies in the [N II] and [S II] BPT diagrams are key pieces of evidence in our arguments regarding the hardness of the ionizing spectrum of local and high-redshift star-forming regions (see Section 3.5.1 and Figure 3.11). One source of uncertainty in the interpretation of these plots is the inclusion of light from the diffuse ionized component of the ISM in integrated-light galaxy spectra. Emission from diffuse ionized gas can be significant, with roughly half of the total Hα emission of local spiral galaxies coming from a diffuse component (Zurita et al., 2000). If the diffuse ionized component has line ratios that are not equivalent to those of HII regions, which is probable because diffuse gas

and HII regions are characterized by different ionizing sources and ionization states, then light from the diffuse component can act as a contaminant when investigating properties of star-forming regions. This issue is especially concerning for low ionization states such as [N II] and [S II] which are easily ionized and can have elevated flux compared to that of Hα when shock-excited (Martin, 1997; Hong et al., 2013). Characterizing the impact of diffuse emission requires knowledge of both the fraction of emission and the emission line ratios coming from the diffuse ionized component, at both low and high redshift.

In the local universe, comparison of integrated galaxy spectra with those of individual HII regions can give insight into the effect of emission from other components of the ISM. Local HII regions have been found to follow a similar sequence to that of local star-forming galaxies in the [N II] BPT diagram, but appear to have systematically lower [S II]/Hα at fixed [O III]/Hβ in the [S II] BPT diagram (Veilleux & Osterbrock, 1987; Pilyugin et al., 2012b; Berg et al., 2015; Croxall et al., 2015). Every emission line in an integrated galaxy spectrum contains a luminosity-weighted contribution from each HII and diffuse emission region falling in the slit or fiber, complicating the comparison of HII region and integrated galaxy spectra. Ongoing spatially-resolved spectroscopic surveys, such as the SDSS-IV/MaNGA IFU (Law et al., 2015) and SAMI (Bryant et al., 2015) galaxy surveys, will provide a dataset capable of unraveling the relative contributions of HII regions and diffuse ionized gas to global galaxy spectra.

The situation is much more uncertain at high redshifts because the structure of the ISM in $z \sim 2$ galaxies is poorly constrained. The ISM is almost certainly different in $z \sim 2$ galaxies, considering the high gas fractions (Tacconi et al., 2013) and compact sizes (van der Wel et al., 2014), combined with high rates of star formation (Shivaei et al., 2015), significant feedback driving outflows (Shapley et al., 2003; Steidel et al., 2010), and high level of turbulence observed in $z \sim 2$ disk galaxies (Förster Schreiber et al., 2009). If high-redshift galaxies are dominated by giant kpc-scale HII regions ionized by super-star clusters that fill a large fraction of the galaxy volume, the filling factor of the diffuse ionized component may be small along with the fraction of line emission originating there. In this case, it may be more appropriate to compare the integrated emission-line spectra of high-redshift galaxies

to those of luminous local HII regions rather than global galaxy spectra. We are only starting to gain rudimentary knowledge of the spatially-resolved structure of the ionized ISM at $z \sim 2$ (Förster Schreiber et al., 2011; Genzel et al., 2011; Jones et al., 2013; Newman et al., 2014). Adaptive optics observations of increased sensitivity and spatial resolution will be required to map the spatially-resolved structure of the ionized component of the ISM at high redshift, including the strength of the [N II] and [S II] emission lines.

3.6 Summary

We have investigated the physical conditions of star-forming regions at $z \sim 2.3$, specifically the electron density and ionization parameter, and made comparisons to local star-forming galaxies in order to understand how these properties evolve with redshift. We performed this investigation using rest-frame optical spectra of $z \sim 2.3$ galaxies from the ongoing MOSDEF survey. We summarize our main conclusions below and discuss future observations that could shed additional light on the ionization state of high-redshift galaxies.

1. We explored the evolution of the electron density in star-forming regions using the [O II]$\lambda\lambda$3726,3729 and [S II]$\lambda\lambda$6716,6731 doublets. We found that $z \sim 2.3$ galaxies have median [O II]λ3729/λ3726 = 1.18 and median [S II]λ6716/λ6718 = 1.13, corresponding to electron densities of 225 cm^{-3} and 290 cm^{-3}, respectively. Local star-forming galaxies from SDSS have median [S II]λ6716/λ6718 = 1.41 which yields a density of 26 cm^{-3}. We found an evolution in electron density of an order of magnitude between $z \sim 0$ and $z \sim 2.3$.

2. We investigated the ionization state of $z \sim 2.3$ and local star-forming galaxies, using O_{32} as a proxy for the ionization parameter. We found that O_{32} decreases with increasing stellar mass in both the local and $z \sim 2.3$ samples. The slope of the $O_{32}-M_*$ anti-correlation is very similar for both samples, but the $z \sim 2.3$ sample is offset ~ 0.6 dex higher in O_{32} relative to the local sample at fixed M_*. This offset can be explained by the evolution of the mass-metallicity relation with redshift, such that high-redshift

galaxies have lower metallicities at fixed M_*, and the existence of an anti-correlation between ionization parameter and O/H.

3. We found that $z \sim 2.3$ galaxies show no systematic offset from local galaxies and follow the distribution of the low-metallicity tail of local galaxies in the O_{32} vs. R_{23} diagram. The high-redshift sample behaves similarly to the local sample in the O_{32} vs. O3N2 diagram, displaying a slight systematic offset from the local distribution. We propose that $z \sim 2.3$ galaxies follow the same anti-correlation between ionization parameter and O/H that is observed in the local universe.

4. Using simple photoionization models, we demonstrated that the translation between O_{32} and ionization parameter is only strongly dependent on the shape of the ionizing spectrum, and has little dependence on the assumed gas density and gas-phase metallicity. This translation will only evolve with redshift if the hardness of the ionizing spectrum at fixed metallicity evolves with redshift.

5. We utilized the position of $z \sim 2.3$ and local galaxies in the [N II] and [S II] BPT diagrams combined with simple photoionization models to show that the hardness of the ionizing spectrum does not significantly increase or decrease with redshift. Photoionization models predict that a hardening of the ionizing spectrum will increase [O III]/Hβ at fixed [N II]/Hα and [S II]/Hα. The $z \sim 2.3$ sample displays an offset from the local sequence in the [N II] BPT diagram but is not significantly offset in the [S II] BPT diagram. We conclude that there is not a significant increase in the hardness of the ionizing spectrum at fixed metallicity between $z \sim 0$ and $z \sim 2.3$.

6. Galaxies at $z \sim 2.3$ show no significant systematic offset from local galaxies in line ratio diagrams involving only lines of oxygen, sulfur, and hydrogen, while they show a systematic offset in line ratio diagrams involving nitrogen. These results suggest that metallicity indicators using line ratios excluding nitrogen (e.g. the combination of O_{32} and R_{23}) do not evolve up to $z \sim 2.3$, while indicators using nitrogen are biased due to an evolution in N/O at fixed O/H.

7. A consequence of conclusions 6 and 7 is that $z \sim 2.3$ have similar ionization parameters to $z \sim 0$ galaxies at fixed metallicity. Higher typical ionization parameters are inferred for $z \sim 2.3$ galaxies compared to those of local galaxies because $z \sim 2.3$ galaxies have lower typical metallicities. The ionization state appears to be set by the metallicity both locally and at $z \sim 2.3$.

8. We investigated the offset between $z \sim 2.3$ and local galaxies in the [N II] BPT diagram. We found that the $z \sim 2.3$ galaxies that display the largest offsets in the [N II] BPT diagram are not significantly offset from the local distribution or the remainder of the $z \sim 2.3$ sample in the O_{32} vs. R_{23} and [S II] BPT diagrams, but are systematically offset in the O_{32} vs. O3N2 and N2 diagrams. We conclude that higher N/O at fixed O/H drives the $z \sim 2.3$ offset in the [N II] BPT diagram. We previously provided evidence against significant evolution of the hardness of the ionizing spectrum or ionization parameter at fixed O/H. We used simple photoionization models to show that an evolution of a factor of 10 in the gas density cannot account for the full offset in the [N II] BPT diagram. We further conclude that an increase in the gas density plays a minor secondary role in driving the $z \sim 2.3$ offset in the [N II] BPT diagram.

There still remain many questions to be answered regarding the ionization state of local and $z \sim 2.3$ galaxies. Emission line contribution from the diffuse ionized component of the ISM is uncertain both locally and at high redshifts. Variety in photoionization modeling leads to variation in estimated ionization parameters. There are some observations that would allow us to test our proposed scenario that $z \sim 2.3$ galaxies have the same ionization parameter as $z \sim 0$ galaxies with the same metallicity. The most obvious of these is direct-method oxygen abundance measurements from auroral lines at $z \sim 2$. Direct-method abundances are insensitive to changes in the electron density, showing variations of $\lesssim 0.01$ dex from 25 cm^{-3} to 250 cm^{-3} (i.e., the observed evolution in density from $z \sim 0$ to $z \sim 2.3$), an advantage over some strong-line methods (see Jones et al., 2015). Currently, only a handful of direct-method abundance measurements have been attained at $z \gtrsim 1$, often utilizing gravitational lensing (Villar-Martín et al., 2004; Yuan & Kewley, 2009; Erb et al., 2010; Rigby

et al., 2011; Brammer et al., 2012b; Christensen et al., 2012; Maseda et al., 2014). Current sensitive near-infrared spectrographs on 10 m class telescopes and upcoming instruments on the Thirty Meter Telescope will allow for observations of auroral lines for more typical galaxies at $z > 1$. Additionally, observations of other ionization-parameter-sensitive emission line ratios could provide a test of this scenario, including [Ne III]λ3869/[O II]$\lambda\lambda$3726,3729 (Levesque & Richardson, 2014) and [S III]$\lambda\lambda$9069,9532/[S II]$\lambda\lambda$6716,6731 (Kewley & Dopita, 2002). Finally, improved stellar and photoionization models that can make self-consistent predictions of the physical properties of star-forming galaxies across the entire local star-forming sequence are needed to create more reliable ionization parameter calibrations. Such models would provide a local foundation for reliable photoionization models of the full suite of strong rest-frame optical emission lines out to $z \sim 2$.

CHAPTER 4

The MOSDEF Survey: Detection of [O III]λ4363 and the Direct-Method Oxygen Abundance of a Star-Forming Galaxy at $z = 3.08$

4.1 Introduction

The gas-phase metallicity of a galaxy is intimately connected to the processes governing galaxy formation and growth, namely the fueling and regulation of star formation. This connection is observed as the mass-metallicity relation (MZR), a correlation between stellar mass (M_*) and gas-phase oxygen abundance for local star-forming galaxies (e.g., Tremonti et al., 2004; Andrews & Martini, 2013). The MZR exists for high-redshift galaxies as well, and is observed to shift toward lower metallicity at fixed M_* out to $z \sim 3$ (e.g., Erb et al., 2006; Troncoso et al., 2014; Sanders et al., 2015; Onodera et al., 2016). Constraining the evolution of the shape and normalization of the MZR with redshift provides insight into how the interplay among star formation, gas accretion, and feedback changes over cosmic history. This approach requires robust estimates of the gas-phase metallicity at all epochs.

The ratio of the flux of the auroral [O III]λ4363 line to that of [O III]$\lambda\lambda$4959,5007 is sensitive to the electron temperature of the ionized gas. Based on estimates of the electron temperature and density, the oxygen abundance can be inferred from ratios of strong oxygen lines (e.g., [O III]$\lambda\lambda$4959,5007 and [O II]λ3727) to Balmer lines. Measurements of [O III]λ4363 have now been obtained for several hundred local H II regions and galaxies (e.g., Izotov et al., 2006; Marino et al., 2013). However, the direct electron-temperature based method cannot be applied to the majority of local galaxies with spectroscopic observations because [O III]λ4363

is typically ~ 100 times weaker than [O III]λ5007 at low metallicity, and much weaker still at solar and higher abundances. For this reason, calibrations to determine metallicity from strong optical emission-line ratios have been constructed based on observations of H II regions and galaxies with direct metallicity measurements (e.g., Pettini & Pagel, 2004; Pilyugin & Thuan, 2005).

Strong-line calibrations have been widely applied at both low and high redshifts, but it is uncertain whether these local calibrations can accurately predict the metallicities of high-redshift galaxies. There is evidence that the physical conditions of the interstellar medium (ISM) in high-redshift galaxies differ from those observed locally. In order to explain offsets between $z \sim 0$ and high-redshift galaxies in diagnostic plots such as the [O III]/Hβ vs. [N II]/Hα diagram, it has been proposed that high-redshift galaxies may have higher ionization parameters (Kewley et al., 2015; Cullen et al., 2016), harder ionizing stellar spectra (Steidel et al., 2014), higher density/ISM pressure (Kewley et al., 2013a; Sanders et al., 2016b), and/or anomalous nitrogen abundance at fixed O/H (Masters et al., 2014; Shapley et al., 2015; Sanders et al., 2016b) compared to $z \sim 0$ galaxies. Depending on which conditions evolve and the magnitude of that evolution, the relation between emission-line ratios and metallicity may change with redshift, potentially rendering current strong-line calibrations significantly biased at high redshifts.

Unbiased metallicity estimates for high-redshift galaxies based on the direct method are needed to evaluate the applicability of local metallicity calibrations at high redshift. However, due to the weakness of [O III]λ4363 and the difficulties of observing in the near-infrared, this line has only been detected in 7 galaxies at $z > 1$ (Yuan & Kewley, 2009; Brammer et al., 2012b; Christensen et al., 2012; Stark et al., 2013; James et al., 2014; Maseda et al., 2014), most of which are gravitationally lensed, and has not been detected at $z > 1.9$. The small, inhomogeneous sample of direct-method metallicities at $z > 1$ has made it difficult to assess the state of metallicity calibrations at high redshifts.

In this letter, we present observations of COSMOS-1908, an unlensed star-forming galaxy at $z = 3.08$ with a detection of [O III]λ4363, observed as part of the MOSFIRE Deep Evolution Field (MOSDEF) survey (Kriek et al., 2015). We investigate the physical conditions of

nebular gas in COSMOS-1908, considering multiple emission lines to evaluate the utility of locally-calibrated strong-line metallicity relations at $z \sim 3$. In Section 4.2, we present details about the observations and data reduction. We describe measurements of the spectral features in Section 4.3. In Section 4.4, we derive galaxy and ionized gas properies of COSMOS-1908. Finally, we discuss the implications of our results in Section 4.5. Throughout this dissertation, the term "metallicity" refers to the gas-phase oxygen abundance (12+log(O/H)). We adopt a Λ-CDM cosmology with $H_0 = 70$ km s^{-1} Mpc^{-1}, $\Omega_m = 0.3$, and $\Omega_\Lambda = 0.7$.

4.2 Observations and Reduction

We utilized data from the MOSDEF survey, described in detail in Kriek et al. (2015). The data were obtained on 23 December 2012 and 1 April 2013 using the MOSFIRE spectrograph (McLean et al., 2012) on the 10 m Keck I telescope. COSMOS-1908 was observed in H and K bands on a MOSFIRE mask with $0\farcs7$ wide slits, resulting in spectral resolutions of ~ 3650 and ~ 3600 in H and K, respectively. Individual exposures were 120 seconds in H and 180 seconds in K. The mask was observed for 72 minutes in H and 144 minutes in K using an ABBA dither pattern with a $1\farcs2$ nod in December, and 64 minutes in H using an ABA'B' dither pattern with $1\farcs5$ and $1\farcs2$ outer and inner nods in April. The total integration time was 136 minutes in H and 144 minutes in K.

The data were reduced using a custom IDL pipeline that produces a two-dimensional science and error spectrum for each slit on the mask that has been flatfielded, sky-subtracted, cleaned of cosmic rays, wavelength-calibrated, and flux-calibrated (Kriek et al., 2015). One-dimensional science and error spectra were optimally extracted from the two-dimensional spectra. Science spectra were corrected for slit losses on an individual basis using *Hubble Space Telescope* F160W images and the average seeing for each filter. Emission-line fluxes were measured by fitting Gaussian profiles to the one-dimensional science spectrum. Uncertainties on line fluxes and all derived and measured quantities were estimated using a Monte Carlo technique, where the 1σ uncertainty bounds were taken to be the 16th and 84th percentile of the cumulative distribution function for each value.

In addition to our MOSFIRE observations, we utilized extensive multiwavelength photometric data that are available in the COSMOS field. COSMOS-1908 has coverage in 44 broad-, medium-, and intermediate-band filters from optical to infrared (rest-UV to rest-NIR), assembled by the 3D-HST team (Skelton et al., 2014; Momcheva et al., 2016).

4.3 The detection of auroral [O III]λ4363

Deep observations with MOSFIRE allow us to identify several emission lines in the H- and K-band spectra of COSMOS-1908, presented in Figure 4.1. We measure a nebular redshift of $z = 3.0768$ using the best-fit centroid of [O III]λ5007, the line with the highest signal-to-noise ratio (S/N). In addition to the strong rest-optical lines [O III]$\lambda\lambda 4959, 5007$, H$\beta$, and [O II]$\lambda\lambda$3726,3729, there are many weak emission lines detected in the H band. These include [Ne III]λ3869, [Ne III]λ3968 blended with Hϵ, Hδ, Hγ, and [O III]λ4363. The observed emission-line fluxes and uncertainties are presented in Table 4.1. COSMOS-1908 displays a high level of excitation and ionization based on the strength of [Ne III] and the large [O III]λ5007 flux compared to that of Hβ and [O II].

The auroral [O III]λ4363 line is detected with a formal signifiance of 4.0σ. The redshift of COSMOS-1908 fortuitously places [O III]λ4363 in a wavelength region that is free of skylines. The centroid of [O III]λ4363 implies a redshift ($z = 3.0769$) that closely matches the one measured from stronger lines. Additionally, emission can be seen at the expected location of [O III]λ4363 in the two-dimensional spectrum (Fig. 4.1, right), and the S/N spectrum shows a coherent peak centered at the expected location of the line, where 7 consecutive pixels have S/N$>$ 1. We conclude that [O III]λ4363 is real and significantly detected, making COSMOS-1908 the highest-redshift galaxy for which [O III]λ4363 has been detected.

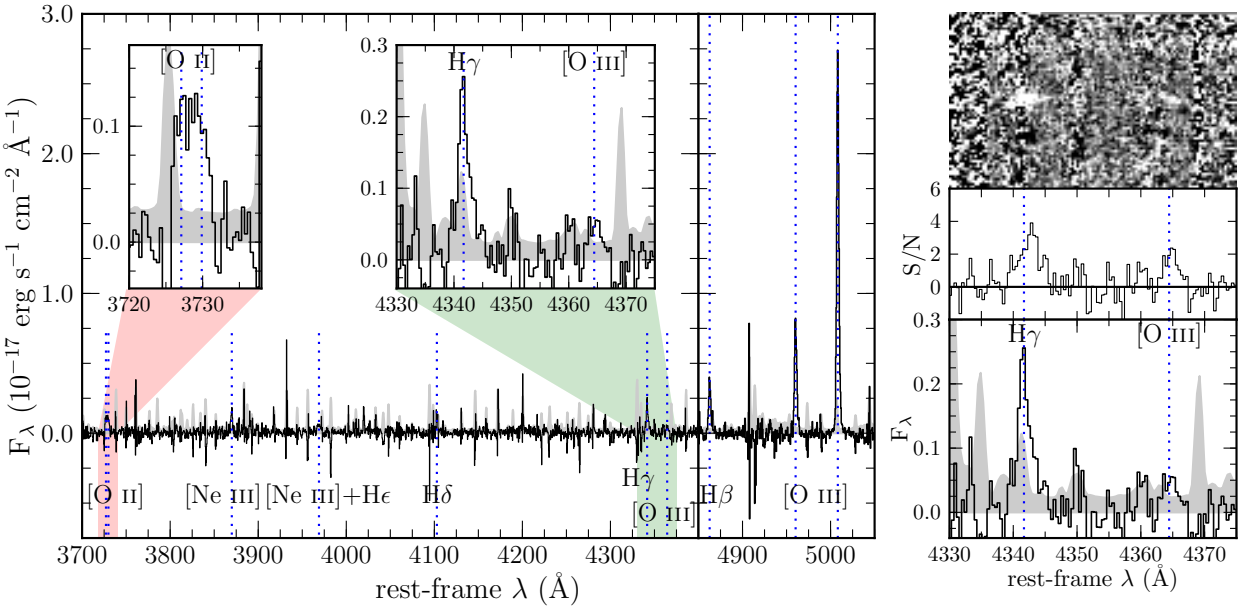

Figure 4.1: Spectrum of COSMOS-1908. Left: H- and K-band spectra of COSMOS-1908. The gray shaded region displays the magnitude of the error spectrum. Emission lines are labeled, and the spectral regions around [O II] and [O III]λ4363 are highlighted. Right: Zoom-in of the wavelength region around Hγ and [O III]λ4363, showing the one-dimensional spectrum (bottom), signal-to-noise ratio spectrum (middle), and two-dimensional spectrum (top).

Table 4.1: Properties of COSMOS-1908.

Observed emission-line fluxes		
Line	Flux (10^{-17} $\frac{\text{erg}}{\text{s cm}^2}$)	Uncertainty (10^{-17} $\frac{\text{erg}}{\text{s cm}^2}$)
[O II]λ3726	1.09	0.19
[O II]λ3729	1.09	0.18
[Ne III]λ3869	1.84	0.21
Hδ	1.49	0.32
Hγ	2.21	0.34
[O III]λ4363	0.56	0.14
Hβ	4.72	0.25
[O III]λ4959	10.8	0.28
[O III]λ5007	33.3	0.70

Galaxy properties	
Property	Value
Right Ascension (J2000)	10h 00m 23.36s
Declination (J2000)	02°11′55.″9
z	3.0768
$\log(M_*/\text{M}_\odot)$	$9.33^{+0.18}_{-0.17}$
$E(B-V)_{\text{gas}}$	$0.0^{+0.14}_{-0.0}$
SFR ($\text{M}_\odot$ yr^{-1})	49^{+30}_{-3}
sSFR (Gyr^{-1})	23^{+23}_{-6}
Area (kpc^2)	4.4
Σ_{SFR} ($\text{M}_\odot$ yr^{-1} $\text{kpc}^{-}2$)	11^{+7}_{-1}
n_e (cm^{-3})	520^{+600}_{-400}
T_e([O III]) (K)	14000^{+1950}_{-1400}
T_e([O II]) (K)	12800^{+1350}_{-1000}
$12+\log(\text{O}^+/\text{H}^+)$	$6.87^{+0.17}_{-0.14}$
$12+\log(\text{O}^{++}/\text{H}^+)$	$7.96^{+0.13}_{-0.14}$
$12+\log(\text{O/H})$	$8.00^{+0.13}_{-0.14}$

4.4 Properties of COSMOS-1908

4.4.1 The stellar content of COSMOS-1908

We estimate the stellar mass of COSMOS-1908 via spectral energy distribution (SED) fitting. The photometry is shown in Figure 4.2. There is a clear excess in the K-band photometry due to emission-line flux from [O III]+Hβ on top of the stellar continuum, as well as a probable excess in the H-band from weaker lines. For this reason, we exclude the H- and K-band photometric points when fitting the SED. The intermediate-band photometry at 5050 Å and 7670 Å were also excluded from the fit because of contributions from strong Lyα and C III]λ1909 emission, respectively. COSMOS-1908 additionally displays excess flux bluewards of the Balmer break in the J-band, which may be due to nebular continuum emission indicatave of a young stellar population (Reines et al., 2010). Since our models are not tuned to fit nebular continuum emission, we exclude the J-band photometry as well. The remaining photometry was fit using the SED-fitting code FAST (Kriek et al., 2009), with the Conroy et al. (2009) stellar population synthesis models, assuming a Chabrier (2003) initial mass function, a delayed-τ star-formation history (SFR $\propto te^{-t/\tau}$), and the Calzetti et al. (2000) attenuation curve. We assume a stellar metallicity of 0.16 $Z_\odot$, the closest metallicity in the library of models to the measured gas-phase metallicity for COSMOS-1908 (see Section 4.4.5). The photometry and best-fit SED model are shown in the left panel of Figure 4.2. The best-fit age of the stellar population is $t = 160^{+200}_{-110}$ Myr with an e-folding time of $\tau = 10$ Gyr, indicating a rising star-formation history. The extinction of the stellar continuum in the best-fit model is $E(B-V)_{\rm stars} = 0.12^{+0.03}_{-0.05}$. The stellar mass is found to be $\log(M_*/{\rm M}_\odot) = 9.33^{+0.18}_{-0.17}$. Fitting including H- and K-band photometry that have been corrected for emission-line contamination using measured line fluxes changes $E(B-V)_{\rm stars}$ by < 0.05, age by $\lesssim 100$ Myr, and stellar mass by < 0.2 dex.

The right panel of Figure 4.2 shows *HST* postage stamp images of COSMOS-1908 in the F160W (rest-optical) and F606W (rest-UV) filters. The galaxy displays a compact morphology that is slightly elongated towards the south. Using the F606W image, we measure a rest-UV area of 4.4 kpc^2 from the number of pixels that are 2σ or more above the background

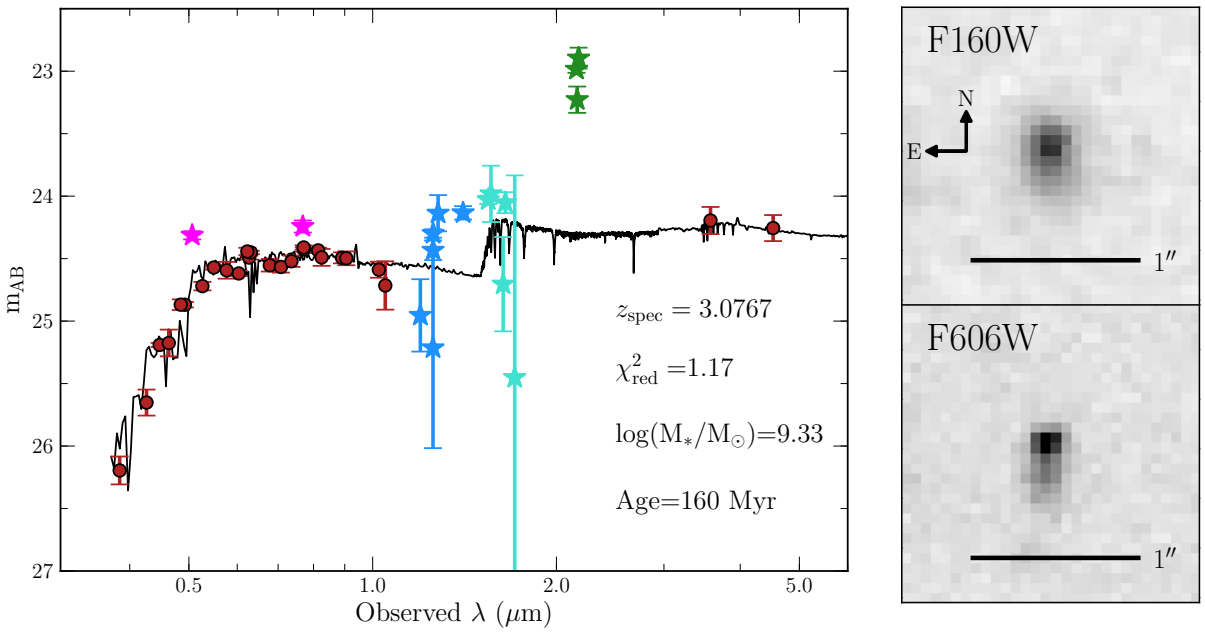

Figure 4.2: LEFT: Observed photometry and best-fit SED model for COSMOS-1908. The red circles indicate photometry used for SED fitting. Stars denote photometry excluded from the SED fitting process due to contamination. Bands removed are: IA505 and IA767 (magenta), J (blue), H (cyan) and K (green). The 3D-HST photometric catalog includes multiple overlapping filters in the J, H, and K bands. RIGHT: Postage stamp images of COSMOS-1908 in the F160W and F606W filters. Images are 1.″5 on a side, and the plate scale is 0.″06/pixel.

noise. It is unlikely that COSMOS-1908 is dominated by ionization from an active galactic nucleus (AGN) due to its low stellar mass and the lack of a strong brightness peak in the central region.

4.4.2 Nebular extinction and star-formation rate

The reddening of nebular emission lines can significantly affect the inferred star-formation rate (SFR), line ratios, and derived metallicities. The amount of nebular extinction can be estimated using ratios of hydrogen Balmer-series lines. Balmer-series line fluxes are first corrected for stellar absorption using the best-fit SED model. Due to the strength of the emission lines, this correction is small, only 0.7%, 2%, and 3.5% for Hβ, Hγ, and Hδ, respectively. Nebular reddening is estimated using Balmer-series line ratios, assuming intrinsic ratios of Hγ/Hβ = 0.468 and Hδ/Hβ = 0.259 (Osterbrock & Ferland, 2006) and the extinction curve of Cardelli et al. (1989). The observed Balmer ratios of COSMOS-1908 are consistent with no reddening; $E(B-V)_{\rm gas} = 0.0^{+0.14}_{-0.0}$, an upper limit that is consistent within the uncertainties with the stellar reddening. The SFR is estimated from Hβ using the relation of Kennicutt (1998) converted to a Chabrier (2003) IMF, assuming an intrinsic ratio of Hα/Hβ=2.847 (Osterbrock & Ferland, 2006). COSMOS-1908 is vigorously forming stars, with SFR= 49^{+30}_{-3} M$_\odot$ yr^{-1}, specific SFR (sSFR; SFR/M_*) of 23^{+23}_{-6} Gyr^{-1}, and SFR surface density ($\Sigma_{\rm SFR}$; SFR/Area) of 11^{+7}_{-1} M$_\odot$ yr^{-1} kpc^{-}2. The galaxy properties of COSMOS-1908 are presented in Table 4.1.

4.4.3 [O III]λ5007 equivalent width

We measure a large [O III]λ5007 rest-frame equivalent width of EW([O III])=1600 Å using the continuum level from the best-fit SED model. Objects with EW([O III]) > 1000 Å are extremely rare at $z \lesssim 2.3$ (Atek et al., 2011), but appear to be common at $z \sim 6-7$ (Smit et al., 2014). Observing an object with such a high EW in the small survey volume of the MOSDEF $z > 3$ observations suggests a significant increase in the occurrence rate of high-EW galaxies from $z \sim 2$ to $z \sim 3$. Analysis of objects like COSMOS-1908 can provide

insight into the nature of $z \sim 7$ star-forming galaxies with similar nebular EWs. COSMOS-1908 displays similar properties to the Lyman-continuum leaking galaxy Ion2 at $z = 3.2$ (de Barros et al., 2016), including EW([O III]) > 1000 Å and [O III]λ5007/[O II]λ3727 > 10, and may be a good candidate for Lyman-continuum detection.

4.4.4 Electron density

The electron density serves as a robust proxy for the hydrogen gas density in H II regions and can affect the strength of collisionally-excited lines. We calculate the electron density using the [O II]λ3729/λ3726 ratio (roughly unity) and the IRAF routine NEBULAR.TEMDEN (Shaw & Dufour, 1994) with updated O II atomic data following Sanders et al. (2016b). We assume an electron temperature of 12,800 K, the estimated T_e([O II]) for COSMOS-1908 (see Section 4.4.5). We find the electron density to be $n_e = 520^{+600}_{-400}$ cm^{-3}. This high electron density compared to those of local star-forming galaxies and H II regions is in agreement with the order-of-magnitude increase in electron density from $z \sim 0$ to $z \sim 2.3$ observed in Sanders et al. (2016b).

4.4.5 Electron temperature and oxygen abundance

We estimate the oxygen abundance following the prescription of Izotov et al. (2006). The relative population of oxygen in ionization states higher than O^{++} is assumed to be negligible, such that the total oxygen abundance is

$$\frac{O}{H} \approx \frac{O^+}{H^+} + \frac{O^{++}}{H^+}. \tag{4.1}$$

The analytic equations of Izotov et al. (2006) for O^+/H^+ and O^{++}/H^+ require knowledge of the electron density, electron temperatures in the O^+ and O^{++} zones, and dust-corrected emission-line fluxes for [O II], Hβ, and [O III].

We calculate T_e([O III]) using NEBULAR.TEMDEN with updated O III collision strengths from Storey et al. (2014) and transition probabilities from the NIST MCHF database (Fischer

& Tachiev, 2014). In the density regime $n_e \lesssim 1,000$ cm^{-3}, T_e is insensitive to changes in density, so we do not iteratively solve for n_e and T_e simultaneously. For COSMOS-1908, we find [O III]$\lambda\lambda$4959,5007/λ4363 = $80.0^{+23.1}_{-20.0}$, which corresponds to an electron temperature in the O^{++} zone of T_e([O III])=$14{,}000^{+1950}_{-1400}$ K. We do not have wavelength coverage of the auroral [O II]$\lambda\lambda$7320, 7330 lines to determine T_e([O II]) directly. Instead, we assume the linear T_e([O III])$-T_e$([O II]) relation of Campbell et al. (1986). We find an electron temperature in the O^+ zone of T_e([O II])=$12{,}800^{+1350}_{-1000}$ K. The total oxygen abundance of COSMOS-1908 is found to be 12+log(O/H)= $8.00^{+0.13}_{-0.14}$ (0.2 $Z_\odot$; Asplund et al., 2009). The oxygen abundance, ionic abundances, electron temperatures, and density are listed in Table 4.1.

4.5 Discussion

We investigate the evolution in the relationship between emission-line ratios and metallicity by comparing COSMOS-1908 to galaxies at lower redshifts with abundance determinations based on [O III]λ4363. Recently, Jones et al. (2015) found that relations between direct-method oxygen abundance and ratios of neon, oxygen, and hydrogen emission lines do not evolve from $z = 0 - 1$, using a sample of 32 star-forming galaxies at $z \sim 0.8$ from the DEEP2 Galaxy Redshift Survey (Newman et al., 2013). We perform a similar comparison using galaxies at higher redshifts. The low-redshift comparison sample includes the $z \sim 0.8$ galaxies from Jones et al. (2015) and 126 star-forming galaxies at $z \sim 0$ from Izotov et al. (2006) that have spectral coverage of [O II]. We additionally compare to three galaxies at $z \sim 1.5$ (Christensen et al., 2012; James et al., 2014; Stark et al., 2013, Mainali et al., in prep.). All galaxies in the comparison samples have detections of [O III]λ4363, and reddening corrections and oxygen abundances recalculated with the methods described in Section 4.4. Uncertainties on emission-line ratios are calculated using a Monte Carlo technique, and include uncertainties in measurement and reddening correction.

The emission-line ratios and oxygen abundances are shown in Figure 4.3. The line ratios displayed in each panel are sensitive to O/H, with the exception of [Ne III]/[O III], which should remain approximately constant with metallicity because it is a ratio of similar ion-

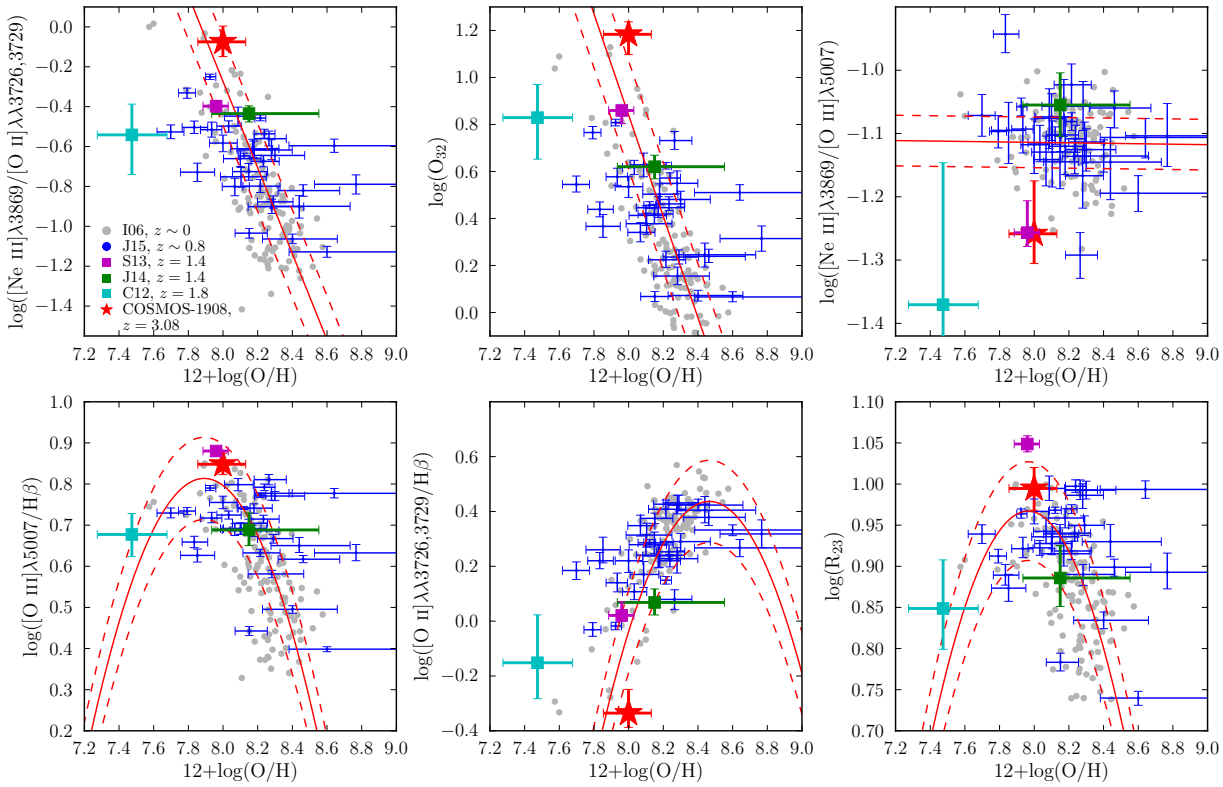

Figure 4.3: Emission-line ratios vs. direct-method oxygen abundance for COSMOS-1908 and lower-redshift comparison samples. In each panel, the red star indicates COSMOS-1908. Gray points show the $z \sim 0$ sample from Izotov et al. (2006, I06), while blue errorbars show the positions of $z \sim 0.8$ galaxies from Jones et al. (2015, J15). The red solid and dashed lines display the best-fit relations to the $z \sim 0$ sample and 1σ scatter (Jones et al., 2015), offset +0.045 dex in 12+log(O/H) to account for the different T_e([O III])$-T_e$([O II]) relation and O III atomic data used in this study. The magenta, green, and cyan squares show the $z = 1.4$ galaxy from Stark et al. (2013, S13; Mainali et al., in prep.), the $z \sim 1.4$ galaxy from James et al. (2014, J14), and the $z \sim 1.8$ galaxy from Christensen et al. (2012, C12), respectively.

ization states of α-capture elements. In all 5 panels with metallicity-sensitive line ratios, COSMOS-1908 is consistent with the local best-fit relations within the uncertainties and instrinsic scatter. There are few galaxies in the low-redshift comparison samples that have the levels of low-metallicity and high-excitation that COSMOS-1908 displays, so this result relies on a small level of extrapolation of the $z \sim 0$ relations. Of the four galaxies at $z > 1$, COSMOS-1908 lies slightly towards the high-excitation side of the local relations, the Stark et al. (2013) and James et al. (2014) galaxies fall very nearly on each local relation, and the Christensen et al. (2012) galaxy lies towards the low-excitation side. Collectively, galaxies at $z > 1$ do not show a systematic offset towards higher excitation at fixed metallicity, and the relation between these line ratios and O/H does not strongly evolve.

The close proximity of COSMOS-1908 to the local relations implies that evolution of the ionization parameter or ionizing spectrum at fixed O/H is small, if present. It has been suggested that high-redshift galaxies may have higher ionization parameters than local galaxies because of a scaling up of the radiation field due to more concentrated star formation (Kewley et al., 2015; Cullen et al., 2016; Kashino et al., 2017). This scenario predicts that COSMOS-1908 should have a much higher ionization parameter than local galaxies at similar O/H due to its extreme sSFR and $\Sigma_{\rm SFR}$, which would be observed as large offsets in [O III]/[O II], [O III]/Hβ, and [Ne III]/[O II] at fixed O/H. The models presented in Cullen et al. (2016) predict that [O III]/Hβ at fixed metallicity will be > 0.1 dex larger at $z = 3.1$ due to an increase in ionization parameter at fixed O/H. Such offsets are not observed in Figure 4.3.

Our results instead suggest a scenario in which high-redshift and $z \sim 0$ galaxies have similar ionization parameters at fixed metallicity, while high-redshift galaxies have higher ionization parameters than local galaxies at fixed M_* due to the evolution of the MZR. This scenario is consistent with our earlier findings in Sanders et al. (2016b) using a sample of $\sim$ 100 star-forming galaxies at $z \sim 2.3$ from the MOSDEF survey. The properties of COSMOS-1908 and the $z \sim 1.5$ and $z \sim 0.8$ comparison samples suggest that the same relationship between metallicity and ionization parameter holds out to $z \sim 3$. Since changes in electron density minimally affect line ratios at subsolar metallicities (Sanders et al., 2016b),

the agreement of the high- and low-redshift samples in Figure 4.3 implies that strong-line metallicity calibrations using only lines of oxygen, neon, and hydrogen can reliably predict abundances from $z \sim 0$ to $z \sim 3$.

Currently, these results are based upon a handful of galaxies at $z \sim 1 - 3.5$, which is not sufficient to statistically constrain the behavior of the entire galaxy population at high redshifts. More detections of [O III]λ4363 for high-redshift galaxies are required to gain a complete understanding of the behavior of metallicity indicators at $z > 1$. One way forward is selecting objects similar to COSMOS-1908 from photometric surveys by identifying objects with large excess flux in the photometric band covering [O III]$\lambda\lambda$4959,5007, suggestive of a large [O III] equivalent width and low metallicity. Such objects are good candidates for [O III]λ4363 detection in deep spectroscopic observations. Detections of weak features such as [O III]λ4363 for large samples at high redshift will be enabled by the next-generation near-infrared facilities such as the *James Webb Space Telescope* and Thirty Meter Telescope.

CHAPTER 5

Biases in Metallicity Measurements from Global Galaxy Spectra: The Effects of Flux-Weighting and Diffuse Ionized Gas Contamination

5.1 Introduction

The formation and growth of galaxies over cosmic history are governed by the relationship between gas accretion, star formation, and feedback. Understanding this process, known as the "cycle of baryons," is of critical importance to gaining a full picture of galaxy growth, but directly observing gas in inflow and outflow stages is observationally challenging. In lieu of direct observations, the cycle of baryons can be probed indirectly by measuring the chemical abundances of galaxies. In particular, the scaling of gas-phase oxygen abundance, which we refer to in this work as "metallicity," with global galaxy properties such as stellar mass (M_*) and star-formation rate (SFR) can give insight into the interplay between inflows, outflows, and star formation.

A monotonic increase in metallicity with increasing stellar mass has been observed for local star-forming galaxies, and is known as the "mass-metallicity relation" (MZR; e.g., Tremonti et al., 2004; Kewley & Ellison, 2008; Andrews & Martini, 2013). The $z \sim 0$ MZR has been found to have a secondary dependence on SFR, with the relationship among M_*, SFR, and metallicity known as the "fundamental metallicity relation" (FMR; e.g., Mannucci et al., 2010; Lara-López et al., 2010; Andrews & Martini, 2013; Salim et al., 2014, but see Sánchez et al. 2013; Barrera-Ballesteros et al. 2017 for conflicting results using spatially-resolved data). Chemical evolution models make predictions for the shape and normalization

of these metallicity scaling relations under different sets of assumptions about the nature of galactic winds and the balance between inflow, outflow, and SFR (e.g., Finlator & Davé, 2008; Peeples & Shankar, 2011; Zahid et al., 2014a; Davé et al., 2017). An accurate comparison between chemical evolution models and the observed MZR and FMR can elucidate the nature of feedback and cosmological accretion. However, such a comparison depends critically on robust measurements of metallicity for observed star-forming galaxy samples, and additionally requires the measurement of a metallicity that is compatible with metallicities extracted from cosmological hydrodynamical simulations. It is thus of paramount importance to eliminate observational biases in galaxy metallicity estimates.

The gas-phase oxygen abundances of galaxies in the local universe are typically estimated using one of two methods. In the so-called "direct method," the temperature-sensitive ratio of the intensities of an auroral emission feature (e.g., [O III]λ4363, [O II]$\lambda\lambda$7320,7330, [N II]λ5755) to strong emission lines from the same ionic species (e.g., [O III]$\lambda\lambda$4959,5007, [O II]$\lambda\lambda$3726,3729, [N II]$\lambda\lambda$6548,6584) is used to measure the electron temperature of the ionized gas (Osterbrock & Ferland, 2006). The cooling efficiency of ionized gas increases as the metal abundance increases. Thus, the gas-phase metallicity can be determined from the equilibrium electron temperature, assuming a heating and cooling balance (Izotov et al., 2006; Pilyugin et al., 2012a). This method is the most accurate method of metallicity determination that can be applied to reasonably large samples (N $>$ 100) of low-redshift galaxies. The utility of the direct-method has been demonstrated by the observation that direct-method metallicities tightly correlate with metallicities obtained from oxygen recombination lines that more directly measure the oxygen abundance, where the relation has a slope of unity but an offset of $\sim$ 0.2 dex from a one-to-one relation (Blanc et al., 2015). Metal recombination lines are $\sim 10^4$ times weaker than strong lines and thus are not a practical metallicity indicator for any large sample. While the accuracy of the direct method is desirable, its use is limited because auroral lines are typically $\sim 50-100$ times weaker than strong optical emission lines at low-metallicities (12+log(O/H)$\lesssim$ 8.2) and become weaker exponentially as metallicity increases, making it extremely difficult to detect these lines in individual metal-rich galaxies. For these reasons, samples of local galaxies with auroral line

detections have sizes of only a few hundred and do not extend to 12+log(O/H)$\gtrsim$ 8.4 (Izotov et al., 2006; Pilyugin et al., 2010).

When auroral lines are not detected, galaxy oxygen abundances may be estimated from methods using only strong optical emission lines. The "strong-line method" utilizes empirical or theoretical calibrations between strong optical emission line ratios and oxygen abundance. Empirical calibrations are based on samples of individual H II regions with direct-method metallicities (e.g., Pettini & Pagel, 2004). Theoretical calibrations instead make use of the predictions of photoionization models to determine the relations between line ratios and oxygen abundance (e.g., Kewley & Dopita, 2002; Kobulnicky & Kewley, 2004; Tremonti et al., 2004; Dopita et al., 2016). Because the strong-line method does not depend on the detection of any intrinsically weak emission lines, it can be applied to much larger samples of galaxies than the direct method. Strong-line metallicities have been estimated for sample sizes of $> 10^4$ galaxies (e.g., Tremonti et al., 2004) thanks to large spectroscopic surveys such as the Sloan Digital Sky Survey (SDSS; York et al., 2000).

Both the strong-line and direct methods share an inherent flaw when used to determine galaxy metallicities: they assume that the object of interest is a single H II region. Empirical strong-line calibrations utilize H II regions as the calibrating dataset, and will therefore not produce a reliable metallicity if the target does not follow the same relations between line ratios and oxygen abundance as H II regions. Theoretical strong-line calibrations are produced from photoionization models of single H II regions (or in many cases a single slab of illuminated gas) and thus also assume that the target behaves similarly to an individual star-forming region. When modeling galaxy emission spectra, it is common practice to illimunate the gas with the spectrum of a stellar population synthesis model (e.g., Starburst99; Leitherer et al., 2014) instead of a single stellar population (as in classical H II regions). However, this treatment fails to account for the variety of physical conditions of gas throughout the galaxy and the correlation of stellar properties with those variations. The direct method suffers from a similar problem, in that it assumes that the auroral and strong emission lines are produced in a single homogeneous H II region ionized by a single star cluster.

Galaxies are not single H II regions, but are instead complex objects with a multiphase

gaseous interstellar medium (ISM) and intricate substructure. The warm ($\sim 10^4$ K) ionized phase includes H II regions with a range of properties, as well as diffuse ionized gas (DIG) not contained in H II regions. H II regions are the line-emitting component associated with recent star formation, in which gas in close proximity to young, massive stars is ionized and emits both recombination and collisionally-excited lines.

While the light from H II regions is of primary interest in determining gas-phase metallicity, other important sources of line emission exist in the ISM. DIG contributes significantly to optical line emission in local galaxies. Studies based on narrowband Hα imaging suggest that DIG emission contributes $30 - 60\%$ of the total Hα flux in local spiral galaxies (Zurita et al., 2000; Oey et al., 2007). Additionally, DIG has different physical conditions and ionizing spectra from those of H II regions, and therefore likely follows different line ratio excitation sequences (Zhang et al., 2017). Hard ionizing radiation from accreting black holes incident on the ISM also produces line emission in galaxies harboring an active galactic nucleus (AGN), but in this study we ignore this source of line emission and focus only on galaxies dominated by star formation. Because of the diversity of ISM sub-components, applying the aforementioned methods to estimate galaxy metallicities while treating the galaxy as a single H II region will inevitably result in some level of bias.

The observed global galaxy spectrum is a flux-weighted combination of light on a line-by-line basis from each of these line-emitting components falling in the spectroscopic slit or fiber. For typical spectroscopic apertures (i.e., SDSS fibers), this mixture includes multiple H II and DIG regions with a spread in physical properties. A proper interpretation of the observed galaxy emission line spectrum cannot be obtained unless the mixture of these components is accounted for.

Robust galaxy gas-phase oxygen abundances are absolutely required when comparing observed metallicity scaling relations such as the MZR and FMR with simulations of galaxy chemical evolution. In this work, we reevaluate the reliability of oxygen abundances estimated from the emission lines of global galaxy spectra. For this analysis, we create simple models based on empirical auroral and strong emission line relations. These models include flux-weighting effects from the combination of emitting regions with a spread in physical

properties, incorporating up-to-date line ratio and electron temperature relations for H II regions. An important novel component of our models is the inclusion of emission from DIG regions based upon recent empirical results on DIG line ratios from the ongoing SDSS-IV MaNGA IFU survey (Zhang et al., 2017). In Section 5.2, we motivate and describe the models and empirical relations upon which they are based. We present results from the models and compare to both composites and individual local galaxies from SDSS in Section 5.3. We characterize the biases in line ratios, electron temperature, and oxygen abundance measurements from global galaxy spectra in Section 5.4, and discuss the effects on metallicity measurements for local galaxies. In Section 5.5, we apply corrections to the local mass-metallicity and fundamental metallicity relations and discuss DIG contamination in the context of other recent $z \sim 0$ galaxy line-ratio studies. In Section 5.6, we discuss the implications for metallicity measurements from both the direct and strong-line methods for high-redshift galaxies. Finally, we summarize and make concluding remarks in Section 5.7. Those readers who wish to skip over the details of the model framework may refer to Section 5.4 for the presentation of the biases in properties derived from global galaxy spectra, and subsequent sections for applications of the results.

Throughout this chapter, we adopt shorthand abbreviations to refer to emission line ratios and present them here for the convenience of the reader. We normalize strong emission line fluxes to the Hβ flux, following the practice of H II region studies. We use the following abbreviations for strong-line ratios throughout this chapter:

$$\mathrm{O3} = \log([\mathrm{O\ III}]\lambda\lambda 4959, 5007/\mathrm{H}\beta), \tag{5.1}$$

$$\mathrm{O2} = \log([\mathrm{O\ II}]\lambda\lambda 3726, 3729/\mathrm{H}\beta), \tag{5.2}$$

$$\mathrm{N2} = \log([\mathrm{N\ II}]\lambda\lambda 6548, 6584/\mathrm{H}\beta), \tag{5.3}$$

$$\mathrm{S2} = \log([\mathrm{S\ II}]\lambda\lambda 6716, 6731/\mathrm{H}\beta), \tag{5.4}$$

$$\mathrm{O3N2} = \mathrm{O3} - \mathrm{N2}. \tag{5.5}$$

These strong-line ratios are always reddening-corrected unless otherwise noted. The strong-line ratios that utilize a single doublet component and/or the Balmer line with the closest proximity in wavelength to the forbidden line, more common in galaxy studies, can be found from these ratios: $\log([\text{O III}]\lambda5007/\text{H}\beta) = \text{O3} - 0.125$; $\log([\text{N II}]\lambda6584/\text{H}\alpha) = \text{N2} - 0.581$; $\log([\text{S II}]\lambda\lambda6716{,}6731/\text{H}\alpha) = \text{S2} - 0.456$; and $\log[([\text{O III}]\lambda5007/\text{H}\beta)/([\text{N II}]\lambda6584/\text{H}\alpha)] = \text{O3N2} + 0.456$. We also adopt abbreviations for the strong-to-auroral line ratios from which electron temperatures are estimated:

$$\text{Q3} = [\text{O III}]\lambda\lambda4959, 5007/\lambda4363, \tag{5.6}$$

$$\text{Q2} = [\text{O II}]\lambda\lambda3726, 3729/\lambda\lambda7320, 7330, \tag{5.7}$$

$$\text{Q2N} = [\text{N II}]\lambda\lambda6548, 6584/\lambda5755. \tag{5.8}$$

Whenever it occurs, the term "metallicity" is used synonymously with gas-phase oxygen abundance (O/H) unless otherwise mentioned. We assume a ΛCDM cosmology with $H_0 = 70$ km s^{-1} Mpc^{-1}, $\Omega_m = 0.3$, and $\Omega_\Lambda = 0.7$.

5.2 Modeling galaxies as ensembles of line-emitting regions

There is clear evidence that global galaxy spectra cannot be described by H II region photoionization models or H II region empirical datasets alone. Local star-forming galaxies follow distinct excitation sequences from those of H II regions in the [O III]$\lambda5007/\text{H}\beta$ vs. [S II]$\lambda\lambda6716{,}6731/\text{H}\alpha$, [O III]$\lambda5007/\text{H}\beta$ vs. [O II]$\lambda\lambda3726{,}3729/\text{H}\beta$, and [O III]$\lambda5007/\text{H}\beta$ vs. [O I]$\lambda6300/\text{H}\alpha$ diagrams (Croxall et al., 2015). Such differences, alongside other pieces of evidence from past studies presented below, motivate a modeling approach that treats galaxies as collections of multiple emitting regions spanning a range of excitation levels and oxygen abundances.

In this section, we discuss past work modeling global galaxy spectra as ensembles of emitting regions, describe the H II region and DIG datasets, present the line ratio relations

and other inputs to the models, and outline the method by which the mock galaxy spectra are created. We evaluate the performance of these models in Section 5.3 by comparing to observations of galaxies from SDSS.

5.2.1 Previous investigations of global galaxy biases

Kobulnicky et al. (1999) investigated the question of whether chemical abundances could be reliably estimated from global galaxy spectra. Using a sample of six dwarf galaxies with both individual H II region and global galaxy spectra, the authors found that the global spectra systematically overestimated electron temperatures by $\sim 1,000 - 3,000$ K while underestimating direct-method 12+log(O/H) by $\sim 0.05 - 0.2$ dex compared to the mean properties of the individual H II regions. These offsets were attributed to flux-weighting effects when combining light from multiple H II regions with different levels of excitation. Kobulnicky et al. also investigated the same question for local spiral galaxies by comparing measurements from individual H II regions to mock global spectra constructed using a weighted sum of the H II region spectra in radial bins. This analysis suggested that strong-line methods reproduced the mean metallicity of the individual H II regions without significant systematic effects despite the range of abundances in the individal H II region distributions. However, their spiral galaxy models did not incorporate dust reddening and, critically, contributions from DIG emission, which were poorly constrained at the time. Additionally, their sample of spiral and dwarf galaxies with direct-method measurements was very small (N=6) and only contained metal-poor (12+log(O/H)$\leq$ 8.15), low-mass objects. An analysis utilizing a more representative sample spanning a wide dynamic range in mass and metallicity is needed to test metallicity estimates from modern spectroscopic surveys.

Pilyugin et al. (2010) found that SDSS galaxies with auroral temperature measurements do not follow the H II region relationship between electron temperature as measured from O^+ (T_2) and O^{++} (T_3), known as the T_2−T_3 relation, but instead have lower T_2 at fixed T_3. A similar galaxy ionic temperature offset of $\sim 1,000 - 1,500$ K lower T_2 at fixed T_3 compared to the H II region T_2−T_3 relation has been observed when T_2 and T_3 are inferred from

composite spectra constructed from local SDSS star-forming galaxies (Andrews & Martini, 2013; Curti et al., 2017). Such composite spectra leverage the large-number statistics of SDSS to measure auroral-line ratios over an unprecedentedly wide range of galaxy properies. Pilyugin et al. (2010) were able to roughly reproduce this offset by combining the spectra of 2-3 H II regions falling on the T_2-T_3 relation but spanning a wide range of temperatures, suggesting that such an offset could be the result of combining light from multiple line-emitting regions with different physical properties. However, the models of Pilyugin et al. (2010) did not include any DIG component and thus were not representative of typical $z \sim 0$ star-forming galaxies. Pilyugin et al. (2012b) expanded on these results by simulating composite nebular spectra using a set of high-quality, self-consistent H II region observations as input components. These authors combined emission on a line-by-line basis from multiple H II regions with abundances within a certain range of a central metallicity value, and found that the combination of multiple H II regions can explain observed auroral-line properties of SDSS galaxies. Furthermore, the bias in inferred nebular abundances relative to the central metallicity value increases with increasing width of the metallicity range. We note that Pilyugin et al. (2012b) did not include any DIG emission regions in their composite spectra models. Collectively, these results imply that galaxy auroral and strong-line ratios do not behave in the same manner as those of individual H II regions. We build upon these previous studies of global galaxy spectra by creating models that treat galaxies ensembles of line-emitting regions with varying physical conditions, and crucially include a prescription for DIG emission.

5.2.2 An empirical approach to modeling galaxy spectra

In order to characterize the biases in measurements of electron temperature, oxygen abundance, and strong-line ratios from global galaxy spectra, we constructed a set of models that are based on observed line-ratio relations of H II and DIG regions. We treat a galaxy as a collection of H II and DIG regions with a distribution of physical properties, and create mock global galaxy spectra by summing the line fluxes from each individual component. These models are simple in nature, and minimize the number of free parameters that can be

tuned to match observations of real galaxies. In the description that follows, we will attempt to make it clear when we were forced to make assumptions due to a lack of constraining observations.

We chose to base our models on empirical relations rather than photoionization models for two reasons. First, photoionization models have a large number of free parameters that can be fine-tuned to match a set of observations, often allowing for multiple degenerate solutions. The interpretation of emission lines through photoionization models depends on the various required assumptions such as the shape of the relation between N/O and O/H, the method of accounting for the depletion of gas-phase elements onto dust grains, and the properties of the ionizing stellar population. In contrast, we prioritize simplicity over flexibility, minimizing the number of free parameters.

Second, DIG emission cannot be properly represented in photoionization models because the relative contributions of various ionization sources for DIG are still not agreed upon. The DIG ionization mechanism appears to be photoionization from some combination of leaking Lyman-continuum from O and B stars in H II regions (Voges & Walterbos, 2006; Haffner et al., 2009; Reynolds et al., 2012) and evolved intermediate-mass post-AGB stars (Flores-Fajardo et al., 2011; Zhang et al., 2017). Although O and B stars appear to provide most of the DIG ionization energy, there is an ongoing discussion about the importance of evolved stars. It has been suggested that additional nonionizing heating sources such as shocks are required to explain DIG observations (Reynolds et al., 1999; Seon et al., 2011). Some emission attributed to DIG may also originate from dust-scattering of emission line photons produced in H II regions (Barnes et al., 2015; Ascasibar et al., 2016). These effects are difficult to include in photoionization models, and introduce significant uncertainties.

By utilizing observed line ratio relations for both DIG and H II regions, we minimize the number of free parameters and only sample regions of parameter space where real objects are found. Thus, the main uncertainty concerning the applicability of these models stems from how representative the input datasets are of the full range of such emitting regions.

5.2.3 Abundances and line emission of H II regions

We obtain line ratio relations for H II regions from the sample of Pilyugin & Grebel (2016), which includes 965 observations of H II regions with auroral line measurements and direct-method abundances. We supplement this sample with recent observations of extragalactic H II regions from Croxall et al. (2016) and Toribio San Cipriano et al. (2016), bringing the total sample size to 1052. While all of the H II regions in this sample have measurements of at least one auroral line, some of these auroral-line measurements have low S/N or are otherwise unreliable. In order to construct a representative sample of H II regions with a range of metallicities and ionization parameters, we select a reference sample of high-quality, self-consistent observations from this parent sample using the counterpart method following Pilyugin et al. (2012a).

The counterpart method is a technique for estimating metallicity that is based on the assumption that a set of H II regions with the same physical properties such as density, electron temperature, and chemical abundance will have identical strong-line ratios. A high-quality reference sample of H II regions with reliable auroral measurements can be selected by requiring the auroral-line ratios of an H II region to closely match those of H II regions with similar strong-line ratios, automatically excluding low-S/N measurements and strong outliers. Here, we only use the counterpart method to cull the H II region parent sample of low-quality measurements. All electron temperatures and metallicities are determined using the direct method in our analysis. For the selection of the reference sample, we require the difference between the direct method and counterpart method oxygen and nitrogen abundances to be less than 0.1 dex, and we interpolate over a metallicity interval of 0.2 dex around the metallicity of the closest counterpart when determining the counterpart-method O/H and N/H. After iterating over the parent sample several times, the selection converges, yielding a reference sample of 475 objects that we refer to as the "reference H II region sample." Objects in this sample have detections of [O II]$\lambda\lambda$3726,3729, Hβ, [O III]λ5007, Hα, [N II]λ6584, [S II]$\lambda\lambda$6716,6731, and at least one of the auroral lines [O III]λ4363 and [N II]λ5755. All line fluxes have been corrected for dust reddening.

Electron temperatures are calculated using a five-level atom approximation and up-to-date atomic data (Sanders et al., 2016b). For the transition probabilities, we use values from the NIST MCHF database (Fischer & Tachiev, 2014) for all ions. We obtain the collision strengths from Stott et al. (2014) for O III, Hudson & Bell (2005) for N II, and Tayal (2007) for O II. The O II ion is only relevant for the models and galaxy comparison samples since auroral [O II]$\lambda\lambda$7320,7330 is not tabulated for the reference H II region sample. The vast majority of the H II region sample has electron densities of $n_e < 200$ cm^{-3} and thus falls in the low density regime where electron temperature calculations are insensitive to the density. We assume an electron density of $n_e = 100$ cm^{-3} for all temperature calculations. Because the five-level atom code is not optimized for speed and we need to calculate electron temperatures many times for each mock galaxy spectrum, we fit analytic formulae to the strong-to-auroral line ratio as a function of temperature obtained from the five-level atom code. Electron temperatures are calculated for a range of line ratios and we fit a function of the form $R = ae^{b/T_e}$, where R is the strong-to-auroral line ratio and T_e is the electron temperature for each ionic species. We obtain the following best-fit equations, which are accurate to $< 1.5\%$ between 5,000 K and 30,000 K:

$$\mathrm{Q3} = 7.892\exp(3.278 \times 10^4 \text{ K}/T_3), \tag{5.9}$$

$$\mathrm{Q2} = 7.519\exp(1.928 \times 10^4 \text{ K}/T_2). \tag{5.10}$$

$$\mathrm{Q2N} = 7.789\exp(2.493 \times 10^4 \text{ K}/T_2), \tag{5.11}$$

To infer the electron temperature from an observed line ratio, we invert these expressions.

For objects that have measurements of both [O III]λ4363 and [N II]λ5755, T_3 and T_2 are calculated using equations 5.9 and 5.11. For objects with a measurement of only one of these auroral lines, we calculate the corresponding ionic temperature and infer the temperature of the other ionic zone assuming the T_2-T_3 relation of Campbell et al. (1986):

$$T_2 = 0.7T_3 + 3,000 \text{ K}. \tag{5.12}$$

We note that calculating the oxygen abundance requires T_2([O II]), while T_2([N II]) is measured for the reference H II region sample because [O II]$\lambda\lambda$7320,7330 fluxes were not tabulated. We make the assumption commonly adopted that O II and N II predominantly trace the same ionic zone in the nebula such that T_2([O II])=T_2([N II]) as expected from photoionization models. We note for completeness that recent observations of H II regions with measurements of both ionic temperatures have shown that this relation has a large dispersion and called the one-to-one correspondence into question (Berg et al., 2015; Croxall et al., 2015, 2016).

Ionic oxygen abundances are calculated using the formulae from Izotov et al. (2006) in the low-density limit:

$$12 + \log(O^+/H^+) = O2 + 5.961 + \frac{1.676}{T_2} - 0.040\log(T_2) - 0.034T_2, \tag{5.13}$$

$$12 + \log(O^{++}/H^+) = O3 + 6.200 + \frac{1.251}{T_3} - 0.55\log(T_3) - 0.014T_3. \tag{5.14}$$

Total oxygen abundance is calculated assuming the fraction of oxygen in higher ionic and neutral states is negligible (Izotov et al., 2006; Pilyugin et al., 2012a):

$$\frac{O}{H} \approx \frac{O^+}{H^+} + \frac{O^{++}}{H^+}. \tag{5.15}$$

In order to create a distribution of realistic H II regions with known metallicities in a mock galaxy, we first need to parameterize the strong line ratios of the observed H II region sample because calculating direct-method metallicities requires the strong-line ratios O2 and O3. Since we are interested in biases in abundance measurements, an obvious choice of parameter is the oxygen abundance. However, because the direct-method oxygen abundance calculation depends on the strong line ratios O3 and O2, parameterizing by O/H will introduce covariances that are not observed in real H II region samples. We instead parameterize the strong line ratios as a function of T_3, which has no dependence on the strong-line ratios and is a good proxy for the oxygen abundance since the relationship between T_3 and 12+log(O/H) is nearly linear over the range of metallicities of interest here,

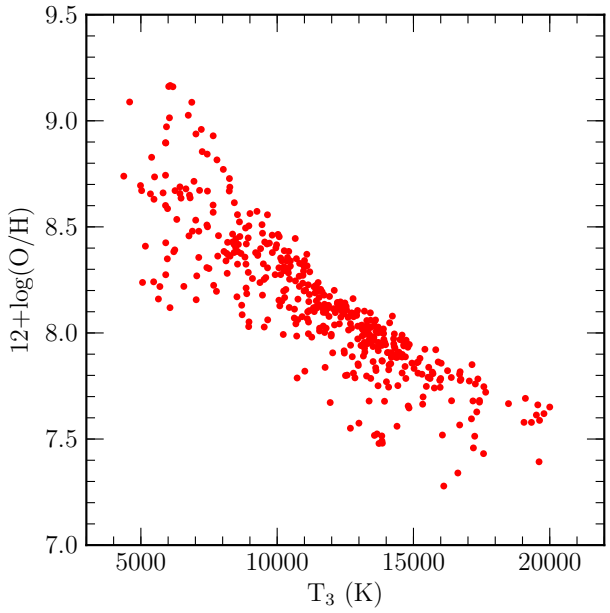

Figure 5.1: Direct-method 12+log(O/H) vs. T3 for the 475 individual H II regions in the reference H II region sample. Metallicities are calculated using up-to-date atomic data. 12+log(O/H) is nearly linearly dependent on T_3, which provides a good proxy for the direct-method metallicity.

as shown in Figure 5.1. Figure 5.2 presents the strong line ratios O3, O2, N2, and S2 as a function of T_3 for the reference H II region sample. For each line ratio, we find the median relation in bins of T_3 and fit polynomials to the median points to obtain functional forms of these relations:

$$\mathrm{O3} = -16.6\log(T_3)^3 + 189\log(T_3)^2 - 711\log(T_3) + 884, \tag{5.16}$$

$$\mathrm{O2} = -5.89\log(T_3)^2 + 46.8\log(T_3) - 92.8, \tag{5.17}$$

$$\mathrm{N2} = -5.48\log(T_3)^2 + 40.3\log(T_3) - 73.9, \tag{5.18}$$

$$\mathrm{S2} = -2.67\log(T_3)^2 + 20.5\log(T_3) - 38.3. \tag{5.19}$$

In Figure 5.2, the points in the right three panels are color coded by O3. It is apparent that at fixed T_3, each of these low-ionization line ratios is anticorrelated with O3. This anticorrelation encodes the range of ionization parameters at fixed T_3: higher ionization

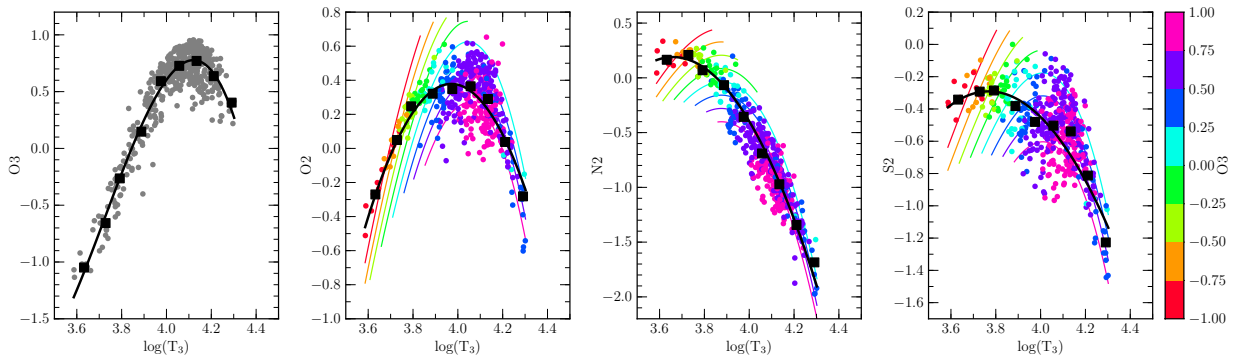

Figure 5.2: Strong-line ratios O3, O2, N2, and S2 as a function of T_3 for the reference H II region sample. In each panel, black squares display the median strong-line ratio in bins of T_3. The black lines show best-fit polynomials to the median points presented in equations 5.16-5.19. In the right three panels, the points are color-coded according to O3. The anticorrelation between O3 and O2, N2, and S2 at fixed T_3 reflects ionization parameter dependence in the strong-line ratio vs. T_3 relations. The solid colored lines display contours of constant O3 according to the analytic parameterization of ionization parameter presented in equations 5.20-5.22. Mock H II region distributions are drawn from the analytic functional fits presented here, including the secondary ionization parameter dependence.

parameter H II regions have higher O3 and lower low-ionization line ratios (N2, O2, and S2) at fixed T_3. We include variations in ionization parameter in our models by encoding ionization parameter changes using ΔX, the difference in line ratio X between the data point and the best-fit polynomial at fixed T_3. We subtract the best-fit polynomials from the data shown in the right three panels of Figure 5.2 and fit linear functions with y-intercept of zero to ΔO2, ΔN2, and ΔS2, all as a function of ΔO3. In this way, we obtain fits with the following values:

$$\Delta\mathrm{O2} = -0.47\Delta\mathrm{O3} \tag{5.20}$$

$$\Delta\mathrm{N2} = -0.42\Delta\mathrm{O3} \tag{5.21}$$

$$\Delta\mathrm{S2} = -0.56\Delta\mathrm{O3} \tag{5.22}$$

Thus, the residuals of the O3 fit, ΔO3, are used as input for the low-ionization line ratios. The standard deviation of the O3 residuals is 0.14 dex and is independent of T_3. Adding the ionization parameter (i.e., ΔO3) terms to the best-fit polynomials yields good fits to the data, with residuals having standard deviations of $\lesssim 0.15$ dex for O2, N2, and S2. We note

that the measurement uncertainty in T_3 is the main source of uncertainty in Figure 5.2, and accounts for some of the scatter about these fits. The solid lines in Figure 5.2 show contours of constant O3 based on the combination of the polynomial fits and ionization parameter terms presented above. These analytic functions represent the relationships between strong-line ratios and T_3 well for observed H II regions.

These formulae allow us to obtain realistic strong-line ratios for H II regions using input T_3 distributions. The strong-line emission from mock H II regions is combined with strong-line emission from DIG in order to produce global galaxy strong-line ratios that are a necessary component for the calculation of direct-method metallicity inferred from global galaxy spectra. We also investigate the impact of DIG emission and flux-weighted combination effects on diagnostic strong-line ratio diagrams and strong-line metallicity indicators. Additionally, we test whether our models simultaneously match the position of real galaxies in multiple strong-line ratio diagrams, a requirement for any realistic model of galaxy line emission.

5.2.4 Line emission from diffuse ionized gas

The models presented herein include emission from DIG, in addition to line emission from multiple H II regions with varying abundances, for the first time. It is of critical importance to account for DIG emission when studying emission-line spectra of local star-forming galaxies since $\sim 30 - 60\%$ of Hα emission in local spiral galaxies can be attributed to DIG (Zurita et al., 2000; Oey et al., 2007). Because of the diffuse nature of DIG, its line emission has a low surface brightness compared to that of H II regions and is thus difficult to observe. DIG was first identified with the discovery of a layer of warm ionized hydrogen permeating the Milky Way ISM (i.e., the Reynolds Layer; Reynolds et al., 1973). Initial observations of DIG line ratios in other galaxies have come from longslit spectroscopy of extra-planar emission around edge-on galaxies (e.g., Otte et al., 2001, 2002) or of low-surface-brightness emission in face-on galaxies probing only a small number of DIG regions (e.g., Hoopes & Walterbos, 2003). These observations showed that low-ionization line ratios (N2, S2) of DIG

are enhanced relative to those typical of H II regions, but sample sizes were too small to establish DIG line ratio trends over a range of physical conditions.

5.2.4.1 MaNGA observations of DIG line ratios

In order to estimate DIG contribution to line emission in local star-forming galaxy spectra with a wide range of stellar masses and metallicities, we need to characterize DIG line ratios over a wide range of excitation levels throughout star-forming disks and tie DIG line ratios in a galaxy to the H II region abundances in the same galaxy in some realistic way. To achieve this task, we characterize the DIG emission line ratios using data from the SDSS-IV Mapping Nearby Galaxies at APO (MaNGA; Bundy et al., 2015; Yan et al., 2016; Law et al., 2016) integral field spectroscopic (IFS) survey. The MaNGA IFS dataset provides spatially-resolved spectroscopic observations of a large number of local star-forming galaxies for which such an analysis of DIG emission is possible (Zhang et al., 2017).

Zhang et al. (2017) recently showed how optical strong emission-line ratios in local galaxies vary with Hα surface brightness ($\Sigma_{\mathrm{H}\alpha}$), with the strength of low ionization lines ([N II], [S II], [O II], and [O I]) relative to Balmer lines increasing with decreasing $\Sigma_{\mathrm{H}\alpha}$ at fixed radius. However, Zhang et al. also found that O3 did not increase or decrease with $\Sigma_{\mathrm{H}\alpha}$ on average. Under the assumption that high-$\Sigma_{\mathrm{H}\alpha}$ regions are dominated by H II region emission and DIG emission becomes increasingly important as $\Sigma_{\mathrm{H}\alpha}$ decreases, this result indicates that the O3 ratios of DIG and H II regions are the same on average within a single galaxy. Thus, we can match a sample of model H II regions with DIG emitting regions in a way that mimics the ISM of real galaxies by matching in O3. We note that Zhang et al. (2017) found some stellar mass dependence for ΔO3 vs. $\Delta\Sigma_{\mathrm{H}\alpha}$, such that DIG O3 is higher than that of H II regions in the most massive third of their sample. We do not include this stellar mass effect in our models because we have no direct way of assigning stellar mass to a mock galaxy, but this effect could be included in future models to increase the accuracy of the DIG representation.

In order to realistically match model distributions of DIG and H II regions, we characterize the DIG excitation sequences of [N II]/Hα, [S II]/Hα, [O II]/Hβ, and [O III]/Hβ as a function

of O3N2. We utilize the sample of galaxies from SDSS Data Release 13 (Albareti et al., 2017) presented in Zhang et al. (2017). From their sample of 365 blue, low-inclination galaxies, we selected a sample of 266 star-forming galaxies by requiring that the central region does not host an AGN according to the demarcation of Kauffmann et al. (2003b) in the [O III]/Hβ vs. [N II]/Hα diagram. In order to determine the line ratios of the central region of a galaxy, we construct a 3″ pseudo-fiber by summing the line fluxes of all spaxels within a 1.5″ radius of the galaxy center. This pseudo-fiber mimics the aperture of an SDSS fiber, matching the observations upon which the Kauffmann et al. (2003b) demarcation are based.

For each galaxy in the DIG galaxy sample, we select all spaxels that have a signal-to-noise ratio S/N$\geq$3 for [O II]$\lambda\lambda$3726,3729, Hβ, [O III]λ5007, Hα, [N II]λ6584, and [S II]$\lambda\lambda$6716,6731. We assume that the highest $\Sigma_{\mathrm{H}\alpha}$ spaxels are dominated by H II region emission, while the lowest $\Sigma_{\mathrm{H}\alpha}$ spaxels are dominated by DIG emission. We identify spaxels with $\Sigma_{\mathrm{H}\alpha}$ below the 10th percentile of the $\Sigma_{\mathrm{H}\alpha}$ distribution in each galaxy as DIG-dominated. The threshold of 10% was selected in order to provide the purest probe of DIG emission while still yielding a large sample of spaxels. Results do not change significantly when varying this threshold from 5% to 15%. The DIG-dominated spaxel sample can be thought of as the diffuse analog of the H II region sample. Before calculating [O II]/Hβ, the [O II] and Hβ fluxes are first corrected for reddening on a spaxel-by-spaxel basis assuming the attenuation law of Cardelli et al. (1989) and an intrinsic ratio of Hα/Hβ = 2.86. The line ratios [O III]/Hβ, [N II]/Hα, and [S II]/Hα are calculated without correcting for dust reddening given the close proximity in wavelength of the relevant emission lines.

We construct the DIG strong-line excitation sequences by taking the median line ratios of the DIG spaxel sample in bins of O3N2. We chose to bin in O3N2 rather than O3 because O3N2 monotonically increases with T_3 in a nearly linear fashion for the reference H II region sample, while O3 is double-valued as a function of T_3. We assume that O3 of DIG regions is also double-valued as a function of T_3, in which case the median relation in bins of O3 would not be a good representation of the actual excitation sequence in the regime where the temperature-dependence of O3 weakens. While there are no constraints on the electron temperatures of DIG, we work under the assumption that DIG electron temperature

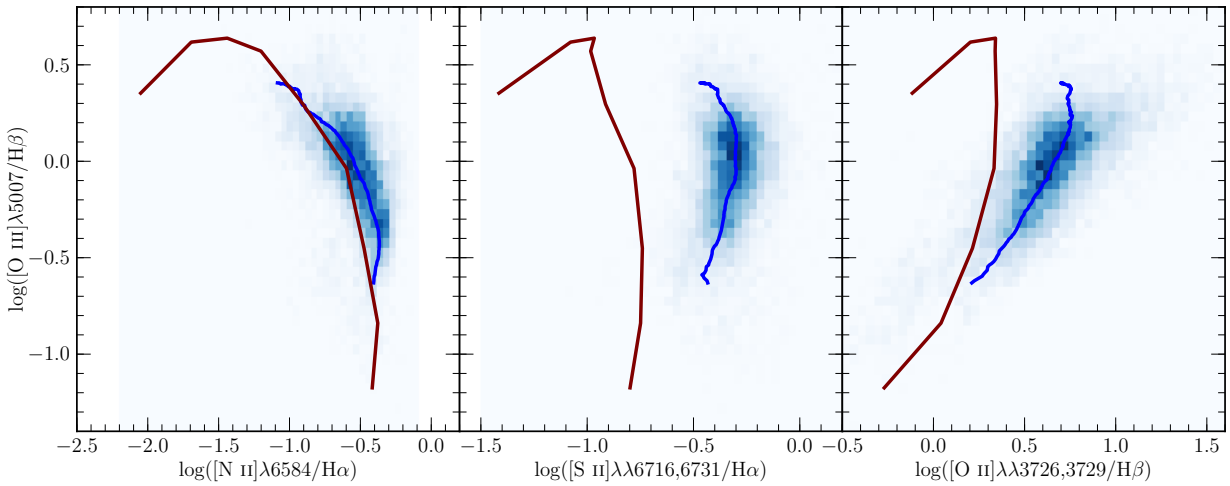

Figure 5.3: The O3N2 (left), O3S2 (middle), and O3O2 (right) strong-line ratio diagrams for DIG-dominated spaxels from MaNGA galaxies (Zhang et al., 2017). The blue two-dimensional histogram shows the distribution of strong-line ratios for the 10% lowest surface-brightness spaxels for each galaxy in the DIG galaxy sample. These spaxels are dominated by emission from DIG rather than H II regions. The running median of the DIG spaxel distribution in bins of O3N2 is displayed as a solid blue line. The maroon line shows the median strong-line excitation sequences of the reference H II region sample in bins of T_3.

decreases with increasing metallicity as for H II regions. Binning excitation sequences and matching H II and DIG regions in O3N2 instead of O3 alone is also motivated by the fact that the sequences of H II regions, $z \sim 0$ star-forming galaxies, and DIG regions are nearly identical in the [O III]/Hβ vs. [N II]/Hα diagram as shown below in Section 5.2.4.2, in agreement with the results of Zhang et al. (2017) that O3 and N2 are minimally affected by DIG compared to other strong-line ratios. The DIG line ratio distributions and median excitation sequences in the [O III]/Hβ vs. [N II]/Hα, [O III]/Hβ vs. [S II]/Hα, and [O III]/Hβ vs. [O II]/Hβ diagrams are presented in Figure 5.3, which we refer to as the O3N2, O3S2, and O3O2 diagrams, respectively. For comparison, the median line ratios of the reference H II region sample in bins of T_3 are shown. As implied by the results of Zhang et al. (2017), we find that at fixed O3, DIG regions display larger low-ionization line ratios than those of H II regions.

5.2.4.2 Extrapolations of DIG excitation sequences

We note that the reference H II region sample spans a wide range of excitation levels with $-1.0 \lesssim \mathrm{O3} \lesssim 1.0$, while the DIG spaxel sample only has sufficient statistics over a smaller range ($-0.6 \lesssim \mathrm{O3} \lesssim 0.4$). This limitation in the range of DIG excitation levels stems from the nature of the MaNGA sample used here, which mostly comprises moderate-metallicity galaxies leaving the low- and high-metallicity tails of the distribution poorly sampled. The dearth of low-O3 DIG measurements is also present due to the trend observed by Zhang et al. (2017) in which DIG O3 is higher than H II region O3 on average in massive ($\log(\mathrm{M}_*/\mathrm{M}_\odot) > 10.08$) star-forming galaxies. Once the survey is completed, the full MaNGA sample will contain ~ 10 times more galaxies than were available at the time of this study, which should allow for direct constraints of the metal-rich and metal-poor tails of the DIG excitation sequences. To allow our models to be applicable for galaxies over a wide range of metallicities, we extend the DIG excitation sequences by making assumptions about the behavior of DIG line ratios in the low- and high-metallicity tails based on the position of H II regions and $z \sim 0$ SDSS galaxies in strong-line excitation diagrams.

In order to compare the positions of galaxies and H II regions in line ratio diagrams, we select a comparison sample of $z \sim 0$ star-forming galaxies from SDSS Data Release 7 (DR7; Abazajian et al., 2009) for which strong-line measurements are available. We take global galaxy properties and emission-line measurements from the MPA-JHU SDSS DR7 catalogs.[3] We use the same selection criterion employed by Andrews & Martini (2013) , and later compare our models to their stacks of SDSS galaxies constructed from this sample of individual star-forming galaxies. We require SDSS galaxies to have $0.027 \leq z \leq 0.25$ and S/N≥ 5 for each of the lines Hβ, Hα, and [N II]λ6584. AGN are rejected by requiring $\log([\mathrm{N\ II}]\lambda6584/\mathrm{H}\alpha) < -0.4$ as well as a location below the star-forming/AGN demarcation of Kauffmann et al. (2003b) in the [O III]/Hβ vs. [N II]/Hα diagram when S/N≥ 3 for [O III]λ5007. This selection yields a sample of 209,513 local star-forming galaxies with a me-

[3]Available online at `http://www.mpa-garching.mpg.de/SDSS/DR7`

dian redshift of $z_{\rm med} = 0.08$, which we refer to as the "SDSS strong-line comparison sample."[4] Before calculation of the line ratios, the emission-line fluxes were corrected for reddening using the attenuation law of Cardelli et al. (1989), assuming an intrinsic Balmer decrement of Hα/Hβ = 2.86. In line-ratio diagrams involving [O II]$\lambda\lambda$3726,3729, [O III]λ5007, or [S II]$\lambda\lambda$6716,6731, only the subset of galaxies with S/N $\geq$ 3 in the relevant emission lines are plotted.

The excitation sequences of H II regions and $z \sim 0$ SDSS star-forming galaxies in the O3N2, O3S2, and O3O2 diagrams are presented in Figure 5.4. These plots demonstrate the necessity of including DIG emission in order to properly interpret SDSS star-forming galaxy line ratios. In the O3N2 diagram, H II regions and SDSS galaxies follow nearly identical sequences, suggesting that the DIG O3N2 sequence is similar to that of H II regions, as observed in the DIG line ratios from MaNGA data (Zhang et al., 2017). In the O3S2 and O3O2 diagrams, SDSS galaxies are offset towards significantly higher [S II]/Hα and [O II]/Hβ at fixed [O III]/Hβ compared to H II regions, suggesting that the galaxy spectra contain a significant DIG contribution based on the observed DIG line ratio relations in Figure 5.3. The interpretation that DIG is largely responsible for the offset between H II regions and SDSS galaxies in these diagrams is supported by the observation of Masters et al. (2016) that SDSS galaxies display a dependence on Hα surface-brightness ($\Sigma_{\rm H\alpha}$) perpendicular to these excitation sequences, such that those galaxies with the lowest $\Sigma_{\rm H\alpha}$ are offset farthest from the H II region sequences. Under the assumption that DIG accounts for a larger fraction of line emission in galaxies with lower $\Sigma_{\rm H\alpha}$ (Oey et al., 2007), the results of Masters et al. imply that DIG emission is most important in those galaxies farthest offset from the H II region sequences, while galaxies with large $\Sigma_{\rm H\alpha}$ and highly-concentrated star formation appear more similar to H II regions in these line ratio spaces.

In the O3S2 diagram, H II regions and SDSS galaxies show the largest offset at moderate

[4]Andrews & Martini additionally rejected galaxies for which the SDSS photometric flags indicated that the spectroscopic fiber targeted the outskirts of a large galaxy instead of a galaxy center, and removed low-mass targets for which the stellar mass was obviously incorrect through visual inspection. We do not apply these additional criteria since such issues affect less than 0.5% of the sample.

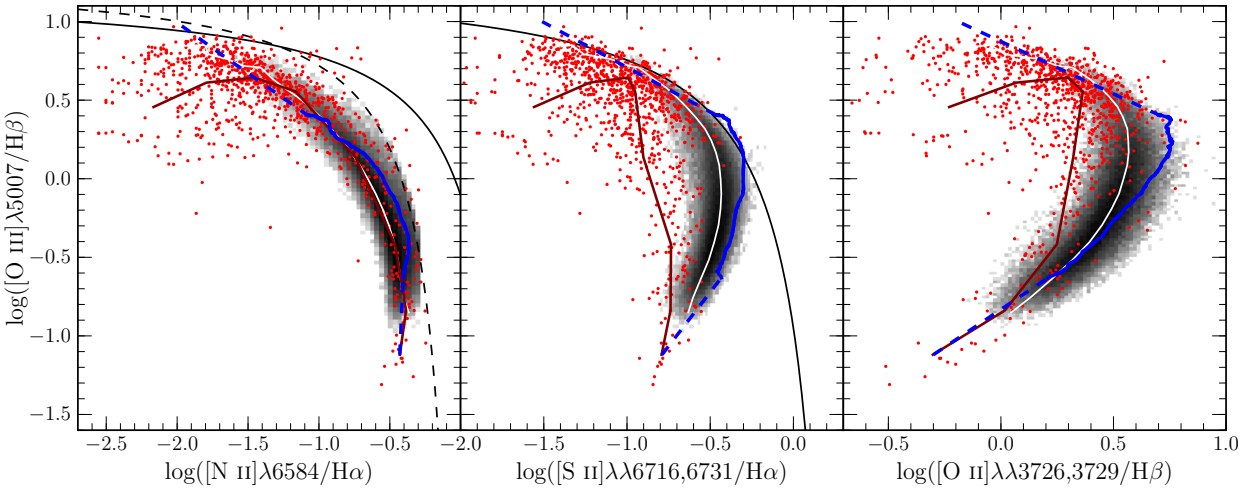

Figure 5.4: Excitation sequences of H II regions, SDSS star-forming galaxies, and DIG regions in the O3N2 (left), O3S2 (middle), and O3O2 (right) diagrams. The gray two-dimensional histogram shows the distribution of $z \sim 0$ star-forming galaxies from the strong-line comparison sample, where the white line represents the running median of the galaxies in bins of O3N2. Individual H II regions in the reference H II region sample are represented by red points, where the maroon line gives the running median of the H II regions. The solid blue line shows the running median of the DIG-dominated spaxels from the MaNGA DIG galaxy sample in bins of O3N2, while the dashed blue lines denote the linear extrapolations that we assume for the DIG excitation sequences. In the left and middle panels, the solid black line shows the "maximum-starburst" line of Kewley et al. (2001), while the empirical demarcation between AGN and star-forming galaxies of Kauffmann et al. (2003b) is displayed as the black dashed line in the left panel.

excitation ([O III]/H$\beta \sim 0$) where the DIG [S II]/Hα reaches a maximum. Above and below this point, the H II region and SDSS sequences appear to converge suggesting that the DIG line ratios become similar to H II region line ratios in the low- and high-excitation tails. A similar behavior is observed in the O3O2 diagram, where the H II regions and SDSS galaxies converge at the lowest and highest metallicities. We therefore adopt simple linear extrapolations of the DIG excitation sequences that approach the point of convergence of H II regions and SDSS galaxies at both high and low metallicities. This behavior is consistent with the turnover in DIG [N II]/Hα and [S II]/Hα at moderate [O III]/Hβ observed in the data. The adopted extrapolations are shown as blue dashed lines in Figure 5.4. It is possible that these linear extrapolations are not accurate representations of the DIG excitation sequences, however the relative locations of the H II region and SDSS sequences suggest these extrapolations provide a good approximation. The region of largest uncertainty is the extreme metal-poor regime in which the H II region sequences turn over in [O III]/Hβ while the DIG sequence extrapolations continue increasing in [O III]/Hβ. Zhang et al. (2017) demonstrated that [O III]/Hβ of DIG and H II regions is the same on average at fixed galactocentric radius for the least-massive third of their sample ($\log(M_*/M_\odot) < 9.43$), suggesting an agreement between DIG and H II region [O III]/Hβ in low-metallicity environments. However, the MaNGA survey only targeted galaxies with $\log(M_*/M_\odot) \gtrsim 9.0$ that do not have low enough stellar masses to populate the extreme low-metallicity tail. The nature of DIG line ratios in this regime therefore cannot be directly constrained. It is possible that the DIG sequences also turn over like the H II region sequences, but this uncertainty only affects a regime where a small fraction of SDSS galaxies lie, and will therefore minimally impact our results.

The low- and high-metallicity convergence of the SDSS and H II region sequences could also arise from a changing DIG contribution with metallicity, such that emission line contribution from DIG is largest at moderate metallicity and is small at low and high metallicities. In this case, the DIG line ratios need not converge with the galaxy and H II region line ratios in either extreme regime. However, individual SDSS galaxies do not show any evidence for a strong dependence of the fractional DIG contribution on O3 or M_* (see Section 5.3.1 below), disfavoring an explanation based on a dynamic level of DIG contribution.

5.2.5 Model framework

We create the individual line-emitting components of mock galaxies using the line-ratio relations of H II and DIG regions described above, and construct fake global galaxy spectra by combining light from the individual components in a manner that mimics the ISM structure of real galaxies. Below we describe the methodology used to create one mock galaxy spectrum, which is repeated many times using a range of input parameters to build up a statistical sample of mock galaxies.

First, we begin with a population of H II regions. As described in Section 5.2.3, the strong line ratios are parameterized by the electron temperature T_3, and thus the oxygen abundance is primarily a function of T_3 in the models. We produce a population of H II regions by randomly selecting N_{HII} samples from an input distribution of T_3. We adopt a log-normal shape for this T_3 distribution, in which the free parameters are the central temperature T_{cent} and the logarithmic width σ_T. A log-normal distribution is observationally motivated by the distributions of T_3 and T_2 of individual H II regions in local star-forming spirals. These distributions are shown in Figure 5.5 using data from three galaxies in the CHAOS survey (Berg et al., 2015; Croxall et al., 2015, 2016). The central temperature T_{cent} is representative of the characteristic metallicity of the galaxy star-forming regions, while the width of the distribution σ_T corresponds to the range of metallicities spanned by individual H II regions. The CHAOS galaxies are characterized by $\sigma_T = 0.03 - 0.08$ dex. We note that a log-normal distribution has symmetric wings in log(T), but the CHAOS galaxies display high-temperature wings, with no corresponding low-temperature wings. This absence is likely an observational bias because of the exponential decline in auroral line strength with decreasing temperature, supported by the fact that the lowest-temperature measurements in each CHAOS galaxy tend to fall only just above the S/N$\geq$ 3 cut on auroral line strength.

We obtain the strong-line ratios for the H II regions using the T_3 distribution as input to equations 5.16-5.19. We add an ionization parameter term to these median relations by assigning ΔO3 to each mock H II region by randomly drawing from a normal distribution with a mean of zero and a standard deviation of 0.14 dex, equal to the observed scatter about

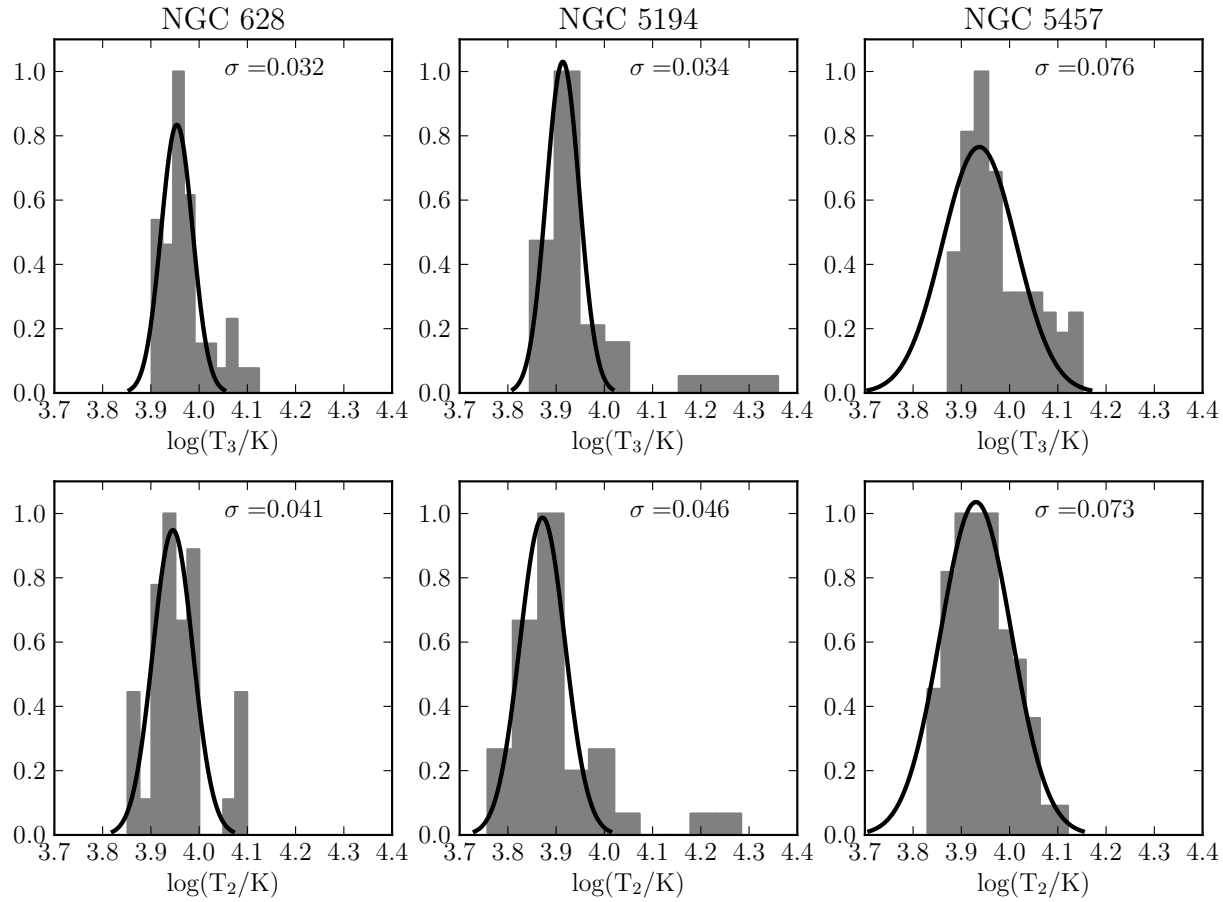

Figure 5.5: T_3 and T_2 distributions of individual H II regions within the local spiral galaxies NGC 628 (Berg et al., 2015), NGC 5194 (Croxall et al., 2015), and NGC 5457 (Croxall et al., 2016). Black lines show log-normal fits to the electron temperature distribution in each panel, where the best-fit width of the log-normal is given in the upper right corner.

the median in the O3 vs. T_3 diagram for the reference H II region sample. ΔO2, ΔN2, and ΔS2 are then calculated for each mock H II region using equations 5.20-5.22. The final strong-line ratios for each mock H II region are obtained by adding ΔO3, ΔO2, ΔN2, and ΔS2 to the O3, O2, N2, and S2 values obtained from the polynomial fits of equations 5.16-5.19. Each of these strong-line ratios has Hβ as the denominator, so we assume an H II region Hβ flux distribution in order to obtain the strong-line fluxes. For simplicity, we assign the same Hβ flux to each H II region. This assumption does not affect our results because Hβ flux does not show any dependence on either T_3 or 12+log(O/H) in the CHAOS H II regions on a galaxy-by-galaxy basis, suggesting that the brightness of an H II region does not depend on its abundance properties (Berg et al., 2015; Croxall et al., 2015, 2016). Thus, using a distribution of Hβ fluxes is simply a source of scatter but has no systematic effect on any of our results. The combination of strong-line ratios and Hβ fluxes yields the intrinsic fluxes of [O II]$\lambda\lambda$3726,3729, Hβ, [O III]$\lambda\lambda$4959,5007, [N II]$\lambda\lambda$6548,6584, and [S II]$\lambda\lambda$6716,6731 for each H II region. The Hα flux is obtained assuming an intrinsic ratio of Hα/Hβ = 2.86 We then combine the [O III]$\lambda\lambda$4959,5007 and [O II]$\lambda\lambda$3726,3729 fluxes with the T_3 values to produce the intrinsic fluxes of the auroral lines [O III]λ4363 and [O II]$\lambda\lambda$7320,7330 using equations 5.9 and 5.10.

The emission lines from each individual H II region are then reddened. The E(B-V) values of individual H II regions in the CHAOS sample do not correlate with T_3 or 12+log(O/H) on a galaxy-by-galaxy basis, suggesting that using a random E(B-V) assuming some distribution shape is appropriate. For each H II region, we draw an E(B-V) value from a normal distribution with a width of 0.15 magnitudes, with negative E(B-V) values set to zero. The E(B-V) distributions of the CHAOS H II regions suggest that this shape and width is appropriate for local star-forming spirals. While individual H II region E(B-V) shows no correlation with metallicity, E(B-V)^{gal} inferred from the global galaxy spectrum does correlate with global galaxy properties such as O3^{gal}, the O3 ratio inferred from global galaxy spectra, as shown in Figure 5.6 for the strong-line comparison sample. The anticorrelation between E(B-V)^{gal} and O3^{gal} suggests that the center of the E(B-V) distribution for the H II regions depends on the characteristic metallicity of the galaxy, reflecting the relationship between galaxy red-

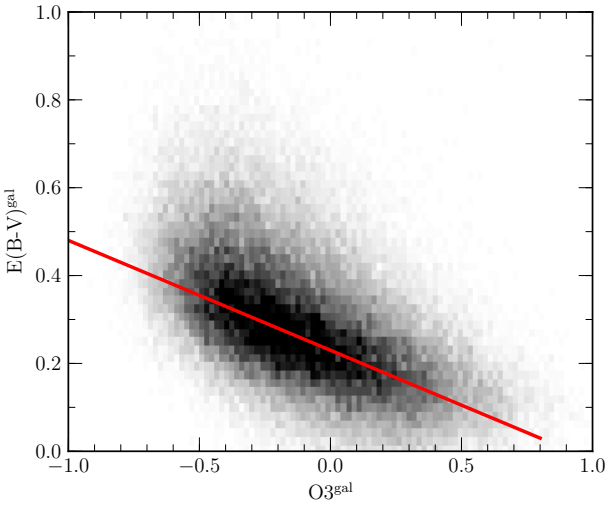

Figure 5.6: $E(B\text{-}V)^{gal}$ as a function of $O3^{gal}$ for the SDSS strong-line comparison sample. The amount of reddening increases with increasing metallicity and decreasing excitation, as represented by decreasing $O3^{gal}$. The red line shows the linear representation of this relationship, given by $E(B\text{-}V)^{gal} = -0.25 \times O3^{gal} + 0.23$.

dening and chemical enrichment (Heckman et al., 1998). We adopt a linear representation of the data in Figure 5.6, and use the median O3 of the simulated H II regions to set the center of the E(B-V) distribution using this linear relation. We note that the relationship shown in Figure 5.6 is derived from the global galaxy ratio $O3^{gal}$, which we later conclude is biased with respect to the median H II region ratio $O3^{HII}$. Iteratively including this bias in the E(B-V) relation changes the central E(B-V) values by < 0.04 magnitudes, which has no impact on our results. We redden the strong and auroral line fluxes from each modeled H II region individually using its assigned E(B-V), assuming the attenuation law of Cardelli et al. (1989).

We produce a number of DIG regions equal to the number of H II regions, and each DIG region is associated with an H II region. DIG emission is observed to be spatially correlated with H II regions (Zurita et al., 2000) and the diffuse gas immediately surrounding an H II region likely has a similar metallicity to that of the gas in that H II region. Each DIG region is assigned the same O3N2 value as its associated H II region. While the results of Zhang et al. (2017) suggest that DIG and H II region O3 is the same on average, O3 is double-valued as a function of electron temperature and metallicity and thus does not provide a

good parameterization of these properties, as described in Section 5.2.4 above. If we matched DIG and H II regions in O3, the double-valued nature of the line ratio would make it unclear how to match DIG and H II regions in the regime where O3 vs. T_3 is flat. We instead match in O3N2, which increases monotonically with increasing T_3 for H II regions. Matching in O3N2 instead of O3 alone should still provide a realistic way of associating DIG and H II regions based on the close agreement of the DIG and H II region sequences in the O3N2 diagram and on the result of Zhang et al. (2017) that the systematic difference between H II and DIG region N2 is small. Given O3N2, the strong-line ratios O3, N2, S2, and O2 of each DIG region are assigned using the DIG excitation sequences shown in Figure 5.4. We use the running median of the DIG sequences if $-0.6 < \log([\text{O III}]\lambda5007/\text{H}\beta) < 0.4$ and use the linear extrapolations of the DIG sequences otherwise.

The DIG fraction, $f_{\rm DIG}$, is defined as the fraction of the total intrinsic Balmer line flux of the galaxy that originates from DIG. The Hα and Hβ line fluxes of each DIG region are assigned such that the intrinsic DIG Balmer line fluxes account for the fraction $f_{\rm DIG}$ of the combined intrinsic Balmer line flux of the H II and DIG region. The same $f_{\rm DIG}$ is used for each H II -DIG region pair in a single mock galaxy. The [O III]$\lambda\lambda$4959,5007, [N II]$\lambda\lambda$6548,6584, [S II]$\lambda\lambda$6716,6731, and [O II]$\lambda\lambda$3726,3729 fluxes are then calculated using the strong-line ratios and Balmer line fluxes. In order to calculate the auroral line fluxes of the DIG regions, we need the DIG electron temperatures T_3 and T_2. However, there are no observational constraints on the electron temperature of DIG because of its low surface brightness and the intrinsic weakness of the auroral lines. We initially assume that the electron temperatures T_3 and T_2 of each DIG region are equal to the electron temperatures of the associated H II region, but we reevaluate this assumption in Section 5.3.1 below. With the assumed DIG T_3 and T_2, the intrinsic DIG auroral-line fluxes [O III]λ4363 and [O II]$\lambda\lambda$7320,7330 are calculated using equations 5.9 and 5.10. The line fluxes of each DIG region are then reddened assuming the same extinction as the associated H II region.

The global galaxy spectrum is produced by summing the reddened flux from each H II and DIG region on a line-by-line basis for [O II]$\lambda\lambda$3726,3729, [O III]λ4363, Hβ, [O III]$\lambda\lambda$4959,5007, [N II]λ5755, Hα, [N II]$\lambda\lambda$6548,6584, [S II]$\lambda\lambda$6716,6731, and [O II]$\lambda\lambda$7320,7330. We then

analyze the global galaxy spectrum as if it were real global galaxy spectroscopic data. The global line fluxes are corrected for reddening using the summed Hα and Hβ fluxes assuming an intrinsic ratio Hα/Hβ = 2.86 and the attenuation law of Cardelli et al. (1989). The strongline ratios are calculated using the dereddened global line fluxes.

The global electron temperatures are calculated from the global dereddened strong-to-auroral line ratios using equations 5.9 and 5.10, and global direct-method oxygen abundances are calculated using equations 5.13 and 5.14. We calculate global 12+log(O/H) under three assumptions: (1) both [O III]λ4363 and [O II]$\lambda\lambda$7320,7330 are detected, (2) only [O III]λ4363 is detected, and (3) only [O II]$\lambda\lambda$7320,7330 is detected. We refer to the three metallicities as 12+log(O/H)$_{\rm T2,T3}$, 12+log(O/H)$_{\rm T3}$, and 12+log(O/H)$_{\rm T2}$, respectively. In cases 2 and 3, the unknown electron temperature is estimated from the known electron temperature using equation 5.12. These three oxygen abundance values will be useful for comparing with different real datasets since it is not uncommon for only one of the auroral oxygen lines to be detected in galaxy spectra, even in stacks.

The process described above is repeated many times while varying $T_{\rm cent}$ in order to build up a statistical sample of mock galaxy spectra, allowing us to average over sources of scatter to find median trends. In order to quantify the bias between the distribution of H II region properties and the global properties as inferred from the galaxy spectrum, for each line ratio or physical property we save both the global value inferred from the galaxy spectrum and the median value of the distribution of individual H II regions for every mock galaxy. Properties derived from the global galaxy spectra will be indicated with the superscript "gal," while median properties of the H II region distribution will be denoted by the superscript "HII."

There are only four free parameters in these models. These free parameters are the number of H II regions per galaxy, $N_{\rm HII}$, the central temperature of the H II region T_3 distribution, $T_{\rm cent}$, the width of the H II region T_3 distribution, $\sigma_{\rm T}$, and the fraction of intrinsic Balmer flux originating from DIG emission, $f_{\rm DIG}$. In practice, $\sigma_{\rm T}$ and $f_{\rm DIG}$ are set to observationally-motivated values appropriate for the real dataset being modeled, while $T_{\rm cent}$ is freely varied to produce galaxies with a range of metallicities. The value of $N_{\rm HII}$ determines how well the T_3 distribution is sampled, and thus simply corresponds to a source

of scatter if N_{HII} is small, but does not change any trends.

5.3 Comparison datasets and fiducial models

We compare our models to observations of local star-forming galaxies in order to verify that the mock galaxy spectra produced following the methodology of Section 5.2.5 resemble spectra of real galaxies. Auroral emission lines are detected for a few hundred individual SDSS galaxies (Izotov et al., 2006; Pilyugin et al., 2010), and we assemble a sample of such galaxies for comparison in Section 5.3.2. However, samples of individual SDSS galaxies for which auroral lines are detected are not representative of typical star-forming galaxies from which the $z \sim 0$ MZR is constructed, generally having much higher SFR at fixed M_* than average and sampling only the low-mass, low-metallicity tail of the local population. Auroral line measurements across a wide dynamic range of galaxy properties have been obtained by stacking SDSS spectra (Andrews & Martini, 2013; Brown et al., 2016; Curti et al., 2017), providing a comparison sample that is more representative than samples of individual galaxies with auroral line detections. We therefore focus primarily on constructing models representing typical $z \sim 0$ star-forming galaxies. We compare these models to the SDSS stacks from Andrews & Martini (2013), Brown et al. (2016), and Curti et al. (2017) (hereafter AM13, B16, and C17, respectively), and quantify biases in metallicity measurements made from global galaxy spectra. The electron temperatures and oxygen abundances for all comparison samples are calculated using the same methods as for the mock galaxy spectra, outlined in Section 5.2.

5.3.1 SDSS stacks with auroral line detections

Auroral line measurements have been obtained across a wide range of stellar masses, SFRs, and excitation levels by stacking the spectra of $z \sim 0$ star-forming galaxies from SDSS. Creating composite spectra in bins of global galaxy properties allows for the detection of the weak auroral lines [O III]λ4363 and [O II]$\lambda\lambda$7320,7330 by leveraging the statistical power of hundreds or thousands of galaxies per bin to increase sensitivity. This method has progressed

metallicity studies of local galaxies by reducing the reliance on strong-line indicators. AM13 utilized measurements of composite spectra binned in M_* alone, as well as M_* and SFR, to investigate the MZR and FMR using direct-method metallicities. B16 constructed composite spectra for SDSS galaxies in bins of M_* and position above or below the mean $z \sim 0$ relation between $M_*$and specific star-formation rate (SSFR; SFR/M_*), demonstrating a systematic dependence of strong-line indicators on position relative to the M_*-SSFR relation. C17 binned galaxies in O3 and O2, and utilized auroral line measurements from stacked spectra to provide fully empirical strong-line metallicity calibrations based on global galaxy spectra rather than H II regions for the first time. Strong and auroral line ratio measurements of the stacked spectra from these studies provide a comparison sample that both spans a wide range of metallicities and is representative of the $z \sim 0$ star-forming population.

Our goal is to quantify the mean bias in metallicity measurements inferred from global galaxy spectra relative to the characteristic metallicity of the H II regions within a galaxy as a function of global galaxy properties. Thus, it is imperative that the samples that are used to test the performance of the models are themselves representative of the normal star-forming population of galaxies. While the stacked spectra from AM13, B16, and C17 are constructed from samples that largely overlap (AM13 and B16 use identical sample selection, while the selection criteria of C17 only slightly differ), we simultaneously compare to stacks from all three works in order to average over differences in selection, binning, and stacking methods. Because of the binning methods of each work, some bins will contain galaxies that are wholly unrepresentative of the typical local population (e.g., M_*-SFR bins that fall far from the mean $z \sim 0$ M_*-SFR relation). We only compare to those stacks from each work that closely follow the mean galaxy property relations of the local population. We use the stacks binned in M_* only from AM13. From B16, we use those stacks that fall within $\pm$0.5 dex in SSFR of the mean $z \sim 0$ M_*-SSFR relation. We select the C17 stacks for which the central O3 and O2 of the bin fall within $\pm$0.1 dex of the median relation of the strong-line comparison sample of individual SDSS galaxies. As described below, we choose observationally-motivated values of the DIG fraction $f_{\rm DIG}$, the number of H II regions per mock galaxy $N_{\rm HII}$, and the T_3 distribution width $\sigma_{\rm T}$ appropriate for the sample of galaxies

from which the stacked spectra were created.

We place constraints on $f_{\rm DIG}$ using the Hα surface brightness, $\Sigma_{\rm H\alpha}$, given by

$$\Sigma_{\rm H\alpha} = \frac{L^{\rm tot}_{\rm H\alpha}}{2\pi R^2_{\rm half,H\alpha}}, \tag{5.23}$$

where $L^{\rm tot}_{\rm H\alpha}$ is the total Hα luminosity, and $R_{\rm half,H\alpha}$ is the half-light radius of the galaxy Hα emission. Oey et al. (2007) demonstrated that $f_{\rm DIG}$ decreases with increasing $\Sigma_{\rm H\alpha}$. The authors argued that a scenario in which H II regions occupy a larger fraction of the ionized ISM volume as star formation becomes more concentrated predicts a dependence of $f_{\rm DIG} \sim \Sigma^{1/3}_{\rm H\alpha}$, which agreed well with the data. Using the dataset from Oey et al. (2007), we fit $f_{\rm DIG}$ as a function of $\Sigma_{\rm H\alpha}$ assuming this theoretically-predicted functional form, and obtain

$$f_{\rm DIG} = -1.50 \times 10^{-14} \times \Sigma^{1/3}_{\rm H\alpha} + 0.748, \tag{5.24}$$

where $\Sigma_{\rm H\alpha}$ is given in units of erg s^{-1} kpc^{-2}. The data and best-fit function are shown in Figure 5.7.

We constrain $f_{\rm DIG}$ for the SDSS stack samples using $\Sigma_{\rm H\alpha}$ of the individual SDSS galaxies in the strong-line comparison sample, which is nearly identical to the sample from which the AM13 and B16 stacks were constructed (see Section 5.2.4). We note that results do not change if the strong-line comparison sample is instead selected using the criteria of C17. To determine $\Sigma_{\rm H\alpha}$ for the strong-line comparison sample, we first aperture-correct the intrinsic fiber Hα luminosities. We obtain aperture corrections by dividing the total SFR by the fiber SFR, and apply these correction factors to the fiber Hα luminosities to obtain total Hα luminosities (Brinchmann et al., 2004). While measurements of the Hα half-light radii are not available, we instead use the optical sizes. R-band sizes of local star-forming galaxies have been shown to be similar to Hα sizes (James et al., 2009). We use the elliptical Petrosian R-band half-light radii from the NASA-Sloan Atlas v1.0.1[5]. Galaxy sizes are not available for all galaxies in the strong-line comparison sample. The NASA-Sloan Atlas contains size

[5] `http://www.nsatlas.org`

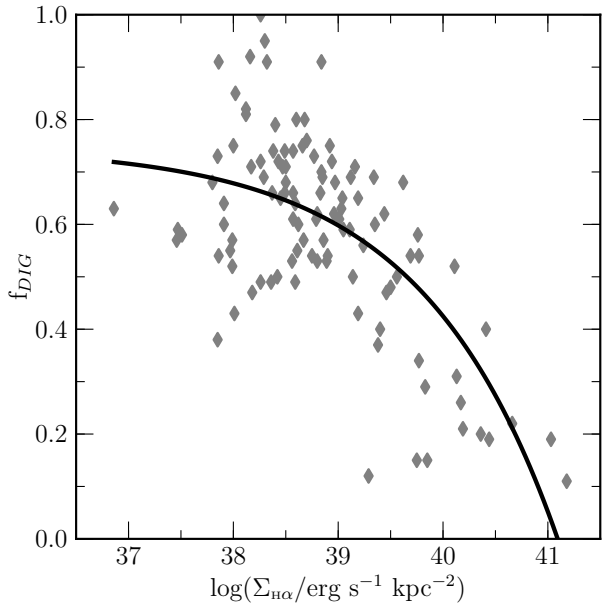

Figure 5.7: The fraction of Balmer emission originating from DIG, $f_{\rm DIG}$, vs. $\Sigma_{\rm H\alpha}$ for galaxies from the SINGG Hα survey (Oey et al., 2007), displayed as gray diamonds. The best-fit function of the form $f_{\rm DIG}\sim\ \Sigma_{\rm H\alpha}^{1/3}$, as suggested by Oey et al. on theoretical grounds, is displayed as a black line and presented in equation 5.24.

measurements for 79% of the full sample ($\sim 165,000$ galaxies) for which we compute the dust-corrected $\Sigma_{\rm H\alpha}$ according to equation 5.23. The DIG fraction for each galaxy is then estimated using equation 5.24.

The distribution of $f_{\rm DIG}$ values and $f_{\rm DIG}$ vs. $O3^{\rm gal}$ for the strong-line comparison sample are shown in Figure 5.8. The strong-line comparison sample has a median $f_{\rm DIG}$ of 0.55 with a standard deviation of 0.08. The distribution shape is nearly Gaussian, with a more significant tail towards low $f_{\rm DIG}$. The DIG fraction shows no significant dependence on excitation across a wide dynamic range, with the median $f_{\rm DIG}$ changing by $< 5\%$ as a function of $O3^{\rm gal}$. Additionally, the scatter in $f_{\rm DIG}$ also shows no strong dependence on $O3^{\rm gal}$. We therefore assign $f_{\rm DIG}$ to each mock galaxy by randomly drawing values from a normal distribution with a mean value of 0.55 and a standard deviation of 0.08. It is important to note that $f_{\rm DIG}$ is not dependent on any line ratios, and is thus independent of all of the line-ratio diagrams that we use to test the models.

As noted above, the number of H II regions per galaxy, $N_{\rm HII}$, does not affect any trends

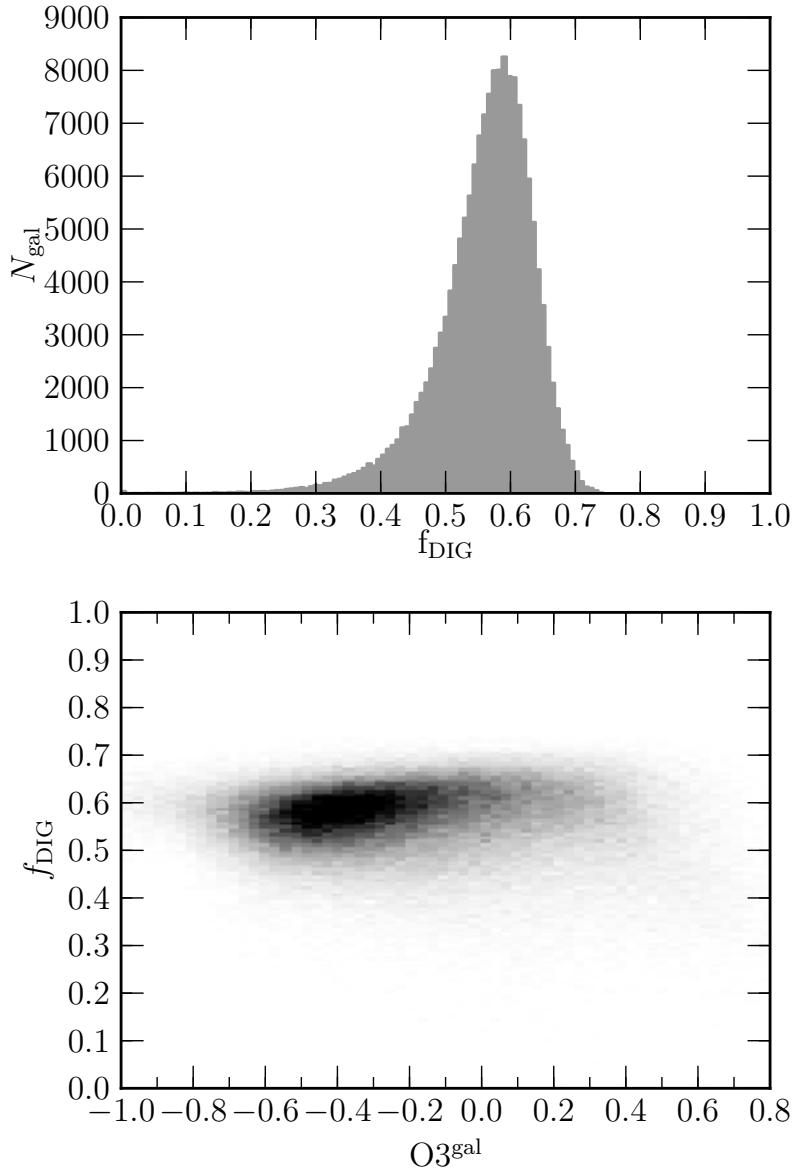

Figure 5.8: The distribution of $f_{\rm DIG}$ (top) and $f_{\rm DIG}$ as a function of O3 (bottom) for SDSS galaxies in the strong-line comparison sample. The $f_{\rm DIG}$ distribution has a median value of 0.55 and a standard deviation of 0.08, and is nearly Gaussian in shape. The DIG fraction $f_{\rm DIG}$ does not show a strong dependence on excitation, as encoded by O3.

but instead corresponds to a source of uncorrelated scatter, which decreases as N_{HII} increases and the T_3 distribution is better sampled. The chosen value of N_{HII} has no systematic effects on our results. Nevertheless, we choose a value of N_{HII} that is appropriate for SDSS fiber observations of local star-forming galaxies. At $z_{med} = 0.08$, the median redshift of the strong-line comparison sample, the $3''$ diameter of an SDSS fiber corresponds to a physical diameter of 4.5 kpc. Based on H II region identification in narrowband Hα surveys (e.g., Zurita et al., 2000), a $\sim$ 4.5 kpc diameter aperture will typically contain tens of H II regions, but may contain as few as a handful of H II regions depending on fiber placement, the ISM structure, and level of star-formation activity in the galaxy. We choose a value of $N_{HII} = 25$ to roughly match the number of H II regions expected to fall within an SDSS fiber aperture.

We set $\sigma_T = 0.07$ dex, a value that appears to be reasonable for $z \sim 0$ star-forming galaxies as described below. This value is within the range of observed σ_T for local spirals in the CHAOS galaxy survey (see Fig. 5.5, Berg et al., 2015; Croxall et al., 2015, 2016). We note that the T_3 distribution width, σ_T, encodes both stochastic variations in metallicity due to inhomogeneities in the ISM and systematic variations from radial metallicity gradients, if the observed aperture covers a large area of the disk compared to the steepness of the gradient. Radial oxygen abundance gradients of local star-forming galaxies tend to have slopes ranging from ~ -0.01 to ~ -0.1 dex kpc^{-1} for galaxies with $8.5 < \log(M_*/M_\odot) < 11.$, with less massive galaxies displaying steeper gradients on average (Sánchez et al., 2014; Ho et al., 2015). At the median redshift of the strong-line comparison sample, $z_{med} = 0.08$, $1''$ corresponds to a physical length of 1.5 kpc. With the assumption that the $3''$ SDSS fiber is placed on the center of each galaxy, the light falling in the fiber probes the inner $\sim$ 2 kpc radially. Thus, the additional temperature variations due to metallicity gradients are likely only significant for the least-massive galaxies in SDSS. After measurement uncertainty is accounted for, the intrinsic scatter of H II regions about the metallicity gradients in local spirals is $\sim 0.05 - 0.1$ dex (Kennicutt et al., 2003; Rosolowsky & Simon, 2008; Bresolin, 2011; Berg et al., 2013; Croxall et al., 2015, 2016), corresponding to $\sim 0.02 - 0.07$ dex in T_3 indicitave of the minimum σ_T in the absence of metallicity gradients for local star-forming galaxies. The shallow gradients of the CHAOS galaxies (0.02-0.04 dex kpc^{-1}) suggest that

stochastic variations in metallicity account for the majority of the width of the electron temeperature distributions in Figure 5.5.

In summary, the model matched to typical SDSS star-forming galaxies assumes a Gaussian $f_{\rm DIG}$ distribution characterized by a mean and standard deviation of 0.55 and 0.08, respectively, $N_{\rm HII} = 25$, and $\sigma_{\rm T} = 0.07$ dex. We create 2500 mock galaxy spectra following the method described in Section 5.2.5, where $T_{\rm cent}$ is drawn from a logarithmic uniform distribution from $\log(T_{\rm cent}/{\rm K}) = 3.7$ to 4.3 (5,000 to 20,000 K), the T_3 range of the reference H II region sample. We infer median line ratio and electron temperature relations from these 2500 mock galaxy spectra. We create an additional model for comparison with the same parameters except $f_{\rm DIG}= 0$ such that the mock galaxies are constructed from H II regions only and include no DIG emission. We refer to this model with no DIG emission as the *hiionly* model.

We compare the model with $f_{\rm DIG}$=0.55 matched to SDSS stacks to AM13, B16, and C17 stacks in Figures 5.9-5.11, and include the *hiionly* model for comparison. The O3N2, O3S2, and O3O2 strong-line ratio diagrams are shown in Figure 5.9. The $f_{\rm DIG}$=0.55 model shows excellent agreement with excitation sequences followed by the SDSS stacks. The *hiionly* model fails to reproduce the O3S2 and O3O2 sequences, displaying lower S2 and O2 at fixed O3 than the AM13, B16, and C17 stacks at nearly all values of O3. The largest disagreement occurs in the moderate metallicity regime where O3 $\sim$ 0.0. This failure of the *hiionly* model confirms that combinations of H II regions alone cannot simultaneously reproduce line ratio sequences in all line-ratio spaces. DIG emission properties are distinct from those of H II regions in S2 and O2, which strongly affects global galaxy line ratios and must be taken into consideration. The close agreement of the $f_{\rm DIG}$=0.55 model to the observations in the O3S2 and O3O2 diagrams suggests that both the DIG excitation sequences in Figure 5.4 and the $f_{\rm DIG}$ relation in equation 5.24 are reasonable.

The strong-line ratios $O3^{\rm gal}$, $O2^{\rm gal}$, $N2^{\rm gal}$, and $S2^{\rm gal}$ are shown as a function of $T_3^{\rm gal}$ and $T_2^{\rm gal}$ in Figure 5.10. $T_3^{\rm gal}$ measurements are only available for the SDSS stacks with $T_3^{\rm gal} > 10^4$ K. The reason for this limited range is twofold. First, the strong-to-auroral line ratio [O III]$\lambda\lambda$5007,4959/λ4363 becomes exponentially weaker at lower T_3 while O3 also drops

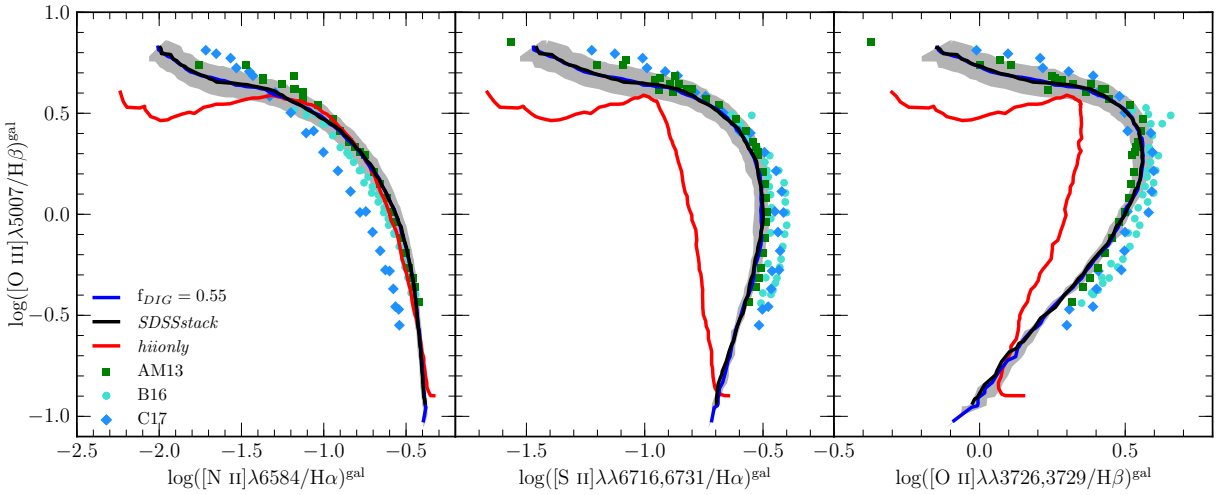

Figure 5.9: The O3N2 (left), O3S2 (middle), and O3O2 (right) strong-line ratio diagrams for stacks of SDSS galaxies and models under different sets of assumptions and input parameters. The stacks of $z \sim 0$ SDSS star-forming galaxies from AM13, B16, and C17 are shown as green squares, light blue circles, and dark blue diamonds, respectively. The blue line shows the running median of mock galaxies in bins of $O3N2^{gal}$ for the model with f_{DIG}=0.55 and equal H II and DIG T_2 at fixed metallicity. The shaded gray region represents the 68th-percentile width of the distribution of mock galaxies around this running median. The black line displays the running median for the *SDSSstack* model with f_{DIG}=0.55 under the assumption that DIG T_2 is 15% lower than H II region T_2 at fixed metallicity, and is identical to the blue line in these strong-line ratio diagrams. The red line shows the *hiionly* model that does not include DIG emission (f_{DIG}=0.0).

off significantly due to a smaller fraction of oxygen in the O^{++} state, leading to an extremely weak [O III]λ4363 at low T_3^{gal} that may not even be detected in stacks. Second, [O III]λ4363 is blended with [Fe II]λ4360, which significantly contaminates [O III]λ4363 measurements for high-metallicity, low-T_3^{gal} galaxies in which [Fe II]λ4360 is stronger (Andrews & Martini, 2013; Curti et al., 2017). T_3^{gal} measurements are not shown for AM13, B16, and C17 stacks with [Fe II]λ4360/[O III]λ4363 > 0.5 for which [O III]λ4363 measurements were deemed unreliable. Due to the combined effect of these two limitations, T_3^{gal} measurements are only shown for stacks of galaxies with $\log(M_*/M_\odot) \lesssim 9.4$. The f_{DIG}=0.55 model matches the observed SDSS stacks well in the T_3^{gal} diagrams within the amount of scatter displayed by the SDSS stacks. The *hiionly* model fails to produce high enough $O2^{gal}$ and $S2^{gal}$ values at moderate T_3^{gal} to match the observations. Due to the limited dynamic range of the T_3^{gal} measurements for the SDSS stacks, the turnover points of the models ($\log(T_3^{gal}) \approx 3.95$ for $O2^{gal}$ and $S2^{gal}$) that would provide an excellent test for agreement are not sampled by the SDSS stacks.

In the right column of Figure 5.10, we again compare the predicted model line ratios with those observed in the SDSS composites, this time as a function of T_2^{gal}. The auroral line [O II]$\lambda\lambda$7320,7330 does not suffer from contamination or severe dropoff in brightness at high metallicities, and is thus robustly measured across a much wider range of temperatures than [O III]λ4363. The *hiionly* model shows large discrepancies in $O2^{gal}$ and $S2^{gal}$ again demonstrating the importance of accounting for DIG emission in global galaxy spectra. The shapes of the f_{DIG}=0.55 model sequences match those of the observed sequences well, but with a systematic offset towards higher T_2^{gal} at fixed line ratio that is seen in all four strong-line ratios.

Since strong-line ratios of H II regions as a function of T_3 and T_2 are directly constrained by observations, this offset in T_2^{gal} must either originate from incorrect assumptions about DIG region line ratios or electron temperatures, or from a systematic effect in the binning and stacking process that is not captured in our models that only produce individual galaxy spectra. It is improbable that incorrect strong-line DIG excitation sequences (see Figure 5.4) are the cause of this offset, because shifting the strong-line ratios of DIG regions alone would

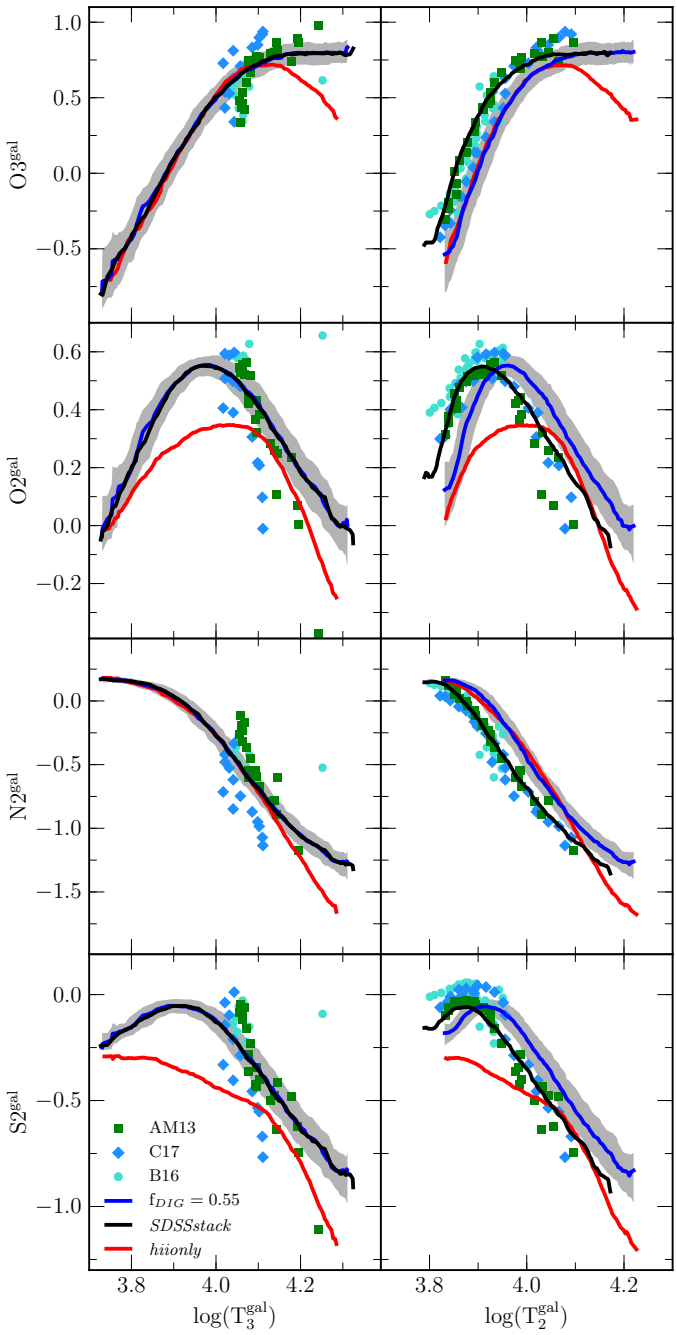

Figure 5.10: Global galaxy strong-line ratios $O3^{gal}$, $O2^{gal}$, $N2^{gal}$, and $S2^{gal}$ as a function of T_3^{gal} (left column) and T_2^{gal} (right column). Lines and points are the same as in Figure 5.9. The f_{DIG}=0.55 model is systemtacially offset towards higher T_2 at fixed line ratio compared to the SDSS stacks. This offset is not present in the *SDSSstack* model, in which we assume that DIG T_2 is lower than H II region T_2 by 15% at fixed metallicity.

lead to a mismatch in the strong-line vs. strong-line sequences shown in Figure 5.9, which agree well under the current set of assumptions. Additionally, no systematic offset is observed the strong-line vs. T_3^{gal} plots in Figure 5.10, and changing the DIG strong-line excitation sequences would introduce a disagreement in these diagrams as well. The T_2^{gal} offset also cannot be resolved by decreasing f_{DIG} as T_2^{gal} increases. This adjustment would introduce disagreement in Figure 5.9 and the left column of Figure 5.10 while still failing to match the high-T_2^{gal} tail of the observations where even the *hiionly* model overestimates $O2^{gal}$, $N2^{gal}$, and $S2^{gal}$ and underestimates $O3^{gal}$ at fixed T_2^{gal}.

The T_2-T_3 diagram is shown in Figure 5.11. In this diagram, the SDSS stacks display lower T_2^{gal} at fixed T_3^{gal} than the H II region relation of Campbell et al. (1986) (equation 5.12). Both the *hiionly* and f_{DIG}=0.55 models fall below the H II region T_2-T_3 relation, but neither show as large of an offset as the SDSS stacks. The small difference between the *hiionly* (f_{DIG}=0.0) and f_{DIG}=0.55 models is predominantly due to the different relation between O2 and T_2 for DIG regions compared to that of H II regions, which changes the relative weight of regions of different T_2 to the T_2^{gal} estimate from the global galaxy spectrum. In order to match the observations, the f_{DIG}=0.55 model must have higher T_3^{gal} at fixed T_2^{gal}or lower T_2^{gal} at fixed T_3^{gal}. No systematic offset in T_3^{gal} is observed in Figure 5.10, suggesting that the mismatch between model and observations in the T_2-T_3 diagram is caused by a mismatch in T_2^{gal} alone. The T_2^{gal} offsets in Figure 5.10 appear to be roughly equivalent for each strong-line ratio, with the model being ~ 0.05 dex higher in T_2^{gal} at fixed line ratio than the observations, corresponding to an offset of $\sim 1,000 - 1,500$ K at $T_2 = 8,000 - 12,000$ K that closely matches the T_2^{gal} discrepancy between the f_{DIG}=0.55 model and observations at fixed T_3^{gal}. We conclude that the discrepancy between the f_{DIG}=0.55 model and SDSS composites originates from T_2^{gal} alone.

The T_2^{gal} discrepancy between model and observations could arise from either an incorrect assumption about DIG electron temperatures in the models or some aspect of the stacking process that is not captured by our individual galaxy models, since we are comparing to data from stacked spectra. We do not have a way of testing the latter hypothesis without matching the scatter in SDSS excitation sequences in detail and obtaining actual line profiles

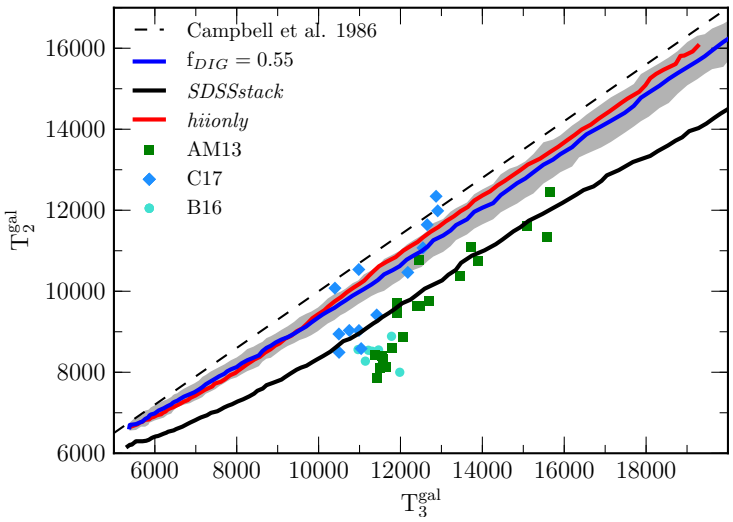

Figure 5.11: The global galaxy ionic temperature diagram of T_2^{gal} vs. T_3^{gal}. The dashed black line shows the H II region T_2-T_3 relation of Campbell et al. (1986) given in equation 5.12. All other lines and points are the same as in Figure 5.9.

from the models in addition to line fluxes, which our models do not do since they are only designed to investigate mean properties of the local galaxy population. However, both AM13 and C17 performed their stacking procedures on individual SDSS galaxies with auroral-line detections and found that the inferred electron temperatures and metallicities of the stacks were not systematically offset from the mean values of the individual galaxies. These tests suggest that the offset in T_2^{gal} does not originate from a systematic effect of the binning and stacking procedures.

The T_2^{gal} discrepancy then most likely arises from an incorrect assumption about T_2 of DIG regions. Up to this point, we have assumed that T_2 and T_3 of a DIG region are the same as those of the associated H II region. The observed T_2^{gal} offset instead suggests that the DIG T_2 is lower than that of H II regions at fixed metallicity, while T_3 remains roughly equivalent. We find that the model can be brought into excellent agreement with the SDSS composities if the T_2 of each DIG region is assumed to be 15% (0.06 dex) lower than that of the associated H II region. Models incorporating the revised DIG T_2 assumption are shown in Figures 5.9-5.11 as black lines, and we refer to this model as the *SDSSstack* model. Results are unchanged for diagrams that do not involve T_2^{gal}, while the shift towards lower T_2^{gal} brings the adjusted model into excellent agreement with the SDSS stacks in Figures 5.10 and 5.11.

We adopt the *SDSSstack* model as the fiducial description for typical $z \sim 0$ star-forming galaxies for the remainder of this work.

Our assumption that DIG T_2 is lower than T_2 of H II regions on average is in conflict with past studies of Milky Way and extragalactic DIG, which suggest that DIG electron temperature is higher on average than that of H II regions. Studies of DIG strong-line ratios in the Milky Way (Haffner et al., 1999) and other galaxies (Otte et al., 2001, 2002; Hoopes & Walterbos, 2003) have suggested that DIG is hotter than H II regions on average based on the larger N2, S2, and O2 ratios observed for DIG. Additionally, Reynolds et al. (2001) detected the auroral line [N II]λ5755 for DIG along one line-of-sight in the Milky Way, and found that DIG along this line-of-sight has a higher temperature than bright Galactic H II regions. However, the Milky Way results only probe a number of distinct sight lines and most extragalactic studies of DIG line-ratios observe extra-planar DIG in edge-on galaxies. It is not clear how representative such observations are of the DIG regions observed in face-on disk galaxies in the MaNGA DIG galaxy sample, and if past comparisons between DIG and H II region temperature have been made at fixed nebular abundance. Additional observations of temperature-sensitive auroral lines for DIG regions are required to unequivocally settle the question of DIG electron temperature. Even if DIG T_2 is not lower than that of H II regions in reality, adopting this assumption in our model framework captures an important systematic effect that is present in global galaxy spectra and will contribute to the bias in direct-method metallicity.

One concern is whether the disagreement in the T_2-T_3 diagram and strong-line ratio vs. T_2 diagrams can be resolved by adjusting other model parameters instead of making an assumption that DIG T_2 is 15% lower than H II region T_2 at fixed metallicity. In particular, the width of the T_3 distribution, σ_T, can change the magnitude of the offset in the T_3-T_2 diagram. This effect has been previously shown by Pilyugin et al. (2012b), who demonstrated that the T_2-T_3 offset increases as the range of metallicities of combined H II regions increases (equivalent to increasing σ_T in our framework). We have set $\sigma_T = 0.07$ dex based on empirical observations of H II regions in individual galaxies (Berg et al., 2015; Croxall et al., 2015, 2016), but it is worthwhile to investigate whether different values of σ_T

may resolve the T_2 discrepancies. Such an investigation is presented in Appendix 5.A.2. To briefly summarize, while increasing σ_T can reproduce the SDSS stack T_2-T_3 offset without any different assumptions regarding DIG T_2, the required values of σ_T lead to significant changes in the predicted global galaxy strong-line ratios that do not match the observations. Adjusting σ_T is thus not a viable option for resolving the T_2 discrepancies, and we continue under the assumption that DIG T_2 is 15% lower than H II region T_2 at fixed metallicity.

5.3.2 The SDSS auroral-line comparison sample

We also test our model framework against observations of individual SDSS galaxies with electron temperature measurements. We use the sample of 181 SDSS galaxies from Pilyugin et al. (2010) for which both [O III]λ4363 and [O II]$\lambda\lambda$7320,7330 have been detected. We expand this sample by adding 271 galaxies from Izotov et al. (2006). Izotov et al. identified 309 SDSS galaxies for which [O III]λ4363 was measured, and we add those galaxies that were not already included as part of the Pilyugin et al. (2010) sample. We note that while all of these additional galaxies have measurements of [O III]λ4363 and [O II]$\lambda\lambda$7320,7330, only 86 have measurements of [O II]$\lambda\lambda$3726,3729 due to their redshifts, and thus not all of them have estimates of $T_2^{\rm gal}$. Those objects lacking [O II]$\lambda\lambda$3726,3729 observations are not plotted in diagrams involving $O2^{\rm gal}$ or $T_2^{\rm gal}$. We refer to this combined sample as the "auroral-line comparison sample."

We determine the DIG fraction for the auroral-line comparison sample following the same method used for the larger SDSS sample. We apply aperture correction factors to the reddening-corrected Hα luminosities, and determine $\Sigma_{\rm H\alpha}$ using the R-band half-light radius for each galaxy in the auroral-line comparison sample. The DIG fractions are found using equation 5.24. The auroral-line comparison sample has an $f_{\rm DIG}$ distribution that is nearly Gaussian, with a mean and standard deviation of 0.4 and 0.13, respectively, and no strong dependence on the level of excitation in the global galaxy spectrum. The lower average $f_{\rm DIG}$ for this sample compared to that of the full SDSS sample reflects the extreme star-forming nature of galaxies in the auroral-line comparison sample. Model $f_{\rm DIG}$ values are drawn

randomly from this normal distribution. We adopt the same value as in the *SDSSstack* model for the number of H II regions per fiber, $N_{HII} = 25$, but find that a smaller width of the T_3 distribution better fits the auroral-line sample, instead using $\sigma_T = 0.02$ dex. A smaller value of σ_T is likely more appropriate for the low-mass, high-sSFR galaxies in the auroral-line comparison sample. Metals can be distributed more homogeneously throughout the ISM in such galaxies than in massive or low-sSFR galaxies because of an increase in feedback efficiency, as suggested by flatter metallicity gradients with decreasing M_* and increasing sSFR (Ho et al., 2015; Ma et al., 2017). We continue to assume that DIG T_2 is 15% lower than H II region T_2 at fixed metallicity, as described in Section 5.3.1. Despite the comparatively narrow T_3^{gal} range of the auroral-line comparison sample, we again randomly draw 2500 samples of T_{cent} from a logarithmic uniform distribution over $\log(T_{cent}/K) = 3.7$ to 4.3, and create mock galaxy spectra following the method described in Section 5.2.5. We refer to this model as the *auroral* model.

We compare the *auroral* model to individual galaxies in the auroral-line comparison sample in Figures 5.12-5.14. We find that the strong-line ratio diagrams (Fig. 5.12), line ratios as a function of T_2^{gal} (Fig. 5.13, right column), and the T_2-T_3 diagram (Fig. 5.14) show excellent agreement between the *auroral* model and observations. However, as a function of T_3^{gal} (Fig. 5.13, left column) the model overestimates $N2^{gal}$, $S2^{gal}$, and $O2^{gal}$ at fixed T_3^{gal} in the high-temperature regime ($\log(T_3^{gal}) > 4.1$). The discrepancies are largest in the high-temperature, low-metallicity regime for which we had to extrapolate the DIG excitation sequences, and thus may suggest that the DIG excitation sequence extrapolations are not completely accurate in this regime, especially for $O2^{gal}$. We caution that results for metal-poor galaxies with observed $O3N2^{gal} \gtrsim 2.0$ and $\log(T_3) \gtrsim 4.15$ rely heavily on the extrapolation of the DIG sequences and should therefore be treated with caution. It is also possible that the extreme star-forming and metal-poor nature of some of the galaxies in the auroral-line comparison sample require some physics that is not captured in the framework of our simple models. However, the model framework appears to perform well overall even for a sample of extreme star-forming galaxies that are unrepresentative of the local star-forming galaxy population. It is also of note that the assumption that DIG T_2 is lower than H II

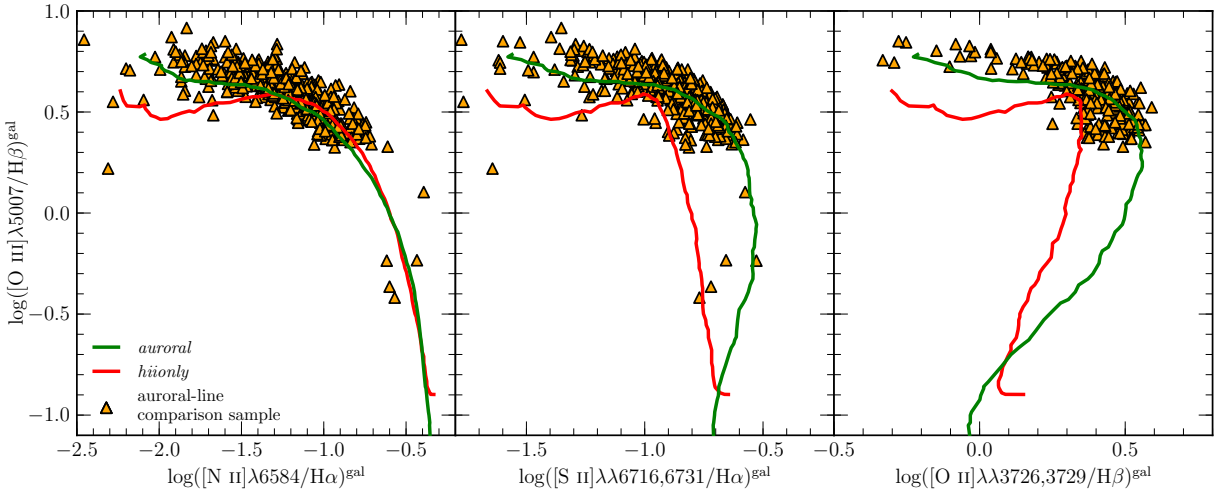

Figure 5.12: The O3N2 (left), O3S2 (middle), and O3O2 (right) strong-line ratio diagrams for individual SDSS galaxies with auroral line detections and models under different sets of assumptions and input parameters. Orange triangles show SDSS galaxies in the auroral-line comparison sample from Pilyugin et al. (2010) and Izotov et al. (2006). The green line displays the running median of mock galaxies in bins of $O3N2^{gal}$ for the *auroral* model with f_{DIG}=0.40 and σ_T = 0.02 dex, under the assumption that DIG T_2 is 15% lower than H II region T_2 at fixed metallicity. The red line shows the *hiionly* model that includes no DIG emission (f_{DIG}=0.0) and follows the same DIG T_2 assumption as the *auroral* model.

region T_2 at fixed metallicity is required to match observations of *individual* galaxies with auroral-line measurements in addition to stacks of SDSS galaxies, suggesting that the T_2 offset is not a result of some systematic effect introduced by the stacking process.

5.4 Results

Using these models, we characterize the biases in strong-line ratios, electron temperatures, and direct-method metallicity measurements from global galaxy spectra. These biases arise as a consequence of DIG contamination of emission lines and flux-weighting effects when combining emission from multiple H II regions with a range of excitation levels. The bias of a particular property is quantified by taking the difference between the value measured from a mock global galaxy spectrum and the median value of the same property for the individual H II regions in that mock galaxy. We represent the bias in property X with the symbol ΔX. For each property, the superscript "gal" (X^{gal}) indicates that the property is derived from the

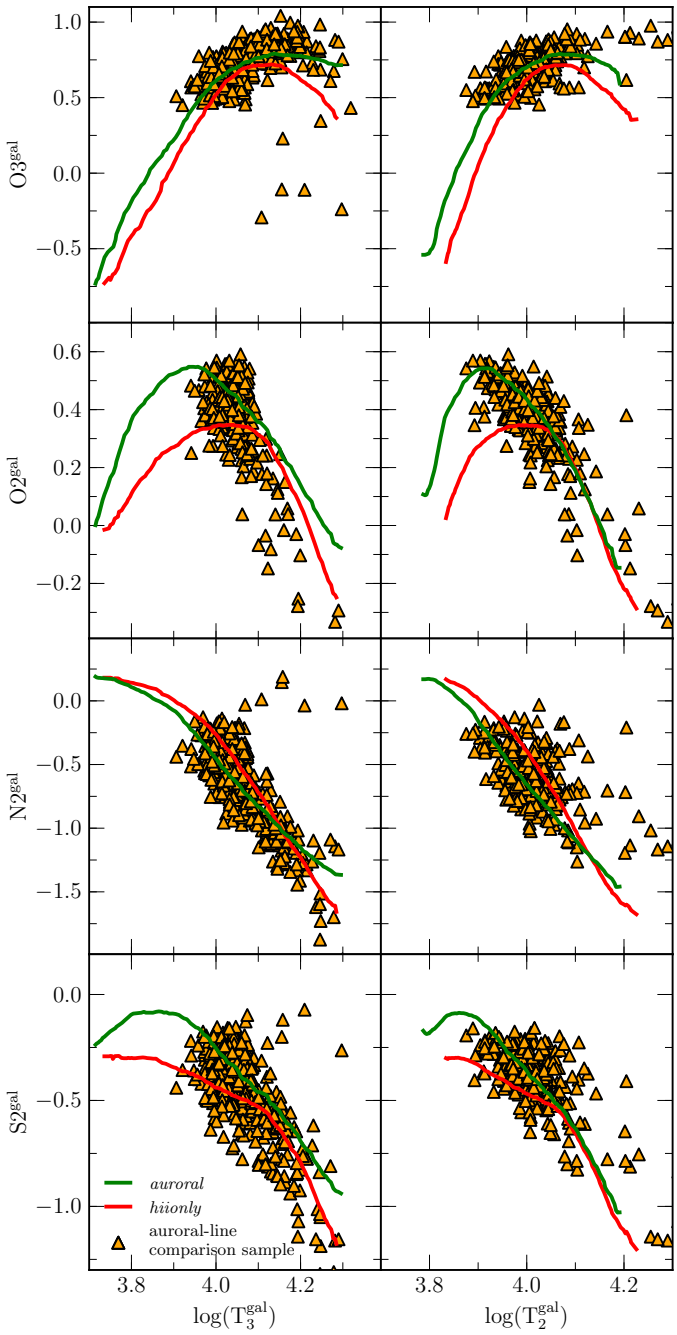

Figure 5.13: Global galaxy strong-line ratios $O3^{gal}$, $O2^{gal}$, $N2^{gal}$, and $S2^{gal}$ as a function of T_3^{gal} (left column) and T_2^{gal} (right column). Lines and points are the same as in Figure 5.12.

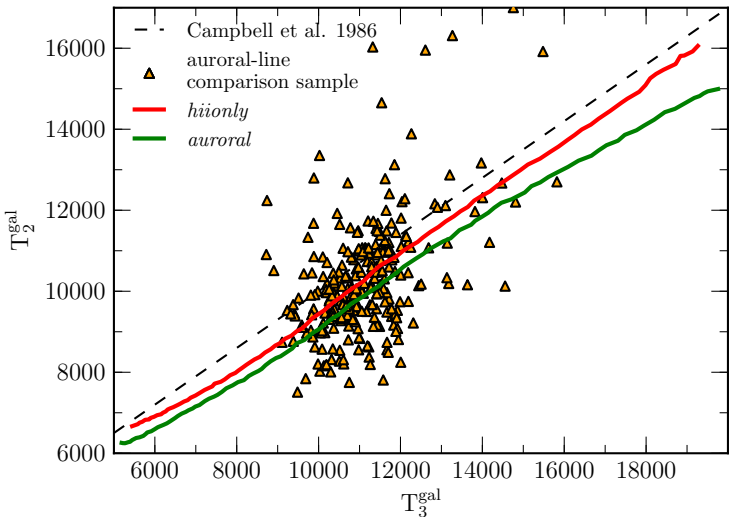

Figure 5.14: The global galaxy ionic temperature diagram of T_2^{gal} vs. T_3^{gal}. The dashed black line shows the H II region T_2-T_3 relation of Campbell et al. (1986) given in equation 5.12. All other lines and points are the same as in Figure 5.12.

observed global galaxy spectrum, while the superscript "HII" (X^{HII}) is used to indicate the median value of the property for the distribution of H II regions within each galaxy. Obtaining measurements that are representative of the H II region distribution in a galaxy is desirable because both strong-line and direct-method metallicity estimates are based on H II regions (real or simulated) rather than ensembles of H II regions surrounded by DIG. Furthermore, the H II regions trace only the most recent generation of star formation. Therefore, they provide a metallicity that is ideal for comparing to cosmological hydrodynamical simulations, which trace the metallicity of star-forming particles.

The bias determinations presented below can be used to correct properties measured from global galaxy spectra in order to obtain values representative of the median H II region distributions. The *SDSSstack* model is designed to reproduce the mean properties and trends of $z \sim 0$ star-forming galaxies, but does not accurately represent deviations of individual galaxies from mean relations.

5.4.1 Biases in the strong-line ratios

We quantify the typical global galaxy bias in the strong-line ratios O3, O2, N2, and S2 for $z \sim 0$ star-forming galaxies from SDSS. These strong-line ratios can be combined to construct strong-line metallicity indicators used in calibrations that are widely applied to estimate galaxy metallicities. Additionally, the strong-line ratios O3 and O2 are used in the calculation of direct-method metallicity (equations 5.13 and 5.14). It is thus of great importance to eliminate biases in galaxy strong-line ratios before using either the direct method or strong-line calibrations to determine galaxy metallicities.

In Figure 5.15, we present the global galaxy biases in O3, O2, N2, and S2 as a function of $O3N2^{gal}$, the O3N2 ratio as observed in global galaxy spectra. To determine the typical biases, we take the running median of individual mock galaxy spectra from each model in bins of $O3N2^{gal}$. The biases are quantified as a function of $O3N2^{gal}$ instead of each individual line ratio (i.e., we show ΔO3 vs. $O3N2^{gal}$ as opposed to ΔO3 vs. $O3^{gal}$) because O3N2 increases monotonically with metallicity and T_3, and does not saturate over the range of metallicities of interest here. O3 and O2 are double-valued such that it would be necessary to determine on which branch a galaxy lies in order to correct the line ratio, and S2 and N2 saturate at high metallicities, limiting the utility of bias estimates as a function of these line ratios. Parameterizing by O3N2 instead should not severely limit the number of galaxies to which these corrections may be applied since O3N2 only involves strong lines that are easily detected in low-redshift star-forming galaxies down to low metallicities and stellar masses. We include the *hiionly* model for comparison in order to understand how much of the bias arises from DIG contamination. Biases in the *hiionly* model arise purely from flux-weighting effects due to combining light on a line-by-line basis from multiple H II regions with different metallicities. Any additional bias in models including DIG is driven by the inclusion of DIG emission in the global spectrum.

The top panel of Figure 5.15 shows the bias in O3. $O3^{gal}$ can be biased high by as much as +0.3 dex in typical local star-forming galaxies, with the maximum bias occuring at $O3N2^{gal} \gtrsim 2.0$. The *SDSSstack* and *hiionly* models display a similar level of $O3^{gal}$ bias at

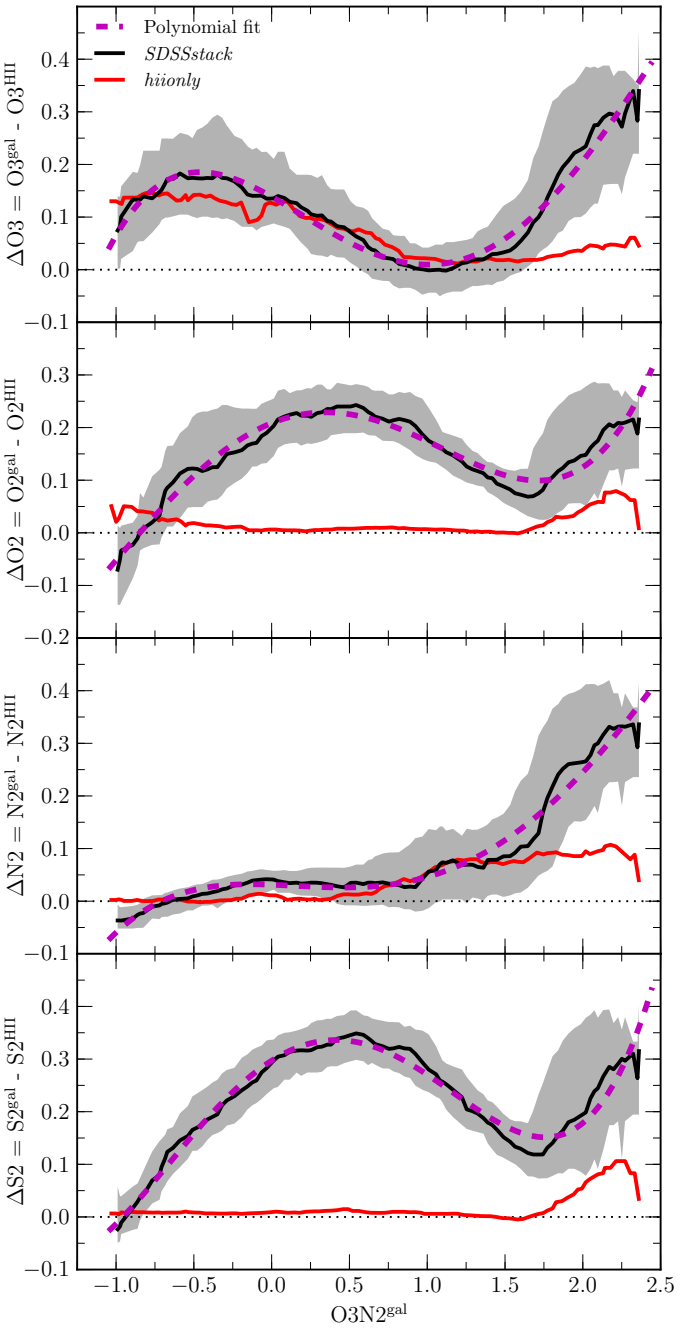

Figure 5.15: The difference between the global galaxy line ratio and median line ratio of the H II region distribution, ΔX, as a function of O3N2$^{\rm gal}$ for the strong-line ratios X=O3, O2, N2, and S2. The red line shows the running median of the 2500 mock galaxy realizations in bins of O3N2$^{\rm gal}$ for the *hiionly* model with $f_{\rm DIG}$=0.0. The running median of the *SDSSstack* model with $f_{\rm DIG}$=0.55 is displayed as a black line, where the gray shaded region corresponds to the 68th-percentile width of the distribution of mock galaxies around the running median. In each panel, the dashed magenta line shows the best-fit fourth-order polynomial to the bias in the global galaxy line ratio, ΔX, for the *SDSSstack* model. The best-fit coefficients are presented in Table 5.1.

$O3N2^{gal} < 1.5$. In this regime, DIG emission has little effect on the global O3 bias because DIG and H II regions are matched in O3N2, and SDSS galaxies, DIG, and H II regions follow similar excitation sequences in the O3N2 diagram. The positive bias at $O3N2^{gal} < 1.5$, reaching +0.2 dex at $O3N2^{gal} \sim -0.5$, is predominantly driven by flux-weighting effects when combining light from H II regions with a range of metallicities due to the shape of the O3 vs. T_3 relation of H II regions (Figure 5.2). Since Hβ luminosity does not correlate with electron temperature for H II regions within a single galaxy (Berg et al., 2015; Croxall et al., 2015, 2016), when the slope of the O3 vs. T_3 relation is steep the global [O III]$\lambda\lambda$4959,5007 flux is dominated by high-O3 H II regions while H II regions of all metallicities contribute equally to the global Hβ flux on average. Thus, a steep slope in the O3 vs. T_3 relation leads to an $O3^{gal}$ value that is higher than $O3^{HII}$, the median of the individual H II regions. The positive bias is largest where the slope is steepest. In contrast, when the O3 vs. T_3 relation is flat near the turnover point ($O3N2^{HII} \sim 1.9$, $\log(T_3) \sim 4.1$) the bias from flux-weighting effects becomes small, as seen in the *hiionly* model at high $O3N2^{gal}$. At $O3N2^{gal} > 1.5$, the *SDSSstack* model diverges from the *hiionly* model, displaying a significant positive ΔO3. In this low-metallicity regime, the DIG and H II region sequences diverge in the O3N2 diagram such that DIG regions have higher O3 and N2 than H II regions at fixed O3N2. This divergence leads to a positive $O3^{gal}$ bias that increases with increasing $O3N2^{gal}$. We note that mock galaxy spectra with $O3N2^{gal} \gtrsim 2.0$ rely almost entirely on the linear extrapolation of the DIG excitation sequence, and predictions in this regime should therefore be used with caution.

A similar relative behavior between the *SDSSstack* and *hiionly* models is observed in the $N2^{gal}$ bias, shown in the second panel from the bottom in Figure 5.15. At $O3N2^{gal} < 1.5$, the two models closely follow one another, while they diverge at $O3N2^{gal} > 1.5$ where DIG emission plays a role in the *SDSSstack* model. The explanation is the same as for the $O3^{gal}$ bias, except that in this case the N2 vs. T_3 relation is flat at low T_3 (low O3N2) and becomes steeper with increasing T_3. Flux-weighting effects therefore lead to no bias at low $O3N2^{gal}$ and a slight increase in the bias at higher $O3N2^{gal}$ reaching +0.1 dex due to H II regions alone. The additional bias in the *SDSSstack* model at $O3N2^{gal} > 1.5$ is again due to the

divergence of DIG and H II regions in the O3N2 diagram, such that DIG regions have higher N2 than H II regions at fixed O3N2.

DIG emission plays a much more important role in the $O2^{gal}$ bias, displayed in the second panel from the top in Figure 5.15. The *hiionly* model shows a negligible $O2^{gal}$ bias of < 0.1 dex at all $O3N2^{gal}$ values. The lack of a significant bias in the *hiionly* model results from the shape of the O2 vs. T_3 relation, which peaks at $\log(T_3^{HII}) \sim 4.0$ ($O3N2^{HII} \sim 1.4$) and does not have a severely steep slope in either extreme. The *SDSSstack* model displays a larger $\Delta O2$ of > 0.1 dex over most of the $O3N2^{gal}$ range, peaking at +0.25 dex, and is primarily caused by DIG contamination in global galaxy spectra. DIG displays higher O2 at fixed O3N2 than H II regions, as can be seen in the O3N2 and O3O2 diagrams (Figure 5.3), leading to an overestimate of O2 relative to the median O2 of the the H II region distribution. The behavior of the *SDSSstack* $O2^{gal}$ bias can be understood through the divergence of the DIG excitation sequence from that of H II regions in the O3O2 diagram at both low metallicities ($O3N2^{gal} \gtrsim 1.75$) and moderate metallicities ($O3N2^{gal} \sim 0.5$).

The $S2^{gal}$ bias, shown in the bottom panel of Figure 5.15, behaves similarly to that of $O2^{gal}$. A flux-weighted combination of H II regions alone only leads to a small positive $\Delta S2$ at $O3N2^{gal} \gtrsim 1.75$. Elevated S2 in DIG regions leads to a bias in $S2^{gal}$ values as high as +0.35 dex at $O3N2^{gal} \sim 0.5$. $S2^{gal}$ displays a larger bias than $O2^{gal}$ because the DIG and H II region excitation sequences have a larger separation in the O3S2 diagram than in the O3O2 diagram (Figure 5.3).

In order to correct for these strong-line ratio biases in observed galaxy samples, we fit each bias as a function of observed $O3N2^{gal}$ with a fourth-order polynomial of the form

$$\Delta R = c_0 + c_1 x + c_2 x^2 + c_3 x^3 + c_4 x^4, \tag{5.25}$$

where $x = O3N2^{gal}$ and R is the strong-line ratio O3, O2, N2 or S2. The best-fit polynomials are shown in Figure 5.15 and the coefficients are given in Table 5.1. These bias functions may be subtracted from observed galaxy strong-line ratios to obtain the median strong-line ratios of the H II region distributions, correcting for DIG contribution and flux-weighting effects.

Table 5.1: Global galaxy bias coefficients.

Strong-line ratios[a]					
ΔR	c_0	c_1	c_2	c_3	c_4
O3	0.138	-0.168	-0.0749	0.140	-0.0262
O2	0.208	0.118	-0.173	-0.00540	0.0260
N2	0.0312	-0.0111	-0.0277	0.0640	-0.0103
S2	0.296	0.188	-0.214	-0.0463	0.0457
Electron temperatures[b]					
ΔT_e	c_0	c_1	c_2	c_3	c_4
T_3	-2,171	6,813	-2,537,	-2,278	1,109
T_2	18,280	-75,610	114,500	-78,200	19,690
Direct-method oxygen abundances[c]					
$\Delta\log(O/H)$	c_0	c_1	c_2	c_3	c_4
T_3 and T_2[d]	0.121	-0.337	0.629	-0.267	0.0333
T_3 only[e]	-0.0266	-0.591	0.530	0.311	-0.362
T_2 only[f]	0.340	-0.459	0.420	-0.0143	-0.00841

(a) Coefficients for equation 5.25.
(b) Coefficients for equation 5.26.
(c) Coefficients for equation 5.27.
(d) The direct-method 12+log(O/H) case where both T_3 and T_2 are directly determined from the galaxy spectrum.
(e) The case where only T_3 is estimated directly, while T_2 is inferred using equation 5.12.
(f) The case where only T_2 is estimated directly, while T_3 is inferred using equation 5.12.

We note that the corrections presented above are only appropriate for a sample of galaxies representative of typical $z \sim 0$ star-forming galaxies with $f_{\rm DIG}$=0.55, and should not be applied to unrepresentative samples of galaxies. See Appendix 5.A.1 for bias characterizations over a range of $f_{\rm DIG}$.

5.4.2 Biases in the electron temperatures

Electron temperatures as inferred from global galaxy spectra also display biases with respect to the median electron temperature of the H II regions. We quantify the bias in $T_3^{\rm gal}$ ($T_2^{\rm gal}$) by taking the running median of ΔT_3 (ΔT_2) of the individual mock galaxy spectra in bins of $T_3^{\rm gal}$ ($T_2^{\rm gal}$). The typical biases in T_3 and T_2, as inferred from global galaxy spectra, are shown in Figure 5.16.

In the *hiionly* model, $T_3^{\rm gal}$ is biased by as much as $\pm 1,000$ K with respect to $T_3{}^{\rm HII}$, the

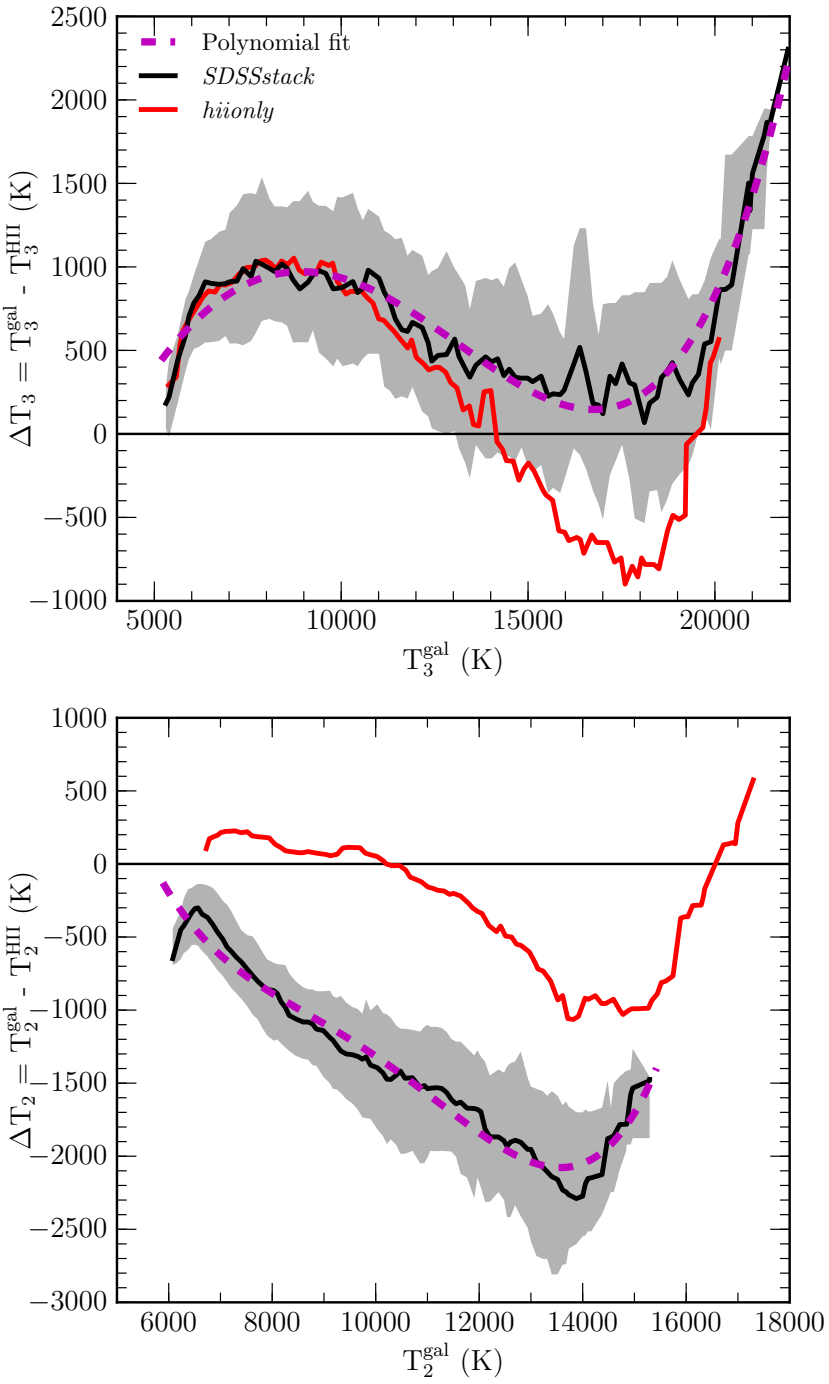

Figure 5.16: The difference between the global galaxy electron temperature, inferred from the observed galaxy spectrum, and the median electron temperature of the H II region distribution as a function of electron temperature. Results for T_3 are shown in the top panel, while the bias in T_2 is presented in the bottom panel. Lines and shading are the same as in Figure 5.15. The best-fit coefficients are given in Table 5.1.

median value of the H II region distribution. Below T_3^{gal}= 14,000 K, the *hiionly* T_3^{gal} is biased high, while ΔT_3 is negative at T_3^{gal}= 14,000 − 19,000 K. Since the *hiionly* model does not include any DIG emission, these biases are a result of flux-weighting effects when combining light from multiple H II regions of different electron temperatures. T_3 sets the strong-to-auroral line ratio Q3 = [O III]$\lambda\lambda$4959,5007/λ4363. As T_3 increases, Q3 decreases exponentially (equation 5.9) such that hotter H II regions contribute more strongly to the global strong-to-auroral line ratio. In isolation, this trend would lead to ΔT_3 that is always positive and increases significantly at high T_3^{gal}. However, since Hβ luminosity does not correlate with T_3 for individual H II regions in single galaxies, on average [O III]λ5007 luminosity depends on T_3 according to the O3 vs. T_3 relation shown in Figure 5.2. Thus, hotter H II regions have more luminous [O III]λ5007 on average below $T_3 < 14,000$ K ($\log(T_3/K) < 4.15$). On the other hand, at $T_3 > 14,000$ K, hotter H II regions typically have *lower* [O III]λ5007 luminosity. Thus, in the *hiionly* model, there is a positive bias in T_3^{gal} at T_3^{gal}< 14,000 K due to the increased weight of hotter H II regions that have both higher O3 and lower Q3. At T_3^{gal}= 14,000 − 19,000 K, cooler H II regions with higher O3 and higher Q3 contribute more to T_3^{gal} because the steepness of the dropoff in the O3 vs. T_3 relation dominates over the decrease in Q3 with increasing T_3 in this regime. However, the exponential nature of the Q3 vs. T_3 relation eventually dominates over the falling O3 vs. T_3 relation, leading to a sharp increase in the T_3^{gal} bias above T_3 = 19,000 K as hotter H II regions again receive more weight in the global T_3^{gal} calculation.

In the *SDSSstack* model, the T_3^{gal} bias mimics that of the *hiionly* model at T_3^{gal}< 12,000 K, the regime where H II regions and DIG follow similar excitation sequences in the O3N2 diagram. At T_3^{gal}> 12,000 K, the DIG and H II region sequences diverge in the O3N2 diagram, such that DIG O3 continues increasing with T_3 whereas H II region O3 turns over. This difference in the DIG O3 vs. T_3 behavior leads to ΔT_3 that is always positive in the *SDSSstack* model that includes DIG emission. Similar to the *hiionly* model, the exponential dependence of Q3 on T_3 begins to dominate at T_3^{gal}> 19,000 K due to flux-weighting effects, as evidenced by a sharp increase in ΔT_3.

The T_2^{gal} bias for the *hiionly* model ranges from −1,000 K to +500 K. The bias can

again be understood as a consequence of combining light from H II regions with a range of temperatures. The strong-to-auroral line ratio Q2 = [O II]$\lambda\lambda$3726,3729/$\lambda\lambda$7320,7330 depends on T_2 according to equation 5.10. As before, the global bias is determined by the interplay of the auroral-line Q2 vs. T_2 and strong-line O2 vs. T_2 relations. The O2 vs. T_3 relation is shown in Figure 5.2. Since T_2 is linearly dependent on T_3, the O2 vs. T_2 relation will have the same shape as the O2 vs. T_3 relation modulo a linear transform to the temperature axis. At $T_2 < 10,000$ K, hotter H II regions have both higher [O II]$\lambda\lambda$3726,3729 luminosity and lower Q2, leading to a positive ΔT_2, although this bias is fairly small since the O2 vs. T_2 relation slope is not extreme in this regime. At $T_2 = 10,000-15,000$ K, the O2 vs. T_2 relation drops off steeply such that cooler H II regions have higher [O II]$\lambda\lambda$3726,3729 luminosity and dominate the T_2^{gal} measurement, leading to a negative ΔT_2 that reaches $-1,000$ K at T_2^{gal}= 14,000 K. The exponential fall of Q2 with increasing T_2 begins to dominate at T_2^{gal}> 15,000 K, leading to a rapid increase in ΔT_2.

The T_2^{gal} bias for the *SDSSstack* model is always negative and can be large, underestimating T_2^{HII} by as much as 2,000 K. There are two effects driving the difference between the T_2^{gal} bias of the *SDSSstack* and *hiionly* models. First, inclusion of DIG emission significantly increases the $O2^{gal}$ ratio. However, ΔO2 is not a strong function of $O3N2^{gal}$ (a good proxy for electron temperature), and will thus not have a large effect on the T_2^{gal} bias, which is sensitive to the slope of the ΔO2 vs. $O3N2^{gal}$ relation rather than the normalization. When the slope of the ΔO2 vs. $O3N2^{gal}$ relation is flat, the bias in $O2^{gal}$ is not a function of electron temperature and thus does not strongly affect the globally-derived T_2^{gal}. The dominant factor separating the *SDSSstack* and *hiionly* models in ΔT_2 is our inference that DIG T_2 is 15% lower than H II region T_2 at fixed metallicity. This choice was motivated by differences between observations and a model in which DIG and H II region T_2 was always equal. An offset between model and stacks of SDSS galaxies was observed in all plots involving T_2 but was not present in plots that only include T_3, suggesting that DIG T_2 is not equivalent to H II region T_2 at fixed metallicity. The difference in DIG and H II region T_2 effectively shifts the globally-derived T_2^{gal} lower and results in a large negative ΔT_2 when DIG emission is included, ultimately resulting in a significant underestimation of T_2^{HII} from global galaxy

spectra at all metallicities.

We fit ΔT_3 and ΔT_2 as a function of T_3^{gal} and T_2^{gal}, respectively, using a fourth-order polynomial:

$$\Delta T_e = c_0 + c_1 y + c_2 y^2 + c_3 y^3 + c_4 y^4, \tag{5.26}$$

where T_e is T_3 or T_2, and $y = T_3^{gal}/10^4$ K or $T_2^{gal}/10^4$ K. The best-fit coefficients are presented in Table 5.1.

5.4.3 Biases in direct-method metallicity measurements

We use the same method employed above to characterize the bias in the direct-method oxygen abundance as inferred from global galaxy spectra. Since it is common for only one auroral line to be measured in a galaxy spectrum, we evaluate the bias in metallicity for the cases where (1) both T_3^{gal} and T_2^{gal} are measured directly from the galaxy spectrum, (2) only T_3^{gal} is measured and T_2^{gal} is inferred from the T_2-T_3 relation of equation 5.12, and (3) only T_2^{gal} is measured and T_3^{gal} is inferred from the T_2-T_3 relation of equation 5.12. The bias in global direct-method metallicity, $\Delta\log(O/H)$, as a function of direct-method metallicity inferred from global galaxy spectra is presented in Figure 5.17 for each of these three cases. The bias is always calculated with respect to the median direct-method metallicity of the individual H II region distribution in each mock galaxy. Having determined the biases in both strong-line ratios and electron temperatures, we can elucidate the origin of direct-method oxygen abundance biases. Once again, we separately report the results from the *hiionly* and *SDSSstack* models to understand the additional effects that DIG contamination introduces.

The formulae for the calculation of the ionic abundances O^+/H and O^{++}/H (equations 5.13 and 5.14) are functions of both the strong-line ratio of each ion (O2 or O3) and the corresponding ionic electron temperature (T_2 or T_3). O^+/H has a linear dependence on O2 and O^{++}/H has a linear dependence on O3 such that a bias in either of these strong-line ratios will result in an equivalent bias in the corresponding ionic abundance. We plot the temperature dependence of the ionic abundance formulae at fixed strong-line ratio for a range of T_3 and T_2 in Figure 5.18. At high temperature (low metallicity) the temperature

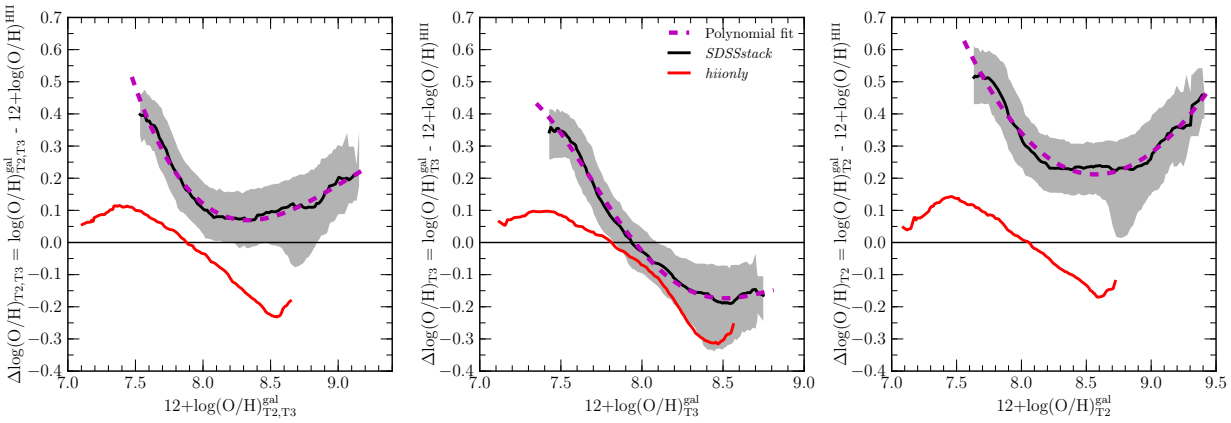

Figure 5.17: The difference between the global galaxy direct-method metallicity, inferred from the observed galaxy spectrum, and the median metallicity of the H II region distribution. We show the bias in global galaxy metallicity for three cases: both T_3 and T_2 are measured from the galaxy spectrum (left panel); only T_3 is measured directly and T_2 is estimated using the T_2-T_3 relation of equation 5.12 (middle panel); and only T_2 is measured directly and T_3 is estimated using equation 5.12 (right panel). Lines and shading are the same as in Figure 5.15. The best-fit fourth-order polynomial coefficients are presented in Table 5.1.

dependence is weak such that even a large bias in electron temperature does not significantly bias the ionic abundance. The temperature dependence is strong at low temperature (high metallicity) such that even a moderate bias of $\pm$500 K can change the ionic abundance by $\sim$ 0.2 dex. How much the bias in a particular ionic abundance affects the total oxygen abundance depends on the relative population of oxygen in O^+ and O^{++}, which is a function of metallicity.

We first focus on the case where both T_3^{gal} and T_2^{gal} are measured directly from the galaxy spectrum. In the low-metallicity limit ($12+\log(O/H)^{gal}_{T2,T3} \lesssim 8.0$), most of the oxygen is in O^{++} such that changes in O^+/H will have a negligible effect on the total oxygen abundance. The global metallicity bias is thus dominated by biases in $O3^{gal}$ and T_3^{gal} in this regime. At low metallicity (high $O3N2^{gal}$), $O3^{gal}$ is biased high by $< +0.05$ dex in the *hiionly* model, contributing only a small amount to $\Delta\log(O/H)_{T2,T3}$. T_3^{gal} is biased $\sim$ 500 K low at low metallicity in the *hiionly* model. When combined, these two effects lead to a bias in the direct-method metallicity of +0.1 dex in the low-metallicity limit from combinations H II regions alone. The *SDSSstack* model has a positive T_3^{gal} bias that increases sharply at the low-metallicity extreme. While higher T_3^{gal} will bias the global metallicity low, the

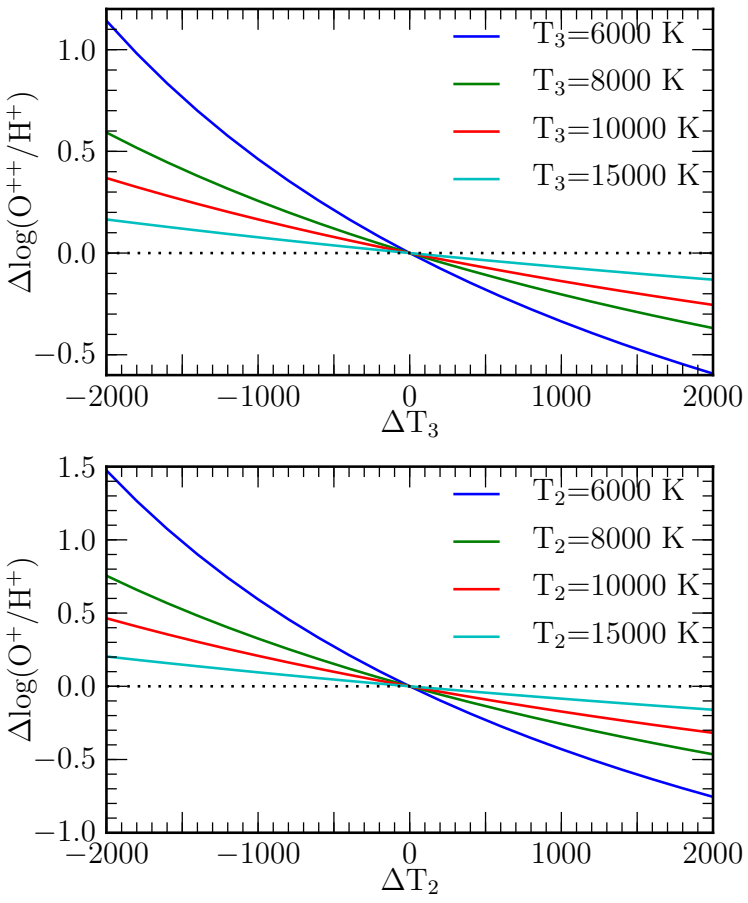

Figure 5.18: Temperature dependence of the ionic oxygen abundances at fixed strong-line ratio. The top panel displays the change in O^{++}/H^{+} with changes in T_3 according to equation 5.14 for a range of T_3 as indicated by the solid lines where color corresponds to the T_3 value. The bottom panel shows the same relationship for O^{+}/H^{+} and T_2 according to equation 5.13. In each panel, the dotted line indicates zero change in the ionic abundance.

temperature dependence of direct-method metallicity is weakest at high temperature. The metallicity bias for the *SDSSstack* model at low metallicity is instead dominated by the positive bias in $O3^{gal}$, which reaches +0.3 dex in the low-metallicity limit. The strong-line bias leads to an overestimate of galaxy direct-method metallicity that grows from +0.1 dex at $12+\log(O/H)^{gal}_{T2,T3} = 8.0$ to +0.4 dex at $12+\log(O/H)^{gal}_{T2,T3} = 7.6$.

In the high-metallicity limit ($12+\log(O/H)^{gal}_{T2,T3} \gtrsim 8.5$), O^+ is the most numerous ionic form of oxygen and biases in $O3^{gal}$ and T_3^{gal} will be subdominant drivers of $\Delta\log(O/H)_{T2,T3}$. In the *hiionly* model, $O2^{gal}$ is relatively unbiased at all metallicities while T_2^{gal} is biased high by ~ 250 K at $T_2^{gal} \sim 7500$ K (high metallicity). While the T_2^{gal} bias is not large, the direct-method metallicity is highly sensitive to temperature changes at low temperature, such that a bias of only ~ 250 K in T_2 leads to a bias in the direct-method metallicity of -0.2 dex. When DIG emission is included in the *SDSSstack* model, $O2^{gal}$ is biased high and T_2^{gal} is biased low, $\Delta\log(O/H)_{T2,T3}$ to +0.2 dex at $12+\log(O/H)^{gal}_{T2,T3} = 9.0$. Including DIG emission leads to significantly different behavior of $\Delta\log(O/H)$ from the case where emission from H II regions alone is considered. Because DIG exhibits higher low-ionization line ratios and lower T_2 than H II regions, DIG contamination in global galaxy spectra leads to an overestimate of $12+\log(O/H)^{HII}$, the median metallicity of the H II region population.

The cases where only one ionic temperature is measured directly can be understood as modulations of the case where both T_2^{gal} and T_3^{gal} are known. Biases from strong-line ratios will remain the same, while the bias arising from the unknown temperature will differ. We note that the *hiionly* bias shows little change when only one ionic temperature is known. This consistency occurs because H II regions closely follow the the T_2-T_3 relation of equation 5.12 from which the unknown temperature is inferred.

The case where only T_3^{gal} is measured from the galaxy spectrum is shown in the middle panel of Figure 5.17. In this case, T_2^{gal} is estimated using the T_2-T_3 relation of equation 5.12. While H II regions follow this relation, ionic temperature measurements from global galaxy spectra show that galaxies do not, instead having lower T_2 at fixed T_3 than H II regions. Assuming that galaxies follow the same ionic temperature relation as H II regions is a common assumption in the literature (e.g., Izotov et al., 2006; Berg et al., 2012; Jones et al., 2015). For

the *SDSSstack* model, this assumption leads to an overestimate of T_2^{gal} by $1,000 - 1,500$ K when inferred using equation 5.12. This discrepancy has little effect at low metallicity where O^+ is negligible, but leads to a negative bias in oxygen abundance of -0.15 dex at $12+\log(O/H)_{T3}^{gal} = 8.4 - 8.7$.

The right panel of Figure 5.17 shows the case where only T_2^{gal} is measured directly from the galaxy spectrum. While this case is less common in the literature for individual galaxies than the case where only [O III]λ4363 is detected, stacked spectra of high-metallicity galaxies often only yield [O II]$\lambda\lambda$7320,7330 detections (Liang et al., 2007; Andrews & Martini, 2013; Brown et al., 2016; Curti et al., 2017). In this case, T_3^{gal} is underestimated by $\sim 2,000$ K at all values of $T_2^{gal}$when T_3^{gal} is inferred from the T_2-T_3 relation of equation 5.12. This incorrect T_3^{gal} value leads to a large $\Delta\log(O/H)_{T2}$ value of +0.3 to +0.5 dex at $12+\log(O/H)_{T2}^{gal} < 8.0$ for the *SDSSstack* model. Overesimating T_3^{gal} by $2,000$ K leads to an overestimate of O^{++}/H by $\sim +0.6$ dex because of the temperature dependence of O^{++}/H at low T_3, as shown for T_3=6,000 K in the top panel of Figure 5.18. While O^{++} is not the main form of oxygen in this high-metallicity, low-temperature regime, the $\sim +0.6$ dex overestimate of O^{++}/H causes O^{++}/H to contribute strongly enough to affect the total oxygen abundance. Thus, the global bias in direct-method metallicity is higher at all metallicities when T_2^{gal} is known and T_3^{gal} is inferred from an H II region T_2-T_3 relation than when both T_2^{gal} and T_3^{gal} are measured directly. The *SDSSstack* model predicts that the additional bias when only T_2^{gal} is known compared to the case when both T_2^{gal} and T_3^{gal} are measured is ~ 0.15 dex and is nearly constant with metallicity. This value is in excellent agreement with the observation of Andrews & Martini (2013) that the metallicities of their M_*-binned stacks were 0.18 dex higher on average if the metallicity was calculated using T_2^{gal} alone instead of both T_2^{gal} and T_3^{gal}(see their Figure 6). We note that if a T_2-T_3 relation fit to galaxy stacks instead of H II regions was used to infer the unknown ionic temperature, then the bias when only one temperature is measured would closely match the bias shown in the left panel of Figure 5.17 where both ionic temperatures are known. The differences between the three panels arise solely because galaxies do not fall on the H II region T_2-T_3 relation.

We fit the direct-method metallicity bias in each of the three ionic temperature cases

with a fourth-order polynomial:

$$\Delta\log(\mathrm{O/H}) = c_0 + c_1 z + c_2 z^2 + c_3 z^3 + c_4 z^4, \tag{5.27}$$

where $z = 12+\log(\mathrm{O/H})^{\mathrm{gal}} - 8$ for the appropriate electron temperature case (T_2 and T_3, T_2 only, or T_3 only). The best-fit coefficients are presented in Table 5.1. These functions may be used to correct direct-method metallicities of galaxies with measured auroral lines in order to obtain a metallicity measurement that is characteristic of the H II region population.

5.4.4 Corrections for individual galaxies or unrepresentative samples

We have presented best-fit polynomials that allow for the correction of strong-line ratios, electron temperatures, and direct-method oxygen abundances obtained from global galaxy spectra to values that are representative of the distribution of H II regions in each galaxy. These corrections are based on a model that is matched to the typical $z \sim 0$ star-forming population as represented by stacks of SDSS galaxies from AM13, B16, and C17. The best-fit polynomials presented above thus provide robust corrections for samples of galaxies that are also representative of the typical local star-forming population, that is, having f_{DIG}=0.55 on average. It may be of interest, however, to correct the line ratios, temperatures, and oxygen abundances of individual galaxies that do not fall on the mean relations, or to provide corrections for an unrepresentative sample of galaxies, as would be necessary for galaxies that do not follow the mean M_*-SFR relation when investigating the SFR dependence of the MZR. We provide a recipe for correcting individual galaxies or unrepresentative samples for which f_{DIG}=0.55 is not appropriate in Appendix 5.A.1.

5.5 Application to the $z \sim 0$ MZR and FMR

In this section, we show examples of how the biases determined from our model framework can be used to correct local metallicity scaling relations, removing the effects of flux-weighting and DIG contamination. We apply corrections to the $z \sim 0$ direct-method MZR and FMR,

and investigate the effects of strong-line ratio biases on the MZR when using strong-line metallicity calibrations. We additionally demonstrate how the expected decrease in $f_{\rm DIG}$ with increasing SFR can explain the observed trends in strong-line ratio at fixed direct-method metallicity from Brown et al. (2016) and Cowie et al. (2016).

5.5.1 The $z \sim 0$ direct-method MZR

We investigate the effects of the biases in direct-method galaxy metallicity presented in Section 5.4.3 on measurements of the local MZR. Using measurements from composite spectra of local star-forming galaxies in bins of M_*, AM13 presented the local MZR over three orders of magnitude in M_* and an order of magnitude in 12+log(O/H). The increase in sensitivity from stacking enabled AM13 to probe an order of magnitude lower in M_* ($\log(M_*/{\rm M}_\odot) = 7.5$) than most previous MZR studies based on strong-line metallicities (e.g., Tremonti et al., 2004), and measure direct-method metallicities representative of galaxies with such a wide dynamic range in properties for the first time.

The direct-method MZR from AM13 stacks is presented in the top panel of Figure 5.19. We show both the MZR using direct-method metallicities as inferred from the stacked spectra without correcting for any biases (gray points) and the galaxy metallicities after correcting for the biases presented in Section 5.4.3 (green points). The original AM13 metallicities were recalculated using our methodology, which includes updated atomic data. Accordingly, our AM13 metallicities prior to correction are systematically shifted with respect to those reported in AM13, yielding $\sim$ 0.1 dex higher metallicities in the highest mass bins, and slightly lower metallicities in the lowest mass bins. We followed the methodology of AM13 to estimate 12+log(O/H) for those high-mass stacks that do not have clean detections of [O III]λ4363 by adjusting the metallicity as calculated using T_2 only by an amount equal to the median difference between $12+\log({\rm O/H})_{\rm T2,T3}$ and $12+\log({\rm O/H})_{\rm T2}$ (see their Section 3.2 and Figure 6). We find this median offset to be -0.24 dex, slightly larger in magnitude than the offset of -0.18 dex reported in AM13 owing to the different atomic data and ionic abundance determinations used here. The values of $12+\log({\rm O/H})_{\rm T2}$ prior this offset

adjustment for stacks with T_2 only are shown as unfilled gray squares. Correcting the stacks with no T_3 measurement yields an uncorrected MZR that shows no obvious break at the point where [O III]λ4363 is no longer cleanly detected.

Corrected direct-method metallicites are obtained by applying the best-fit corrections shown in Figure 5.17. Stacks with measurements of both [O III]λ4363 and [O II]$\lambda\lambda$7320,7330 are corrected using the $12+\log(O/H)_{T2,T3}$ fit, while stacks with only [O II]$\lambda\lambda$7320,7330 are corrected by applying the $12+\log(O/H)_{T2}$ fit to the uncorrected $12+\log(O/H)_{T2}$ prior to the offset adjustment. Our models naturally account for the offset in metallicity when only T_2 is measured without the need for an ad hoc adjustment to the normalization as in AM13. It is important to note that the range of uncorrected galaxy metallicities ($12+\log(O/H)^{gal}_{T2,T3} = 7.8-8.7$; $12+\log(O/H)^{gal}_{T2} = 8.9-9.1$) fall within the range of the models and do not fall close to the lowest or highest model galaxy metallicities where extrapolations are heavily relied upon. Thus, our choice of extrapolations does not strongly impact our results. The bottom panel of Figure 5.19 shows the difference between the uncorrected and corrected AM13 metallicities, where the original uncorrected AM13 metallicites have been recalculated with our updated atomic data.

We fit the uncorrected and corrected direct-method MZRs with the asymptotic logarithmic formula of Moustakas et al. (2011), also used by AM13:

$$12+\log(O/H) = 12+\log(O/H)_{asm} - \log\left[1+\left(\frac{M_{TO}}{M_*}\right)^{\gamma}\right]. \quad (5.28)$$

This function is a power law of slope γ at low stellar masses, and approaches the asymptotic metallicity $12+\log(O/H)_{asm}$ at high stellar masses, where the turnover mass M_{TO} controls the transition point between the two behaviors. The best-fit values for the uncorrected AM13 direct-method MZR are $[12+\log(O/H)_{asm}, M_{TO}, \gamma] = [8.87 \pm 0.03, 8.99 \pm 0.09, 0.67 \pm 0.02]$ (compare to [8.80, 8.90, 0.64] in AM13), and the fit is shown as a gray line in Figure 5.19. The best fit to the corrected AM13 direct-method MZR is shown as a green line, with best-fit parameters $[12+\log(O/H)_{asm}, M_{TO}, \gamma] = [8.80 \pm 0.02, 8.98 \pm 0.08, 0.75 \pm 0.03]$.

We find lower corrected metallicities at all stellar masses compared to the uncorrected

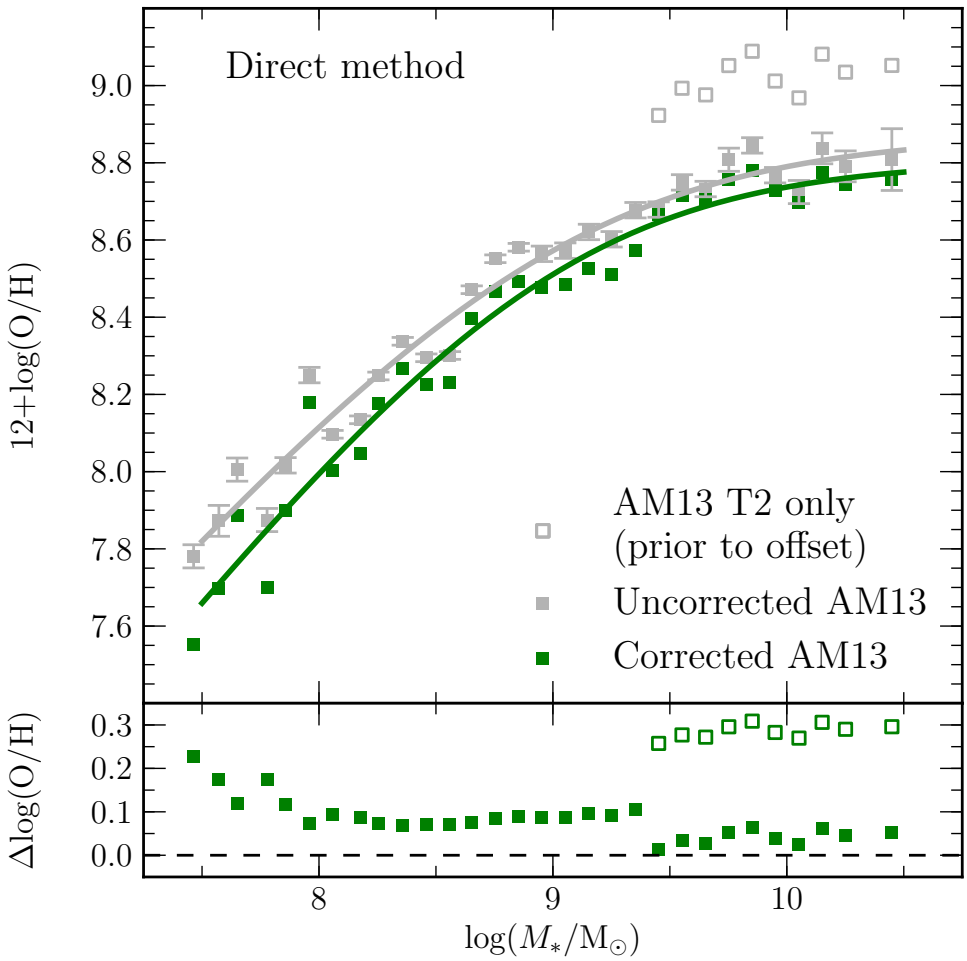

Figure 5.19: TOP: The direct-method MZR for stacks of SDSS star-forming galaxies in bins of M_* from AM13. Filled gray squares use uncorrected AM13 metallicities recalculated using updated atomic data, while filled green squares show the metallicities after correcting for the effects of flux-weighting and DIG emission. Error bars on the uncorrected points only include measurement uncertainties, and would thus be identical for the corrected points. Hollow gray squares present $12+\log(\mathrm{O/H})_{\mathrm{T2}}$ for stacks with only T_2 estimates, prior to offsetting to account for the difference between $12+\log(\mathrm{O/H})_{\mathrm{T2}}$ and $12+\log(\mathrm{O/H})_{\mathrm{T2,T3}}$. The gray and green lines show the best-fit MZR function of Moustakas et al. (2011) (equation 5.28) using uncorrected and corrected metallicities, respectively. The corrected MZR displays a lower normalization and steeper low-mass slope than before correction. BOTTOM: The difference between uncorrected and corrected metallicities as a function of M_*. Hollow points present $\Delta\log(\mathrm{O/H})$ between uncorrected $12+\log(\mathrm{O/H})_{\mathrm{T2}}$ prior to applying the offset and the corrected metallicity. The corrections produced by our models naturally account for the offset between $12+\log(\mathrm{O/H})_{\mathrm{T2}}$ and $12+\log(\mathrm{O/H})_{\mathrm{T2,T3}}$.

metallicites (reflected in the 0.07 dex lower $12+\log(\mathrm{O/H})_{\mathrm{asm}}$), with the lowest-mass bins displaying the largest shift. This trend results in a steeper low-mass slope of 0.75 after correcting for the effects of flux-weighting and DIG contamination, compared to a slope of 0.67 for the uncorrected AM13 MZR. Accurately determining the low-mass slope of the MZR is of primary importance since it is set by the scaling of outflow efficiency with stellar mass, as parameterized by the mass loading factor defined as the ratio of outflow rate and SFR, which in turn reflects the nature of galactic winds (Finlator & Davé, 2008). In particular, energy-driven galactic winds predict a steeper low-mass slope than momentum-driven winds (Peeples & Shankar, 2011). The turnover mass identifies the stellar mass at which galactic winds become inefficient and unable to remove sufficient material in large-scale outflows, and is unaffected by our corrections. In summary, correcting for flux-weighting and DIG contamination results in a lower normalization and steeper low-mass slope of the $z \sim 0$ direct-method MZR, and these changes have a significance of $\sim 2\sigma$.

5.5.2 Strong-line MZR at $z \sim 0$

The direct-method MZR provides a robust measurement of the shape of the $z \sim 0$ MZR since it is constructed using a reliable metallicity determination that can be applied to a large number of galaxies through the stacking process. Nevertheless, we investigate the effects of biases in global galaxy line ratios on the MZR as determined using strong-line metallicity calibrations. Such calibrations have been widely applied in the local universe, and strong-line calibrations are currently the only method available to determine gas-phase metallicities of high-redshift galaxies due to the difficulty of detecting faint auroral lines at cosmological distances. Whenever investigating redshift evolution of the MZR, it is crucial that all samples being compared at least have metallicities determined using the same calibration to eliminate known systematic differences between various strong-line calibrations (Kewley & Ellison, 2008). Correcting strong-line MZRs for biases can thus provide more robust determinations of the evolution of the MZR. However, potential evolution of physical conditions of star-forming regions with redshift may ultimately require a reevaluation of strong-line calibrations at high redshift (Steidel et al., 2014; Sanders et al., 2015; Shapley et al., 2015). Even so,

eliminating observational biases from $z \sim 0$ strong-line MZR measurements provides a more robust baseline relative to which metallicity evolution can be inferred.

We analyze the $z \sim 0$ strong-line MZRs using measurements of strong-line ratios from the AM13 stacks. We investigate the effects of global galaxy strong-line ratio biases on the MZR using four widely-applied metallicity calibrations: two empirical calibrations (Pettini & Pagel 2004 N2 and O3N2; PP04N2 and PP04O3N2, respectively) and two theoretical calibrations (Kewley & Dopita 2002 N2O2 and Tremonti et al. 2004 R23; KD02N2O2 and T04R23, respectively). The original AM13 strong-line metallicities are calculated using the dust-corrected line fluxes appropriate to each calibration as reported in AM13. In order to determine the corrected AM13 strong-line metallicities, we first apply corrections to each strong-line indicator based on the best-fit polynomials presented in Figure 5.15 and then estimate strong-line metallicities using each calibration. The individual strong-line ratio biases in Figure 5.15 may be combined to provide a correction to any strong-line metallicity indicator. The uncorrected and corrected strong-line MZRs using each of the four calibrations are presented in the top row of Figure 5.20, while the bias in log(O/H) is shown in the center row, and the bias in the strong-line ratio is presented in the bottom row. The best-fit corrected AM13 direct-method MZR is shown for comparison.

There is a large spread in the normalization of the MZR when using different strong-line calibrations, as first pointed out by Kewley & Ellison (2008). Empirical calibrations based on H II region samples with auroral-line measurements (PP04N2, PP04O3N2) yield metallicities that are ~ 0.3 dex lower than those obtained from theoretical calibrations based on photoionization models (KD02N2O2, T04R23). It is unsurprising that the empirical calibrations produce metallicities that most closely match the direct-method AM13 MZR, since the calibration dataset is dominated by objects with direct-method metallicities. Correcting for flux-weighting and DIG effects does not reduce the offset between empirical and theoretical calibrations, but instead increases the magnitude of the disagreement by shifting the KD02N2O2 and T04R23 MZRs towards higher metallicity at fixed M_*. That the conflict between theoretical and empirical calibrations remains suggests that the disagreement between MZRs based on theoretical and empirical calibrations is not a result of observational

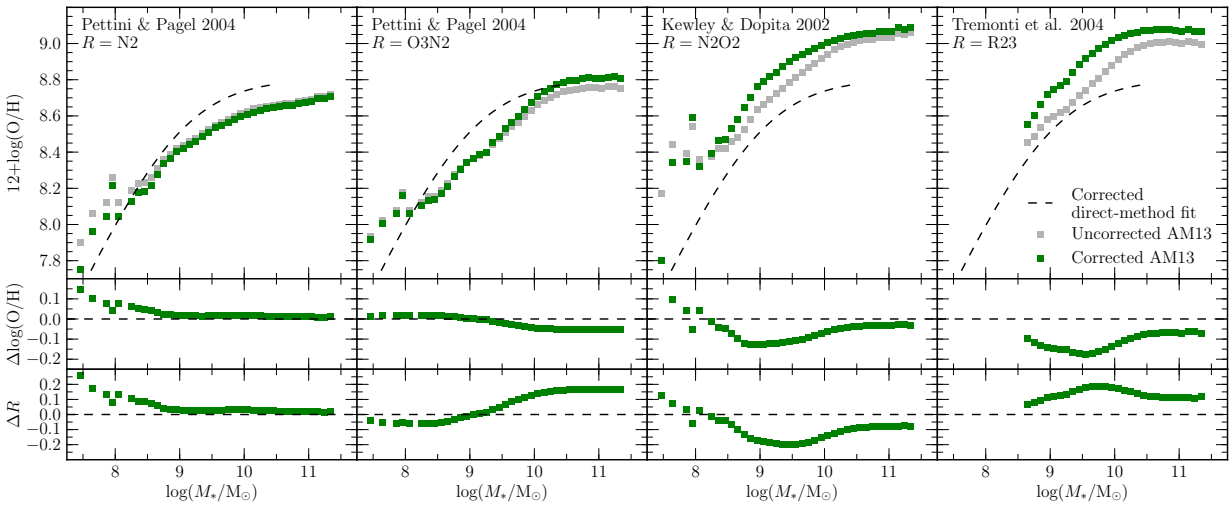

Figure 5.20: The MZR based on strong-line metallicities for the M_* stacks of AM13 is displayed in the top row. We show results for four commonly-used strong-line indicators: the empirical N2 and O3N2 calibrations of Pettini & Pagel (2004), the theoretical N2O2 calibration of Kewley & Dopita (2002), and the theoretical R23 calibration of Tremonti et al. (2004). In each panel, filled gray squares use the uncorrected strong-line ratio to infer the metallicity, while filled green squares utilize the strong-line ratio after correcting for flux-weighting effects and DIG emission. For reference, the corrected direct-method MZR best-fit function from Section 5.5.1 is shown as a dashed black line. The middle row displays the difference Δlog(O/H) between uncorrected and corrected metallicity, while the bottom row presents the difference ΔR between the uncorrected and corrected strong-line ratio. The bias in strong-line metallicity, primarily driven by DIG contamination, can exceed 0.1 dex.

biases in global galaxy spectra. Instead, the problem appears to be a manifestation of a long-standing disagreement in normalization of the metallicity scale between direct-method and theoretical strong-line calibrations observed for extragalactic H II regions (Kennicutt et al., 2003).

It is unclear which method provides a metallicity scale closer to the truth since there are potential systematic issues on both sides. Empirical direct-method calibrations may be biased towards lower metallicities due to the presence of temperature gradients and inhomogeneities within the ionized gas (Stasińska, 2005; Bresolin, 2007), although this problem primarily affects high-metallicity, low-temperature H II regions. Direct-method metallicities may indeed have a normalization bias, but have been shown to tightly correlate with metallicities determined from oxygen recombination lines with a slope of unity (Blanc et al., 2015) and an offset of ~ -0.2 dex. For photoionization models, it is difficult to determine the proper combination of input parameters and physical conditions that produce realistic H II regions because of degeneracies among parameters. Additionally, observed nearby H II regions often have filamentary gas structures and cluster stars distributed throughout the ionized gas (e.g., 30 Dor; Pellegrini et al., 2011), a very different geometry from the ionizing point source and uniform-density sphere or slab of gas utilized in most photoionization codes (Kewley & Dopita, 2002; Gutkin et al., 2016).

All strong-line MZRs display a high-mass flattening, although this is more apparent with some calibrations than others. In general, the turnover mass is higher than that measured with the direct-method. The PP04N2 and PP04O3N2 turnover masses do not change significantly once the galaxy metallicities are corrected for flux-weighting effects and DIG contamination. In contrast, the KD02N2O2 and T04R23 MZRs have turnover masses that are shifted lower when using corrected metallicities, bringing the turnover mass into better agreement with that of the direct-method MZR.

AM13 found that various strong-line calibrations produce MZRs that have low-mass slopes much shallower than that of the direct-method MZR. We also find that all strong-line MZRs using uncorrected metallicities have low-mass slopes close to $\gamma \sim 0.3-0.4$, significantly shallower than the slope of 0.75 for the direct-method MZR. For all strong-line MZRs except

PP04O3N2, correcting for flux-weighting effects and DIG emission yields steeper low-mass slopes. The KD02N2O2 and T04R23 slopes appear to be close to that of the direct-method MZR after correction, relieving some tension between the theoretical strong-line and direct-method MZR shapes.

In summary, after correction for flux-weighting effects and DIG contamination in global galaxy line ratios, theoretical strong-line calibrations appear to match the direct-method MZR low-mass slope and turnover mass, but retain a large offset in normalization. Empirical strong-line calibrations provide a much closer match in normalization, but display higher turnover mass and shallower low-mass slope than those measured with the direct-method. Tensions between empirical and theoeretical strong-line metallicities remain even after correcting for contamination from DIG emission.

5.5.3 The direct-method $z \sim 0$ FMR

The FMR as determined using direct-method metallicities will also be subject to biases from flux-weighting effects and DIG emission. We investigate the effects of flux-weighting and DIG contamination on the FMR using the M_*-SFR stacks of AM13. We recalculate the direct-method metallicities of the AM13 M_*-SFR stacks using the methodology in Section 5.2.3 that includes updated atomic data. In order to reproduce the results of AM13 using new atomic data, we calculate the original metallicities for those stacks with only T_2 measurements by subtracting the median difference between $12+\log(O/H)_{T2}$ and $12+\log(O/H)_{T2,T3}$ from $12+\log(O/H)_{T2}$ for those stacks with measurements of both temperatures in the same SFR bin. This process yields the uncorrected AM13 FMR, shown in the left panel of Figure 5.21 as filled squares color-coded by SFR. The hollow squares show $12+\log(O/H)_{T2}$ for bins with T_2 only prior to the application of the offset.

We correct the AM13 metallicities of each M_*-SFR bin for the effects of flux-weighting and DIG contamination. The strength of the SFR dependence of the MZR may change after correcting for metallicity biases since $f_{\rm DIG}$ decreases as SFR increases at fixed M_*. Because $f_{\rm DIG}$ depends on SFR, we cannot use the *SDSSstack* model with $f_{\rm DIG}$=0.55 to correct the

metallicities in each M_*-SFR bin, but must instead use a different $f_{\rm DIG}$ for each M_*-SFR bin. Accordingly, from the strong-line comparison sample that is selected following AM13, we select the subset of galaxies in a particular M_*-SFR bin and determine the median $f_{\rm DIG}$ using the method outlined in Section 5.3.1. We then produce a model for each M_*-SFR bin with the inferred $f_{\rm DIG}$, while all other input parameters are the same as for the *SDSSstack* model. Using these new models, we fit the metallicity biases using equation 5.27 and apply these new fits to correct the direct-method metallicity of each M_*-SFR bin.

The corrected direct-method FMR for AM13 M_*-SFR stacks is presented in the right panel of Figure 5.21. The difference between the uncorrected and corrected log(O/H) for each bin is presented in the bottom-right panel, where the hollow triangles show Δlog(O/H) between the corrected value and the uncorrected 12+log(O/H)$_{\rm T2}$ before applying the offset. SFR dependence is still clearly present in the corrected direct-method FMR with higher-SFR galaxies having lower metallicities at fixed M_*, in agreement with other observations of the SFR dependence of the local MZR (Mannucci et al., 2010; Lara-López et al., 2010; Andrews & Martini, 2013). However, the SFR dependence is weaker after correcting for biases in the metallicity estimates. At fixed M_*, Δlog(O/H) correlates with SFR such that galaxies with lower SFR have larger positive biases, while galaxies with high SFR have smaller positive or sometimes slight negative biases. This effect weakens the strength of the SFR dependence, occurring because DIG contamination causes galaxies to appear more metal rich when direct-method metallicities are employed due to increased low-ionization line strength and decreased T_2. This bias is strongest in low-SFR galaxies in which DIG emission begins to dominate the line fluxes, leading to large corrections at low-SFR and smaller corrections as SFR increases.

Mannucci et al. (2010) parameterized the SFR dependence with a planar projection using the parameter μ_α that is a linear combination of M_* and SFR:

$$\mu_\alpha = \log(M_*/{\rm M}_\odot) - \alpha \times \log({\rm SFR}/{\rm M}_\odot\ {\rm yr}^{-1}). \tag{5.29}$$

We evaluate the SFR strength of the direct-method FMR based on uncorrected and corrected

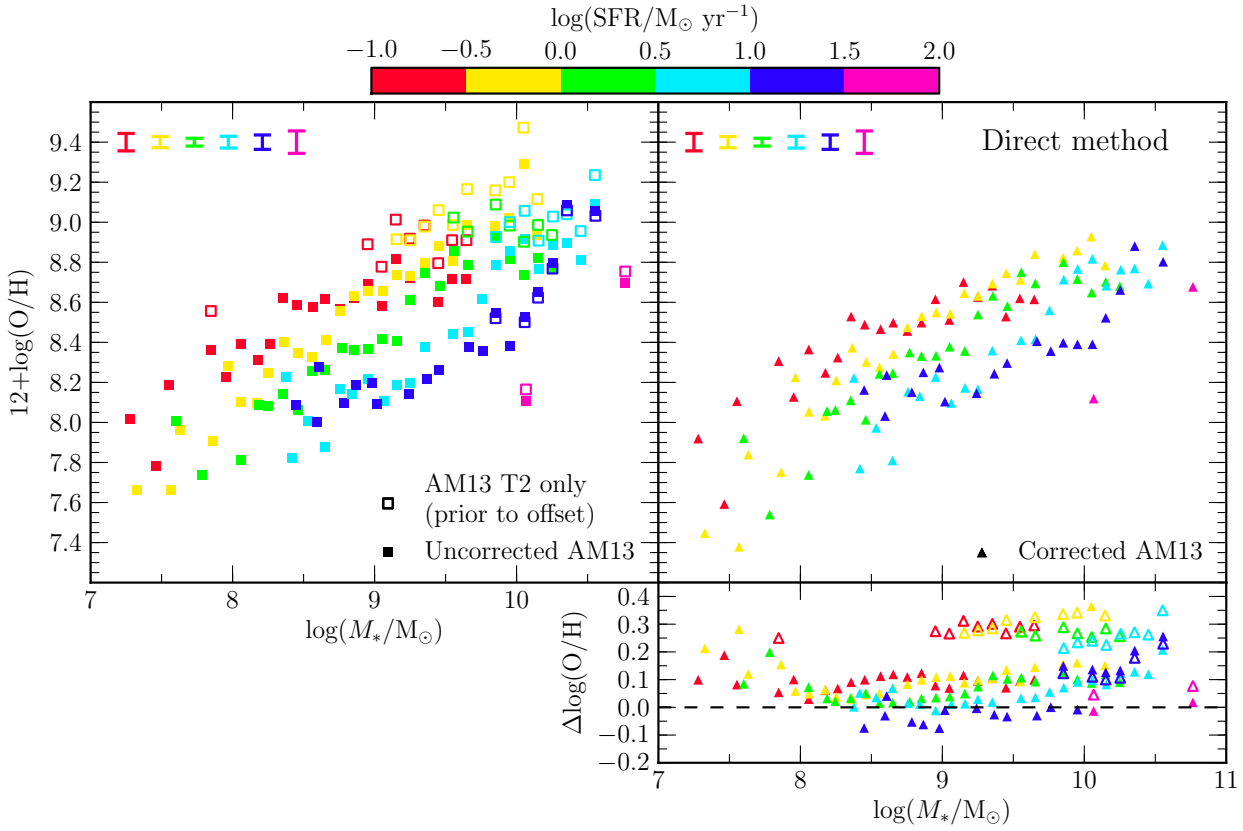

Figure 5.21: The direct-method FMR for M_*-SFR stacks from AM13, color-coded by SFR. Metallicities in the left panel have not been corrected for the effects of flux-weighting or DIG contamination. Filled squares denote points using the uncorrected AM13 metallicities, while hollow squares show 12+log(O/H)$_{\rm T2}$ assuming the T_2-T_3 relation of equation 5.12 for those stacks with T_2 estimates but no T_3 estimates. In the right panel, metallicities have been corrected for flux-weighting effects and DIG contamination. The mean uncertainty in metallicity for each SFR bin is displayed in the upper left corner. Filled triangles in the bottom-right panel show the difference between the uncorrected and corrected direct-method metallicities, where hollow symbols show the difference between uncorrected 12+log(O/H)$_{\rm T2}$ and corrected 12+log(O/H) for those bins with T_2 only. After correction, the SFR dependence in the FMR is weaker since there is a positive correlation between Δlog(O/H) and SFR at most stellar masses.

metallicities by finding the value of α that minimizes the scatter around a linear fit in each case. We find that the uncorrected AM13 metallicities yield $\alpha = 0.70 \pm 0.015$ (compare to $\alpha = 0.66$ reported in AM13), while the SFR dependence is slightly weaker after correcting the metallicities, with $\alpha = 0.63 \pm 0.016$. The best-fit projections of the uncorrected and corrected direct-method FMRs are presented in the top and bottom panels of Figure 5.22. The smaller value of α after correcting the metallicities confirms that DIG contamination leads to an overestimation of the strength of the SFR dependence. However, this small decrease in α does not bring estimates using the direct-method into agreement with those made using strong-line metallicities. Investigations using strong-line indicators find much weaker SFR dependence ranging from $\alpha = 0.19$ (Yates et al., 2012) to $\alpha = 0.32$ (Mannucci et al., 2010).

5.5.4 B16 and Cowie et al. 2016 results are primarily caused by DIG contamination

B16 estimated direct-method metallicites of stacks of SDSS galaxies in bins of M_* and distance from the $z \sim 0$ M_*-SSFR relation (ΔSSFR), and showed that empirical strong-line metallicity calibrations have a systematic dependence on ΔSSFR. In particular, these authors found that galaxies with higher ΔSSFR display systematically higher N2, lower O3N2, and higher N2O2 values at fixed direct-method metallicity. B16 provided new calibrations that include a ΔSSFR term to account for this variation. Cowie et al. (2016) found similar results based on individual $z \sim 0$ SDSS galaxies with auroral-line detections, instead using Hβ luminosity as the secondary parameter. These authors found that, at fixed direct-method metallicity, galaxies with higher Hβ luminosity displayed higher N2, N2O2, and N2S2. Cowie et al. (2016) provided new strong-line calibrations including an additional Hβ luminosity term, and interpreted the trends as an increase in both N/O and ionization parameter as SFR increases. Since SSFR and Hβ luminosity are strongly correlated, it appears that the two studies observed the same phenomenon using different parameterizations.

In Figure 5.23, we show direct-method metallicity as a function of the strong-line ratios

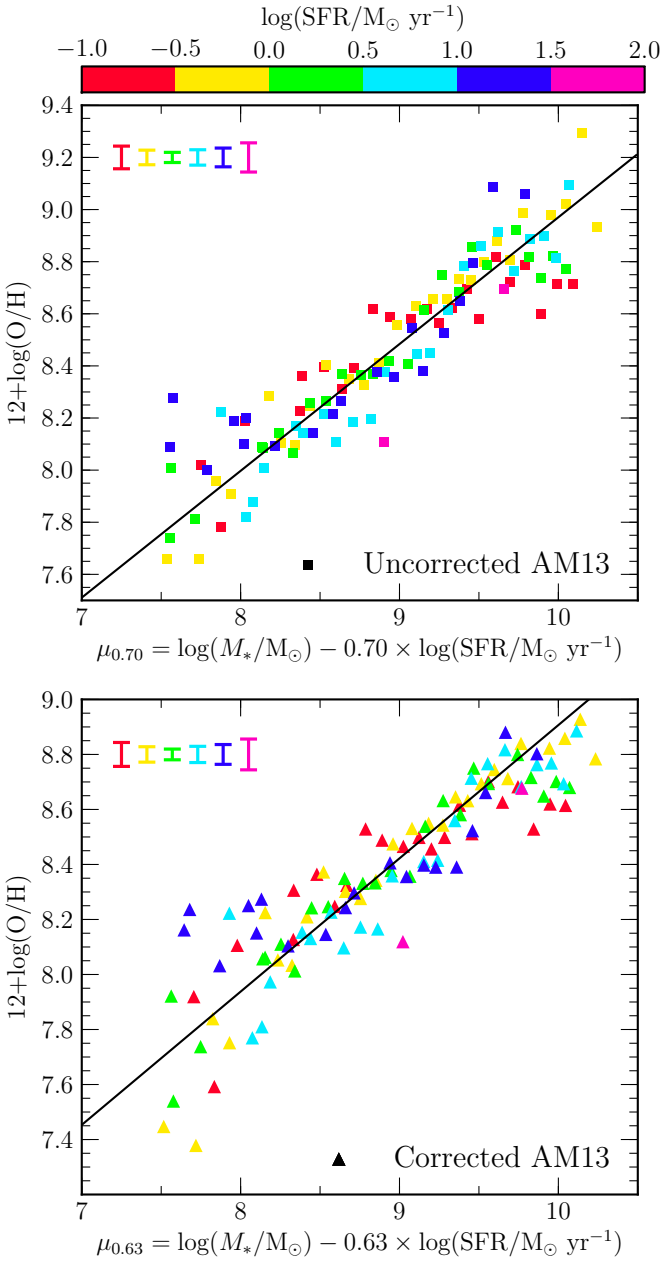

Figure 5.22: The planar projection of the FMR for AM13 M_*-SFR stacks. We use the FMR parameterization of (Mannucci et al., 2010), and show the FMR projection using uncorrected (top) and corrected (bottom) direct-method metallicities. In each panel, the black line shows the best-fit linear relation around which the scatter is minimized for the best-fit value of α. The value of the parameter α that minimizes the scatter around the plane was found to be $\alpha = 0.70 \pm 0.015$ when using uncorrected metallicities and $\alpha = 0.63 \pm 0.016$ after correction. Correcting for flux-weighting effects and DIG contamination slightly decreases the strength of the SFR dependence of the FMR. Error bars in the upper left corner show the mean uncertainty in 12+log(O/H) for each SFR bin.

N2a, O3N2, N2O2, and N2S2. We plot the points from the M_*-ΔSSFR stacks of B16, color-coded by Δlog(SSFR). We recalculate uncorrected B16 direct-method metallicities using our methodology and updated atomic data presented in Section 5.2.3. Following AM13 and B16, we estimate the uncorrected metallicities of stacks for which only T_2 was measured by adjusting 12+log(O/H)$_{T2}$ by the median offset between 12+log(O/H)$_{T2}$ and 12+log(O/H)$_{T2,T3}$ for those stacks with both T_2 and T_3 measurements in the same ΔSSFR bin. There are no stacks in the Δlog(SSFR) $= -0.25$ bin with T_3 estimates, thus the offset for T_2-only metallicities cannot be determined in the same way for this bin. B16 did not apply any offset to the metallicities of stacks in this lowest-ΔSSFR bin, instead adopting the value of 12+log(O/H)$_{T2}$ assuming the T_2-T_3 relation followed by H II regions. To place the metallicities in the Δlog(SSFR) $= -0.25$ bin onto the same scale as those of the other bins, we apply the offset for the closest ΔSSFR bin (Δlog(SSFR) $= 0.25$) to 12+log(O/H)$_{T2}$. This solution is robust because, while the offset increases with decreasing ΔSSFR, the rate of change of the offset size with ΔSSFR decreases with decreasing ΔSSFR. The two bins closest in ΔSSFR to the Δlog(SSFR) $= -0.25$ bin have the smallest difference in offset of only 0.026 dex, so this solution should yield the uncorrected metallicities of the Δlog(SSFR) $= -0.25$ stacks within $\lesssim 0.02$ dex. It is important to note that these metallicities and strong-line ratios are inferred directly from the observed line fluxes of each stack, and have not been corrected for any biases.

We expect $f_{\rm DIG}$ to correlate with ΔSSFR since $\Sigma_{\rm H\alpha}$, from which $f_{\rm DIG}$ is estimated, correlates strongly with SFR and SSFR, but does not show a strong dependence on M_*. It is therefore expected that $f_{\rm DIG}$ will change significantly across samples that vary greatly in SSFR and SFR, as in B16 and Cowie et al. (2016). If $f_{\rm DIG}$ changes significantly between bins of ΔSSFR or Hβ luminosity, then the bias arising from DIG contamination will also vary systematically between such bins. We investigate the connection between DIG emission and the B16 and Cowie et al. (2016) results by determining the median $f_{\rm DIG}$ for subsets of the B16 sample. We begin with the SDSS strong-line comparison sample of individual galaxies that is selected in a nearly identical manner to the samples of AM13 and B16. We divide the full sample into subsamples in 0.5 dex-wide bins of Δlog(SSFR) using the parameterization of the

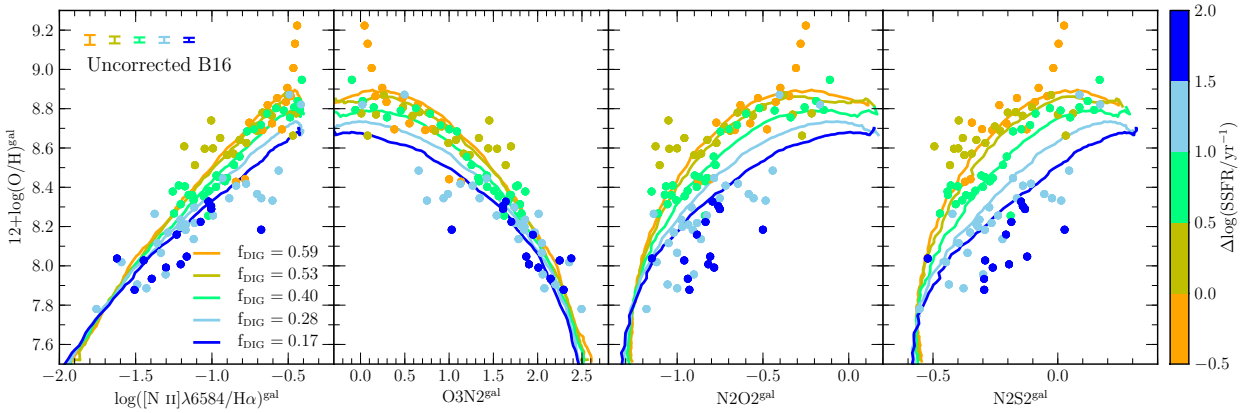

Figure 5.23: Global galaxy direct-method metallicity as a function of observed strong-line ratios for the M_*-ΔSSFR stacks of B16. Filled circles denote data from B16 color-coded by Δlog(SSFR), where the metallicities have been recalculated using updated atomic data. Metallicities and line ratios have not been corrected for flux-weighting effects or DIG contamination. Predicted global galaxy metallicity and uncorrected line ratios from models matched in $f_{\rm DIG}$ to each ΔSSFR bin are shown as solid lines of the corresponding color. Error bars in the upper left corner display the mean uncertainty in 12+log(O/H) for each Δlog(SSFR) bin.

mean $z \sim 0$ M_*-SSFR relation from B16. For each subsample, we determine $\Sigma_{\rm H\alpha}$ and $f_{\rm DIG}$ for the individual galaxies and use the distribution of $f_{\rm DIG}$ values to infer the median $f_{\rm DIG}$ following the methods described in Section 5.3.1. We find the median $f_{\rm DIG}$ for bins centered on $\Delta\log({\rm SSFR/yr}^{-1}) = [-0.25, 0.25, 0.75, 1.25, 1.75]$ to be $f_{\rm DIG}^{\rm med} = [0.59, 0.53, 0.40, 0.28, 0.17]$. We create a set of five models that have all model parameters set to the same values as for the *SDSSstack* model except for $f_{\rm DIG}$, which is set to the $f_{\rm DIG}^{\rm med}$ value for each ΔSSFR bin. In Figure 5.23, we plot the predicted global galaxy strong-line ratios and uncorrected direct-method metallicities for the models matched to each ΔSSFR bin. The values plotted for the models are the predicted observed values as would be inferred from global galaxy spectra before correcting for any biases.

For each line ratio, we find that the predicted global galaxy line ratios and uncorrected metallicites from the models are in excellent agreement with the observations of B16, although the models somewhat underpredict the deviation in N2O2 and N2S2 that is observed in the highest ΔSSFR bins. This disagreement at high ΔSSFR may indicate that the $f_{\rm DIG}$-$\Sigma_{\rm H\alpha}$ relation of equation 5.24 overpredicts $f_{\rm DIG}$ at high $\Sigma_{\rm H\alpha}$ and may require some revision.

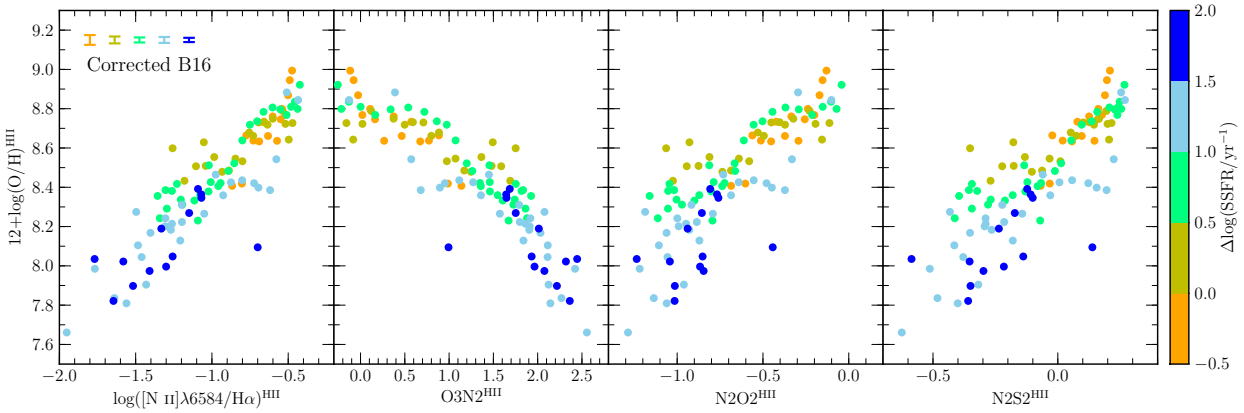

Figure 5.24: Corrected direct-method metallicity as a function of corrected strong-line ratios for the M_*-ΔSSFR stacks of B16. The effects of flux-weighting and DIG emission have been corrected for using the models shown in Figure 5.23. Correcting for DIG contamination reduces the scatter and systematic dependence on Δlog(SSFR) in these relations. Mean uncertainties on the metallicity for each ΔSSFR bin are shown in the upper left corner.

Additionally, lines of constant $f_{\rm DIG}$ in the models match lines of constant ΔSSFR in the B16 stacks. It is therefore plausible that the systematic trends observed in B16 and Cowie et al. (2016) can be explained by variation of $f_{\rm DIG}$ with ΔSSFR and Hβ luminosity. Following Sections 5.4.1 and 5.4.3, we fit the strong-line ratio and direct-method metallicity biases using equations 5.25 and 5.27, respectively, for each of the models matched to the B16 ΔSSFR bins. These best-fit polynomials are then used to correct the strong-line ratios and direct-method metallicites of the points in each B16 ΔSSFR bin for flux-weighting effects and DIG contamination. Figure 5.24 shows the corrected direct-method metallicities as a function of corrected strong-line ratios for the B16 M_*-SSFR stacks. The dependence on ΔSSFR of each strong-line ratio at fixed metallicity has decreased or disappeared once biases in both properties are accounted for. This resolution is most apparent in N2O2 and N2S2, which displayed the strongest ΔSSFR dependence prior to correction because DIG contamination affects O2 and S2 more strongly than O3 or N2.

We conclude that the majority of the systematic offsets as a function of ΔSSFR and Hβ luminosity observed by B16 and Cowie et al. (2016) are a result of the decreasing importance of DIG emission as star formation intensity increases. Offsets in strong-line ratios at fixed direct-method metallicity occur because both the strong-line ratio and the direct-method

metallicity are biased, predominantly due to DIG contamination. The spread in line ratio at fixed metallicity is largest at high metallicities (12+log(O/H) $>$ 8.3), where singly-ionized oxygen is the dominant ionic species, because DIG contamination strongly affects O2, T_2, and, consequently, the O^+/H estimate. After accounting for $f_{\rm DIG}$ variation as a function of ΔSSFR, any remaining systematic offset as a function of ΔSSFR is small and does not require large systematic changes in the physical conditions of the H II region gas to explain. Since the B16 results appear to be equivalent to those of Cowie et al. (2016), a large systematic increase in N/O and ionization parameter with increasing SFR is not needed to explain the shift in strong-line ratios at fixed direct-method metallicity observed by Cowie et al. (2016).

5.5.5 Correcting the Curti et al. (2017) empirical calibrations

C17 recently used stacks of SDSS star-forming galaxies in bins of O3 and O2 to construct a set of fully-empirical strong-line calibrations for a range of commonly applied line ratios using direct-method metallicities. Utilizing a fully-empirical calibration dataset with a large dynamic range in metallicity improves upon past metallicity calibrations based upon galaxy spectra, which required the use of photoionization models at high metallicities where auroral lines are not detected for individual SDSS galaxies (Maiolino et al., 2008). While the C17 calibrations can be used over a wider range of metallicities than any other empirical calibration to date, both the direct-method metallicities and strong-line ratios used in the calibrations are subject to biases from flux-weighting effects and DIG contamination as described in this work. In order to use the C17 calibrations to estimate the characteristic metallicity of the star-forming regions in galaxies by removing DIG contamination or flux-weighted combination effects, we recommend first using the observed uncorrected galaxy line ratios to determine the uncorrected metallicity, then correcting the metallicity inferred from the C17 calibrations using the fit to the bias in $12+\log(O/H)_{T2,T3}$ (left panel of Figure 5.17). The best-fit coefficients are given in Table 5.1. This method will yield robust corrected metallicities that are representative of the distribution of H II region metallicities galaxies.

5.6 Implications for high-redshift studies

The MZR is known to evolve with redshift such that galaxies have lower metallicities at fixed stellar mass as redshift increases (e.g., Erb et al., 2006; Maiolino et al., 2008; Steidel et al., 2014; Troncoso et al., 2014; Sanders et al., 2015; Onodera et al., 2016). High-redshift metallicity studies have relied nearly uniformly on strong-line calibrations to estimate metallicity because of the difficulty of detecting faint auroral lines at $z > 1$. We have shown how contamination from DIG emission can affect strong-line ratios and thus impact strong-line metallicity estimates. Correcting for these biases can lead to significant changes in the inferred shape of the local MZR. It is of interest to consider what effects DIG contamination might have on the interpretation of high-redshift strong-line ratios.

High redshift galaxies have both smaller size (van der Wel et al., 2014) and higher SFR (Whitaker et al., 2014; Shivaei et al., 2015) at fixed M_*than $z \sim 0$ galaxies on average. Thus, typical $\Sigma_{\mathrm{H}\alpha}$ values are much higher at high redshift than for local galaxies, with typical $z \sim 2$ galaxies having $\Sigma_{\mathrm{H}\alpha}$ as high as local starburst galaxies. If the relationship between $\Sigma_{\mathrm{H}\alpha}$ and f_{DIG} in equation 5.24 holds in the same form at high redshifts, then DIG emission should only account for a small fraction ($\sim 0 - 20\%$) of line emission in high-redshift star-forming galaxies. Based on the observations and simple model of Oey et al. (2007), we expect that DIG emission becomes increasingly less important with increasing redshift. Accordingly, correction of high-redshift galaxy line ratios should be performed using models that have f_{DIG}=0, such as the *hiionly* model. Additionally, the high SSFR of high-redshift galaxies and accompanying strong feedback may efficiently mix metals into the ISM such that the width of the H II region metallicity distribution is small. Such a scenario can explain the flat metallicity gradients observed in some high-redshift galaxies (Jones et al., 2013; Leethochawalit et al., 2016; Wang et al., 2017; Ma et al., 2017), and is similar to the inferred reason behind flatter gradients in lower mass local galaxies (Ho et al., 2015). If efficient metal distribution is a common feature at high redshift, then an appropriate model should also have smaller σ_{T} than the *SDSSstack* model.

If DIG emission is negligible at high redshift, it carries implications for the interpretation

of the evolution of strong-line ratios. Galaxies at $z \sim 1-2$ display systematically different emission-line ratios from those typically observed in local galaxies, including an offset towards higher [O III]/Hβ and/or [N II]/Hα in the O3N2 diagram (Shapley et al., 2005; Liu et al., 2008; Kewley et al., 2013b; Steidel et al., 2014; Shapley et al., 2015) and higher O3 and [O III]/[O II] values at fixed M_* than those observed in the local universe (Nakajima & Ouchi, 2014; Onodera et al., 2016; Sanders et al., 2016b). Such evolution in galaxy strong-line ratios may imply that local strong-line metallicity calibrations do not produce reliable metallicity estimates for high-redshift galaxies. By comparing the positions of high-redshift galaxies to those of local galaxies in diagnostic emission line diagrams, such evolution in strong-line ratios has been explained with evolving physical conditions of the ionized gas in H II regions, including gas density, ionization parameter, N/O abundance ratio, and shape of the ionizing spectrum. These interpretations have assumed that all of the emission line flux from both $z \sim 0$ and high-redshift galaxies originates from H II regions. If DIG emission is negligible in high-redshift star-forming galaxies, then the amount of inferred evolution in gas physical conditions such as the ionization parameter or hardness of the ionizing spectrum is likely overestimated because DIG emission tends to shift $z \sim 0$ global galaxy line ratios towards lower-excitation states compared to their constituent H II regions. It would then be more appropriate to compare high-redshift strong-line ratios to those of individual H II regions instead of SDSS global galaxy spectra, or else first correct SDSS line ratios using the best-fit functions in Figure 5.15 before inferring evolution of H II region physical conditions. Such corrections are most important in line-ratio spaces that are significantly affected by DIG emission, such as the O3S2 and [O III]/[O II] vs. M_* diagrams. Evolution in some ionized gas physical properties is still clearly required because DIG contamination (or lack thereof) cannot drive an offset in the O3N2 diagram (see Figure 5.4) for example.

Revealing the true DIG contribution to global galaxy line fluxes in high-redshift galaxies requires high-spatial-resolution emission-line maps to disentangle H II and DIG regions and determine their relative importance. The SDSS-IV MaNGA IFU survey has shown that line ratio maps from such a dataset can efficiently identify H II and DIG regions based on systematic changes in strong-line ratios as a function of Hα surface brightness (Zhang et al.,

2017). Similar high-redshift datasets should be able to identify significant DIG emission if the spatial resolution is sufficient to begin to resolve H II regions ($\lesssim$ 1 kpc). Such maps have been obtained for a small number of gravitationally-lensed objects (e.g., Jones et al., 2010; Yuan et al., 2011; Leethochawalit et al., 2016), but understanding the typical DIG contribution at high redshift necessitates larger samples spanning a wide range of galaxy properties. Confirming the nature of DIG emission at high-redshift is crucial for properly interpreting the evolution in galaxy strong-line ratios.

5.7 Summary and conclusions

We have presented a set of empirically-motivated models that treat galaxies as a collection of multiple line-emitting regions with different physical properties. In addition to line emission from classical H II regions, these models incorporate DIG emission based on observed DIG strong-line ratio excitation sequences for the first time. We present the first measurement of DIG region excitation sequences over a range of excitation levels using data from the SDSS-IV MaNGA IFU survey (Zhang et al., 2017). Our model framework tracks contributions from DIG and H II regions to both strong and auroral optical emission lines. Previous models of galaxy line emission have treated galaxies as single H II regions with effective physical properties. Such descriptions of galaxy line emission are not sufficient to simultaneously match strong and auroral emission line properties in all line-ratio diagrams simulaneously. Including multiple H II regions with a range of excitation levels is required to reproduce the offset of global galaxy spectra in the T_2-T_3 diagram (Figures 5.11 and 5.14; Pilyugin et al., 2010, 2012a; Andrews & Martini, 2013). Furthermore, inclusion of DIG emission is necessary to properly reproduce galaxy excitation sequences in strong-line ratio diagrams, as evidenced by the distinct excitation sequences of H II regions, SDSS galaxies, and DIG regions in the O3N2, O3S2, and O3O2 diagrams (Figure 5.4).

We constructed the *SDSSstack* model in which DIG emission contributes 55% of the total Balmer emission, which provides a good description of typical $z \sim 0$ star-forming galaxies as represented by stacks of SDSS galaxies from Andrews & Martini (2013), Brown et al.

(2016), and Curti et al. (2017). We find that the ionic temperature T_2 of DIG regions must be $\sim 15\%$ lower than T_2 of H II regions at fixed metallicity to match the strong-line ratios of SDSS stacks at fixed T_2. This result may indicate that DIG region electron temperature systematically deviates from the electron temperature of associated H II regions, but may also represent a systematic effect in the process of combining line emission from multiple regions to form a global galaxy spectrum. Observations of auroral lines from DIG regions are needed to investigate this effect. When following this assumption about DIG T_2, the *SDSSstack* model is in excellent agreement with SDSS stacks simultaneously in diagrams involving strong-line ratios, electron temperatures, and direct-method oxygen abundances.

We used the *SDSSstack* model to characterize biases in strong-line ratios, electron temperatures, and direct-method oxygen abundances as inferred from global galaxy spectra. Contamination of the global galaxy spectrum by DIG emission is the primary driver of biases in the *SDSSstack* model. DIG contamination tends to inflate the strength of low-ionization lines and lower the ionic temperature T_2, making global galaxy spectra appear more metal-rich than is true of the metallicity distribution of star-forming regions within each galaxy. We quantified biases in these properties as the difference between the value inferred from a global galaxy spectrum and the median value of the H II region distribution of that property within each galaxy. We provided polynomial fits to the bias in each property (Table 5.1) that can be subtracted from global galaxy values to correct for the effects of flux-weighting and DIG contamination. The corrections presented in Section 5.4 are appropriate for samples of galaxies that are representative of the local star-forming population. A recipe for correcting individual galaxies or unrepresentative samples is given in Appendix 5.A.1 in which the *SDSSstack* model is generalized to have any value of $f_{\rm DIG}$.

We applied these corrections to investigate observational biases in the $z \sim 0$ MZR and FMR. Nearly all metallicity calibrations are based on H II regions, including the direct-method and both empirical and theoretical strong-line metallicity calibrations. It is thus imperative that emission-line ratios of global galaxy spectra are corrected to be representative of the underlying H II region distribution before using calibrations based on H II regions to estimate metallicity. After correcting for flux-weighting effects and DIG contamination,

we found that the $z \sim 0$ direct-method MZR has ~ 0.1 dex lower normalization and a slightly steeper low-mass slope ($\gamma = 0.75$) compared to the uncorrected MZR ($\gamma = 0.67$). These changes in the MZR shape have a significance of 2σ. The direct-method FMR displays slightly weaker SFR dependence after correction since DIG tends to make low-SFR galaxies appear more metal-rich, artificially strengthening the trend with SFR. We also investigated the effects of DIG contamination and flux-weighting on the local MZR as determined using multiple strong-line calibrations. DIG contamination can substantially affect the inferred shape of the MZR, flattening the low-mass slope and changing the normalization of theoretical calibrations in particular. Future studies of metallicity scaling relations can use the corrections given in this work to obtain robust galaxy metallicity estimates that are placed on a scale that can be compared directly to gas-phase metallicities reported by chemical evolution models.

We showed that the systematic trends in strong-line ratios at fixed direct-method metallicity with SSFR and Hβ luminosity observed by Brown et al. (2016) and Cowie et al. (2016) can be explained almost entirely by a decreasing $f_{\rm DIG}$ with increasing SSFR. The importance of DIG is naturally expected to decrease with increasing star-formation intensity as classical H II regions occupy a larger volume of the ionized ISM and dominated line emission (Oey et al., 2007). This result demonstrates the importance in correcting for DIG contamination before inferring correlations of H II region physical properties with galaxy properties.

Our results have implications for the inferred evolution of H II region physical properties with redshift. If the trend between $f_{\rm DIG}$ and $\Sigma_{\rm H\alpha}$ holds out to high redshifts, we expect that DIG emission is negligible in typical high-redshift galaxies that are more highly star-forming (Whitaker et al., 2014) and more compact (van der Wel et al., 2014) than their $z \sim 0$ counterparts at fixed M_*. Inferring evolution in H II region properties by comparing positions of high-redshift galaxies to those of global galaxy spectra in strong-line ratio diagrams will likely overestimate the magnitude of evolution in, e.g., metallicity and ionization parameter. DIG contamination increases low-ionization line ratios in local star-forming galaxies, making them appear to have a lower level of excitation than the ionized gas in their constituent H II regions. Such an effect can artificially augment the offset between $z \sim 0$ and $z > 1$ star-

forming regions in strong-line ratio diagrams, leading to incorrect assumptions about the evolution of ionized gas properties. A more robust comparison can be achieved by correcting $z \sim 0$ global galaxy observations for DIG contamination prior to comparing to high-redshift samples.

We stress that, in cases where it is desirable to measure properties that are characteristic of the H II regions within galaxies, deriving properties directly from observed line ratios of global galaxy spectra will not yield the desired result, but instead will be systematically biased. This is true of any dataset where the spectroscopic aperture (e.g., fiber, slit, etc.) contains light from multiple H II regions and the diffuse gas that exists between H II regions. Models of galaxy line-emission must incorporate both multiple emitting regions with a spread in properties and DIG emission in order to accurately match the emission-line properties of real galaxies. The increasing number of spatially-resolved spectroscopic surveys of local galaxies (e.g., MaNGA, SAMI, CALIFA) will allow for an accurate determination of the strong-line properties of DIG regions. Observational constraints are still needed on the auroral-line properties and electron temperatures of diffuse gas. We encourage future studies modeling the line emission of star-forming galaxies to avoid treating galaxies as single emitting regions with a set of effective properties, and instead design models that reflect the substructure and diversity observed in the ISM of real galaxies.

5.A Appendix

5.A.1 A recipe for correcting individual galaxies or unrepresentative samples

In Section 5.4, we presented polynomial functions that represent the median bias in strong-line ratios, electron temperatures, and direct-method metallicities when these properties are inferred directly from global galaxy spectra. However, the *SDSSstack* model with $f_{\rm DIG}$=0.55, upon which the corrections in Section 5.4 are based, is only appropriate to apply to a sample of galaxies that is representative of the typical $z \sim 0$ star-forming population or to individual galaxies that fall near the mean relations. In this appendix, we present generalized results

for a set of models in which $f_{\rm DIG}$ is varied from 0.0 (equivalent to the *hiionly* model) to 0.8, and supply a recipe to follow when applying these generalized results.

The relative contribution of DIG to Balmer emission, $f_{\rm DIG}$, is inferred using $\Sigma_{\rm H\alpha}$ and equation 5.24. Thus, the inferred $f_{\rm DIG}$ depends on the star formation properties of the galaxy, since $\Sigma_{\rm H\alpha}$ will increase with increasing SFR. If a galaxy falls near the mean $z \sim 0$ M_*-SFR relation, or if the mean of a sample of galaxies lies near the mean local relation, then the corrections given in Section 5.4 may be applied. However, it is often of interest to study unrepresentative or extreme objects. For example, the sample of individual $z \sim 0$ SDSS galaxies with auroral-line detections have higher SFR at fixed M_* than is typical of the local star-forming population, and thus requires a lower median $f_{\rm DIG}$ value as demonstrated in Section 5.3.2. Investigating SFR dependence of local scaling relations requires dividing the local galaxy population into subsamples that are unrepresentative by construction, as in studies of the $z \sim 0$ FMR (Mannucci et al., 2010; Lara-López et al., 2010; Andrews & Martini, 2013). Extreme local galaxies are also of interest because they may provide local analogs of the ISM conditions in high-redshift galaxies (e.g., Brown et al., 2014; Bian et al., 2016). We therefore provide results for models spanning a wide range in $f_{\rm DIG}$ so that flux-weighting effects and DIG contamination may be corrected for in individual galaxies and samples with a wide range in SFR and SSFR.

Following the methodology presented in Section 5.2.5, we create five models with the same input parameters as for the *SDSSstack* model ($N_{\rm HII}$=25, $\sigma_{\rm T}$=0.07 dex, $f_{\rm DIG}$=0.55), except we vary the value of $f_{\rm DIG}$ from 0.0 to 0.8 in increments of 0.2. For this set of models, the bias in properties inferred from global galaxy spectra relative to the median properties of the distribution of H II regions in each galaxy is shown in Figure 5.25 for strong-line ratios, Figure 5.26 for electron temperatures, and Figure 5.27 for direct-method oxygen abundances. As before, we display the bias in direct-method oxygen abundance for three scenarios in which (1) both T_3 and T_2 are estimated directly from the galaxy spectrum, (2) only T_3 is known and T_2 is estimated from equation 5.12, and (3) only T_2 is known and T_3 is estimated from equation 5.12. For each model, we fit the bias in each property with the fourth-order polynomials of equations 5.25-5.27. The best-fit coefficients for the strong-line

bias are presented in Table 5.2, while the best-fit coefficients for the electron temperature and direct-method oxygen abundance biases are given in Tables 5.3 and 5.4, respectively.

We recommend using the following procedure to apply corrections to individual galaxies or samples that are unrepresentative of the $z \sim 0$ star-forming population. First, estimate $f_{\rm DIG}$ for each galaxy or the median $f_{\rm DIG}$ of the sample using $\Sigma_{\rm H\alpha}$ and equation 5.24. Identify the models presented in this appendix that bracket this $f_{\rm DIG}$ value. Interpolate between the best-fit polynomials of these bracketing models to obtain corrections for strong-line ratios, electron temperatures, or direct-method metallicities appropriate for the galaxy or sample of galaxies. Subtract the interpolated correction values for a given property from the values of that property as inferred from the global galaxy spectrum in order to correct for flux-weighting effects and DIG contamination. This procedure should yield robust corrections to individual galaxies or samples of galaxies that do not follow the mean local M_*-SFR relation. When inferring metallicities from strong-line calibrations, we recommend first correcting the simple strong-line ratios O3, O2, N2, and S2, then constructing the corrected metallicity indicator (e.g., R23, O3N2) from these corrected simple ratios before using strong-line calibrations (empirical or theoretical) based on H II regions to estimate metallicity.

5.A.2 How do changes in $\sigma_{\rm T}$ affect predicted line ratios and electron temperatures?

In our models of $z \sim 0$ galaxies, we assume that T_2 of DIG regions is 15% lower than T_2 of H II regions at fixed metallicity. This assumption was motivated by offsets between observations of $z \sim 0$ galaxies and the $f_{\rm DIG}$=0.55 model in the strong-line ratio vs. T_2 diagrams (Fig. 5.10) when we assumed that DIG and H II region T_2 were the same at fixed metallicity. Our assumption regarding lower DIG T_2 additionally brought the magnitude of the predicted offset between H II regions and $z \sim 0$ galaxies in the T_2-T_3 diagram into agreement with observations (Fig. 5.11). Given that there are no direct observational constraints of the electron temperature of DIG other than along one line-of-sight in the Milky Way (Reynolds et al., 2001), and the ionizing spectrum and gas physical conditions differ for DIG and H II

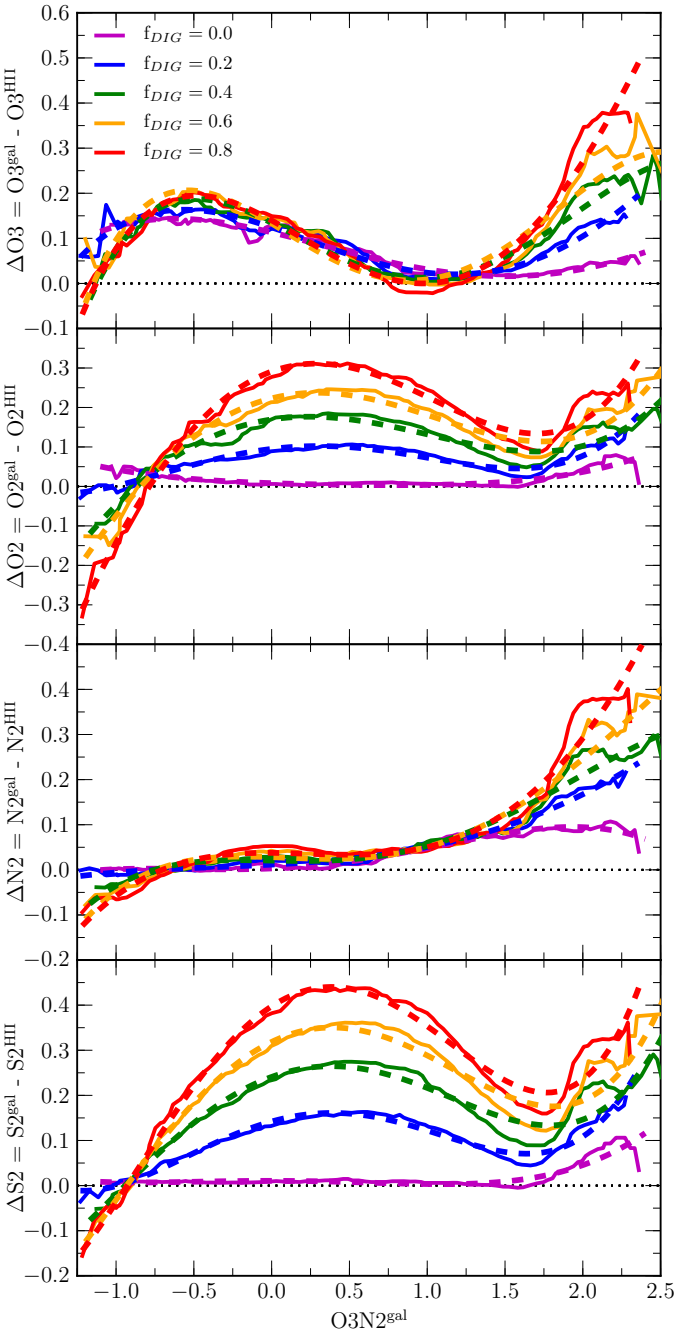

Figure 5.25: The difference between the global galaxy line ratio and median line ratio of the H II region distribution, ΔX, as a function of $O3N2^{gal}$ for the strong-line ratios X=O3, O2, N2, and S2. Solid lines show the running median of 2500 mock galaxy realizations in bins of $O3N2^{gal}$ for models with f_{DIG}=0.0 to 0.8. In each panel, the dashed lines display the best-fit fourth-order polynomial to the bias in the global galaxy line ratio, ΔX, for the model of the corresponding color. The best-fit coefficients are presented in Table 5.2.

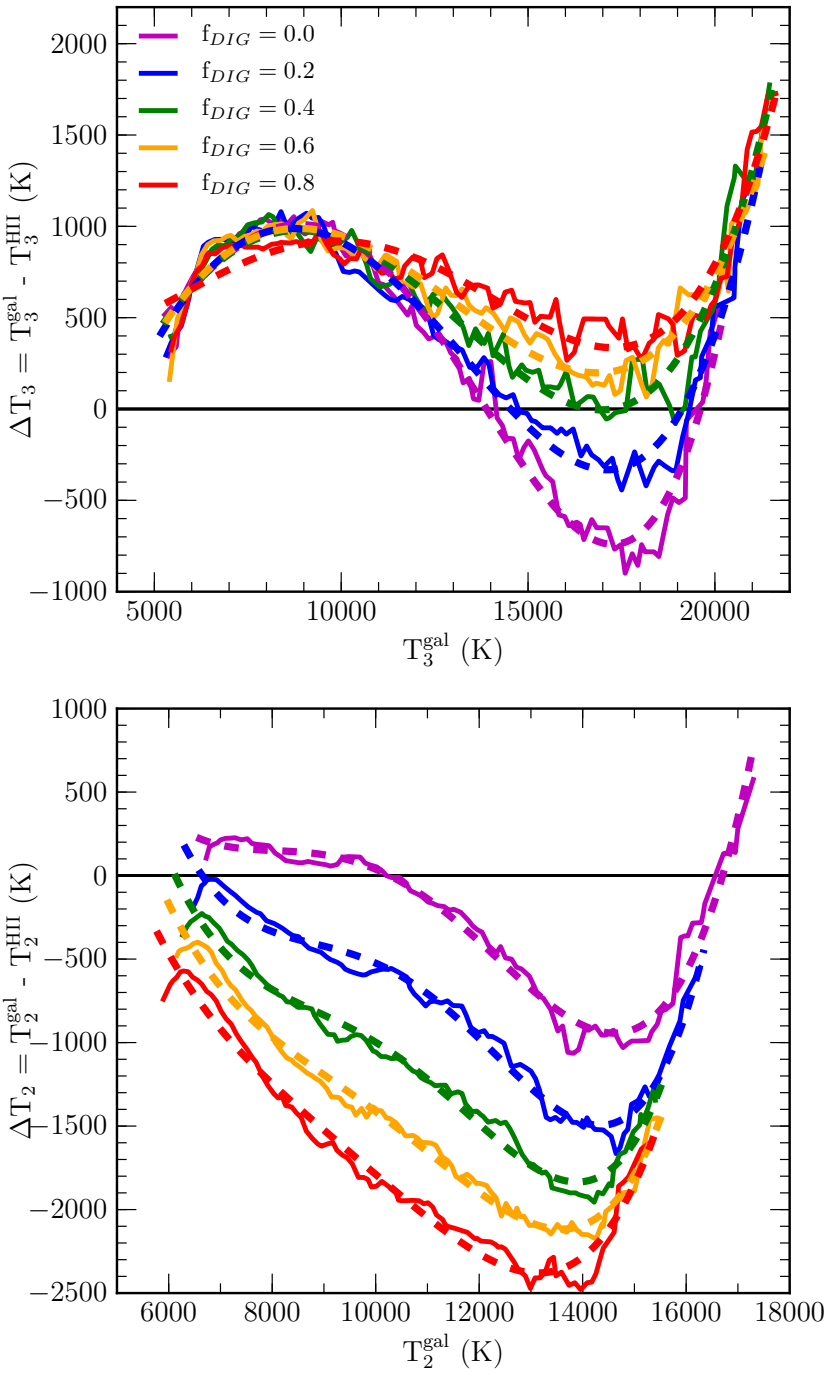

Figure 5.26: The difference between the electron temperature inferred from the global galaxy spectrum and the median electron temperature of the H II region distribution as a function of electron temperature. Results for T_3 are shown in the top panel, while the bias in T_2 is presented in the bottom panel, for models with DIG contribution ranging from $f_{\rm DIG}$=0.0 to 0.8. Best-fit fourth-order polynomials for each model are presented as dashed lines of the corresponding color. The best-fit coefficients are given in Table 5.3.

Table 5.2: Global galaxy bias coefficients for strong-line ratios (equation 5.25)

ΔO3					
$f_{\rm DIG}$	c_0	c_1	c_2	c_3	c_4
0.0	0.113	-0.0816	-0.0299	0.0341	-0.00443
0.2	0.124	-0.115	-0.0417	0.0663	-0.00948
0.4	0.134	-0.175	-0.0571	0.145	-0.0343
0.6	0.133	-0.211	-0.0364	0.167	-0.0437
0.8	0.139	-0.188	-0.0769	0.150	-0.0241
ΔO2					
$f_{\rm DIG}$	c_0	c_1	c_2	c_3	c_4
0.0	0.00828	-0.0132	0.0112	-0.00632	0.00377
0.2	0.0950	0.0472	-0.0756	-0.0115	0.0176
0.4	0.169	0.0591	-0.134	0.0308	0.00655
0.6	0.223	0.0989	-0.183	0.0288	0.0132
0.8	0.291	0.143	-0.269	0.0413	0.0211
ΔN2					
$f_{\rm DIG}$	c_0	c_1	c_2	c_3	c_4
0.0	0.00307	0.0145	0.0295	0.00878	-0.00786
0.2	0.0115	0.0180	0.0113	0.0102	-0.000491
0.4	0.0204	-0.00620	0.00106	0.0503	-0.0128
0.6	0.0280	-0.0123	-0.0147	0.0618	-0.0120
0.8	0.0376	-0.00259	-0.0388	0.0565	-0.002357
ΔS2					
$f_{\rm DIG}$	c_0	c_1	c_2	c_3	c_4
0.0	0.0105	-0.000192	-0.0110	-0.00180	0.00586
0.2	0.142	0.0960	-0.112	-0.0343	0.0313
0.4	0.240	0.125	-0.166	-0.00721	0.0235
0.6	0.318	0.166	-0.219	-0.00621	0.0289
0.8	0.397	0.223	-0.287	-0.0283	0.0479

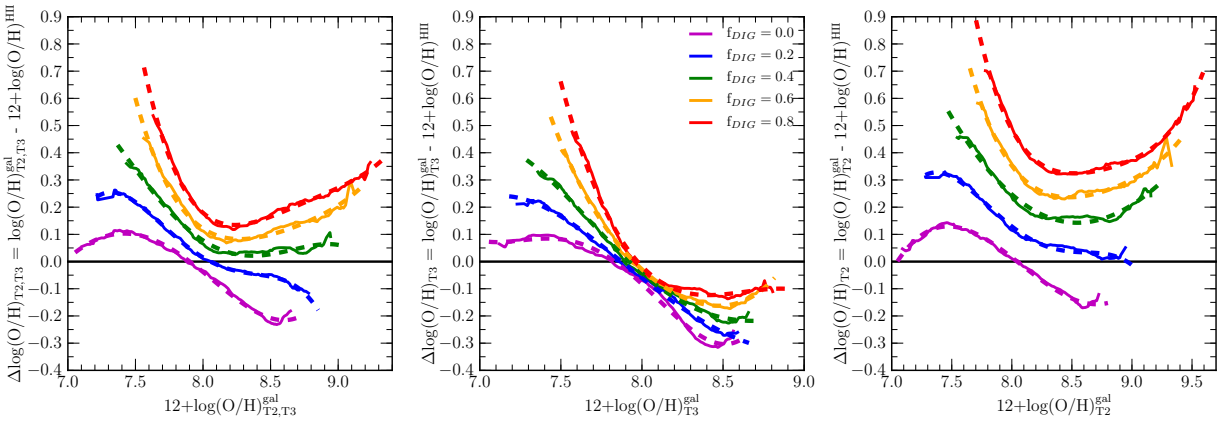

Figure 5.27: The difference between the global galaxy direct-method metallicity, inferred from the observed galaxy spectrum, and the median metallicity of the H II region distribution for models with $f_{\rm DIG}$=0.0 to 0.8. We show the bias in global galaxy metallicity for three cases: both T_3 and T_2 are measured from the galaxy spectrum (left panel); only T_3 is measured directly and T_2 is estimated using the T_2-T_3 relation of equation 5.12 (middle panel); and only T_2 is measured directly and T_3 is estimated using equation 5.12 (right panel). Dashed lines show the best-fit fourth-order polynomials for the model with the corresponding color. The best-fit coefficients are presented in Table 5.4.

Table 5.3: Global galaxy bias coefficients for electron temperatures (equation 5.26)

ΔT_3					
$f_{\rm DIG}$	c_0	c_1	c_2	c_3	c_4
0.0	407.9	-4,953	16,610	-15,140	4,031
0.2	-2,444	7,038	-1,307	-3,995	1,623
0.4	-1,949	5,794	-795.2	-3,512	1,394
0.6	-2,796	9,447	-6,403	120.1	580.6
0.8	854.9	-3,791	9,842	-7,991	2,005
ΔT_2					
$f_{\rm DIG}$	c_0	c_1	c_2	c_3	c_4
0.0	14,810	-63,090	99,850	-68,230	16,690
0.2	28,460	-114,500	169,400	-109,900	25,970
0.4	25,560	-103,700	154,300	-101,800	24,640
0.6	18,980	-76,430	112,600	-75,170	18,620
0.8	13,370	-54,490	80,700	-55,920	14,550

Table 5.4: Global galaxy bias coefficients for direct-method oxygen abundances (equation 5.27)

$\Delta\log(O/H)$ (T_3 and T_2)[a]					
f_{DIG}	c_0	c_1	c_2	c_3	c_4
0.0	-0.0382	-0.402	-0.0948	0.381	0.123
0.2	0.0150	-0.299	0.408	0.100	-0.565
0.4	0.0776	-0.320	0.472	0.0335	-0.201
0.6	0.121	-0.327	0.847	-0.692	0.257
0.8	0.178	-0.431	1.26	-1.10	0.358
$\Delta\log(O/H)$ (T_3 only)[b]					
f_{DIG}	c_0	c_1	c_2	c_3	c_4
0.0	-0.0825	-0.550	-0.241	0.662	0.514
0.2	-0.0604	-0.473	0.0717	0.192	-0.0671
0.4	-0.0424	-0.518	0.320	0.202	-0.164
0.6	-0.0287	-0.545	0.586	-0.211	0.310
0.8	-0.0177	-0.617	1.13	-0.650	0.0385
$\Delta\log(O/H)$ (T_2 only)[c]					
f_{DIG}	c_0	c_1	c_2	c_3	c_4
0.0	0.0152	-0.341	-0.0727	0.306	-0.0113
0.2	0.129	-0.346	0.266	0.283	-0.346
0.4	0.246	-0.387	0.364	0.00148	-0.0165
0.6	0.352	-0.590	0.999	-0.662	0.203
0.8	0.485	-0.813	1.44	-1.08	0.347

(a) The direct-method 12+log(O/H) case where both T_3 and T_2 are directly determined from the galaxy spectrum.

(b) The case where only T_3 is estimated directly, while T_2 is inferred using equation 5.12.

(c) The case where only T_2 is estimated directly, while T_3 is inferred using equation 5.12.

regions, our assumption regarding DIG T_2 is not unreasonable. Nevertheless, it is worthwhile to consider whether the T_2 discrepancies can be resolved under a different set of assumptions.

The adopted value of the width of the input H II region T_3 distribution, σ_T, can significantly affect the electron temperatures inferred from mock global galaxy spectra. This effect has been demonstrated by Pilyugin et al. (2012b), who were able to reproduce the offset between H II regions and $z \sim 0$ galaxies in the T_2-T_3 diagram by modeling galaxies as ensembles of H II regions with a range of metallicities (equivalent to a range of T_3). These authors found that the magnitude of the T_2-T_3 offset increased as the range of metallicities of the combined H II regions increased. In our model framework, a wider range in metallicity is equivalent to increasing the value of σ_T. We adopted a value of σ_T=0.07 dex based on the observed T_3 distributions of H II regions in nearby spiral galaxies (Berg et al., 2015; Croxall et al., 2015, 2016). The results of Pilyugin et al. (2012b) suggest that adopting a larger value of σ_T could potentially resolve the discrepancy between models and observations in the T_2-T_3 diagram without assuming different H II and DIG T_2 at fixed metallicity. We investigate the effects of adopting different values of σ_T on the predicted strong-line ratios and electron temperatures in order to determine whether different values of σ_T offer a viable solution to the discrepancies present in diagrams involving T_2.

We produce a set of models that have the same input parameters except for σ_T, which is varied. We consider five values of the width of the log-normal T_3 distribution: σ_T=[0.04, 0.07, 0.1, 0.15, 0.2]. Other parameters are set to the values adopted in our fiducial models (N_{HII} = 25, f_{DIG}=0.55, $\log(T_{cent}/K)$ = 3.7 to 4.3). In these models, we do not assume a lower DIG T_2 at fixed metallicity, but instead assume that T_2 of H II and DIG regions is equal at fixed metallicity.

The models with varied σ_T are shown in the T_2-T_3 diagram in Figure 5.28. When working under the assumption that H II region and DIG T_2 are equal at fixed metallicity, $\sigma_T \approx 0.15$ dex is required to match $z \sim 0$ observations in the T_2-T_3 diagram. This value of σ_T is roughly twice the value observed for H II region distributions in local spiral galaxies (Berg et al., 2015; Croxall et al., 2015, 2016). We show predictions from the same set of models in the strong-line ratio O3N2, O3S2, and O3O2 diagrams in Figure 5.29. Increasing σ_T results in

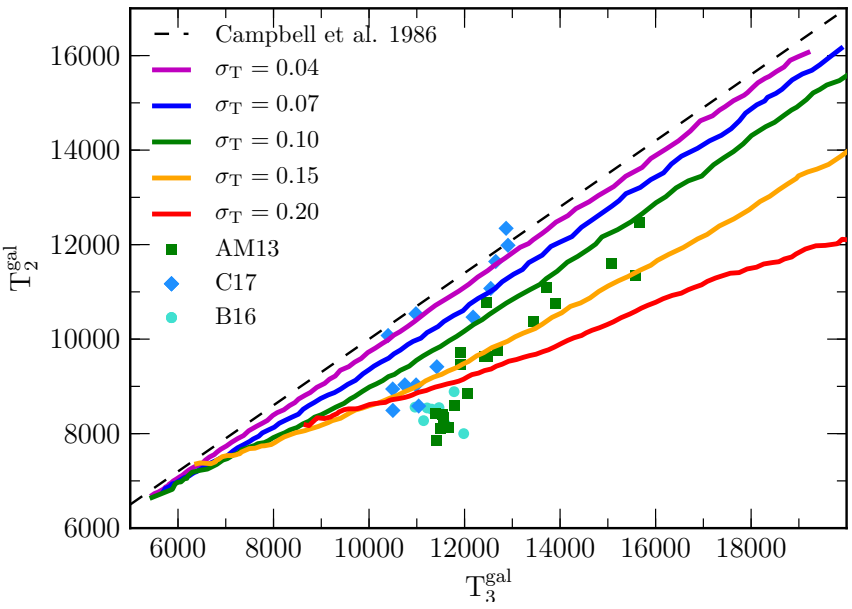

Figure 5.28: The global galaxy ionic temperature diagram of T_2^{gal} vs. T_3^{gal}, including models for which only σ_T is varied. The solid colored lines show predictions of models with f_{DIG}=0.55 and different values of σ_T, under the assumption that DIG and H II region T_2 is the same at fixed metallicity. The dashed black line shows the H II region T_2-T_3 relation of Campbell et al. (1986) given in equation 5.12. The colored points indicate stacks of $z \sim 0$ SDSS galaxies with auroral-line measurements.

lower [S II]/Hα and [O II]/Hβ at fixed [O III]/Hβ. Changes to the global galaxy strong-line excitation sequences come about because increasing the range of H II region T_3 also increases the range of H II and DIG region strong-line ratios (Fig. 5.2). Combining light from H II and DIG regions with a wider range of strong-line ratios results in different average excitation sequences because the relation between each strong-line ratio and T_3 is different.

The σ_T=0.15 model significantly underpredicts [S II]/Hα and [O II]/Hβ at fixed [O III]/Hβ for $z \sim 0$ galaxies. While this discrepancy could potentially be resolved by adopting both a larger σ_T and larger f_{DIG}, reconciling the σ_T=0.15 model with observations in the O3S2 and O3O2 diagrams would require $f_{DIG} \gtrsim 0.8$. Such a high fraction of Balmer emission originating from DIG is in conflict with narrowband Hα studies of nearby galaxies which place the DIG fraction at $30-60\%$ (Zurita et al., 2000; Oey et al., 2007). While adopting a larger σ_T than our fiducial value of 0.07 dex can reproduce the T_2-T_3 offset without additional assumptions regarding DIG T_2, this assumption also results in strong-line ratios that disagree signifi-

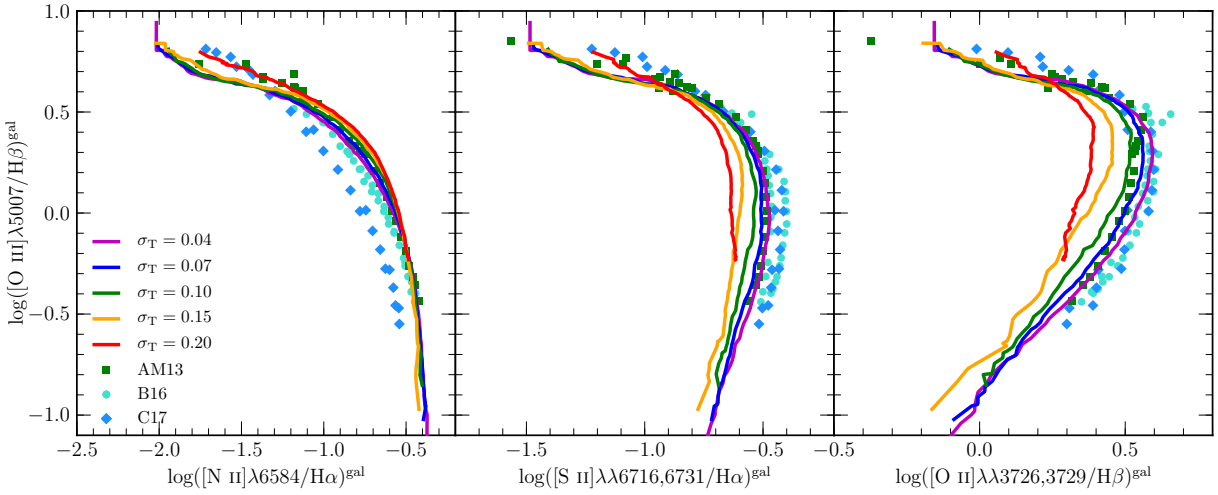

Figure 5.29: The O3N2 (left), O3S2 (middle), and O3O2 (right) strong-line ratio diagrams for stacks of SDSS galaxies and models with varying σ_T. Colored lines and points are the same as in Figure 5.28.

cantly with observations of galaxies. We conclude that our assumed value of σ_T=0.07 dex is reasonable alongside the assumption that DIG T_2 is lower than that of H II regions at fixed metallicity. Increasing the adopted values of σ_T and f_{DIG} while assuming equal DIG and H II region T_2 at fixed metallicity cannot provide a solution to the T_2 discrepancies in Figures 5.10 and 5.11.

CHAPTER 6

The MOSDEF Survey: A Stellar Mass-SFR-Metallicity Relation Exists at $z \sim 2.3$

6.1 Introduction

The formation and growth of the dark matter structure of the universe is now well-understood because of the relatively simple associated physics and the success of cosmological N-body simulations (e.g., Springel et al., 2005). In contrast, the physics governing the formation and growth of the baryonic content of galaxies that inhabit dark matter haloes is more complex. Thus, the buildup of the gaseous and stellar content of galaxies is still not fully understood. The chemical enrichment of the interstellar medium (ISM) and its scaling with galaxy properties provides a sensitive probe of the key processes governing galaxy growth, including accretion of pristine and recycled gas from the intergalactic medium (IGM) and circum-galactic medium (CGM), processing of that gas through star formation, and feedback from massive stars, supernovae, and AGN that can heat gas and drive outflows. The connection between ISM abundance and baryon cycling leads to a tight correlation between the stellar masses (M_*) and gas-phase oxygen abundances (12+log(O/H) or Z) of star-forming galaxies in the local universe, known as the mass-metallicity relation (MZR; e.g., Tremonti et al., 2004; Kewley & Ellison, 2008; Andrews & Martini, 2013). The MZR has been shown to exist out to $z \sim 3.5$, but evolves with redshift such that metallicity at fixed M_* decreases with increasing redshift (e.g., Erb et al., 2006; Maiolino et al., 2008; Troncoso et al., 2014; Sanders et al., 2015; Onodera et al., 2016).

In addition to a fundamental scaling between stellar mass and metallicity, a secondary dependence of the $z \sim 0$ MZR on star-formation rate (SFR) has been observed (e.g., Ellison

et al., 2008; Mannucci et al., 2010; Lara-López et al., 2010; Yates et al., 2012; Andrews & Martini, 2013). The existence of a secondary SFR dependence was first reported by Ellison et al. (2008) as a separation in the M_*-Z plane as a function of specific SFR (sSFR=SFR/M_*). Subsequently, Mannucci et al. (2010) and Lara-López et al. (2010) independently reported a relation among M_*, metallicity, and SFR for $z \sim 0$ galaxies and found that the intrinsic scatter around the M_*-SFR-Z relation is smaller than that of the MZR. The M_*-SFR-Z relation is such that at fixed M_*, galaxies with higher SFRs have lower metallicities. This relation has been interpreted through a theoretical picture in which the accretion of pristine or low-metallicity gas from the IGM increases the SFR while diluting the metallicity of the ISM. At the same time, metallicity increases as the gas reservoir is used up in galaxies for which this reservoir is not being replenished. Mannucci et al. (2010) further claim that galaxies up to $z \sim 2.5$ lie on the same M_*-SFR-Z relation as $z \sim 0$ galaxies, which led these authors to conclude that the M_*-SFR-Z relation is redshift invariant at $z < 2.5$. This non-evolving M_*-SFR-Z relation is known as the "fundamental metallicity relation" (FMR). In the context of the FMR, the observed evolution of the MZR with redshift is tied to the evolution of the SFR-M_* relation: at earlier epochs, galaxies have higher SFR at fixed M_* on average, corresponding to a lower metallicity. The evolution of SFR at fixed M_* with redshift is also tied to an evolution toward higher gas fraction at earlier times (Reddy et al., 2012; Tacconi et al., 2013).

A M_*-SFR-Z relation is a fundamental feature of galaxy chemical evolution models, including the equilibrium model in which the accretion rate is equal to the sum of the SFR and outflow rates (Finlator & Davé, 2008; Davé et al., 2012), and the gas-regulator model in which the mass of the gas reservoir regulates the SFR that in turn determines the outflow rate (Lilly et al., 2013). The relationships between inflow rate, outflow rate, and SFR have a similar form at all redshifts in these models. As such, the theoretical framework through which we understand galaxy growth predicts the existence of both the MZR and a M_*-SFR-Z relation at high redshifts.

When investigating the evolution of the M_*-SFR-Z relation with redshift, there are two questions that must be addressed. First, do high-redshift galaxies fall on the locally-defined

FMR such that the M_*-SFR-Z relation is redshift invariant? Second, do high-redshift galaxies show evidence for the existence of a M_*-SFR-Z relation independent of the $z \sim 0$ data? It is of interest to confirm SFR dependence of the MZR at high redshifts, in addition to understanding the relation between high-redshift galaxies and the $z \sim 0$ M_*-SFR-Z relation. If the metallicities of high-redshift galaxies do not vary with SFR at fixed M_*, then this conflict with current theoretical predictions must be understood in order to obtain a more complete picture of galaxy evolution.

There have been many recent studies investigating both of the aforementioned questions at $z > 1$, but no concensus has been reached about the existence of a high-redshift M_*-SFR-Z relation and its possible redshift invariance. Several studies have claimed that galaxies at $z \sim 1 - 3$ are consistent with the $z \sim 0$ M_*-SFR-Z relation, suggesting the existence of a redshift invariant M_*-SFR-Z relation (Christensen et al., 2012; Wuyts et al., 2012, 2016; Belli et al., 2013; Henry et al., 2013; Stott et al., 2013; Maier et al., 2014; Yabe et al., 2015; Hunt et al., 2016). Many other studies have demonstrated that galaxies at the same redshifts do not follow the predictions of the $z \sim 0$ FMR, suggesting an evolving M_*-SFR-Z relation (Cullen et al., 2014; Yabe et al., 2014; Zahid et al., 2014b; Wuyts et al., 2014; Sanders et al., 2015; Salim et al., 2015; Grasshorn Gebhardt et al., 2016; Kashino et al., 2017). The majority of the literature investigating whether a non-evolving M_*-SFR-Z relation exists compare the predictions of a parameterization of the $z \sim 0$ M_*-SFR-Z relation to high-redshift data, and thus often rely on an extrapolation of the $z \sim 0$ relation into a SFR regime that few if any galaxies in the $z \sim 0$ samples occupy. Sanders et al. (2015) and Salim et al. (2015) showed the advantages of instead performing direct, non-parametric comparisons of $z \sim 0$ and high-redshift galaxies at fixed M_*, avoiding the uncertainty associated with extrapolations. Both studies found that $z \sim 2.3$ galaxies have lower metallicities than $z \sim 0$ galaxies at fixed M_* and SFR. It is worth noting that potential redshift evolution of the relations between strong-line ratios and metallicity due to evolving gas physical conditions may systematically bias comparisons of metallicity over wide redshift ranges and must be carefully considered when investigating the validity of the FMR (Steidel et al., 2014, 2016; Shapley et al., 2015; Sanders et al., 2016b).

The question of whether the MZR has a secondary SFR dependence at $z > 1$ is naturally more difficult to address because it requires detection of a weak secondary effect within the high-redshift sample. Several works have searched for a high-redshift M_*-SFR-Z relation and failed to detect any significant SFR dependence within the uncertainties (Wuyts et al., 2012, 2014, 2016; Steidel et al., 2014; Yabe et al., 2014, 2015; Sanders et al., 2015; Grasshorn Gebhardt et al., 2016). While these studies did not observe significant secondary SFR dependence, it is not ruled out due to the expected subtlety of the effect. The predicted metallicity difference at fixed M_* over the range of SFR probed by such studies is small ($\lesssim 0.1$ dex), and thus requires either high-precision measurements or large sample sizes to detect.

A handful of studies have claimed to detect a M_*-SFR-Z relation at high redshifts. Salim et al. (2015) perform a non-parametric comparison between $z \sim 0$ galaxies and a sample of ~ 130 $z \sim 2.3$ star-forming galaxies. By comparing metallicity as a function of offset from the $z \sim 0$ M_*-sSFR relation, these authors claim to resolve secondary SFR dependence at fixed M_*, albeit with very large scatter and low significance. Kacprzak et al. (2016) divided a sample of 117 $z \sim 2.3$ star-forming galaxies at the median SFR, and by fitting linear relations to the subsamples found that galaxies with lower SFRs tend to have higher metallicities at $\log(M_*/\mathrm{M}_\odot) < 10.0$. These authors additionally claim that the slope of the $z \sim 2.3$ MZR changes with SFR. However, roughly half of the low-SFR subsample have only upper limits on the metallicity, and the low- and high-SFR subsamples overlap in a narrow M_* range where limits are also present, making it difficult to interpret the significance of these results. Recently, Kashino et al. (2017) found some evidence for a M_*-SFR-Z relation at $z \sim 1.6$ among individual galaxies with metallicity estimates based on [N II]λ6584/Hα, but do not observe the same trends in stacks including non-detections. The authors conclude that the exclusion of galaxies with non-detections of [N II] may introduce a bias that falsely makes a M_*-SFR-Z relation appear. Zahid et al. (2014b) presented a detection of the $z \sim 1.6$ M_*-SFR-Z relation, finding a coherent systematic shift in the MZR in three M_* bins when dividing their sample of 168 $z \sim 1.6$ galaxies at the median SFR.

To date, studies of the high-redshift M_*-SFR-Z have either been based on large samples

($\gtrsim 100$) with low S/N individual measurements, or small samples with moderate S/N measurements. Previous studies have also largely relied on a single metallicity indicator (most often [N II]λ6584/Hα or R23=([O III]$\lambda\lambda$4959,5007+[O II]$\lambda\lambda$3726,3729)/Hβ), which makes it difficult to ascertain the accuracy of results given the potential redshift evolution of various strong-line metallicity calibrations. Whether or not a M_*-SFR-Z relation exists at $z > 1$ remains an open question as evidenced by the disagreement in the literature. A clear confirmation of such a relation is needed to test the applicability of current galaxy chemical evolution models over cosmic time.

In this chapter, we present a study of the $z \sim 2.3$ M_*-SFR-Z relation using data from the MOSFIRE Deep Evolution Field (MOSDEF) survey (Kriek et al., 2015). We present the first analysis of the high-redshift M_*-SFR-Z relation that is based upon multiple metallicity-sensitive emission-line ratios, in combination with robust dust-corrected SFRs from measurements of Hα and Hβ. The simultaneous use of multiple metallicity indicators allows us to evaluate whether evolution of metallicity calibrations could falsely introduce apparent SFR dependence and therefore provides a more robust test of the high-redshift M_*-SFR-Z relation than previous studies. This chapter is organized as follows. We describe the observations, measurements, sample selection, and stacking methodology that we employ in Section 6.2. In Section 6.3, we search for a M_*-SFR-Z relation at $z \sim 2.3$ and perform a direct comparison to $z \sim 0$ galaxies to investigate the redshift evolution of the M_*-SFR-Z relation. We discuss our results and consider the effect of potential biases in Section 6.4, and summarize in Section 6.5. Throughout this chapter, we adopt the following abbrevations for emission-line ratios:

$$\mathrm{O3} = [\mathrm{O\ III}]\lambda5007/\mathrm{H}\beta\ , \tag{6.1}$$

$$\mathrm{N2} = [\mathrm{N\ II}]\lambda6584/\mathrm{H}\alpha\ , \tag{6.2}$$

$$\mathrm{O3N2} = \mathrm{O3}/\mathrm{N2}\ , \tag{6.3}$$

$$\mathrm{N2O2} = [\mathrm{N\ II}]\lambda6584/[\mathrm{O\ II}]\lambda\lambda3726,3729\ , \tag{6.4}$$

$$\mathrm{O32} = [\mathrm{O\ III}]\lambda5007/[\mathrm{O\ II}]\lambda\lambda3726,3729\ , \tag{6.5}$$

$$\mathrm{R23} = ([\mathrm{O\ III}]\lambda\lambda 4959, 5007 + [\mathrm{O\ II}]\lambda\lambda 3726, 3729)/\mathrm{H}\beta\ . \tag{6.6}$$

We use the term "metallicity" to refer to the gas-phase oxygen abundance (12+log(O/H)) unless otherwise specified. Emission-line wavelengths are given in air. We assume a ΛCDM cosmology with $H_0 = 70$ km s^{-1} Mpc^{-1}, $\Omega_m = 0.3$, and $\Omega_\Lambda = 0.7$.

6.2 Observations, Data, and Measurements

6.2.1 The MOSDEF survey

The MOSDEF survey was a 4-year program in which we utilized the Multi-Object Spectrometer For Infra-Red Exploration (MOSFIRE; McLean et al., 2012) on the 10 m Keck I telescope to obtain near-infrared (rest-frame optical) spectra of galaxies at $1.4 \leq z \leq 3.8$ (Kriek et al., 2015). Galaxies were targeted in three redshift ranges such that strong optical emission lines fall in near-infrared windows of atmospheric transmission: $1.37 \leq z \leq 1.70$, $2.09 \leq z \leq 2.61$, and $2.95 \leq z \leq 3.80$. In this study, we focus on the middle redshift range at $z \sim 2.3$. Targets were selected from the photometric catalogs of the 3D-HST survey (Brammer et al., 2012a; Skelton et al., 2014; Momcheva et al., 2016) based on their redshifts and observed H-band (rest-frame optical) magnitudes. Spectroscopic or *HST* grism redshifts were used when available; otherwise photometric redshifts were utilized for selection. For the $z \sim 2.3$ redshift bin, galaxies were targeted down to a fixed H-band AB magnitude of $H = 24.5$ as measured from *HST*/WFC3 F160W imaging. This targeting scheme effectively selects galaxies down to a rough stellar mass limit of $\log(M_*/\mathrm{M}_\odot) \sim 9.0$, although the sample is not complete below $\log(M_*/\mathrm{M}_\odot) \sim 9.5$ (see Shivaei et al., 2015). At $2.09 \leq z \leq 2.61$, [O II]$\lambda\lambda$3726,3729 falls in the J band; Hβ and [O III]$\lambda\lambda$4959,5007 fall in the H band; and Hα, [N II]$\lambda\lambda$6548,6584 and [S II]$\lambda\lambda$6716,6731 fall in the K band. Observations were completed in 2016 May, with the full survey having targeted $\sim$ 1500 galaxies and measured robust redshifts for $\sim$ 1300 galaxies, with $\sim$ 700 at $z \sim 2.3$ and $\sim$ 300 at $z \sim 1.5$ and 3.4, respectively. Full technical details of the MOSDEF survey observing strategy and data reduction can be found in Kriek et al. (2015).

6.2.2 Measurements and derived quantities

6.2.2.1 Stellar mass

MOSDEF targets have photometric coverage spanning the observed optical to mid-infrared (*Spitzer*/IRAC), from which stellar masses can be robustly determined. Stellar masses were estimated by fitting the broad- and medium-band photometry from the 3D-HST photometric catalogs (Skelton et al., 2014; Momcheva et al., 2016) using the SED fitting code FAST (Kriek et al., 2009) with the flexible stellar population synthesis models of Conroy et al. (2009). A Chabrier (2003) initial mass function (IMF), the Calzetti et al. (2000) dust reddening curve, solar metallicity, and constant star-formation histories were assumed. Photometric bands containing significant contamination from high equivalent width emission lines (Hα in K band and [O III]+Hβ in H band) were excluded when fitting the SED. Uncertainties on the stellar masses were estimated by perturbing the input photometry according to the uncertainties and refitting 500 times.

6.2.2.2 Emission-line fluxes and redshift

Emission-line fluxes were determined by fitting Gaussian profiles to the 1D science spectra where spectral emission features of interest are expected. Uncertainties on the emission-line fluxes were taken to be the 68th-percentile width of the distribution of line fluxes obtained by perturbing the spectrum according to the error spectrum and remeasuring the line fluxes 1000 times (Reddy et al., 2015). After fitting and subtracting a linear continuum, all lines were fit by single Gaussian profiles except for [N II]$\lambda\lambda$6548,6584+Hα and [O II]$\lambda\lambda$3726,3729, which were respectively fit by triple and double Gaussians simultaneously. In the case of [O II], the width of each component of the doublet was required to be identical. Redshifts were measured from the line with the highest S/N ratio for each object, most often Hα or [O III]λ5007, and its width was used to constrain the width of weaker emission lines. Prior to the measurement of line fluxes, science spectra were corrected for slit losses on an object-by-object basis, as described in Kriek et al. (2015). Hydrogen Balmer line fluxes were corrected for underlying stellar Balmer absorption by estimating the absorption flux from the best-fit

SED template, since the stellar continuum is not significantly detected for typical MOSDEF targets (Reddy et al., 2015). The Balmer absorption corrections were typically $\sim 1\%$ for Hα and $\sim 10\%$ for Hβ.

6.2.2.3 Reddening correction and star-formation rate

SFRs were estimated using dust-corrected Hα luminosities by applying the calibration of Hao et al. (2011), an update to the Kennicutt (1998) calibration, converted to a Chabrier (2003) IMF. Reddening corrections were applied by estimating E(B-V)$_{\rm gas}$ from the Balmer decrement (Hα/Hβ) assuming an intrinsic ratio of 2.86 and the Cardelli et al. (1989) Milky Way extinction curve. Emission-line ratios involving lines significantly separated in wavelength were calculated using reddening-corrected line fluxes (N2O2, O32, R23), while uncorrected line fluxes were used otherwise (O3N2, N2, O3). Uncertainties on both SFRs and reddening-corrected line ratios include the uncertainty in E(B-V)$_{\rm gas}$ in addition to the measurement uncertainties of the line fluxes, and SFR uncertainties include an additional 16% uncertainty added in quadrature to account for uncertainty in the slit loss corrections (Kriek et al., 2015). With the assumption that the source size is not a strong function of wavelength, the additional uncertainty associated with slit loss corrections does not affect the uncertainty of ratios of emission lines in the same filter, and does not significantly increase the uncertainty of line ratios with lines in multiple filters.

6.2.3 Sample selection

6.2.3.1 MOSDEF $z \sim 2.3$ sample

We selected a sample of star-forming galaxies from the full MOSDEF data set with which we can investigate the existence of a M_*-SFR-Z relation at $z \sim 2.3$. We required a secure redshift determination at $2.0 \leq z \leq 2.7$, $\log(M_*/{\rm M}_\odot) \geq 9.0$, and a detection of both Hα and Hβ at signal-to-noise ratio S/N$\geq$3 so that robust estimates of the reddening-corrected SFR may be obtained. The stellar mass cut removed six objects with lower stellar masses than the MOSDEF targeting scheme was designed to select. Four of these objects were not main

targets but were instead serendipitously detected. Both the number of objects targeted and spectroscopic success rate drops precipitously below $\log(M_*/\mathrm{M}_\odot) = 9.0$ (Kriek et al., 2015). We rejected objects identified as AGN by their X-ray or infrared properties (Coil et al., 2015; Azadi et al., 2017), and additionally removed objects with [N II]λ6584/H$\alpha > 0.5$ when [N II]λ6584 is detected at S/N$\geq$3, which are not likely to be dominated by star formation. We additionally rejected objects with significant sky-line contamination of Hα or Hβ such that the line flux is unreliable. The requirement that Hβ is cleanly detected at S/N$\geq$3 was the most restrictive of these cuts, removing 45% of 462 galaxies that satisfy all other criteria. We discuss potential biases introduced by the Hβ detection requirement below. This selection yielded a sample of 260 galaxies at $z_{\mathrm{med}} = 2.29$ with stellar masses spanning the range $\log(M_*/\mathrm{M}_\odot) = 9.0 - 11.4$ and SFRs ranging from 1.4 to 260 $\mathrm{M}_\odot$ yr^{-1}. The median stellar mass and SFR of the sample is $\log(M_*/\mathrm{M}_\odot) = 9.92$ and 22 $\mathrm{M}_\odot$ yr^{-1}, respectively.

The redshift distribution, and the SFR and specific SFR (sSFR=SFR/M_*) as a function of stellar mass, of the $z \sim 2.3$ sample are shown in Figure 6.1. Galaxies in this sample scatter about the mean SFR-M_* relation at $z \sim 2.0 - 2.5$, with the mean properties falling on the relations seen in past studies (e.g., Whitaker et al., 2012; Speagle et al., 2014; Shivaei et al., 2015). At $\log(M_*/\mathrm{M}_\odot) < 9.5$, galaxies below the mean SFR-M_* relation begin to fall below the MOSDEF Hβ detection threshold at $z \sim 2.3$ (Kriek et al., 2015). Shivaei et al. (2015) showed that excluding objects with Hβ non-detections did not significantly bias a smaller sample of MOSDEF star-forming galaxies at $\log(M_*/\mathrm{M}_\odot) > 9.5$. Galaxies for which H$\alpha$ is detected but Hβ is not detected, shown as SFR and sSFR lower limits in Figure 6.1 due to a lack of constraints on reddening, are distributed relatively uniformly with M_*. Above $\log(M_*/\mathrm{M}_\odot)$=9.5, most limits lie well above the Hβ detection threshold at $z \sim 2.3$, suggesting that most of the Hβ non-detections are due to sky-line contamination. Since sky-line contamination is essentially a uniform redshift selection that does not correlate with other galaxy properties, excluding these Hβ non-detections does not bias our sample (see Section 6.3.2 for additional discussion of Hβ selection effects). Shivaei et al. (2015) also demonstrated that below $\log(M_*/\mathrm{M}_\odot) = 9.5$, MOSDEF samples may be incomplete due to a bias against young objects with small Balmer and 4000 Å breaks for which the photometric

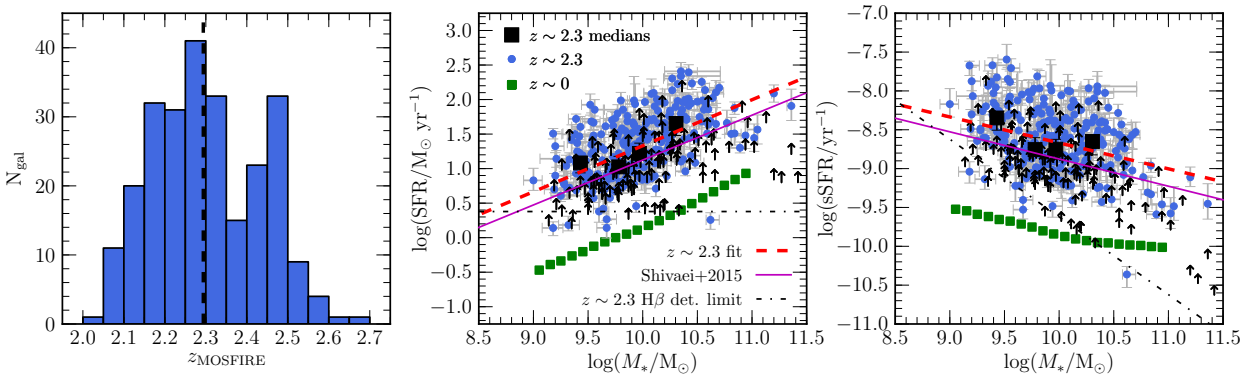

Figure 6.1: Sample properties of the $z \sim 2.3$ star-forming galaxy sample from the MOSDEF survey. LEFT: Redshift distribution of the $z \sim 2.3$ sample with Hα and Hβ detections, where the dashed vertical line displays the median redshift of $z_{\rm med} = 2.29$. MIDDLE: The SFR-M_* relation for the $z \sim 2.3$ sample. Galaxies at $z \sim 2.3$ with detections of both Hα and Hβ are shown as blue circles with error bars. Black squares display the median M_* and SFR of $z \sim 2.3$ galaxies with Hα and Hβ detections in four bins of M_* over the range $9.0 < \log(M_*/{\rm M}_\odot) < 10.5$. The best-fit linear relation to the M_* bins is displayed as a red dashed line, with best-fit coefficients given in Table 6.2. The purple line is the SFR-M_* relation at $1.4 < z < 2.6$ from Shivaei et al. (2015). Black arrows show 3σ lower limits on SFR and sSFR for galaxies with detected Hα but Hβ non-detections. The 3σ Hβ detection threshold at $z \sim 2.3$ for MOSDEF observations is indicated by the dot-dashed line, scaled from the 5σ value in Kriek et al. (2015). Green squares denote the M_*-binned stacks of $z \sim 0$ SDSS star-forming galaxies from Andrews & Martini (2013). RIGHT: The M_*-sSFR relation for the $z \sim 2.3$ sample, with symbols and lines the same as in the middle panel.

redshifts used in our target selection may be inaccurate. This incompleteness does not significantly affect our results because the majority of our sample lies above $\log(M_*/{\rm M}_\odot) = 9.5$. The results of our analysis do not significantly change if we restrict the sample to $\log(M_*/{\rm M}_\odot) > 9.5$.

We also investigated whether spectroscopic incompleteness biases our sample. Of ~ 700 galaxies targeted at $2.0 \leq z \leq 2.7$ in the MOSDEF survey, 93 failed to produce spectroscopic redshifts. Half of these (45/93) are quiescent galaxies based on their rest-frame UVJ colors and thus do not affect our sample of star-forming galaxies. Red star-forming galaxies at $z \sim 2.3$ failed to yield redshifts 15% of the time, while redshifts were not measured for only 6% of blue star-forming galaxies. These statistics agree with what Kriek et al. (2015) reported based on one-third of the full MOSDEF data set. The spectroscopic failures do not occupy any region of UVJ color space in which there are no objects with measured redshifts.

Our sample is thus slightly biased against red star-forming galaxies. However, our sample is dominated by blue star-forming galaxies (>85%) such that the bias against red star-forming galaxies has minimal impact on our results.

6.2.3.2 SDSS $z \sim 0$ comparison sample

We compare the high-redshift sample to $z \sim 0$ star-forming galaxies using measurements from the composite spectra of Andrews & Martini (2013, hereafter AM13). These authors selected a sample of 208,529 star-forming galaxies at $\langle z \rangle = 0.078$ from the SDSS (York et al., 2000) Data Release 7 (Abazajian et al., 2009) MPA-JHU catalog,[11], which includes derived stellar masses (Kauffmann et al., 2003b) and aperture-corrected SFR estimates based on emission lines (Brinchmann et al., 2004; Salim et al., 2007). The spectra of these galaxies were stacked in 0.1 dex wide bins in M_* alone, as well as 0.1×0.1 dex bins in both M_* and SFR. The M_* and SFR assigned to each stack was taken to be the median stellar mass and median SFR of the individual galaxies in each bin. We restricted the AM13 stacks to $9.0 < \log(M_*/\mathrm{M}_\odot) < 11.0$ in order to match the stellar mass range in which the majority of the $z \sim 2.3$ sample falls. We utilize the AM13 M_*-only stacks to determine the mean $z \sim 0$ relations between M_*, SFR, sSFR, and emission-line ratios, and investigate the scatter about these mean relations using the M_*-SFR stacks. The $z \sim 0$ comparison sample has the same set of emission lines measured as the $z \sim 2.3$ sample and SFR measurements based on optical emission lines. This similarity allows us to estimate metallicities in the same way as for the $z \sim 2.3$ sample, and perform a direct comparison of line ratios and metallicities at fixed M_* and SFR.

6.2.4 Metallicities

The MOSDEF data set crucially provides coverage of several strong rest-optical emission features, allowing us to measure multiple metallicity indicators widely applied in the local universe. We utilize multiple emission-line ratios to estimate metallicity in this analysis,

[11]Available at http://www.mpa-garching.mpg.de/SDSS/DR7/.

including N2, O3N2, N2O2, and O32. We do not utilize R23 to estimate metallicity for reasons described below, but retain the use of this metallicity-sensitive line ratio empirically, along with O3.

For N2 and O3N2, we use the empirically calibrated relations of Pettini & Pagel (2004) based on individual $z \sim 0$ H II regions:

$$12 + \log(\mathrm{O/H}) = 8.90 + 0.57 \times \log(\mathrm{N2}), \tag{6.7}$$

and

$$12 + \log(\mathrm{O/H}) = 8.73 - 0.32 \times \log(\mathrm{O3N2}). \tag{6.8}$$

The intrinsic uncertainties associated with these calibrations are 0.14 and 0.18 dex for N2 and O3N2, respectively. The N2 calibration is valid over the range $-2.5 < \log(\mathrm{N2}) < -0.3$, while the O3N2 calibration is applicable for $\log(\mathrm{O3N2}) \lesssim 2.0$. All of the $z \sim 0$ sample and the entire high-redshift MOSDEF sample except for six galaxies fall within these bounds.

Brown et al. (2016) provided a calibration of galaxy metallicity as a function of N2O2 and offset from the mean $z \sim 0$ sSFR-M_* sequence ($\Delta\log(\mathrm{sSFR})$):

$$12 + \log(\mathrm{O/H}) = 9.20 + 0.54 \times \log(\mathrm{N2O2}) - 0.36 \times \Delta\log(\mathrm{sSFR}). \tag{6.9}$$

The $\Delta\log(\mathrm{sSFR})$ term was included because these authors found that N2O2 systematically increases at fixed direct-method metallicity as $\Delta\log(\mathrm{sSFR})$ increases. Sanders et al. (2017) demonstrated that the separation of galaxies of different $\Delta\log(\mathrm{sSFR})$ in the N2O2-metallicity plane is a result of contamination of the integrated emission-line fluxes from diffuse ionized gas (DIG), which more strongly affects galaxies with lower $\Delta\log(\mathrm{sSFR})$. After correcting the Brown et al. (2016) strong-line ratios and direct-method metallicities for DIG contamination, the dependence on $\Delta\log(\mathrm{sSFR})$ disappears and the galaxies are shifted onto the H II region metallicity scale. To estimate metallicities from N2O2, we perform a linear fit to the corrected

Brown et al. (2016) datapoints from Sanders et al. (2017), obtaining the following expression:

$$12 + \log(\mathrm{O/H}) = 8.94 + 0.73 \times \log(\mathrm{N2O2}). \tag{6.10}$$

The intrinsic scatter around this relation is 0.2 dex, and the calibration is valid over the range $-1.3 < \log(\mathrm{N2O2}) < 0.0$. The entire $z \sim 0$ comparison sample falls in this range. Only 10 galaxies in the $z \sim 2.3$ sample have $\log(\mathrm{N2O2}) < -1.3$, while the remainder fall in the range over which the calibration is valid.

We utilize the O32 calibration of Jones et al. (2015):

$$12 + \log(\mathrm{O/H}) = 8.3439 - 0.4640 \times \log(\mathrm{O32}). \tag{6.11}$$

The intrinsic calibration uncertainty is 0.11 dex. This relation was calibrated using a sample of 113 $z \sim 0$ star-forming galaxies with metallicity estimates based on electron temperatures, and no evolution in this calibration is seen out to $z \sim 0.8$ (Jones et al., 2015). The calibrating data set only covers the range $0.0 \lesssim \log(\mathrm{O32}) \lesssim 1.0$, with the majority of the data set lying at $0.0 < \log(\mathrm{O32}) < 0.5$. While 91 galaxies in the $z \sim 2.3$ sample and all of the local comparison sample has $\log(\mathrm{O32})<0.0$, other empirical and theoretical calibrations do not show significant changes to the slope of O32 calibrations below $\log(\mathrm{O32})=0.0$ (Maiolino et al., 2008; Curti et al., 2017). We therefore apply the Jones et al. (2015) O32 calibration to galaxies with $-1.0 < \log(\mathrm{O32}) < 1.0$ while noting that a systematic bias in metallicity estimates from this calibration may be introduced at $\log(\mathrm{O32})<0.0$.

While R23 is commonly employed as a metallicity indicator in the local universe, we do not estimate metallicity from R23. R23 is double-valued as a function of metallicity, with the turnover occurring at $8.0 \lesssim 12 + \log(\mathrm{O/H}) \lesssim 8.4$ and $0.7 \lesssim \log(\mathrm{R23}) \lesssim 1.0$ (e.g., McGaugh, 1991; Kewley & Dopita, 2002; Pilyugin & Thuan, 2005). The majority of our $z \sim 2.3$ sample lies in this region of parameter space, where small observational uncertainties lead to large uncertainties in metallicity and assigning an object to the upper or lower R23 branch is non-trivial. Breaking the upper and lower branch degeneracy is usually achieved

using N2 or N2O2 in combination with R23 (e.g., Kewley & Dopita, 2002). Star-forming galaxies at $z \sim 2.3$ display significant offsets from the $z \sim 0$ population in strong-line ratio diagrams involving lines of nitrogen (Masters et al., 2014; Steidel et al., 2014; Shapley et al., 2015; Sanders et al., 2016b), however, suggesting that the criterion for upper or lower R23 branch assignment based on N2 or N2O2 evolves with redshift. Due to these uncertainties in R23-based metallicities for the high-redshift sample, we do not convert R23 values to metallicities but instead utilize R23 in an empirical sense only.

While all 260 individual galaxies in the $z \sim 2.3$ sample have detections of Hα and Hβ, some do not have S/N$\geq$3 for [N II]λ6584, [O II]$\lambda\lambda$3726,3729, and/or [O III]λ5007. The sample contains 143 N2 detections, 126 O3N2 detections, 118 N2O2 detections, 169 O32 and R23 detections, and 223 O3 detections. Each of the detected line-ratio subsets has median stellar mass in the range $9.9 < \log(M_*/M_\odot) < 10.1$ and median SFR within $22 < SFR/M_\odot\ yr^{-1} < 32$. We incorporate information from galaxies with metal line non-detections using a stacking analysis as described below.

6.2.5 Correcting for diffuse ionized gas contamination

As mentioned previously, DIG is a significant contaminant of global galaxy spectra at $z \sim 0$ and introduces systematic biases in galaxy emission-line ratios and metallicity estimates (Sanders et al., 2017). In order to obtain accurate metallicities from strong-line calibrations, both the measured line ratios and the metallicity calibrations must be free of the effects of DIG contamination. Relations calibrated using individual H II regions such as the Pettini & Pagel (2004) N2 and O3N2 calibrations are free from this issue. We have explicitly corrected the $z \sim 0$ sample of Brown et al. (2016) to the H II region metallicity scale. While the calibrating data set of the Jones et al. (2015) O32 relation has not been corrected, we do not expect a high level of DIG contamination in this case. The galaxies selected by Jones et al. (2015) are highly star-forming and have high sSFR and large Hα surface brightness. Oey et al. (2007) found that the importance of DIG to total galaxy emission decreases with increasing Hα surface brightness, such that DIG emission is negligible in starburst galaxies.

Using the calibration from Sanders et al. (2017) based on the Oey et al. (2007) data set, we estimate that the fraction of total Balmer emission originating from DIG ($f_{\rm DIG}$) is $\lesssim 30\%$ for the galaxies in the Jones et al. (2015) sample based on their Hα surface brightnesses. This result suggests that H II region emission dominates the Jones et al. (2015) calibrating sample and the correction for DIG contamination would be minor compared to what is required for typical $z \sim 0$ galaxies with $f_{\rm DIG} \approx 55\%$ (Sanders et al., 2017).

We corrected the $z \sim 0$ comparison sample for DIG contamination using the results of Sanders et al. (2017), which are based upon empirical models treating galaxies as ensembles of H II and DIG regions. These models also correct for flux-weighting biases present in integrated galaxy measurements because the line-emitting regions falling in the spectroscopic aperture have a range of metallicites. The AM13 M_* stacks were corrected using the $z \sim 0$ model with $f_{\rm DIG}$=0.55. For the AM13 SFR-M_* bins, Sanders et al. (2017) determined the median Hα surface brightness in each bin and constructed a model matched to the corresponding $f_{\rm DIG}$, since the relative importance of DIG varies with SFR. These corrections allow us to obtain more robust metallicity estimates for the $z \sim 0$ comparison sample by using the corrected line ratios with the metallicity calibrations described above.

There are currently no observational constraints on the importance of DIG at high redshifts. However, if high-redshift galaxies follow a similar relation between $f_{\rm DIG}$ and Hα surface brightness as local galaxies, the high SFRs and compact sizes of high-redshift galaxies suggest that DIG emission is negligible at $z \sim 2.3$. We operate under this assumption, although high-resolution spatially resolved emission-line observations of high-redshift galaxies are ultimately required to reveal the role of DIG in the early universe. In addition to compact sizes and high SFRs, galaxies have much larger gas fractions at fixed M_* at $z \sim 2$ than at $z \sim 0$ (Tacconi et al., 2013), and likely display differences in the distribution and importance of different ISM phases. In light of such differences, the assumption that the relation between $f_{\rm DIG}$ and Hα surface brightness does not change with redshift may need to be revisited.

6.2.6 Stacking methodology

We selected a subset of the sample of 260 $z \sim 2.3$ star-forming galaxies with which we perform a stacking analysis. For this stacking subsample, we additionally required that the spectrum of each object had wavelength coverage of [O II]$\lambda\lambda$3726,3729, Hβ, [O III]λ5007, Hα, and [N II]λ6584, and that the stellar mass fell in the range $9.0 \leq \log(M_*/\mathrm{M}_\odot) \leq 10.5$. The wavelength coverage criterion allows for the measurement of all emission-line ratios of interest in this study from the stacked spectra. The stellar mass criterion is designed to only stack over the mass range in which the MOSDEF $z \sim 2.3$ star-forming sample is not obviously incomplete based on target selection and/or spectroscopic success rate. Kriek et al. (2015) showed that both the number of galaxies targeted and the spectroscopic success rate sharply decrease at $\log(M_*/\mathrm{M}_\odot) < 9.0$ using data from the first 2 years of the MOSDEF survey. Such behavior is expected because of the target selection down to fixed H-band magnitude and the inherent faintness of low-mass targets. A drop in the spectroscopic success rate at $\log(M_*/\mathrm{M}_\odot) > 10.5$ was also identified and found to be partially caused by a significantly lower success rate for red star-forming and quiescent galaxies compared to blue star-forming galaxies (Kriek et al., 2015). We have confirmed these trends in success rate with the full MOSDEF $z \sim 2.3$ sample. Applying the above criteria yields a stacking subsample of 195 galaxies at $z_{\mathrm{med}} = 2.29$ with median stellar mass $\log(M_*/\mathrm{M}_\odot) = 9.89$ and median SFR of 18 $\mathrm{M}_\odot$ yr^{-1}. The stacking subsample has slightly lower median stellar mass and SFR than the larger $z \sim 2.3$ sample it was selected from, primarily because of the upper stellar mass cut.

We used two different binning methods for this analysis. We binned in stellar mass in order to determine mean $z \sim 2.3$ line-ratio and metallicity relations as a function of stellar mass. Galaxies were stacked in four stellar mass bins selected such that an equal number of galaxies fell in each bin (48-49 galaxies per bin). We refer to the stacks binned in stellar mass only as the "M_* stacks." We also binned in both stellar mass and offset from the mean $z \sim 2.3$ sSFR-M_* relation (Δlog(sSFR)) in order to assess the presence of a M_*-SFR-Z relation at $z \sim 2.3$ and its evolution from $z \sim 0$. We found that dividing the

stacking sample at $\Delta\log(\mathrm{sSFR}/\mathrm{yr}^{-1}) = \pm 0.2$ splits the sample into three roughly equal parts, with 68 galaxies in the highly star-forming subsample with $\Delta\log(\mathrm{sSFR}) > 0.2$, 67 galaxies falling within 0.2 dex of the mean relation, and 60 galaxies with $\Delta\log(\mathrm{sSFR}) < -0.2$. Since these bins were selected with respect to the mean $z \sim 2.3$ sSFR-M_* relation, the stellar mass distribution in each bin is similar except for the $\Delta\log(\mathrm{sSFR}) < -0.2$ bin, in which objects with $\log(M_*/\mathrm{M}_\odot) \lesssim 9.5$ fall below the MOSDEF Hβ detection limit at $z \sim 2.3$. The $\Delta\log(\mathrm{sSFR}) < -0.2$ bin is thus biased toward higher M_*. After dividing the sample in $\Delta\log(\mathrm{sSFR})$, galaxies in each $\Delta\log(\mathrm{sSFR})$ bin were stacked in two stellar mass bins divided at the median stellar mass, yielding a total of 6 M_*-$\Delta\log(\mathrm{sSFR})$ bins. We refer to the stacks binned in both M_* and $\Delta\log(\mathrm{sSFR})$ as the "M_*-ΔsSFR stacks."

We produced composite spectra by first shifting each spectrum into the rest frame and converting from flux density to luminosity density using the spectroscopic redshift. Since some of the line ratios of interest require reddening correction, we corrected each individual spectrum for reddening by applying a reddening correction to the luminosity density at each wavelength element based on the Balmer decrement (Hα/Hβ) of each galaxy, assuming the Cardelli et al. (1989) extinction curve. This process effectively only corrects the nebular lines, since the continuum is not significantly detected for individual galaxies in our stacking sample. Each reddening-corrected spectrum was then normalized by the dust-corrected Hα luminosity. Spectra were interpolated onto a wavelength grid with spacing equal to the wavelength sampling at the median redshift of the sample, equal to 0.40 Å in J band, 0.50 Å in H band, and 0.66 Å in K band. Normalized composite spectra were created by taking the median value of the normalized spectra at each wavelength increment, and multiplying by the median dust-corrected Hα luminosity to produce the final composite spectrum in units of luminosity density.

Emission-line luminosities were measured from stacked spectra by fitting a flat continuum to regions around emission features and Gaussian profiles to the emission lines following the fitting methodology for individual spectra. Uncertainties on emission-line fluxes were estimated using a Monte Carlo technique in which we perturbed the stellar masses according to the uncertainties and divided the perturbed sample into the same stellar mass bins as be-

fore, bootstrap resampled each bin to account for sample variance, perturbed the individual spectra according to the error spectra, perturbed the individual $E(B\text{-}V)_{gas}$ values and applied them to correct the individual spectra for reddening, stacked according to the method described above, and remeasured the emission-line luminosities. This process was repeated 100 times, and the uncertainties on line luminosities were obtained from the 68th-percentile width of the distribution of remeasured line luminosities. The median Balmer absorption luminosity of the individual galaxies in each bin was utilized to apply Balmer absorption corrections to the stacked Hα and Hβ luminosities.

Emission-line ratios and uncertainties were calculated using the line luminosities and uncertainties measured from the stacked spectra. We found that the stacking method described above robustly reproduces line ratios characteristic of the individual galaxies in a stack by comparing the stacked line ratios to median line ratios of individual galaxies with significant detections of all of the emission lines of interest. Stellar mass and SFR were assigned to each stack using the median M_* and median SFR of the individual galaxies in each bin. Uncertainties on the median M_* and SFR were estimated using the distribution of median values produced by the Monte Carlo simulations. The median M_* and SFR of galaxies in each bin and measured line ratios of the M_* and M_*-ΔsSFR stacks are presented in Table 6.1.

6.3 Results

A sensitive test of secondary dependences in the MZR is to look for correlations between deviations from the mean MZR and deviations from mean relations of other galaxy properties as a function of stellar mass, such as SFR, or H I and H_2 gas fraction. In particular, a signature of a M_*-SFR-Z relation is an anticorrelation between residuals about the mean MZR ($\Delta\log(O/H)$) and residuals about the mean sSFR-M_* relation ($\Delta\log(sSFR)$). We search for this signature of a M_*-SFR-Z relation at $z \sim 2.3$. We first fit the mean sSFR-M_* relation, as well as the mean relations between M_* and the emission-line ratios O3N2, N2, N2O2, O32, O3, and R23. We additionally fit the mean MZR based on metallicities determined using each of the line ratios O3N2, N2, N2O2, and O32. We then examine the relationship between

Table 6.1: Galaxy properties and emission-line ratios from stacks of $z \sim 2.3$ star-forming galaxy spectra.

N_{gal}^{a}	$\log\left(\frac{M_*}{M_\odot}\right)^{b}$	SFR_{med}^{c}	$\log\left(\frac{sSFR}{yr^{-1}}\right)^{d}$	log(N2)	log(O3)	log(O3N2)	log(N2O2)	log(O32)	log(R23)
				M_* stacks					
49	9.0-9.62; $9.43^{+0.01}_{-0.03}$	$12.1^{+3.4}_{-1.2}$	$-8.34^{+0.16}_{-0.05}$	$-1.22^{+0.10}_{-0.05}$	$0.66^{+0.04}_{-0.02}$	$1.89^{+0.06}_{-0.10}$	$-1.13^{+0.20}_{-0.08}$	$0.28^{+0.10}_{-0.13}$	$0.93^{+0.04}_{-0.03}$
49	9.62-9.89; $9.78^{+0.02}_{-0.01}$	$10.6^{+0.8}_{-4.4}$	$-8.75^{+0.03}_{-0.15}$	$-1.08^{+0.06}_{-0.09}$	$0.55^{+0.05}_{-0.02}$	$1.63^{+0.11}_{-0.07}$	$-1.12^{+0.09}_{-0.18}$	$0.07^{+0.16}_{-0.11}$	$0.89^{+0.06}_{-0.05}$
49	9.89-10.13; $9.97^{+0.01}_{-0.04}$	$16.6^{+2.8}_{-6.8}$	$-8.75^{+0.11}_{-0.13}$	$-0.90^{+0.05}_{-0.06}$	$0.45^{+0.02}_{-0.04}$	$1.36^{+0.06}_{-0.06}$	$-0.93^{+0.13}_{-0.14}$	$-0.05^{+0.07}_{-0.17}$	$0.84^{+0.05}_{-0.05}$
48	10.14-10.50; $10.30^{+0.01}_{-0.02}$	$45.1^{+14.9}_{-9.3}$	$-8.65^{+0.17}_{-0.07}$	$-0.71^{+0.03}_{-0.03}$	$0.37^{+0.02}_{-0.05}$	$1.09^{+0.03}_{-0.06}$	$-0.80^{+0.21}_{-0.15}$	$-0.20^{+0.23}_{-0.19}$	$0.83^{+0.07}_{-0.16}$
				M_*-ΔsSFR stacks: $\Delta\log(sSFR/yr^{-1}) < -0.2$					
30	9.18-9.90; $9.72^{+0.04}_{-0.01}$	$5.7^{+0.2}_{-1.5}$	$-8.96^{+0.01}_{-0.12}$	$-1.05^{+0.10}_{-0.11}$	$0.43^{+0.04}_{-0.04}$	$1.49^{+0.13}_{-0.14}$	$-1.04^{+0.13}_{-0.16}$	$0.00^{+0.08}_{-0.11}$	$0.80^{+0.05}_{-0.04}$
30	9.90-10.49; $10.04^{+0.02}_{-0.05}$	$11.1^{+1.9}_{-0.6}$	$-8.99^{+0.10}_{-0.01}$	$-0.79^{+0.09}_{-0.06}$	$0.34^{+0.04}_{-0.05}$	$1.14^{+0.06}_{-0.10}$	$-0.75^{+0.13}_{-0.09}$	$-0.11^{+0.04}_{-0.12}$	$0.76^{+0.05}_{-0.04}$
				M_*-ΔsSFR stacks: $-0.2 \leq \Delta\log(sSFR/yr^{-1}) \leq +0.2$					
34	9.00-9.86; $9.50^{+0.01}_{-0.03}$	$9.2^{+0.4}_{-2.1}$	$-8.53^{+0.03}_{-0.07}$	$-1.16^{+0.04}_{-0.17}$	$0.59^{+0.03}_{-0.04}$	$1.76^{+0.14}_{-0.07}$	$-1.09^{+0.10}_{-0.19}$	$0.21^{+0.09}_{-0.13}$	$0.88^{+0.03}_{-0.05}$
33	9.86-10.47; $10.1^{+0.05}_{-0.01}$	$26.2^{+4.4}_{-0.1}$	$-8.68^{+0.07}_{-0.03}$	$-0.81^{+0.07}_{-0.04}$	$0.41^{+0.04}_{-0.04}$	$1.23^{+0.05}_{-0.08}$	$-0.83^{+0.11}_{-0.08}$	$-0.11^{+0.04}_{-0.09}$	$0.84^{+0.05}_{-0.02}$
				M_*-ΔsSFR stacks: $\Delta\log(sSFR/yr^{-1}) > +0.2$					
34	9.20-9.92; $9.55^{+0.01}_{-0.05}$	$32.1^{+3.0}_{-4.1}$	$-8.04^{+0.07}_{-0.04}$	$-1.23^{+0.07}_{-0.10}$	$0.69^{+0.03}_{-0.01}$	$1.93^{+0.11}_{-0.08}$	$-1.22^{+0.11}_{-0.11}$	$0.25^{+0.15}_{-0.06}$	$0.97^{+0.03}_{-0.04}$
34	9.92-10.5; $10.25^{+0.01}_{-0.03}$	$88.2^{+17.3}_{-1.0}$	$-8.30^{+0.12}_{-0.02}$	$-0.78^{+0.05}_{-0.05}$	$0.46^{+0.03}_{-0.03}$	$1.24^{+0.08}_{-0.05}$	$-0.97^{+0.07}_{-0.07}$	$-0.18^{+0.09}_{-0.06}$	$0.92^{+0.03}_{-0.04}$

(a) Number of galaxies in a bin.

(b) Range and median $\log(M_*/M_\odot)$ of galaxies in a bin.

(c) Median dust-corrected Hα SFR of galaxies in a bin.

(d) The sSFR assigned to each stack is calculated using the median SFR and median M_* of galaxies in each bin.

the residuals in line ratios (and the corresponding metallicity values) and sSFR relative to the mean relations. A similar method was employed by Salim et al. (2015) and Kashino et al. (2017).

While we use sSFR residuals in order to make a comparison to the simulation predictions of Davé et al. (2017), we note that using residuals around the mean SFR-M_* relation would give the same result since an offset of a galaxy above or below the mean SFR-M_* relation in log(SFR) is equal to the offset of that galaxy from the mean sSFR-M_* relation in log(sSFR). Accordingly, the slope of the Δlog(O/H) vs. Δlog(sSFR) relation provides a direct probe of the dependence of O/H on SFR at fixed M_*.

6.3.1 Mean $z \sim 2.3$ relations

The M_* stacks are shown in the SFR-M_* and sSFR-M_* planes in Figure 6.1. We determine the mean $z \sim 2.3$ sSFR-M_* relation by fitting a linear function to the M_* stacks in the sSFR-M_* plane. The best-fit coefficients are listed in Table 6.2. We determine the residuals about the mean M_*-sSFR relation by subtracting this mean relation from the sSFR estimate for each galaxy in the $z \sim 2.3$ sample. In Figure 6.1, we compare our mean relation to that obtained by Shivaei et al. (2015) using the first 2 years of MOSDEF data. The two relations are generally consistent, although we find a slightly higher normalization, likely due in part to different SED fitting assumptions and the resulting stellar masses. We note that the MOSDEF $z \sim 2.3$ Hβ detection limit biases the SFR in the lowest-mass bin high, and thus the fit we derive here may be steeper in the sSFR-M_* plane and shallower in the SFR-M_* plane than the true mean relation of the $z \sim 2.3$ star-forming population. However, our results do not change significantly if we instead fit mean relations excluding the lowest-mass bin. Incompleteness in the lowest-mass bin due to the Hβ detection limit thus does not affect our conclusions.

In Figure 6.2, we present the excitation- and metallicity-sensitive line ratios O3N2, N2, N2O2, and O32 vs. M_*. The line ratios O3N2 and O32 are sensitive to the ionization parameter, containing both a high and low ionization energy ionic species. N2 is also sensitive

Table 6.2: Best-fit linear coefficients to $z \sim 2.3$ galaxy properties as a function of stellar mass.

property	slope	intercept
star formation[a]		
SFR	0.67	−5.33
sSFR	−0.33	−5.33
line ratios[a]		
O3N2	−0.94	10.72
N2	0.59	−6.82
N2O2	0.41	−5.03
O32	−0.56	5.51
O3	−0.34	3.90
R23	−0.12	2.03
12+log(O/H)[b]		
O3N2	0.30	5.30
N2	0.34	5.01
N2O2	0.30	5.27
O32	0.26	5.79

(a) Coefficients for $\log(X) = m \times \log(M_*/\mathrm{M}_\odot) + b$, where X is the appropriate galaxy property, m is the slope, and b is the intercept.

(b) Coefficients for $12 + \log(\mathrm{O/H}) = m \times \log(M_*/\mathrm{M}_\odot) + b$, where m is the slope, b is the intercept, and 12+log(O/H) is determined using the corresponding line ratio.

to changes in ionization parameter, as well as the nitrogen abundance (N/H), such that higher ionization parameter and lower N/H lead to lower N2. In contrast, N2O2 is primarily sensitive to changes in the N/O abundance ratio (Kewley & Dopita, 2002). We observe a clear progression toward higher ionization parameter and lower N/O and N/H at fixed stellar mass from $z \sim 0$ to $z \sim 2.3$. These results are in agreement with what has been found for other samples at $z > 2$ (e.g., Erb et al., 2006; Steidel et al., 2014; Shapley et al., 2015; Holden et al., 2016). While recent results for high-redshift samples have suggested the possibility of redshift evolution of physical conditions such as the ionizing spectrum, ionization parameter, or N/O at fixed O/H (e.g., Kewley et al., 2013b; Masters et al., 2014, 2016; Steidel et al., 2014, 2016; Shapley et al., 2015; Sanders et al., 2016b; Strom et al., 2017), the observation of both higher ionization parameter and lower nitrogen abundance at fixed M_* is difficult to explain without chemical evolution (i.e., lower O/H at fixed M_*

with increasing redshift) playing a major role. We determine the mean relation between these strong-line ratios and M_* by fitting linear functions to the M_* stacks, and present the best-fit coefficients in Table 6.2.

All four line ratios indirectly trace oxygen abundance, since ionization parameter is tightly anticorrelated with metallicity (Dopita et al., 2006a,b; Pérez-Montero, 2014; Sánchez et al., 2015), while N/O and N/H are correlated with metallicity due to the secondary production channel of nitrogen (Kewley & Dopita, 2002; Pettini & Pagel, 2004; Pérez-Montero & Contini, 2009). The observation of such correlations in the local universe has led to the construction of metallicity calibrations based on these strong-line ratios. The translation of the strong-line ratios O3N2, N2, N2O2, and O32 into metallicity is shown by the right set of y-axes in Figure 6.2. All four panels are matched to the same range in metallicity ($7.7<12+\log(\mathrm{O/H})<8.9$). Under the assumption that metallicity calibrations do not strongly evolve with redshift, the presence of higher excitation and lower N/O at $z \sim 2.3$ corresponds to lower metallicity at fixed M_* compared to $z \sim 0$. We find that $z \sim 2.3$ galaxies are offset toward lower metallicities at fixed $M_*$by 0.37, 0.25, 0.46, and 0.25 dex on average for metallicities based on O3N2, N2, N2O2, and O32, respectively. The best-fit linear MZR for these indicators can be found by passing the line-ratio vs. M_* fits through the metallicity calibrations (equations 6.7, 6.8, 6.10, and 6.11). We list the best-fit coefficients for the MZR in Table 6.2, and calculate O/H residuals relative to these best-fit linear relations.

The ability of such locally calibrated relations to accurately estimate nebular metallicities in high-redshift galaxies has been called into question by recent studies (e.g., Steidel et al., 2014; Sanders et al., 2015; Shapley et al., 2015; Steidel et al., 2016; Strom et al., 2017). We note here that the method we employ to search for a M_*-SFR-Z relation at $z \sim 2$ using residuals around mean relations is immune to changes in the normalizations of metallicity calibrations since we are looking at *relative* differences in metallicity, but would be affected by changes in the slopes. The interpretation of our results could also be affected by changes in ionized gas physical conditions that correlate with sSFR at fixed M_*. We discuss these potential systematic effects on our results in Section 6.4.1.

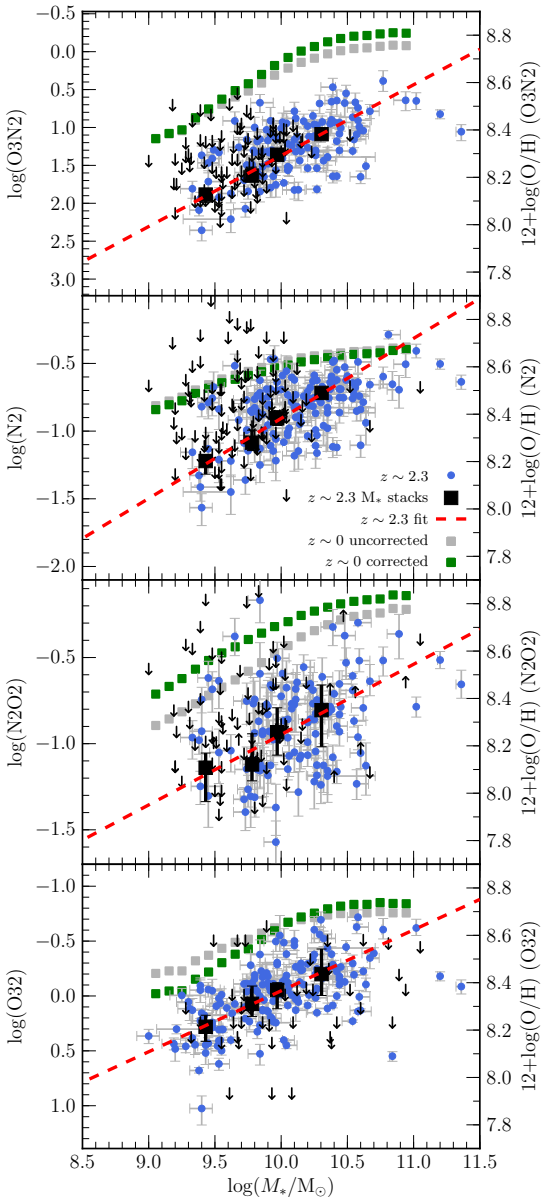

Figure 6.2: The emission-line ratios O3N2, N2, N2O2, and O32 vs. M_* for the $z \sim 2.3$ and $z \sim 0$ comparison samples. The left y-axis displays the emission-line ratio values, while the right y-axis displays the translation into metallicity according to equations 6.7, 6.8, 6.11, and 6.10. All y-axes are oriented such that metallicity increases upwards, and span the same range in metallicity. The $z \sim 2.3$ galaxies with SFR measurements are shown as blue circles when all of the required emission lines are detected for each line ratio, while black arrows display 3σ limits when one or more of the required lines is not detected. Stacks of both detections and non-detections in bins of M_* are indicated by black squares. The red dashed line is the best-fit linear relation to the stacks in each panel, with the best-fit parameters given in Table 6.2. Gray squares show the $z \sim 0$ M_* stacks of Andrews & Martini (2013) prior to correction for DIG contamination, while green squares show the same stacks after correcting for contamination from DIG using the models of Sanders et al. (2017).

6.3.2 Is there SFR dependence of the $z \sim 2.3$ MZR?

As previously mentioned, while it is of interest to determine whether or not $z \sim 0$ and high-redshift galaxies lie on the same M_*-SFR-Z relation (i.e., the FMR holds out to high redshifts), it is more fundamental to establish whether the metallicities of high-redshift galaxies display a secondary dependence on SFR at fixed M_*. The existence of a high-redshift M_*-SFR-Z relation is a prerequisite for interpreting the position of high-redshift galaxies relative to the FMR observed at $z \sim 0$. We look for a M_*-SFR-Z relation at $z \sim 2.3$ by searching for correlated scatter around the MZR and M_*-sSFR relation.

In the left column of Figure 6.3, we show the $z \sim 2.3$ residuals around the mean M_* relations for the line ratios O3N2, N2, and N2O2, and the corresponding O/H residuals, all as a function of residuals around the $z \sim 2.3$ mean M_*-sSFR relation. We show both $z \sim 2.3$ individual galaxies and the M_*-ΔsSFR stacks, the latter color-coded by stellar mass. There is a clear trend among both the stacks and individual galaxies such that the sSFR residuals correlate with O3N2 residuals and anticorrelate with residuals in N2 and N2O2. These trends are as expected in the presence of a M_*-SFR-Z relation, given that O3N2 decreases with increasing metallicity while N2 and N2O2 increase. Furthermore, the correlations are statistically significant based on Spearman correlation tests. The correlation coefficients and p-values are shown in Table 6.3. The corresponding trends in $\Delta\log(\mathrm{O/H})$ are similar for all three metallicity indicators: $\Delta\log(\mathrm{O/H})$ decreases with increasing $\Delta\log(\mathrm{sSFR})$. This trend in the residuals demonstrates that $z \sim 2.3$ galaxies with higher SFR have lower O/H at fixed stellar mass, confirming the existence of a M_*-SFR-Z relation at $z \sim 2.3$. This is the first time that such a relation has been clearly demonstrated to exist at this redshift.

We quantify the strength of the $z \sim 2.3$ M_*-SFR-Z relation by fitting linear relations to the median $\Delta\log(\mathrm{O/H})$ in bins of $\Delta\log(\mathrm{sSFR})$. The best-fit lines are shown in the middle column of Figure 6.3, and the best-fit slopes are given in Table 6.3. These slopes are inconsistent with a flat relation (i.e., no dependence of O/H on SFR at fixed M_*) at $3-4\sigma$. The M_*-ΔsSFR stacks fall on the same relations as the medians of the individual $z \sim 2.3$ galaxies. The high-mass M_*-ΔsSFR stacks most clearly follow the same relation as the medians

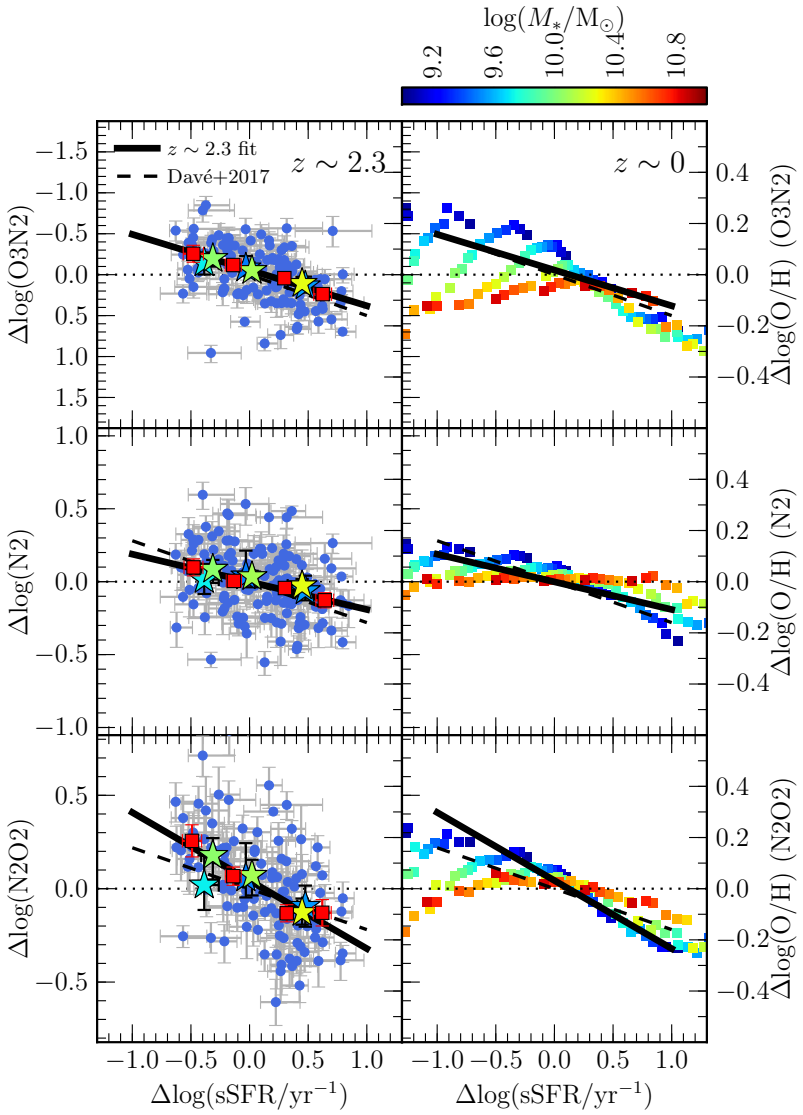

Figure 6.3: Deviation plots comparing the residuals around mean line ratio and metallicity vs. M_* relations (Δlog(line ratio) and Δlog(O/H)) to residuals around the mean M_*-sSFR relation (Δlog(sSFR/yr^{-1})). The top, middle, and bottom rows display residuals for line ratio and metallicities based upon O3N2, N2, and N2O2, respectively. In each panel, the left vertical axis shows the scale of the residuals in each line ratio, while the right vertical axis displays the scale of the corresponding residuals in metallicity. The $z \sim 2.3$ sample is shown in the left column, while the right column presents residuals for the $z \sim 0$ M_*-SFR stacks of Andrews & Martini (2013), color-coded by M_*. In the left column, blue circles denote individual $z \sim 2.3$ galaxies, red squares show medians in bins of Δlog(sSFR/yr^{-1}), and colored stars display the $z \sim 2.3$ M_*-ΔsSFR stacks, color-coded by M_*. The solid black line shows the best fit to the $z \sim 2.3$ medians, with best-fit slope given in Table 6.3. The prediction from the cosmological simulations of Davé et al. (2017) is presented as the black long-dashed line.

Table 6.3: Best-fit slopes and correlation tests of $\Delta\log(\mathrm{O/H})$ vs. $\Delta\log(\mathrm{sSFR/yr^{-1}})$, where O/H is estimated using the indicated strong-line ratio.

line ratio	slope	$r_{\mathrm{s}}^{\mathrm{a}}$	p-value[b]
O3N2	-0.14 ± 0.034	0.48	1.5×10^{-8}
N2	-0.11 ± 0.037	-0.32	8.6×10^{-5}
N2O2	-0.27 ± 0.067	-0.54	3.2×10^{-10}
O32	-0.037 ± 0.022	0.14	0.07

(a) Spearmen correlation coefficient.
(b) Probability of the sample being drawn from an uncorrelated distribution.

of the individual points, while the low-mass M_*-ΔsSFR stacks are noisier but all fall within 1σ of the best-fit relations. The position of the stacks relative to the individual detections suggests that galaxies with non-detections in these emission-line ratios lie on the same anti-correlations. We conclude that requiring line-ratio detections in the individual galaxies does not significantly bias these results.

The right column of Figure 6.3 displays the line-ratio and O/H residuals as a function of $\Delta\log(\mathrm{sSFR})$ for the $z \sim 0$ M_*-SFR stacks, color-coded by M_*. In each panel, we include the best-fit line to the $z \sim 2.3$ sample for comparison. The $z \sim 0$ stacks show similar trends at $\log(M_*/\mathrm{M}_\odot) \lesssim 10.0$, but display the well-known decrease in the strength and disappearance of the SFR dependence at high stellar masses (Mannucci et al., 2010; Yates et al., 2012; Salim et al., 2014), as evidenced by the tendency of high-mass stacks to lie closer to $\Delta\log(\mathrm{O/H}) = 0$ at fixed $\Delta\log(\mathrm{sSFR/yr^{-1}})$. A weakening of the $z \sim 0$ sSFR dependence at $\Delta\log(\mathrm{sSFR/yr^{-1}}) < 0$ is also apparent in all three indicators, as pointed out by Salim et al. (2014). There is no evidence for such a flattening of the M_*-SFR-Z relation at high masses or $\Delta\log(\mathrm{sSFR/yr^{-1}}) < 0$ among the $z \sim 2.3$ M_*-ΔsSFR stacks. However, we note that the mass range in which the $z \sim 0$ sample displays little to no SFR dependence ($\log(M_*/\mathrm{M}_\odot) \gtrsim 10.5$) lies above the mass range probed by the $z \sim 2.3$ sample.

We show the line-ratio and MZR residual plots for O32 in Figure 6.4. There is no clear trend toward lower metallicity with increasing $\Delta\log(\mathrm{sSFR})$ among the $z \sim 2.3$ galaxies when utilizing the O32 indicator. There is no statistically significant correlation present (Table 6.3). In contrast, a clear M_*-SFR-Z relation is present at $z \sim 0$ for O32. We discuss

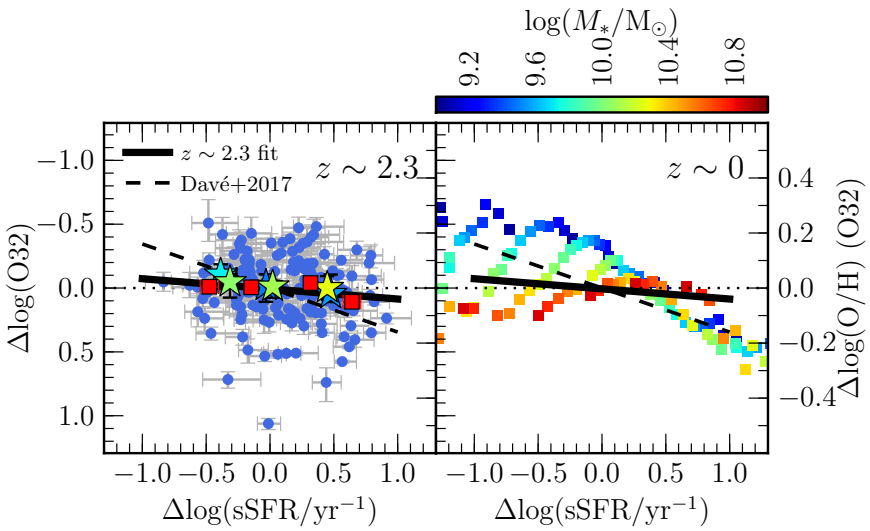

Figure 6.4: Deviation plots for O32 and metallicity estimated using O32, with points and lines the same as in Figure 6.3. In each panel, the left vertical axis shows the scale of the residuals in each line ratio, while the right vertical axis displays the scale of the corresponding residuals in metallicity. The best-fit slope for the $z \sim 2.3$ Δlog(O/H) (O32) vs. Δlog(sSFR/yr^{-1}) relation is presented in Table 6.3.

the lack of SFR dependence at $z \sim 2.3$ for the O32 MZR in Section 6.4.3.

The strong-line ratio O3 is sensitive to both ionization parameter and metallicity. As such, trends indicative of a M_*-SFR-Z relation should be present in the O3 residuals as well. We show O3 as a function of M_* in the left panel of Figure 6.5. The best-fit coefficients are given in Table 6.2. The right panel of Figure 6.5 displays the O3 residuals as a function of sSFR residuals for individual $z \sim 2.3$ galaxies and the M_*-ΔsSFR stacks. A clear correlation is present, with Spearman correlation coefficient $r_s = 0.47$ and probability of being drawn from an uncorrelated distribution of 1.6×10^{-13}. The correlation between Δlog(O3) and Δlog(sSFR) is consistent with a decrease in metallicity (increase in O3) as sSFR increases at fixed M_*. This result agrees with what is found using O3N2, N2, and N2O2.

The strong-line ratio R23 as a function of M_* and the Δlog(R23) vs. Δlog(sSFR) deviation plot are presented in Figure 6.6. R23 is primarily sensitive to O/H because it is a ratio of both low and high ionization state oxygen lines to a hydrogen Balmer line, but has significant ionization parameter dependence as well (Kewley & Dopita, 2002). R23 is not a strong function of M_* for the $z \sim 2.3$ sample, which is anticipated since the R23 values lie close

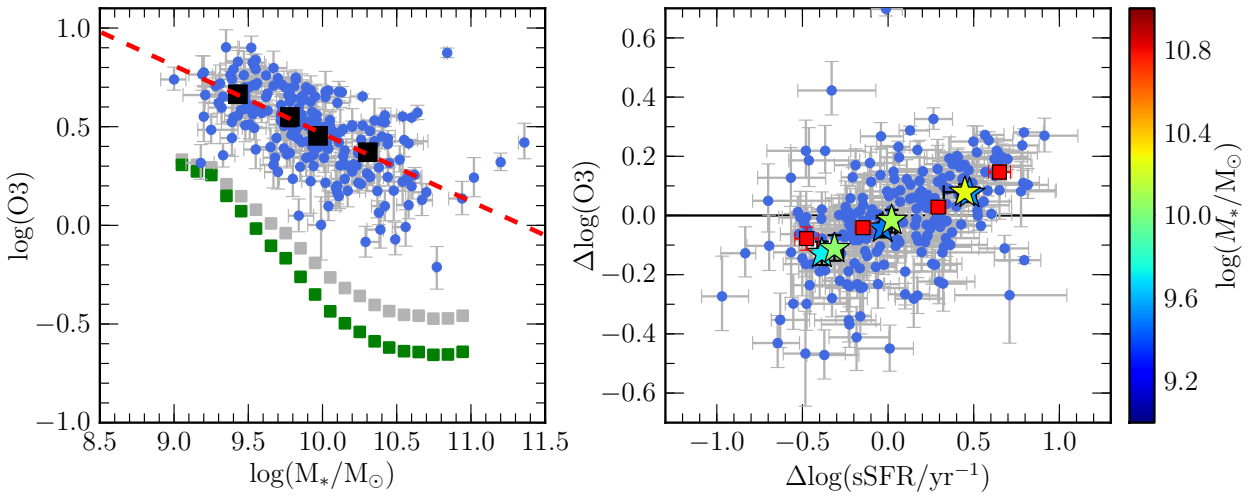

Figure 6.5: LEFT: The line ratio O3 as a function of M_* for the $z \sim 2.3$ and $z \sim 0$ samples, with points and lines the same as in Figure 6.2. RIGHT: The deviation plot of $\Delta\log(\mathrm{O3})$ vs. $\Delta\log(\mathrm{sSFR/yr^{-1}})$ for $z \sim 2.3$ galaxies, with points the same as in the middle column of Figure 6.3.

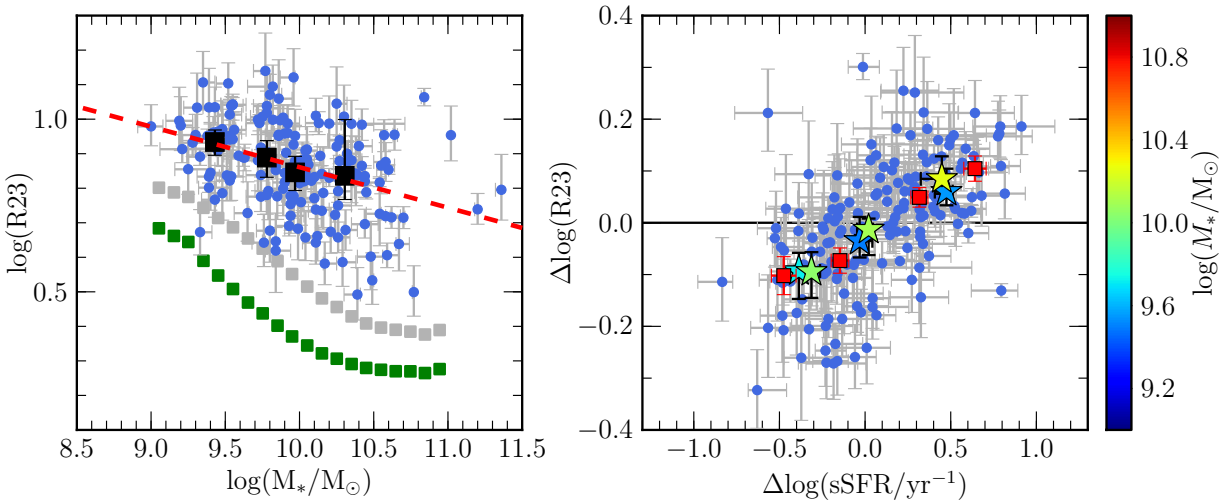

Figure 6.6: LEFT: The line ratio R23 as a function of M_* for the $z \sim 2.3$ and $z \sim 0$ samples, with points and lines the same as in Figure 6.2. RIGHT: The deviation plot of $\Delta\log(\mathrm{R23})$ vs. $\Delta\log(\mathrm{sSFR/yr^{-1}})$ for $z \sim 2.3$ galaxies, with points the same as in the middle column of Figure 6.3.

to the turnover regime in the R23-O/H relation, as described in Section 6.2.4. However, R23 does increase slightly with decreasing M_*, suggesting that our sample mostly lies on the upper metal-rich R23 branch where R23 increases with decreasing O/H. In this case, a positive correlation between Δlog(R23) vs. Δlog(sSFR) is expected if a M_*-SFR-Z relation is present. This positive correlation is observed in the right panel of Fig. 6.6 with high statistical significance ($r_s = 0.60$, p-value $= 7.3 \times 10^{-18}$), in agreement with the trends observed using O3N2, N2, N2O2, and O3.

One important question is whether the SFR dependence we find in the $z \sim 2.3$ MZR is a result of selection effects. We investigated the effect of requiring Hβ S/N$\geq$3 on these results by repeating the analysis to search for a M_*-SFR-Z relation at $z \sim 2.3$ without this requirement. Because we cannot reliably correct for reddening without detections of both Hβ and Hα, we utilized SFRs estimated from FAST SED fitting instead of dust-corrected Hα luminosities. Furthermore, this test could only be performed for the portions of the analysis that involve line ratios that do not require reddening correction (i.e., O3, N2, and O3N2). We found similar results based on these line ratios, although the trends were somewhat weaker for a few reasons. First, there is significant scatter in the correlation between SFR(SED) and SFR(Hα) (Reddy et al., 2015). Second, SFR(Hα) traces star formation on $<$10 Myr timescales while SFR(SED) probes longer timescales of $\sim$100 Myr. It is thus expected that signatures of a M_*-SFR-Z relation are weaker when relying on SFR(SED) since the M_*-SFR-Z relation is thought to be driven by a reaction of SFR and metallicity on short timescales to recent accretion of metal-poor gas (Mannucci et al., 2010; Davé et al., 2012). Finally, a smaller dynamic range of SFR at fixed M_* is probed in this test because M_* and SFR(SED) are not independent of one another, both being estimated by FAST SED fitting. This covariance artificially tightens the M_*-(s)SFR relation, making it more difficult to resolve SFR dependence of metallicity at fixed M_*. Because our results persist when utilizing SFR(SED) without the Hβ detection criterion, we conclude that requiring Hβ S/N$\geq$3 does not strongly bias our results.

6.3.3 Do $z \sim 2.3$ galaxies lie on the $z \sim 0$ FMR?

Having established the existence of a M_*-SFR-Z relation for $z \sim 2.3$ star-forming galaxies, we next address the question of whether or not these galaxies lie on the $z \sim 0$ M_*-SFR-Z relation. In other words, we test whether or a FMR exists that extends out to $z \sim 2.3$. Many studies have attempted to address this question by extrapolating parameterizations of the $z \sim 0$ FMR (e.g., Mannucci et al., 2010; Lara-López et al., 2010) to the high-SFR and high-sSFR regime occupied by high-redshift galaxies (e.g., Wuyts et al., 2012, 2014; Christensen et al., 2012; Belli et al., 2013; Henry et al., 2013; Cullen et al., 2014; Yabe et al., 2014; Zahid et al., 2014b; Kashino et al., 2017). Such extrapolations may not be representative of the true $z \sim 0$ M_*-SFR-Z relation because a parametric form must be assumed that may not represent the underlying physical relation, and the small fraction of $z \sim 0$ objects with SFRs similar to those of high-redshift galaxies will not carry much weight toward the fit, allowing the possibility of a poor fit in the high-SFR regime. Recent studies have shown the benefit of performing non-parametric comparisons instead, relying on the small number of $z \sim 0$ objects with extreme SFRs to directly compare at fixed M_* and SFR (Sanders et al., 2015; Salim et al., 2015; Ly et al., 2016).

We directly compare the position of the $z \sim 2.3$ M_*-ΔsSFR stacks and the $z \sim 0$ M_*-SFR stacks in the mass-metallicity plane in Figure 6.7, with metallicities based on the O3N2, N2, and N2O2 indicators. Both high- and low-redshift stacks are color-coded by SFR on the same scale so that a direct comparison of metallicity at fixed M_* and SFR is possible. The highest-SFR $z \sim 2.3$ stack, with $\log(\mathrm{M_*/M_\odot}) = 10.2$ and $\log(\mathrm{SFR/M_\odot\ yr^{-1}}) \approx 2.0$, does not have any local analogue in the AM13 M_*-SFR sample. However, all other $z \sim 2.3$ stacks have analogous $z \sim 0$ counterparts matched in M_* and SFR. In the O3N2, N2, and N2O2 M_*-Z planes, $z \sim 2.3$ galaxies display metallicities that are systematically lower than their $z \sim 0$ counterparts by ~ 0.1 dex at fixed M_* and SFR. This offset is consistent across a range of M_* and $\Delta\log(\mathrm{sSFR})$ using three different metallicity indicators. We found a similar offset using only O3N2 and N2 with a smaller $z \sim 2.3$ MOSDEF sample in Sanders et al. (2015). We conclude that there is not a FMR that can simultaneously match the properties

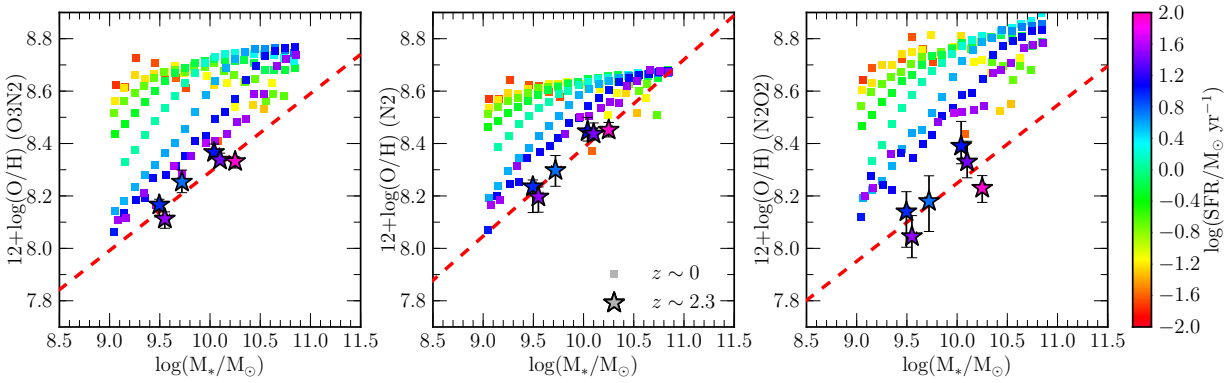

Figure 6.7: The mass-metallicity relation based on O3N2 (left), N2 (middle), and N2O2 (right) for $z \sim 0$ and $z \sim 2.3$ stacks, color-coded by SFR. Colored squares indicate the $z \sim 0$ M_*-SFR stacks of Andrews & Martini (2013). Colored stars with error bars show the $z \sim 2.3$ M_*-ΔsSFR stacks. Both samples are color-coded by SFR on the same scale. The red dashed line denotes the best-fit $z \sim 2.3$ MZR for each line ratio, given in Table 6.2.

of star-forming galaxies from $z \sim 0$ out to $z \sim 2.3$.

We note that the presence of a $z \sim 2.3$ M_*-SFR-Z relation can be seen in Figure 6.7 in the M_*-ΔsSFR stacks, with the lowest-SFR bins at a given M_* falling above the mean $z \sim 2.3$ relation and the highest-SFR bins falling below. This trend is most evident in the O3N2 and N2O2 mass-metallicity planes (Fig. 6.7) for the $z \sim 2.3$ stacks with $\log(M_*/M_\odot) = 10.0-10.3$, as shown by a progression from higher to lower O/H as SFR increases, and the symbol color changes from blue to purple to pink. The presence of such SFR gradients perpendicular to the mean $z \sim 2.3$ MZR is a manifestation of the sSFR dependence shown in Figure 6.3.

We directly compare the strong-line ratios O3, O32, and R23 at fixed $M_*$and SFR for $z \sim 0$ and $z \sim 2.3$ stacks in Figure 6.8. The $z \sim 2.3$ stacks display higher O3 and R23 than $z \sim 0$ stacks at fixed M_* and SFR, suggesting higher excitation and lower metallicity at fixed M_* and SFR at $z \sim 2.3$. This result is consistent with what was found using O3N2, N2, and N2O2. The $z \sim 2.3$ M_*-ΔsSFR stacks also display separation perpendicular to the mean O3-M_* and R23-M_* relations as a function of SFR, consistent with the existence of a M_*-SFR-Z relation at $z \sim 2.3$. The O32 values of the $z \sim 2.3$ stacks are not obviously offset from the $z \sim 0$ stacks matched in M_* and SFR. Once again, results based upon O32 are inconsistent with those from O3N2, N2, N2O2, O3, and R23. We discuss the differences in results based on O32 in Section 6.4.3.

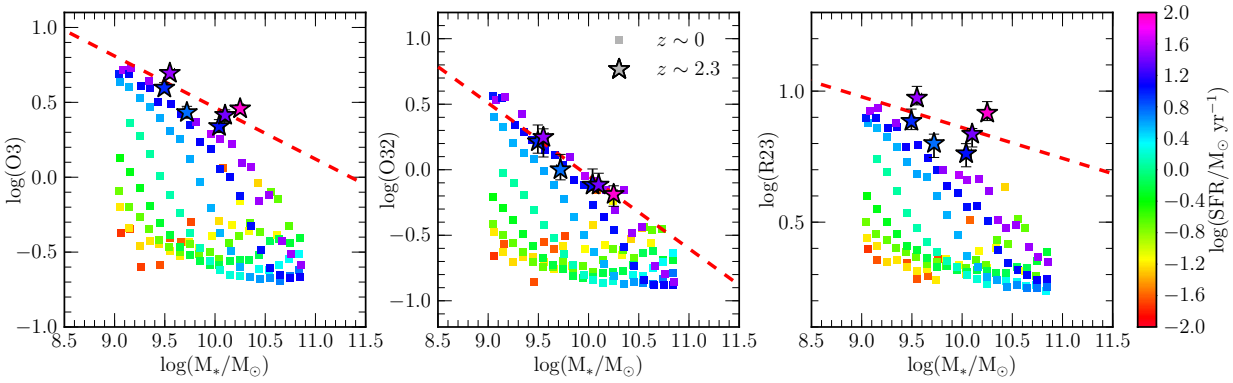

Figure 6.8: The line ratios O3 (left), O32 (middle), and R23 (right) as a function of M_*. Points and lines are the same as in Figure 6.7.

6.4 Discussion

6.4.1 Potential evolution in metallicity calibrations and ionized gas physical conditions

We have clearly demonstrated the existence of a M_*-SFR-Z relation at $z \sim 2.3$ based on multiple emission-line ratios (O3N2, N2, N2O2, O3, and R23) and metallicities inferred using $z \sim 0$ calibrations. We furthermore showed that $z \sim 2.3$ galaxies are offset ~ 0.1 dex lower in metallicity from $z \sim 0$ galaxies at fixed M_* and SFR, arguing against the existence of a redshift invariant M_*-SFR-Z relation. We now consider whether the appearance of a M_*-SFR-Z relation at $z \sim 2.3$ and its evolution with respect to $z \sim 0$ could be produced by other effects in the absence of metallicity variations. Recent work has suggested that the physical conditions of ionized gas in star-forming regions evolve with redshift (e.g., Steidel et al., 2014, 2016; Shapley et al., 2015; Sanders et al., 2016b; Strom et al., 2017; Kashino et al., 2017). The physical conditions of interest are the ionization parameter, N/O abundance ratio, electron density, and the shape of the ionizing spectrum. Changes in these properties lead to changes in emission-line ratios at fixed nebular oxygen abundance (Kewley et al., 2013b). The ionization parameter, N/O ratio, and shape of the ionizing spectrum must be considered at fixed metallicity because of correlations between these properties and the nebular and stellar metallicity.

The only evolving physical condition for which there is a consensus is the electron density.

The typical electron density in star-forming regions increases with redshift, and is an order of magnitude higher at $z \sim 2$ compared to $z \sim 0$ (e.g., Steidel et al., 2014; Sanders et al., 2016b; Kashino et al., 2017). The typical densities at $z \sim 0$ and $z \sim 2.3$ (25 and 250 cm^{-3}, respectively) are both well below the density where strong-line ratios become strongly affected ($\sim$1000 cm^{-3}; Steidel et al., 2014). Thus, evolution in electron density has a negligible impact on our results.

There is not a consensus about the evolution (or lack thereof) of N/O, ionization parameter, and hardness of the ionizing spectrum at fixed metallicity. While this ambiguity makes it difficult to assess the impact of such evolution on metallicity studies, the MOSDEF sample crucially provides access to multiple strong-line ratios, enabling us to determine if evolution in a particular property leads to false conclusions. It has been suggested that high-redshift galaxies have elevated N/O at fixed O/H compared to $z \sim 0$ galaxies, explaining observed evolution in line-ratio diagrams involving nitrogen (Masters et al., 2014; Steidel et al., 2014; Shapley et al., 2015; Sanders et al., 2016b). The elevated N/O could be caused by an unusually high occurrence rate of Wolf-Rayet stars (Masters et al., 2014) or a dilution of O/H by pristine gas inflows while N/O remains roughly constant (Köppen & Hensler, 2005; Amorín et al., 2010; Sanders et al., 2016b). Other studies have argued for a harder ionizing spectrum at fixed nebular abundance in high-redshift star-forming regions (Steidel et al., 2016; Strom et al., 2017). Some have also suggested a higher ionization parameter at fixed metallicity as sSFR increases, leading to an elevated ionization parameter in high-redshift galaxies due to their larger sSFR than $z \sim 0$ galaxies on average (Kewley et al., 2013b,a, 2015, 2016; Kashino et al., 2017). In what follows, we consider the possible effects of these proposed scenarios on our results.

6.4.1.1 Nitrogen-to-oxygen ratio

We observe the $z \sim 2.3$ M_*-SFR-Z relation using the O3N2, N2, and N2O2 metallicity indicators (Fig. 6.3), all of which involve nitrogen. Even if high-redshift galaxies have elevated N/O at fixed O/H, such an effect could only lead to a false inference of a M_*-SFR-Z relation

at $z \sim 2.3$ if N/O depends on SFR and sSFR at fixed M_*. We observe higher O3N2, lower N2, and lower N2O2 with increasing sSFR at fixed M_*. For these trends to be introduced by variations in nitrogen abundance in the absence of metallicity variation, N/O would have to decrease with increasing sSFR at fixed O/H. Such a relation between N/O and sSFR at fixed O/H is inconsistent with the Wolf-Rayet scenario because it requires that high-sSFR environments underproduce Wolf-Rayet stars and thus have lower N/O values at fixed O/H. In contrast, evolutionary scenario proposed by Masters et al. (2014) predicts that high-sSFR environments *overproduce* Wolf-Rayet stars, leading to elevated N/O at fixed O/H in high-redshift galaxies. Accordingly, this scenario cannot reproduce our results on the M_*-SFR-Z relation involving N-based indicators.

In addition to a $z \sim 2.3$ M_*-SFR-Z relation, we found that $z \sim 2.3$ galaxies are offset ~ 0.1 dex lower in metallicity at fixed M_* and SFR compared to the $z \sim 0$ sample (Fig. 6.7). If N/O is higher at fixed O/H at high redshifts, then high-redshift metallicities based on O3N2, N2, and N2O2 would be overestimated. Consequently, the ~ 0.1 dex metallicity offset would be underestimated and our conclusion that the M_*-SFR-Z relation evolves with redshift from $z \sim 0$ to $z \sim 2.3$ still holds, as argued in Sanders et al. (2015). At fixed M_*, we observe an offset toward lower N2 and N2O2, and higher O3N2, for the $z \sim 2.3$ sample. For this offset to be the product of N/O evolution at fixed O/H, high-redshift galaxies would need to have lower N/O at fixed O/H compared to $z \sim 0$. Such a scenario would shift high-redshift galaxies toward lower N2 at fixed O/H. In fact, high-redshift galaxies are observed to be offset significantly *higher* N2 at fixed O3 compared to the $z \sim 0$ star-forming population in the N2 vs. O3 diagram (e.g., Shapley et al., 2005, 2015; Steidel et al., 2014; Sanders et al., 2016b; Strom et al., 2017). It is thus implausible that evolution toward lower N/O at fixed O/H drives the redshift evolution of O3N2, N2, and N2O2 at fixed M_* and SFR.

It is important to note that both the $z \sim 2.3$ M_*-SFR-Z relation and the offset toward lower O/H at fixed M_* and SFR compared to $z \sim 0$ are also observed using O3 and R23, which have no dependence on variations in N/O at fixed O/H (Figs. 6.5, 6.7 and 6.8, left and right panels). Simultaneously obtaining consistent results in N-based and O-based metallicity-sensitive line ratios strongly suggests that possible evolution in N/O at fixed O/H

does not lead us to false conclusions regarding the $z \sim 2.3$ M_*-SFR-Z relation, demonstrating the power of using multiple line ratios to study the evolution of metallicity scaling relations.

6.4.1.2 Ionization parameter and hardness of the ionizing spectrum

Steidel et al. (2016) suggested that the ionizing spectrum is harder at fixed nebular metallicity at high redshifts because of low Fe/O (and therefore low Fe/H at fixed O/H) driven by the young ages of high-redshift stellar populations (see also Strom et al., 2017). This deficiency of Fe relative to O is thought to be a result of the time-delayed nature of Fe enrichment from Type Ia supernovae compared to the prompt enrichment of O from Type II supernovae. In a harder ionizing spectrum, the increased abundance of high-energy ultraviolet photons relative to those at lower energy leads to larger fractions of ions in high ionization states (i.e., [O III]) relative to low-ionization states (i.e., [O II]). Thus a harder ionizing spectrum at fixed metallicity would result in higher excitation-sensitive line ratios at fixed O/H, including O3 and O3N2. The scenario in which the ionization parameter is higher at fixed O/H due to higher sSFR or more concentrated star-formation at high-redshift similarly predicts higher O3 and O3N2 at fixed O/H (Kewley et al., 2013b, 2016; Kashino et al., 2017). However, the two scenarios predict different changes in N2, with a harder ionizing spectrum increasing N2 at fixed O/H, while a higher ionization parameter decreases N2 at fixed O/H.

In the scenario proposed by Steidel et al. (2016), galaxies with the highest sSFR should also have the youngest stellar populations in which Fe/H is lowest. This low Fe abundance in turn produces a harder ionizing spectrum at fixed O/H, such that the highest-sSFR galaxies should have the hardest ionizing spectra at fixed M_*. If this scenario holds, then it could introduce the observed trends in $\Delta\log(\mathrm{O3})$ and $\Delta\log(\mathrm{O3N2})$ as a function of $\Delta\log(\mathrm{sSFR})$ in the absence of a M_*-SFR-Z relation. However, if a harder ionizing spectrum at fixed oxygen abundance is present, then N2 should increase with increasing sSFR at fixed M_*. We observe the opposite trend. Additionally, this scenario predicts that $z \sim 2.3$ galaxies should have higher O3N2, O3, and N2 than $z \sim 0$ galaxies at fixed O/H. We observe higher O3N2 and O3, but lower N2 at $z \sim 2.3$ compared to $z \sim 0$ galaxies at fixed M_* and SFR.

Therefore, a harder ionizing spectrum at fixed metallicity driven by Fe/O variations cannot simultaneously reproduce the observed trends in O3N2, O3, and N2, and if present would not lead us to falsely infer the presence of both a $z \sim 2.3$ M_*-SFR-Z relation and an evolving M_*-SFR-Z relation.

Since the evolving ionization parameter scenario suggests that ionization parameter increases at fixed O/H with increasing sSFR, it is straighforward to understand how the trends of Δlog(O3), Δlog(O3N2), and Δlog(N2) vs. Δlog(sSFR) could appear in the absence of metallicity variation. A higher ionization parameter at fixed O/H at high redshift could also introduce the offsets observed in O3N2, N2, and O3 between $z \sim 0$ and $z \sim 2.3$ galaxies at fixed M_* and SFR. It is thus possible that an increase in ionization parameter at fixed O/H that is dependent on sSFR could reproduce the observed trends in O3N2, N2, and O3 at $z \sim 2.3$.

However, N2O2 would not be significantly affected by changes in the ionization parameter, since it is a ratio of collisionally excited lines of two low-ionization species with similar ionization energies (Kewley & Dopita, 2002). The observation of the $z \sim 2.3$ M_*-SFR-Z relation and the metallicity offset between $z \sim 0$ and $z \sim 2.3$ galaxies at fixed M_* and SFR based on N2O2 suggests that the trends in O3, O3N2, and N2 are not purely driven by changes in ionization parameter at fixed metallicity. We conclude that our evidence for the existence of a $z \sim 2.3$ M_*-SFR-Z relation is not introduced by changes in ionization parameter at fixed O/H as a function of sSFR, and that the inferred evolution of the M_*-SFR-Z relation from $z \sim 0$ to $z \sim 2.3$ is also not a consequence of such evolution.

Collectively, our analyses of potential biases introduced by evolving N/O, ionization parameter, and ionizing spectrum at fixed metallicity suggest that the observed trends in O3N2, N2, N2O2, and O3 are primarily driven by metallicity variations, and that the $z \sim 2.3$ M_*-SFR-Z relation and evolution in O/H at fixed M_* and SFR are real. We note that the above discussion does not preclude evolution in gas physical conditions with redshift, but instead shows that the examined evolutionary scenarios cannot simultaneously produce our results over the range of emission-line ratios used here in the absence of metallicity variation. We have considered evolution in each property separately, but it may be the

case that a combination of the proposed evolutionary scenarios is required to explain high-redshift observations (e.g., both a harder ionizing spectrum and higher N/O at fixed O/H). In that case, a more careful analysis accounting for the magnitude of shifts in line ratios from changes in each property would be needed. However, our results are consistent with a change in metallicity with SFR at fixed M_* being the primary driver of the observed trends in O3, O3N2, N2, and N2O2. Evolution in other gas properties likely has a secondary effect on the strength of these trends.

6.4.2 Implications of the evolution of the M_*-SFR-Z relation

The existence of a M_*-SFR-Z relation at $z \sim 2.3$ confirms that the current theoretical framework for galaxy growth through the interplay of inflows, outflows, and star formation is applicable at high redshifts. A M_*-SFR-Z relation is predicted to exist at high redshifts in analytical chemical evolution models (Finlator & Davé, 2008; Davé et al., 2012; Lilly et al., 2013) as well as cosmological hydrodynamical simulations including chemical evolution (Ma et al., 2016; Davé et al., 2017; De Rossi et al., 2017). There are both observational evidence and theoretical predictions that the M_*-SFR-Z relation is a manifestation of a more fundamental relation with gas mass, where the SFR is modulated by the amount of gas in a galaxy (Hughes et al., 2013; Bothwell et al., 2013, 2016a,b; Zahid et al., 2014a; Ma et al., 2016; Davé et al., 2017). Confirmation of a M_*-SFR-Z relation at $z \sim 2.3$ suggests that galaxy chemical evolution is linked to gas content at high redshifts as well. The increasing number of observations of the cold gas content of high-redshift galaxies (e.g., Tacconi et al., 2013) will allow for investigations of the relation between M_*, SFR, Z, and gas fraction at high redshifts.

By comparing residuals in metallicity and sSFR around the MZR and mean M_*-sSFR relation, we have quantified the strength of the SFR dependence of the M_*-SFR-Z relation at both $z \sim 0$ and $z \sim 2.3$. Current cosmological hydrodynamical simulations predict that the strength of the SFR dependence does not change with redshift (Davé et al., 2017; De Rossi et al., 2017). Using the MUFASA simulations (Davé et al., 2016), Davé et al. (2017)

predicted the slope of the $\Delta\log(\mathrm{O/H})$ vs. $\Delta\log(\mathrm{sSFR})$ relation, finding the preferred slope to be -0.16 and independent of redshift. We have quantified this measure of the M_*-SFR-Z relation for our $z \sim 2.3$ sample, providing best-fit slopes based on the O3N2, N2, and N2O2 metallicity indicators in Table 6.3.

We compare our observed $z \sim 2.3$ $\Delta\log(\mathrm{O/H})$ vs. $\Delta\log(\mathrm{sSFR})$ relations to the prediction of Davé et al. (2017) in the middle column of Figure 6.3, and perform the same comparison for the $z \sim 0$ sample in the right column. In each panel, the solid black line is the best-fit $z \sim 2.3$ relation and the dashed black line shows the prediction of Davé et al. (2017). We find weaker SFR dependence at $z \sim 2.3$ than predicted by Davé et al. (2017) based on O3N2 and N2, and stronger SFR dependence when using N2O2 to estimate metallicites. The O3N2, N2, and N2O2 best-fit slopes all agree with the Davé et al. (2017) prediction within 2σ. Taking the uncertainty-weighted average of the three $z \sim 2.3$ slopes yields a slope of -0.14 ± 0.022, which is within 1σ of a slope of -0.16. Our results are thus consistent with the predictions of the MUFASA simulations, although both the measurement and systematic uncertainties remain large.

The SFR dependence of the $z \sim 2.3$ sample displays a similar strength to that of $z \sim 0$ galaxies with $\log(M_*/\mathrm{M}_\odot) < 10.0$ and $\Delta\log(\mathrm{sSFR/yr}^{-1}) > 0$ when using the N2 and N2O2 indicators (Fig. 6.3). When using the O3N2 indicator, the $z \sim 0$ relation appears to be somewhat stronger than at $z \sim 2.3$. Overall, the observations do not suggest large changes in the strength of the SFR dependence of metallicity at fixed M_* and SFR over the past 10.5 Gyr. We caution that a detailed comparison of the strength of the $z \sim 0$ and $z \sim 2.3$ M_*-SFR-Z relation requires a more complete understanding of the redshift evolution of gas physical conditions and the corresponding effects on metallicity indicators. Recalibration of strong-line ratio metallicity relations at high redshift using electron-temperature-based direct metallicities provides a promising avenue to eliminate these systematics (e.g., Jones et al., 2015; Sanders et al., 2016a).

The ~ 0.1 dex offset toward lower metallicity at fixed M_* and SFR observed from $z \sim 0$ to $z \sim 2.3$ demonstrates that the M_*-SFR-Z relation is not redshift invariant. While this shift in metallicity is fairly small, a systematic offset is observed across more than an order

of magnitude in M_* and SFR using four different metallicity-sensitive line ratios (O3N2, N2, N2O2, and O3). Observing the evolution of the M_*-SFR-Z relation in multiple line ratios simultaneously allowed us to show that this metallicity offset cannot be a false inference due to potential evolution of metallicity calibrations with redshift.

In Sanders et al. (2015), we found a similar evolution in O/H at fixed M_* and SFR, and speculated that such an offset could be introduced if the inflow rate exceeded the sum of the SFR and outflow rate such that the gas reservoir grows faster than it can be processed via star formation. While such a gas-accumulation phase is predicted to exist, both models and observations suggest that it should only occur at $z > 4$ (Davé et al., 2012; Papovich et al., 2011). This phase can be made to reach $z \sim 2$ in models with no outflows (Davé et al., 2012), which are clearly unphysical given the observational constraints on the occurrence of galactic winds at high redshifts (e.g., Steidel et al., 2010). It is thus unlikely that we are observing the buildup of galaxy gas reservoirs.

If the most fundamental relation is between M_*, metallicity, and gas content and that relation is redshift invariant, then an evolving M_*-SFR-Z relation would be indicative of an evolving relation between SFR and gas mass. If a non-evolving relation between M_*, gas fraction, and metallicity exists, then galaxies at $z \sim 0$ and $z \sim 2.3$ have the same gas mass at fixed M_* and metallicity. The observed trend of decreasing metallicity at fixed M_* and SFR with increasing redshift could then be understood as decreasing SFR at fixed M_* and gas fraction (i.e., lower star-formation efficiency). However, an inferred decrease in $z \sim 2$ star-formation efficiency at fixed M_* is in conflict with the interpretation of recent observations of cold gas in high-redshift galaxies. Scoville et al. (2016, 2017) found that, at fixed M_* star-formation efficiency per unit ISM gas mass *increases* with increasing redshift using ALMA observations of luminous star-forming galaxies at $z \sim 1 - 6$. Furthermore, molecular gas depletion timescales of galaxies on the mean M_*-SFR relation are shorter at $z \sim 1 - 3$ than at $z \sim 0$ (Tacconi et al., 2013; Genzel et al., 2015), suggesting an increase in star-formation efficiency with redshift. Reconciling these observations with the observed evolution of the M_*-SFR-Z relation requires an evolving relationship among M_*, gas fraction, and metallicity such that metallicity decreases at fixed M_* and gas fraction with increasing redshift. Since

a decreasing star-formation efficiency with increasing redshift at fixed M_* conflicts with observational constraints, we must investigate other drivers of M_*-SFR-Z evolution.

The cause of an evolving M_*-SFR-Z relation can also be understood through analytical chemical evolution models. The gas-regulator model of Lilly et al. (2013) allows for an evolving M_*-SFR-Z relation if the gas consumption timescale and/or the mass-loading factor (η=outflow rate/SFR) at fixed M_* change with redshift. In this context, an evolving relation toward lower metallicity at fixed M_* and SFR with increasing redshift suggests that, at fixed M_*, either the gas consumption timescale is longer (i.e., star-formation efficiency is lower) at higher redshifts or η is higher at earlier times. The equilibrium model of Davé et al. (2012) similarly predicts lower O/H at fixed M_* and SFR at high redshifts if η increases at fixed M_* with increasing redshift. Although a lower star-formation efficiency at higher redshift appears to be in conflict with the observations detailed above, a larger typical high-redshift mass-loading factor is at least broadly consistent with observational constraints over a wide range of M_* and redshift (e.g., Pettini et al., 2002; Rupke et al., 2005; Weiner et al., 2009; Steidel et al., 2010; Heckman et al., 2015; Chisholm et al., 2017). We do note, however, that estimates of η carry large systematic uncertainties.

In both the equilibrium model of Davé et al. (2012) and the gas-regulator model of Lilly et al. (2013), the ISM metallicity at fixed M_* and SFR decreases if the metallicity of the inflowing gas decreases. Although accreted gas is relatively unenriched compared to the ISM, it is not metal-free. Numerical simulations have shown that accreted gas is a mix of relatively pristine gas from the IGM and enriched gas that was ejected in past outflows (e.g., Oppenheimer et al., 2010; Segers et al., 2016; Anglés-Alcázar et al., 2017). Recycled gas can even become the dominant source of fuel for star formation at $z < 1$ (Oppenheimer et al., 2010). Thus evolution toward lower metallicity at fixed M_* and SFR at $z \sim 2.3$ could also be explained by a decrease in the metallicity of infalling gas at high redshift caused by a lower importance of recycled gas accretion relative to pristine accretion from the IGM. Numerical simulations agree with this scenario. Indeed, in the models of Davé et al. (2011), an increase in the metallicity of infalling gas relative to that of the ISM was the primary driver of the increase in metallicity at fixed M_* with decreasing redshift. Anglés-Alcázar et al.

(2017) found that the relative importance of recycled gas to total accretion increases with decreasing redshift in the FIRE zoom-in simulations and additionally suggest that transfer of metals between galaxies via galactic winds occurs at $z = 0$, further increasing the metallicity of infalling gas at $z \sim 0$ compared to that at $z \sim 2$.

We conclude that the offset toward lower O/H at fixed M_* and SFR with increasing redshift is most likely caused by an increase in the mass-loading factor at fixed M_* from $z \sim 0$ to $z \sim 2$ and a decrease in the metallicity of infalling gas due to a higher relative importance of pristine accretion from the IGM at $z \sim 2$.

6.4.3 The inconsistency of results based on O32

While results based on O3N2, N2, N2O2, O3, and R23 are all consistent with respect to both the existence of a $z \sim 2.3$ M_*-SFR-Z relation and the ~ 0.1 dex offset toward lower metallicity at fixed M_* and SFR, performing the same analysis using O32 yields different results. The Δlog(O32) vs. Δlog(sSFR) diagram shows no evidence for SFR dependence of O/H at fixed M_* (Fig. 6.4). Furthermore, there is little if any evolution in O32 at fixed M_* and SFR from $z \sim 0$ to $z \sim 2.3$ (Fig. 6.8, middle panel). The disagreement between results based on O32 compared to those based on the other line ratios requires closer examination.

Since the emission lines in O32 are widely separated in wavelength, it is natural to suspect that incorrect reddening corrections may give rise to discrepant results based on O32. If there are large galaxy-to-galaxy deviations from the assumed Cardelli et al. (1989) attenuation curve, a trend in O32 with SFR at fixed M_* could be washed out. However, systematic effects associated with galaxy-to-galaxy variations in the attenuation curve do not appear to have a significant effect on the O32 results, since we see strong trends in N2O2 and R23 (which also require a reddening correction) with SFR at fixed M_*.

SFR dependence of O32 at fixed M_* could also be hidden if our assumed dust-correction recipe overestimates $E(B\text{-}V)_{gas}$ for galaxies lying above the mean $z \sim 2.3$ SFR-M_* relation and/or underestimates $E(B\text{-}V)_{gas}$ in the opposite regime. In this case, O32 values at low Δlog(sSFR) would be overestimated while the opposite would occur at high Δlog(sSFR),

masking the presence of a M_*-SFR-Z relation. Interestingly, such a scenario would *steepen* Δlog(R23) vs. Δlog(sSFR) and Δlog(N2O2) vs. Δlog(sSFR) beyond what is expected based on the M_*-SFR-Z relation because R23 increases and N2O2 decreases with increasing SFR at fixed M_* (Figs. 6.3 and 6.6). Indeed, we find that the slope of Δlog(O/H) vs. Δlog(sSFR) is steepest when metallicities are based on N2O2, and that Δlog(R23) vs. Δlog(sSFR) displays the strongest correlation of all line ratios considered here. It is therefore possible that our dust-correction recipe leads to either underestimated $\mathrm{E(B\text{-}V)_{gas}}$ for $z \sim 2.3$ galaxies below the SFR-M_* relation, overestimated $\mathrm{E(B\text{-}V)_{gas}}$ for objects above the SFR-M_* relation, or both. If true, a bias in $\mathrm{E(B\text{-}V)_{gas}}$ dependent on SFR suggests that the nebular attenuation curve systematically changes with SFR at fixed M_* at $z \sim 2.3$. Studies of the stellar continuum attenuation curve and the differential reddening between the continuum and nebular emission lines at high redshifts have similarly suggested a systematic dependence of the shape of the attenuation curve on SFR and sSFR (Kriek & Conroy, 2013; Price et al., 2014; Reddy et al., 2015). We note that the resulting bias would affect the measured strength of the SFR dependence of O/H at fixed M_* using O3N2, N2, and O3 as well, since biases in $\mathrm{E(B\text{-}V)_{gas}}$ will change Δlog(sSFR).

Biases in reddening corrections may also explain why no evolution in O32 at fixed M_* and SFR is observed from $z \sim 0$ to $z \sim 2.3$. If $\mathrm{E(B\text{-}V)_{gas}}$ is systematically overestimated in the $z \sim 2.3$ sample, then the high-redshift O32 values would be underestimated and fall closer to the $z \sim 0$ galaxies, reducing any offset present. If this is the case, then the offset in O/H at fixed M_* and SFR based on N2O2 is *overestimated*. In Figure 6.7, the metallicity offset at fixed M_* and SFR based on N2O2 is larger than what is found using O3N2 and N2, consistent with an overestimate of the reddening correction at $z \sim 2.3$. It is thus plausible that biases in the dust-correction can explain the discrepant O32 results.

Unlike O3, O3N2, N2, N2O2, and R23, O32 directly probes the ionization parameter and is only sensitive to metallicity because of the anticorrelation between ionization parameter and metallicity. This anticorrelation arises because gas-phase metallicity and stellar metallicity are correlated, giving rise to harder ionizing spectra and, consequently, higher ionization parameters in lower metallicity star-forming regions (Dopita et al., 2006a,b). The

O32 results could be explained if ionization parameter does not depend on metallicity at $z \sim 2.3$. However, such a scenario would weaken trends in O3N2 and O3, both of which are strongly sensitive to ionization parameter in addition to metallicity. We observe clear trends in O3N2 and O3 as a function of SFR at fixed M_*. Furthermore, O32 is clearly still related to metallicity given that O32 is anticorrelated with stellar mass, and a similar MZR is obtained when using O32 compared to those based on O3N2, N2, and N2O2 (Fig. 6.2). We conclude that ionization parameter and metallicity are still anticorrelated at $z \sim 2.3$, though not necessarily in the same form as at $z \sim 0$.

Another possibility is that the scatter in the ionization parameter vs. metallicity relation is significantly larger at high redshifts than at $z \sim 0$. If this is the case, additional scatter would be introduced in the relationship between O32 and metallicity, potentially washing out trends in O32 with SFR at fixed M_*. This scenario can be tested by measuring the scatter in O32 at fixed metallicity at $z \sim 2.3$, where metallicity is based on temperature-sensitive auroral-line measurements, but a data set on which to perform such an analysis does not yet exist.

Based on the information currently available, biases arising from the reddening correction are the most likely explanation of the discrepant O32 results. These biases are such that $\mathrm{E(B\text{-}V)_{gas}}$ is systematically overestimated at $z \sim 2.3$, and the magnitude of this overestimate increases with increasing SFR at fixed M_*.

6.5 Summary and conclusions

We have investigated the relationship between M_*, SFR, and gas-phase oxygen abundance at high redshifts using a large, representative sample of $z \sim 2.3$ star-forming galaxies from the MOSDEF survey. The MOSDEF data set allows us to study this relation using multiple metallicity- and excitation-sensitive line ratios (O3N2, N2, N2O2, O32, O3, R23), and derive robust dust-corrected SFRs based on Hα luminosity. We searched for the presence of a M_*-SFR-Z relation at $z \sim 2.3$ by looking for correlations between the scatter around the MZR and the mean $z \sim 2.3$ M_*-sSFR relation. We additionally performed a direct comparison of

stacks of $z \sim 2.3$ and $z \sim 0$ galaxies matched in M_* and SFR to determine whether or not the M_*-SFR-Z relation evolves with redshift. Our main results are summarized below.

We presented the detection of a M_*-SFR-Z relation at $z \sim 2.3$ based on metallicities estimated using three different emission-line ratios (O3N2, N2, and N2O2). While it is non-trivial to estimate metallicity using O3 and R23 due to a double-valued nature, results based on observed O3 and R23 are consistent. This study uniquely performed an analysis of the M_*-SFR-Z relation using multiple emission lines simultaneously, which allowed us to rule out the possibility of evolving physical conditions in high-redshift star-forming regions introducing the observed trends in the absence of a M_*-SFR-Z relation. Our results cannot be reproduced by the proposed redshift evolution of electron density, N/O, ionization parameter, or shape of the ionizing spectrum at fixed metallicity in the absence of metallicity variations. However, our analysis does not confirm or rule out the presence of any of the proposed evolutionary scenarios in our high-redshift sample. We find that the SFR dependence of the observed $z \sim 2.3$ M_*-SFR-Z relation is similar in strength to the predictions from the recent MUFASA cosmological hydrodynamical simulations of Davé et al. (2017).

We show strong evidence that the M_*-SFR-Z relation is not redshift invariant, but evolves with redshift such that $z \sim 2.3$ galaxies have ~ 0.1 dex lower metallicity than $z \sim 0$ galaxies at fixed M_* and SFR. Our results are consistent between five different line ratios (O3N2, N2, N2O2, O3, and R23). These results argue against the existence of a non-evolving M_*-SFR-Z relation (Mannucci et al., 2010). The evolving M_*-SFR-Z relation suggests an evolving relation between M_*, gas fraction, and metallicity based on observations implying higher star-formation efficiency and lower molecular gas depletion times at high redshifts (Tacconi et al., 2013; Genzel et al., 2015; Scoville et al., 2016, 2017). Furthermore, we found that the trend toward lower O/H at fixed M_* and SFR is likely driven by an increase in the mass-loading factor and a decrease in the metallicity of infalling gas with redshift at fixed M_*. The latter suggests that accretion of recycled gas is less important relative to accretion of pristine gas from the IGM at $z \sim 2$ than at $z \sim 0$.

Despite observing consistent trends using O3N2, N2, N2O2, O3, and R23, we found that results based upon O32 do not display the presence of a M_*-SFR-Z relation or significant

redshift evolution in metallicity at fixed M_* and SFR. Given the agreement of results based on all other line ratios, we conclude that systematic effects must bias the observed trends in O32. A comparison of results based on O32, N2O2, and R23 (all of which require reddening corrections) suggests that E(B-V)$_{\rm gas}$ is overestimated at $z \sim 2.3$ when E(B-V)$_{\rm gas}$ is determined using Hα/Hβ and the Cardelli et al. (1989) Milky Way extinction curve, and that the magnitude of this overestimate increases with increasing SFR at fixed M_*. Reevaluation of the nebular attenuation curve may be required at high redshifts.

The existence of a M_*-SFR-Z relation at $z \sim 2.3$ confirms that the theoretical framework through which we view galaxy evolution is applicable at high redshifts. Interplay among gas inflows, the gas reservoir, star formation, feedback, and gas outflows have shaped the growth history of the baryonic content of galaxies since at least $z \sim 2.3$. This analysis shows the promise of statistical high-redshift samples to make higher-order tests of cosmological hydrodynamical simulations including chemical evolution. Our ability to utilize rich high-redshift spectroscopic data sets such as the MOSDEF data set to the fullest requires a complete understanding of the evolution of physical conditions in star-forming regions and metallicity calibrations with redshift. Until such understanding is attained, detailed quantitative comparisons of high-redshift data and chemical evolution models will necessarily need caveats. New observational facilities on the horizon such as the James Webb Space Telescope (JWST) and Thirty Meter Telescope (TMT) will obtain large samples of temperature-sensitive auroral-line measurements for high-redshift galaxies that will revolutionize the determination of metallicities at high redshifts.

CHAPTER 7

Summary and Closing Remarks

7.1 Summary

In this dissertation, I have presented five studies focused on characterizing the physical conditions in star-forming galaxies throughout cosmic history with the goal of obtaining robust galaxy metallicity measurements. This work has improved the characterization of metallicity scaling relations at $z \sim 2$, yielding new insights into the nature of gas flows and galaxy growth, and additionally addressed a number of systematic biases affecting metallicity measurements at $z \sim 0$ and $z \gtrsim 2$. The main results and conclusions from each investigation are summarized below.

In Chapter 2, I presented results on the $z \sim 2.3$ mass-metallicity relation using early observations from the MOSDEF survey. I used an initial sample of 87 star-forming galaxies with spectroscopic coverage of Hβ, [O III]λ5007, Hα, and [N II]λ6584 rest-frame optical emission lines, finding a positive correlation between stellar mass and metallicity among individual $z \sim 2.3$ galaxies using both the N2 and O3N2 metallicity indicators. Results based on composite spectra of galaxies in bins of stellar mass were consistent, displaying a monotonic increase in metallicity with increasing stellar mass offset $\sim 0.15-0.3$ dex below the local MZR. When the sample was divided at the median SFR, significant SFR dependence of the $z \sim 2.3$ MZR was not observed among either individual galaxies or composite spectra. I furthermore found that $z \sim 2.3$ galaxies have metallicities ~ 0.1 dex lower at a given stellar mass and SFR than is observed locally. This offset suggests that high-redshift galaxies do not fall on the local "fundamental metallicity relation" among stellar mass, metallicity, and SFR, and may provide evidence of a phase of galaxy growth in which the gas reservoir is

built up due to inflow rates that are higher than star-formation and outflow rates. However, robust conclusions regarding the gas-phase oxygen abundances of high-redshift galaxies await a systematic reappraisal of the application of locally calibrated metallicity indicators at high redshift.

I investigated the electron density and ionization state of star-forming regions in $z \sim 2.3$ galaxies in Chapter 3. From measurements of the [O II]$\lambda\lambda$3726,3729 and [S II]$\lambda\lambda$6716,6731 doublets, I found a median electron density of ~ 250 cm^{-3} at $z \sim 2.3$, an increase of an order of magnitude compared to measurements of galaxies at $z \sim 0$. While $z \sim 2.3$ galaxies are offset towards significantly higher O_{32} values relative to local galaxies at fixed stellar mass, the high-redshift sample follows a similar distribution to the low-metallicity tail of the local distribution in the O_{32} vs. R_{23} and O3N2 diagrams. Based on these results, I proposed that $z \sim 2.3$ star-forming galaxies have the same ionization parameter as local galaxies at fixed metallicity. In combination with simple photoionization models, the position of local and $z \sim 2.3$ galaxies in excitation diagrams suggests that there is no significant change in the hardness of the ionizing spectrum at fixed metallicity from $z \sim 0$ to $z \sim 2.3$. Star-forming galaxies at $z \sim 2.3$ show no offset compared to low-metallicity local galaxies in emission line ratio diagrams involving only lines of hydrogen, oxygen, and sulfur, but display a systematic offset in diagrams involving [N II]λ6584. These results suggest that the offset of $z \sim 2.3$ galaxies from the local star-forming sequence in the [N II] BPT diagram is primarily driven by elevated N/O at fixed O/H compared to local galaxies. The local gas-phase and stellar metallicity appears to set the ionization state of star-forming regions at both $z \sim 0$ and $z \sim 2$.

In Chapter 4, I presented measurements of the electron-temperature based oxygen abundance for a highly star-forming galaxy at $z = 3.08$. This is the highest redshift at which [O III]λ4363 has been detected, and the first time that this line has been measured at $z > 2$. The galaxy, COSMOS-1908, is a low-mass ($10^{9.3}$ M$_\odot$), highly star-forming (~ 50 M$_\odot$ yr^{-1}) system that hosts a young stellar population ($\sim$ 160 Myr). Based on the derived electron temperature, COSMOS-1908 has an oxygen abundance of $12+\log(\mathrm{O/H}) = 8.00^{+0.13}_{-0.14}$ (20% solar metallicity). An investigation of the physical conditions of the ionized gas in

COSMOS-1908 showed that this galaxy has a high ionization parameter, little nebular reddening ($E(B-V)_{\rm gas} < 0.14$), and a high electron density ($n_e \sim 500$ cm^{-3}). I compared the ratios of strong oxygen, neon, and hydrogen lines to the direct-method oxygen abundance for COSMOS-1908 and additional star-forming galaxies at $z = 0 - 1.8$ with [O III]λ4363 measurements, and demonstrated that galaxies at $z \sim 1 - 3$ follow the same strong-line correlations as galaxies in the local universe. This agreement suggests that the relationship between ionization parameter and O/H is similar for $z \sim 0$ and high-redshift galaxies. These results imply that metallicity calibrations based on lines of oxygen, neon, and hydrogen do not strongly evolve with redshift and can reliably estimate abundances out to $z \sim 3$, paving the way for robust measurements of the evolution of the mass-metallicity relation to high redshift.

Obtaining unbiased global galaxy gas-phase oxygen abundances requires proper treatment of the various line-emitting sources within spectroscopic apertures. In Chapter 5, I described a model framework that treats galaxies as ensembles of H II and diffuse ionized gas regions of varying metallicities. These models are based upon empirical relations between line ratios and electron temperature for H II regions, and DIG strong-line ratio relations from SDSS-IV MaNGA IFU data. Flux-weighting effects and DIG contamination can significantly affect properties inferred from global galaxy spectra, biasing metallicity estimates by more than 0.3 dex in some cases. I used observationally-motivated inputs to construct a model matched to typical local star-forming galaxies, and quantify the biases in strong-line ratios, electron temperatures, and direct-method metallicities as inferred from global galaxy spectra relative to the median values of the H II region distributions in each galaxy. A generalized set of models and a correction recipe that can be applied to individual galaxies or galaxy samples in atypical regions of parameter space is provided. These models were used to correct for the effects of flux-weighting and DIG contamination in the local direct-method mass-metallicity and fundamental metallicity relations, and in the mass-metallicity relation based on strong-line metallicities. Future photoionization models of galaxy line emission need to include DIG emission and represent galaxies as ensembles of emitting regions with varying metallicity, instead of as single H II regions with effective properties, in order to

obtain unbiased estimates of key underlying physical properties.

In Chapter 6, I investigated the nature of the relation among stellar mass, star-formation rate, and gas-phase metallicity (the M_*-SFR-Z relation) at high redshifts using a sample of 260 star-forming galaxies at $z \sim 2.3$ from the MOSDEF survey. I presented an analysis of the high-redshift M_*-SFR-Z relation based on several emission-line ratios for the first time. I showed that a M_*-SFR-Z relation clearly exists at $z \sim 2.3$. The strength of this relation is similar to predictions from cosmological hydrodynamical simulations. A direct comparison of stacks of $z \sim 0$ and $z \sim 2.3$ galaxies demonstrates that $z \sim 2.3$ galaxies have ~ 0.1 dex lower metallicity at fixed M_* and SFR. In the context of chemical evolution models, this evolution of the M_*-SFR-Z relation suggests an increase with redshift of the mass-loading factor at fixed M_*, as well as a decrease in the metallicity of infalling gas that is likely due to a lower importance of gas recycling relative to accretion from the intergalactic medium at high redshifts. Performing this analysis simultaneously with multiple metallicity-sensitive line ratios allows us to rule out the evolution in physical conditions (e.g., N/O ratio, ionization parameter, and hardness of the ionizing spectrum) at fixed metallicity as the source of the observed trends with redshift and with SFR at fixed M_* at $z \sim 2.3$. While this study highlights the promise of performing high-order tests of chemical evolution models at high redshifts, detailed quantitative comparisons ultimately await a full understanding of the evolution of metallicity calibrations with redshift.

7.2 Ongiong and future work

In combination, the studies presented in this dissertation represent a step forward in our understanding of the chemical evolution of galaxies, collectively improving constraints on the physical conditions in star-forming regions in the early universe and highlighting several important systematic biases affecting metallicity measurements at low and high redshifts. There are many avenues for further investigation to address remaining systematic metallicity biases, improve measurements of metallicity scaling relations, and expand the investigation of metallicity scaling relations at high-redshift beyond dependence on M_* and SFR. I describe

ongoing efforts to expand upon the work presented herein and discuss the future outlook with the advent of new observational facilities below.

In Chapter 3, I concluded that the lack of an offset between $z \sim 0$ and $z \sim 2.3$ galaxies in diagrams involving lines of sulfur and oxygen pointed to evolution of N/O at fixed metallicity while ionization parameter and the ionizing spectrum did not significantly evolve. Since DIG emission strongly affects [S II] and [O II] in $z \sim 0$ galaxy spectra (Chapter 5), the comparison between $z \sim 0$ and $z \sim 2$ was biased such that there likely is a high-redshift offset in line-ratio diagrams involving [S II] and [O II]. Results from Chapter 3 regarding evolution of the ionization state and shape of the ionizing spectrum at fixed metallicity must be revisited accordingly.

The impact of DIG emission on high-redshift metallicity estimates is not yet constrained. In the local universe, the relative importance of DIG emission decreases with increasing concentration of star formation such that DIG emission is negligible in starburst galaxies (Oey et al., 2007; Zhang et al., 2017). Assuming similar behavior at high redshifts, it is expected that DIG is not an important emission component in $z > 1$ galaxies because of their high SFRs and small sizes (Sanders et al., 2017). However, the presence of DIG emission or lack thereof at high redshift is yet to be tested observationally, requiring high-resolution spatially-resolved spectroscopy to separate and identify H II and DIG-dominated regions. I am currently leading the analysis in an observing program obtaining spatially-resolved emission-line maps of bright MOSDEF targets using adaptive optics and the OSIRIS integral field spectrograph on the Keck I telescope. These maps will be used to estimate the importance of DIG in typical $z \sim 2$ galaxies, and will allow us to search for additional non-stellar sources of line emission such as low-luminosity AGN and shocked gas.

Results presented in Chapter 6 confirmed that the M_*-SFR-Z relation evolves with redshift, as hinted at in Chapter 2. Furthermore, the analysis in Chapter 6 showed that the $z \sim 2.3$ MZR does indeed have a dependence on SFR that was not seen in Chapter 2 due to a smaller sample and less sensitive methodology. At $z \sim 0$, the M_*-SFR-Z relation has been shown to be a manifestation of a more fundamental relation beween M_*, metallicity, and cold gas content (Bothwell et al., 2013; Zahid et al., 2014a; Bothwell et al., 2016b,a).

Numerical simulations likewise suggest that dependence on molecular gas fraction (f_{H2}) is more fundamental than on SFR (Ma et al., 2016; Davé et al., 2017). Given our recent detection of the $z \sim 2.3$ M_*-SFR-Z relation, it is of interest to test whether a M_*-f_{H2}-Z relation exists at high redshifts as well. While samples of galaxies at $z > 1$ with measurements of molecular gas content are approaching statistical sizes, very few high-redshift galaxies have both metallicity and molecular gas measurements (e.g., Tacconi et al., 2013). Along with MOSDEF collaborators, I have led a recently-submitted ALMA proposal to obtain measurements of CO emission to estimate moloecular gas masses and f_{H2} for $z \sim 2.3$ star-forming galaxies with metallicity estimates. These proposed data will enable the first search for a relation among M_*, metallicity, and f_{H2} at high redshifts, providing new insights into baryon cycling in the early universe.

The temperature-based metallicity derived from auroral [O III]λ4363 for a galaxy at $z \sim 3$ (Chapter 4) was the first robust metallicity measurement at $z > 2$ independent of $z \sim 0$ strong-line metallicity calibraitons. While a single measurement is insufficient to revise metallicity calibrations at high redshifts, it shows the promise of using auroral line measurements to construct new metallicity calibrations based solely on high-redshift samples instead of relying on $z \sim 0$ calibration samples. Analysis is ongoing on three additional MOSDEF galaxies with detections of [O III]λ4363, and spectra of many galaxies can be stacked to obtain an average electron temperature for the MOSDEF sample. However, a robust recalibration of strong-line metallicity relations at high redshifts requires at least tens of individual objects with auroral-line measurements spanning an interesting dynamic range in metallicity. We have proposed to obtain deeper spectroscopic observations of several MOSDEF targets that should yield auroral-line detections with increased integration times. These data will bring the number of $z > 2$ galaxies with temperature-based metallicities to ~ 10, enabling a preliminary assessment of the applicability of $z \sim 0$ metallicity calibrations at high redshifts.

Currently, auroral-line detections can only be obtained for low-metallicity, high-SFR objects that are unrepresentative of the typical high-redshift star-forming population. Producing high-redshift metallicity calibrations with comparable accuracy to $z \sim 0$ calibrations will

ultimately require hundreds of auroral-line measurements for typical galaxies at $z > 2$. Obtaining such a sample with current ground-based facilities would be prohibilitively expensive due to the sensitivity of current-generation near-infrared spectrographs, and is additionally made difficult by the limited range of redshifts at which the auroral and strong emission-lines of interest fall within windows of atmospheric transmission. Observational facilities coming online over the next decade will be able to measure auroral-line strengths for large samples of galaxies at $z > 2$ over a wider range in metallicity and SFR than is currently possible. Instruments on the Thirty Meter Telescope (TMT) will achieve spectroscopic sensitivity an order of magnitude larger than that of Keck/MOSFIRE. TMT is expected to have first light in 2027. In the near-term future, the launch of the James Webb Space Telescope (JWST) in 2020 will usher in an era of unprecedented spectroscopic exploration in the infrared. Spectroscopic instruments onboard JWST will deliver the first large samples of galaxies with auroral-line measurements at high redshifts, revolutionizing our understanding of the metal content of galaxies at $z > 2$ and providing a clear picture of galaxy formation and growth in the early universe.

Bibliography

Abazajian, K. N., Adelman-McCarthy, J. K., Agüeros, M. A., Allam, S. S., Allende Prieto, C., An, D., Anderson, K. S. J., Anderson, S. F., Annis, J., Bahcall, N. A., & et al. 2009, ApJS, 182, 543

Albareti, F. D., Allende Prieto, C., Almeida, A., Anders, F., Anderson, S., Andrews, B. H., Aragón-Salamanca, A., Argudo-Fernández, M., Armengaud, E., Aubourg, E., & et al. 2017, ApJS, 233, 25

Amorín, R. O., Pérez-Montero, E., & Vílchez, J. M. 2010, ApJ, 715, L128

Andrews, B. H., & Martini, P. 2013, ApJ, 765, 140

Anglés-Alcázar, D., Faucher-Giguère, C.-A., Kereš, D., Hopkins, P. F., Quataert, E., & Murray, N. 2017, MNRAS, 470, 4698

Ascasibar, Y., Guidi, G., Casado, J., Scannapieco, C., & Díaz, A. I. 2016, ArXiv e-prints, arXiv:1602.08474

Asplund, M., Grevesse, N., Sauval, A. J., & Scott, P. 2009, ARA&A, 47, 481

Atek, H., Siana, B., Scarlata, C., Malkan, M., McCarthy, P., Teplitz, H., Henry, A., Colbert, J., Bridge, C., Bunker, A. J., Dressler, A., Fosbury, R. A. E., Hathi, N. P., Martin, C., Ross, N. R., & Shim, H. 2011, ApJ, 743, 121

Azadi, M., Coil, A. L., Aird, J., Reddy, N., Shapley, A., Freeman, W. R., Kriek, M., Leung, G. C. K., Mobasher, B., Price, S. H., Sanders, R. L., Shivaei, I., & Siana, B. 2017, ApJ, 835, 27

Baldwin, J. A., Phillips, M. M., & Terlevich, R. 1981, PASP, 93, 5

Barnes, J. E., Wood, K., Hill, A. S., & Haffner, L. M. 2015, MNRAS, 447, 559

Barrera-Ballesteros, J. K., Sánchez, S. F., Heckman, T., Blanc, G. A., & The MaNGA Team. 2017, ApJ, 844, 80

Belli, S., Jones, T., Ellis, R. S., & Richard, J. 2013, ApJ, 772, 141

Berg, D. A., Skillman, E. D., Croxall, K. V., Pogge, R. W., Moustakas, J., & Johnson-Groh, M. 2015, ApJ, 806, 16

Berg, D. A., Skillman, E. D., Garnett, D. R., Croxall, K. V., Marble, A. R., Smith, J. D., Gordon, K., & Kennicutt, Jr., R. C. 2013, ApJ, 775, 128

Berg, D. A., Skillman, E. D., Marble, A. R., van Zee, L., Engelbracht, C. W., Lee, J. C., Kennicutt, Jr., R. C., Calzetti, D., Dale, D. A., & Johnson, B. D. 2012, ApJ, 754, 98

Bian, F., Kewley, L. J., Dopita, M. A., & Juneau, S. 2016, ApJ, 822, 62

Bian, F., Fan, X., Bechtold, J., McGreer, I. D., Just, D. W., Sand, D. J., Green, R. F., Thompson, D., Peng, C. Y., Seifert, W., Ageorges, N., Juette, M., Knierim, V., & Buschkamp, P. 2010, ApJ, 725, 1877

Blanc, G. A., Kewley, L., Vogt, F. P. A., & Dopita, M. A. 2015, ApJ, 798, 99

Bothwell, M. S., Maiolino, R., Cicone, C., Peng, Y., & Wagg, J. 2016a, A&A, 595, A48

Bothwell, M. S., Maiolino, R., Kennicutt, R., Cresci, G., Mannucci, F., Marconi, A., & Cicone, C. 2013, MNRAS, 433, 1425

Bothwell, M. S., Maiolino, R., Peng, Y., Cicone, C., Griffith, H., & Wagg, J. 2016b, MNRAS, 455, 1156

Brammer, G. B., van Dokkum, P. G., Franx, M., Fumagalli, M., Patel, S., Rix, H.-W., Skelton, R. E., Kriek, M., Nelson, E., Schmidt, K. B., Bezanson, R., da Cunha, E., Erb, D. K., Fan, X., Förster Schreiber, N., Illingworth, G. D., Labbé, I., Leja, J., Lundgren, B., Magee, D., Marchesini, D., McCarthy, P., Momcheva, I., Muzzin, A., Quadri, R., Steidel, C. C., Tal, T., Wake, D., Whitaker, K. E., & Williams, A. 2012a, ApJS, 200, 13

Brammer, G. B., Sánchez-Janssen, R., Labbé, I., da Cunha, E., Erb, D. K., Franx, M., Fumagalli, M., Lundgren, B., Marchesini, D., Momcheva, I., Nelson, E., Patel, S., Quadri,

R., Rix, H.-W., Skelton, R. E., Schmidt, K. B., van der Wel, A., van Dokkum, P. G., Wake, D. A., & Whitaker, K. E. 2012b, ApJ, 758, L17

Bresolin, F. 2007, ApJ, 656, 186

—. 2011, ApJ, 730, 129

Bresolin, F., Kennicutt, R. C., & Ryan-Weber, E. 2012, ApJ, 750, 122

Brinchmann, J., Charlot, S., White, S. D. M., Tremonti, C., Kauffmann, G., Heckman, T., & Brinkmann, J. 2004, MNRAS, 351, 1151

Brinchmann, J., Pettini, M., & Charlot, S. 2008, MNRAS, 385, 769

Brown, J. S., Croxall, K. V., & Pogge, R. W. 2014, ApJ, 792, 140

Brown, J. S., Martini, P., & Andrews, B. H. 2016, MNRAS, 458, 1529

Bryant, J. J., Owers, M. S., Robotham, A. S. G., Croom, S. M., Driver, S. P., Drinkwater, M. J., Lorente, N. P. F., Cortese, L., Scott, N., Colless, M., Schaefer, A., Taylor, E. N., Konstantopoulos, I. S., Allen, J. T., Baldry, I., Barnes, L., Bauer, A. E., Bland-Hawthorn, J., Bloom, J. V., Brooks, A. M., Brough, S., Cecil, G., Couch, W., Croton, D., Davies, R., Ellis, S., Fogarty, L. M. R., Foster, C., Glazebrook, K., Goodwin, M., Green, A., Gunawardhana, M. L., Hampton, E., Ho, I.-T., Hopkins, A. M., Kewley, L., Lawrence, J. S., Leon-Saval, S. G., Leslie, S., McElroy, R., Lewis, G., Liske, J., López-Sánchez, Á. R., Mahajan, S., Medling, A. M., Metcalfe, N., Meyer, M., Mould, J., Obreschkow, D., O'Toole, S., Pracy, M., Richards, S. N., Shanks, T., Sharp, R., Sweet, S. M., Thomas, A. D., Tonini, C., & Walcher, C. J. 2015, MNRAS, 447, 2857

Bundy, K., Bershady, M. A., Law, D. R., Yan, R., Drory, N., MacDonald, N., Wake, D. A., Cherinka, B., Sánchez-Gallego, J. R., Weijmans, A.-M., Thomas, D., Tremonti, C., Masters, K., Coccato, L., Diamond-Stanic, A. M., Aragón-Salamanca, A., Avila-Reese, V., Badenes, C., Falcón-Barroso, J., Belfiore, F., Bizyaev, D., Blanc, G. A., Bland-Hawthorn, J., Blanton, M. R., Brownstein, J. R., Byler, N., Cappellari, M., Conroy, C., Dutton,

A. A., Emsellem, E., Etherington, J., Frinchaboy, P. M., Fu, H., Gunn, J. E., Harding, P., Johnston, E. J., Kauffmann, G., Kinemuchi, K., Klaene, M. A., Knapen, J. H., Leauthaud, A., Li, C., Lin, L., Maiolino, R., Malanushenko, V., Malanushenko, E., Mao, S., Maraston, C., McDermid, R. M., Merrifield, M. R., Nichol, R. C., Oravetz, D., Pan, K., Parejko, J. K., Sanchez, S. F., Schlegel, D., Simmons, A., Steele, O., Steinmetz, M., Thanjavur, K., Thompson, B. A., Tinker, J. L., van den Bosch, R. C. E., Westfall, K. B., Wilkinson, D., Wright, S., Xiao, T., & Zhang, K. 2015, ApJ, 798, 7

Calzetti, D., Armus, L., Bohlin, R. C., Kinney, A. L., Koornneef, J., & Storchi-Bergmann, T. 2000, ApJ, 533, 682

Campbell, A., Terlevich, R., & Melnick, J. 1986, MNRAS, 223, 811

Cardelli, J. A., Clayton, G. C., & Mathis, J. S. 1989, ApJ, 345, 245

Chabrier, G. 2003, PASP, 115, 763

Chisholm, J., Tremonti, C. A., Leitherer, C., & Chen, Y. 2017, MNRAS, 469, 4831

Christensen, L., Laursen, P., Richard, J., Hjorth, J., Milvang-Jensen, B., Dessauges-Zavadsky, M., Limousin, M., Grillo, C., & Ebeling, H. 2012, MNRAS, 427, 1973

Coil, A. L., Aird, J., Reddy, N., Shapley, A. E., Kriek, M., Siana, B., Mobasher, B., Freeman, W. R., Price, S. H., & Shivaei, I. 2015, ApJ, 801, 35

Conroy, C., Gunn, J. E., & White, M. 2009, ApJ, 699, 486

Cowie, L. L., Barger, A. J., & Songaila, A. 2016, ApJ, 817, 57

Cresci, G., Mannucci, F., Maiolino, R., Marconi, A., Gnerucci, A., & Magrini, L. 2010, Nature, 467, 811

Croxall, K. V., Pogge, R. W., Berg, D. A., Skillman, E. D., & Moustakas, J. 2015, ApJ, 808, 42

—. 2016, ApJ, 830, 4

Cullen, F., Cirasuolo, M., Kewley, L. J., McLure, R. J., Dunlop, J. S., & Bowler, R. A. A. 2016, MNRAS, 460, 3002

Cullen, F., Cirasuolo, M., McLure, R. J., Dunlop, J. S., & Bowler, R. A. A. 2014, MNRAS, 440, 2300

Curti, M., Cresci, G., Mannucci, F., Marconi, A., Maiolino, R., & Esposito, S. 2017, MNRAS, 465, 1384

Davé, R., Finlator, K., & Oppenheimer, B. D. 2011, MNRAS, 416, 1354

—. 2012, MNRAS, 421, 98

Davé, R., Rafieferantsoa, M. H., Thompson, R. J., & Hopkins, P. F. 2017, MNRAS, 467, 115

Davé, R., Thompson, R., & Hopkins, P. F. 2016, MNRAS, 462, 3265

de Barros, S., Vanzella, E., Amorín, R., Castellano, M., Siana, B., Grazian, A., Suh, H., Balestra, I., Vignali, C., Verhamme, A., Zamorani, G., Mignoli, M., Hasinger, G., Comastri, A., Pentericci, L., Pérez-Montero, E., Fontana, A., Giavalisco, M., & Gilli, R. 2016, A&A, 585, A51

De Rossi, M. E., Bower, R. G., Font, A. S., Schaye, J., & Theuns, T. 2017, MNRAS, 472, 3354

Dekel, A., & Silk, J. 1986, ApJ, 303, 39

Díaz, A. I., Castellanos, M., Terlevich, E., & Luisa García-Vargas, M. 2000, MNRAS, 318, 462

Donley, J. L., Koekemoer, A. M., Brusa, M., Capak, P., Cardamone, C. N., Civano, F., Ilbert, O., Impey, C. D., Kartaltepe, J. S., Miyaji, T., Salvato, M., Sanders, D. B., Trump, J. R., & Zamorani, G. 2012, ApJ, 748, 142

Dopita, M. A., & Evans, I. N. 1986, ApJ, 307, 431

Dopita, M. A., Kewley, L. J., Sutherland, R. S., & Nicholls, D. C. 2016, Ap&SS, 361, 61

Dopita, M. A., Sutherland, R. S., Nicholls, D. C., Kewley, L. J., & Vogt, F. P. A. 2013, ApJS, 208, 10

Dopita, M. A., Fischera, J., Sutherland, R. S., Kewley, L. J., Tuffs, R. J., Popescu, C. C., van Breugel, W., Groves, B. A., & Leitherer, C. 2006a, ApJ, 647, 244

Dopita, M. A., Fischera, J., Sutherland, R. S., Kewley, L. J., Leitherer, C., Tuffs, R. J., Popescu, C. C., van Breugel, W., & Groves, B. A. 2006b, ApJS, 167, 177

Dors, Jr., O. L., Krabbe, A., Hägele, G. F., & Pérez-Montero, E. 2011, MNRAS, 415, 3616

Ekström, S., Georgy, C., Eggenberger, P., Meynet, G., Mowlavi, N., Wyttenbach, A., Granada, A., Decressin, T., Hirschi, R., Frischknecht, U., Charbonnel, C., & Maeder, A. 2012, A&A, 537, A146

Eldridge, J. J., Langer, N., & Tout, C. A. 2011, MNRAS, 414, 3501

Eldridge, J. J., & Stanway, E. R. 2012, MNRAS, 419, 479

Ellison, S. L., Patton, D. R., Simard, L., & McConnachie, A. W. 2008, ApJ, 672, L107

Erb, D. K., Pettini, M., Shapley, A. E., Steidel, C. C., Law, D. R., & Reddy, N. A. 2010, ApJ, 719, 1168

Erb, D. K., Shapley, A. E., Pettini, M., Steidel, C. C., Reddy, N. A., & Adelberger, K. L. 2006, ApJ, 644, 813

Esteban, C., Bresolin, F., Peimbert, M., García-Rojas, J., Peimbert, A., & Mesa-Delgado, A. 2009, ApJ, 700, 654

Esteban, C., Carigi, L., Copetti, M. V. F., García-Rojas, J., Mesa-Delgado, A., Castañeda, H. O., & Péquignot, D. 2013, MNRAS, 433, 382

Esteban, C., García-Rojas, J., Carigi, L., Peimbert, M., Bresolin, F., López-Sánchez, A. R., & Mesa-Delgado, A. 2014, MNRAS, 443, 624

Ferland, G. J., Porter, R. L., van Hoof, P. A. M., Williams, R. J. R., Abel, N. P., Lykins, M. L., Shaw, G., Henney, W. J., & Stancil, P. C. 2013, RMxAA, 49, 137

Finlator, K., & Davé, R. 2008, MNRAS, 385, 2181

Fischer, C. F., & Tachiev, G. 2014, MCHF/MCDHF Collection, Version 2, Ref No. 10 & 20, Available online at http://physics.nist.gov/mchf, National Institude of Standards and Technology

Flores-Fajardo, N., Morisset, C., Stasińska, G., & Binette, L. 2011, MNRAS, 415, 2182

Förster Schreiber, N. M., Genzel, R., Bouché, N., Cresci, G., Davies, R., Buschkamp, P., Shapiro, K., Tacconi, L. J., Hicks, E. K. S., Genel, S., Shapley, A. E., Erb, D. K., Steidel, C. C., Lutz, D., Eisenhauer, F., Gillessen, S., Sternberg, A., Renzini, A., Cimatti, A., Daddi, E., Kurk, J., Lilly, S., Kong, X., Lehnert, M. D., Nesvadba, N., Verma, A., McCracken, H., Arimoto, N., Mignoli, M., & Onodera, M. 2009, ApJ, 706, 1364

Förster Schreiber, N. M., Shapley, A. E., Genzel, R., Bouché, N., Cresci, G., Davies, R., Erb, D. K., Genel, S., Lutz, D., Newman, S., Shapiro, K. L., Steidel, C. C., Sternberg, A., & Tacconi, L. J. 2011, ApJ, 739, 45

Freeman, W. R., Siana, B., Kriek, M., Shapley, A. E., Reddy, N., Coil, A. L., Mobasher, B., Muratov, A. L., Azadi, M., Leung, G., Sanders, R., Shivaei, I., Price, S. H., DeGroot, L., & Kereš, D. 2017, ArXiv e-prints, arXiv:1710.03230

García-Rojas, J., Esteban, C., Peimbert, A., Peimbert, M., Rodríguez, M., & Ruiz, M. T. 2005, MNRAS, 362, 301

García-Rojas, J., Esteban, C., Peimbert, A., Rodríguez, M., Peimbert, M., & Ruiz, M. T. 2007, RMxAA, 43, 3

García-Rojas, J., Esteban, C., Peimbert, M., Costado, M. T., Rodríguez, M., Peimbert, A., & Ruiz, M. T. 2006, MNRAS, 368, 253

García-Rojas, J., Simón-Díaz, S., & Esteban, C. 2014, A&A, 571, A93

Genzel, R., Newman, S., Jones, T., Förster Schreiber, N. M., Shapiro, K., Genel, S., Lilly, S. J., Renzini, A., Tacconi, L. J., Bouché, N., Burkert, A., Cresci, G., Buschkamp, P., Carollo, C. M., Ceverino, D., Davies, R., Dekel, A., Eisenhauer, F., Hicks, E., Kurk, J., Lutz, D., Mancini, C., Naab, T., Peng, Y., Sternberg, A., Vergani, D., & Zamorani, G. 2011, ApJ, 733, 101

Genzel, R., Tacconi, L. J., Lutz, D., Saintonge, A., Berta, S., Magnelli, B., Combes, F., García-Burillo, S., Neri, R., Bolatto, A., Contini, T., Lilly, S., Boissier, J., Boone, F., Bouché, N., Bournaud, F., Burkert, A., Carollo, M., Colina, L., Cooper, M. C., Cox, P., Feruglio, C., Förster Schreiber, N. M., Freundlich, J., Gracia-Carpio, J., Juneau, S., Kovac, K., Lippa, M., Naab, T., Salome, P., Renzini, A., Sternberg, A., Walter, F., Weiner, B., Weiss, A., & Wuyts, S. 2015, ApJ, 800, 20

Georgy, C., Ekström, S., Eggenberger, P., Meynet, G., Haemmerlé, L., Maeder, A., Granada, A., Groh, J. H., Hirschi, R., Mowlavi, N., Yusof, N., Charbonnel, C., Decressin, T., & Barblan, F. 2013, A&A, 558, A103

Grasshorn Gebhardt, H. S., Zeimann, G. R., Ciardullo, R., Gronwall, C., Hagen, A., Bridge, J. S., Schneider, D. P., & Trump, J. R. 2016, ApJ, 817, 10

Grogin, N. A., Kocevski, D. D., Faber, S. M., Ferguson, H. C., Koekemoer, A. M., Riess, A. G., Acquaviva, V., Alexander, D. M., Almaini, O., Ashby, M. L. N., Barden, M., Bell, E. F., Bournaud, F., Brown, T. M., Caputi, K. I., Casertano, S., Cassata, P., Castellano, M., Challis, P., Chary, R.-R., Cheung, E., Cirasuolo, M., Conselice, C. J., Roshan Cooray, A., Croton, D. J., Daddi, E., Dahlen, T., Davé, R., de Mello, D. F., Dekel, A., Dickinson, M., Dolch, T., Donley, J. L., Dunlop, J. S., Dutton, A. A., Elbaz, D., Fazio, G. G., Filippenko, A. V., Finkelstein, S. L., Fontana, A., Gardner, J. P., Garnavich, P. M., Gawiser, E., Giavalisco, M., Grazian, A., Guo, Y., Hathi, N. P., Häussler, B., Hopkins, P. F., Huang, J.-S., Huang, K.-H., Jha, S. W., Kartaltepe, J. S., Kirshner, R. P., Koo, D. C., Lai, K., Lee, K.-S., Li, W., Lotz, J. M., Lucas, R. A., Madau, P., McCarthy, P. J., McGrath, E. J., McIntosh, D. H., McLure, R. J., Mobasher, B., Moustakas, L. A., Mozena, M., Nandra, K., Newman, J. A., Niemi, S.-M., Noeske, K. G., Papovich, C. J., Pentericci,

L., Pope, A., Primack, J. R., Rajan, A., Ravindranath, S., Reddy, N. A., Renzini, A., Rix, H.-W., Robaina, A. R., Rodney, S. A., Rosario, D. J., Rosati, P., Salimbeni, S., Scarlata, C., Siana, B., Simard, L., Smidt, J., Somerville, R. S., Spinrad, H., Straughn, A. N., Strolger, L.-G., Telford, O., Teplitz, H. I., Trump, J. R., van der Wel, A., Villforth, C., Wechsler, R. H., Weiner, B. J., Wiklind, T., Wild, V., Wilson, G., Wuyts, S., Yan, H.-J., & Yun, M. S. 2011, ApJS, 197, 35

Gutkin, J., Charlot, S., & Bruzual, G. 2016, MNRAS, 462, 1757

Haffner, L. M., Reynolds, R. J., & Tufte, S. L. 1999, ApJ, 523, 223

Haffner, L. M., Dettmar, R.-J., Beckman, J. E., Wood, K., Slavin, J. D., Giammanco, C., Madsen, G. J., Zurita, A., & Reynolds, R. J. 2009, Reviews of Modern Physics, 81, 969

Hainline, K. N., Shapley, A. E., Kornei, K. A., Pettini, M., Buckley-Geer, E., Allam, S. S., & Tucker, D. L. 2009, ApJ, 701, 52

Hao, C.-N., Kennicutt, R. C., Johnson, B. D., Calzetti, D., Dale, D. A., & Moustakas, J. 2011, ApJ, 741, 124

Heckman, T. M., Alexandroff, R. M., Borthakur, S., Overzier, R., & Leitherer, C. 2015, ApJ, 809, 147

Heckman, T. M., Robert, C., Leitherer, C., Garnett, D. R., & van der Rydt, F. 1998, ApJ, 503, 646

Henry, A., Scarlata, C., Domínguez, A., Malkan, M., Martin, C. L., Siana, B., Atek, H., Bedregal, A. G., Colbert, J. W., Rafelski, M., Ross, N., Teplitz, H., Bunker, A. J., Dressler, A., Hathi, N., Masters, D., McCarthy, P., & Straughn, A. 2013, ApJ, 776, L27

Ho, I.-T., Kudritzki, R.-P., Kewley, L. J., Zahid, H. J., Dopita, M. A., Bresolin, F., & Rupke, D. S. N. 2015, MNRAS, 448, 2030

Holden, B. P., Oesch, P. A., González, V. G., Illingworth, G. D., Labbé, I., Bouwens, R., Franx, M., van Dokkum, P., & Spitler, L. 2016, ApJ, 820, 73

Hong, S., Calzetti, D., Gallagher, III, J. S., Martin, C. L., Conselice, C. J., & Pellerin, A. 2013, ApJ, 777, 63

Hoopes, C. G., & Walterbos, R. A. M. 2003, ApJ, 586, 902

Hopkins, A. M., & Beacom, J. F. 2006, ApJ, 651, 142

Horne, K. 1986, PASP, 98, 609

Hudson, C. E., & Bell, K. L. 2005, A&A, 430, 725

Hughes, T. M., Cortese, L., Boselli, A., Gavazzi, G., & Davies, J. I. 2013, A&A, 550, A115

Hunt, L., Dayal, P., Magrini, L., & Ferrara, A. 2016, MNRAS, 463, 2002

Izotov, Y. I., Stasińska, G., Meynet, G., Guseva, N. G., & Thuan, T. X. 2006, A&A, 448, 955

James, B. L., Pettini, M., Christensen, L., Auger, M. W., Becker, G. D., King, L. J., Quider, A. M., Shapley, A. E., & Steidel, C. C. 2014, MNRAS, 440, 1794

James, P. A., Bretherton, C. F., & Knapen, J. H. 2009, A&A, 501, 207

Jones, T., Ellis, R., Jullo, E., & Richard, J. 2010, ApJ, 725, L176

Jones, T., Ellis, R. S., Richard, J., & Jullo, E. 2013, ApJ, 765, 48

Jones, T., Martin, C., & Cooper, M. C. 2015, ApJ, 813, 126

Kacprzak, G. G., van de Voort, F., Glazebrook, K., Tran, K.-V. H., Yuan, T., Nanayakkara, T., Allen, R. J., Alcorn, L., Cowley, M., Labbé, I., Spitler, L., Straatman, C., & Tomczak, A. 2016, ApJ, 826, L11

Kashino, D., Silverman, J. D., Sanders, D., Kartaltepe, J. S., Daddi, E., Renzini, A., Valentino, F., Rodighiero, G., Juneau, S., Kewley, L. J., Zahid, H. J., Arimoto, N., Nagao, T., Chu, J., Sugiyama, N., Civano, F., Ilbert, O., Kajisawa, M., Le Fèvre, O., Maier, C., Masters, D., Miyaji, T., Onodera, M., Puglisi, A., & Taniguchi, Y. 2017, ApJ, 835, 88

Kauffmann, G., Heckman, T. M., White, S. D. M., Charlot, S., Tremonti, C., Brinchmann, J., Bruzual, G., Peng, E. W., Seibert, M., Bernardi, M., Blanton, M., Brinkmann, J., Castander, F., Csábai, I., Fukugita, M., Ivezic, Z., Munn, J. A., Nichol, R. C., Padmanabhan, N., Thakar, A. R., Weinberg, D. H., & York, D. 2003a, MNRAS, 341, 33

Kauffmann, G., Heckman, T. M., Tremonti, C., Brinchmann, J., Charlot, S., White, S. D. M., Ridgway, S. E., Brinkmann, J., Fukugita, M., Hall, P. B., Ivezić, Ž., Richards, G. T., & Schneider, D. P. 2003b, MNRAS, 346, 1055

Kennicutt, Jr., R. C. 1984, ApJ, 287, 116

—. 1998, ARA&A, 36, 189

Kennicutt, Jr., R. C., Bresolin, F., & Garnett, D. R. 2003, ApJ, 591, 801

Kewley, L. J., & Dopita, M. A. 2002, ApJS, 142, 35

Kewley, L. J., Dopita, M. A., Leitherer, C., Davé, R., Yuan, T., Allen, M., Groves, B., & Sutherland, R. 2013a, ApJ, 774, 100

Kewley, L. J., Dopita, M. A., Sutherland, R. S., Heisler, C. A., & Trevena, J. 2001, ApJ, 556, 121

Kewley, L. J., & Ellison, S. L. 2008, ApJ, 681, 1183

Kewley, L. J., Maier, C., Yabe, K., Ohta, K., Akiyama, M., Dopita, M. A., & Yuan, T. 2013b, ApJ, 774, L10

Kewley, L. J., Zahid, H. J., Geller, M. J., Dopita, M. A., Hwang, H. S., & Fabricant, D. 2015, ApJ, 812, L20

Kewley, L. J., Yuan, T., Nanayakkara, T., Kacprzak, G. G., Tran, K.-V. H., Glazebrook, K., Spitler, L., Cowley, M., Dopita, M., Straatman, C., Labbé, I., & Tomczak, A. 2016, ApJ, 819, 100

Kobulnicky, H. A., Kennicutt, Jr., R. C., & Pizagno, J. L. 1999, ApJ, 514, 544

Kobulnicky, H. A., & Kewley, L. J. 2004, ApJ, 617, 240

Koekemoer, A. M., Faber, S. M., Ferguson, H. C., Grogin, N. A., Kocevski, D. D., Koo, D. C., Lai, K., Lotz, J. M., Lucas, R. A., McGrath, E. J., Ogaz, S., Rajan, A., Riess, A. G., Rodney, S. A., Strolger, L., Casertano, S., Castellano, M., Dahlen, T., Dickinson, M., Dolch, T., Fontana, A., Giavalisco, M., Grazian, A., Guo, Y., Hathi, N. P., Huang, K.-H., van der Wel, A., Yan, H.-J., Acquaviva, V., Alexander, D. M., Almaini, O., Ashby, M. L. N., Barden, M., Bell, E. F., Bournaud, F., Brown, T. M., Caputi, K. I., Cassata, P., Challis, P. J., Chary, R.-R., Cheung, E., Cirasuolo, M., Conselice, C. J., Roshan Cooray, A., Croton, D. J., Daddi, E., Davé, R., de Mello, D. F., de Ravel, L., Dekel, A., Donley, J. L., Dunlop, J. S., Dutton, A. A., Elbaz, D., Fazio, G. G., Filippenko, A. V., Finkelstein, S. L., Frazer, C., Gardner, J. P., Garnavich, P. M., Gawiser, E., Gruetzbauch, R., Hartley, W. G., Häussler, B., Herrington, J., Hopkins, P. F., Huang, J.-S., Jha, S. W., Johnson, A., Kartaltepe, J. S., Khostovan, A. A., Kirshner, R. P., Lani, C., Lee, K.-S., Li, W., Madau, P., McCarthy, P. J., McIntosh, D. H., McLure, R. J., McPartland, C., Mobasher, B., Moreira, H., Mortlock, A., Moustakas, L. A., Mozena, M., Nandra, K., Newman, J. A., Nielsen, J. L., Niemi, S., Noeske, K. G., Papovich, C. J., Pentericci, L., Pope, A., Primack, J. R., Ravindranath, S., Reddy, N. A., Renzini, A., Rix, H.-W., Robaina, A. R., Rosario, D. J., Rosati, P., Salimbeni, S., Scarlata, C., Siana, B., Simard, L., Smidt, J., Snyder, D., Somerville, R. S., Spinrad, H., Straughn, A. N., Telford, O., Teplitz, H. I., Trump, J. R., Vargas, C., Villforth, C., Wagner, C. R., Wandro, P., Wechsler, R. H., Weiner, B. J., Wiklind, T., Wild, V., Wilson, G., Wuyts, S., & Yun, M. S. 2011, ApJS, 197, 36

Köppen, J., & Hensler, G. 2005, A&A, 434, 531

Kriek, M., & Conroy, C. 2013, ApJ, 775, L16

Kriek, M., van Dokkum, P. G., Labbé, I., Franx, M., Illingworth, G. D., Marchesini, D., & Quadri, R. F. 2009, ApJ, 700, 221

Kriek, M., Shapley, A. E., Reddy, N. A., Siana, B., Coil, A. L., Mobasher, B., Freeman, W. R., de Groot, L., Price, S. H., Sanders, R., Shivaei, I., Brammer, G. B., Momcheva,

I. G., Skelton, R. E., van Dokkum, P. G., Whitaker, K. E., Aird, J., Azadi, M., Kassis, M., Bullock, J. S., Conroy, C., Davé, R., Kereš, D., & Krumholz, M. 2015, ApJS, 218, 15

Lara-López, M. A., Cepa, J., Bongiovanni, A., Pérez García, A. M., Ederoclite, A., Castañeda, H., Fernández Lorenzo, M., Pović, M., & Sánchez-Portal, M. 2010, A&A, 521, L53

Lara-López, M. A., Hopkins, A. M., López-Sánchez, A. R., Brough, S., Gunawardhana, M. L. P., Colless, M., Robotham, A. S. G., Bauer, A. E., Bland-Hawthorn, J., Cluver, M., Driver, S., Foster, C., Kelvin, L. S., Liske, J., Loveday, J., Owers, M. S., Ponman, T. J., Sharp, R. G., Steele, O., Taylor, E. N., & Thomas, D. 2013, MNRAS, 434, 451

Law, D. R., Yan, R., Bershady, M. A., Bundy, K., Cherinka, B., Drory, N., MacDonald, N., Sánchez-Gallego, J. R., Wake, D. A., Weijmans, A.-M., Blanton, M. R., Klaene, M. A., Moran, S. M., Sanchez, S. F., & Zhang, K. 2015, AJ, 150, 19

Law, D. R., Cherinka, B., Yan, R., Andrews, B. H., Bershady, M. A., Bizyaev, D., Blanc, G. A., Blanton, M. R., Bolton, A. S., Brownstein, J. R., Bundy, K., Chen, Y., Drory, N., D'Souza, R., Fu, H., Jones, A., Kauffmann, G., MacDonald, N., Masters, K. L., Newman, J. A., Parejko, J. K., Sánchez-Gallego, J. R., Sánchez, S. F., Schlegel, D. J., Thomas, D., Wake, D. A., Weijmans, A.-M., Westfall, K. B., & Zhang, K. 2016, AJ, 152, 83

Leethochawalit, N., Jones, T. A., Ellis, R. S., Stark, D. P., Richard, J., Zitrin, A., & Auger, M. 2016, ApJ, 820, 84

Lehnert, M. D., Nesvadba, N. P. H., Le Tiran, L., Di Matteo, P., van Driel, W., Douglas, L. S., Chemin, L., & Bournaud, F. 2009, ApJ, 699, 1660

Leitherer, C., Ekström, S., Meynet, G., Schaerer, D., Agienko, K. B., & Levesque, E. M. 2014, ApJS, 212, 14

Lequeux, J., Peimbert, M., Rayo, J. F., Serrano, A., & Torres-Peimbert, S. 1979, A&A, 80, 155

Levesque, E. M., & Richardson, M. L. A. 2014, ApJ, 780, 100

Liang, Y. C., Hammer, F., Yin, S. Y., Flores, H., Rodrigues, M., & Yang, Y. B. 2007, A&A, 473, 411

Lilly, S. J., Carollo, C. M., Pipino, A., Renzini, A., & Peng, Y. 2013, ApJ, 772, 119

Liu, X., Shapley, A. E., Coil, A. L., Brinchmann, J., & Ma, C.-P. 2008, ApJ, 678, 758

López-Sánchez, Á. R., Esteban, C., García-Rojas, J., Peimbert, M., & Rodríguez, M. 2007, ApJ, 656, 168

Ly, C., Malkan, M. A., Rigby, J. R., & Nagao, T. 2016, ApJ, 828, 67

Ma, X., Hopkins, P. F., Faucher-Giguère, C.-A., Zolman, N., Muratov, A. L., Kereš, D., & Quataert, E. 2016, MNRAS, 456, 2140

Ma, X., Hopkins, P. F., Feldmann, R., Torrey, P., Faucher-Giguère, C.-A., & Kereš, D. 2017, MNRAS, 466, 4780

Madau, P., & Dickinson, M. 2014, ARA&A, 52, 415

Maier, C., Lilly, S. J., Ziegler, B. L., Contini, T., Pérez Montero, E., Peng, Y., & Balestra, I. 2014, ApJ, 792, 3

Maiolino, R., Nagao, T., Grazian, A., Cocchia, F., Marconi, A., Mannucci, F., Cimatti, A., Pipino, A., Ballero, S., Calura, F., Chiappini, C., Fontana, A., Granato, G. L., Matteucci, F., Pastorini, G., Pentericci, L., Risaliti, G., Salvati, M., & Silva, L. 2008, A&A, 488, 463

Mannucci, F., Cresci, G., Maiolino, R., Marconi, A., & Gnerucci, A. 2010, MNRAS, 408, 2115

Marino, R. A., Rosales-Ortega, F. F., Sánchez, S. F., Gil de Paz, A., Vílchez, J., Miralles-Caballero, D., Kehrig, C., Pérez-Montero, E., Stanishev, V., Iglesias-Páramo, J., Díaz, A. I., Castillo-Morales, A., Kennicutt, R., López-Sánchez, A. R., Galbany, L., García-Benito, R., Mast, D., Mendez-Abreu, J., Monreal-Ibero, A., Husemann, B., Walcher, C. J., García-Lorenzo, B., Masegosa, J., Del Olmo Orozco, A., Mourão, A. M., Ziegler, B.,

Mollá, M., Papaderos, P., Sánchez-Blázquez, P., González Delgado, R. M., Falcón-Barroso, J., Roth, M. M., van de Ven, G., & Califa Team. 2013, A&A, 559, A114

Martin, C. L. 1997, ApJ, 491, 561

Maseda, M. V., van der Wel, A., Rix, H.-W., da Cunha, E., Pacifici, C., Momcheva, I., Brammer, G. B., Meidt, S. E., Franx, M., van Dokkum, P., Fumagalli, M., Bell, E. F., Ferguson, H. C., Förster-Schreiber, N. M., Koekemoer, A. M., Koo, D. C., Lundgren, B. F., Marchesini, D., Nelson, E. J., Patel, S. G., Skelton, R. E., Straughn, A. N., Trump, J. R., & Whitaker, K. E. 2014, ApJ, 791, 17

Masters, D., Faisst, A., & Capak, P. 2016, ApJ, 828, 18

Masters, D., McCarthy, P., Siana, B., Malkan, M., Mobasher, B., Atek, H., Henry, A., Martin, C. L., Rafelski, M., Hathi, N. P., Scarlata, C., Ross, N. R., Bunker, A. J., Blanc, G., Bedregal, A. G., Domínguez, A., Colbert, J., Teplitz, H., & Dressler, A. 2014, ApJ, 785, 153

McGaugh, S. S. 1991, ApJ, 380, 140

McLean, I. S., Steidel, C. C., Epps, H. W., Konidaris, N., Matthews, K. Y., Adkins, S., Aliado, T., Brims, G., Canfield, J. M., Cromer, J. L., Fucik, J., Kulas, K., Mace, G., Magnone, K., Rodriguez, H., Rudie, G., Trainor, R., Wang, E., Weber, B., & Weiss, J. 2012, in Society of Photo-Optical Instrumentation Engineers (SPIE) Conference Series, Vol. 8446, Society of Photo-Optical Instrumentation Engineers (SPIE) Conference Series

Momcheva, I. G., Brammer, G. B., van Dokkum, P. G., Skelton, R. E., Whitaker, K. E., Nelson, E. J., Fumagalli, M., Maseda, M. V., Leja, J., Franx, M., Rix, H.-W., Bezanson, R., Da Cunha, E., Dickey, C., Förster Schreiber, N. M., Illingworth, G., Kriek, M., Labbé, I., Ulf Lange, J., Lundgren, B. F., Magee, D., Marchesini, D., Oesch, P., Pacifici, C., Patel, S. G., Price, S., Tal, T., Wake, D. A., van der Wel, A., & Wuyts, S. 2016, ApJS, 225, 27

Moustakas, J., Zaritsky, D., Brown, M., Cool, R., Dey, A., Eisenstein, D. J., Gonzalez,

A. H., Jannuzi, B., Jones, C., Kochanek, C. S., Murray, S. S., & Wild, V. 2011, ArXiv e-prints, arXiv:1112.3300

Nakajima, K., & Ouchi, M. 2014, MNRAS, 442, 900

Nakajima, K., Ouchi, M., Shimasaku, K., Hashimoto, T., Ono, Y., & Lee, J. C. 2013, ApJ, 769, 3

Newman, J. A., Cooper, M. C., Davis, M., Faber, S. M., Coil, A. L., Guhathakurta, P., Koo, D. C., Phillips, A. C., Conroy, C., Dutton, A. A., Finkbeiner, D. P., Gerke, B. F., Rosario, D. J., Weiner, B. J., Willmer, C. N. A., Yan, R., Harker, J. J., Kassin, S. A., Konidaris, N. P., Lai, K., Madgwick, D. S., Noeske, K. G., Wirth, G. D., Connolly, A. J., Kaiser, N., Kirby, E. N., Lemaux, B. C., Lin, L., Lotz, J. M., Luppino, G. A., Marinoni, C., Matthews, D. J., Metevier, A., & Schiavon, R. P. 2013, ApJS, 208, 5

Newman, S. F., Buschkamp, P., Genzel, R., Förster Schreiber, N. M., Kurk, J., Sternberg, A., Gnat, O., Rosario, D., Mancini, C., Lilly, S. J., Renzini, A., Burkert, A., Carollo, C. M., Cresci, G., Davies, R., Eisenhauer, F., Genel, S., Shapiro Griffin, K., Hicks, E. K. S., Lutz, D., Naab, T., Peng, Y., Tacconi, L. J., Wuyts, S., Zamorani, G., Vergani, D., & Weiner, B. J. 2014, ApJ, 781, 21

Nicholls, D. C., Dopita, M. A., Sutherland, R. S., Kewley, L. J., & Palay, E. 2013, ApJS, 207, 21

Oey, M. S., Meurer, G. R., Yelda, S., Furst, E. J., Caballero-Nieves, S. M., Hanish, D. J., Levesque, E. M., Thilker, D. A., Walth, G. L., Bland-Hawthorn, J., Dopita, M. A., Ferguson, H. C., Heckman, T. M., Doyle, M. T., Drinkwater, M. J., Freeman, K. C., Kennicutt, Jr., R. C., Kilborn, V. A., Knezek, P. M., Koribalski, B., Meyer, M., Putman, M. E., Ryan-Weber, E. V., Smith, R. C., Staveley-Smith, L., Webster, R. L., Werk, J., & Zwaan, M. A. 2007, ApJ, 661, 801

Onodera, M., Carollo, C. M., Lilly, S., Renzini, A., Arimoto, N., Capak, P., Daddi, E., Scoville, N., Tacchella, S., Tatehora, S., & Zamorani, G. 2016, ApJ, 822, 42

Oppenheimer, B. D., Davé, R., Kereš, D., Fardal, M., Katz, N., Kollmeier, J. A., & Weinberg, D. H. 2010, MNRAS, 406, 2325

Osterbrock, D. E., & Ferland, G. J. 2006, Astrophysics of gaseous nebulae and active galactic nuclei

Otte, B., Gallagher, III, J. S., & Reynolds, R. J. 2002, ApJ, 572, 823

Otte, B., Reynolds, R. J., Gallagher, III, J. S., & Ferguson, A. M. N. 2001, ApJ, 560, 207

Papovich, C., Finkelstein, S. L., Ferguson, H. C., Lotz, J. M., & Giavalisco, M. 2011, MNRAS, 412, 1123

Peeples, M. S., & Shankar, F. 2011, MNRAS, 417, 2962

Peimbert, A., Peña-Guerrero, M. A., & Peimbert, M. 2012, ApJ, 753, 39

Pellegrini, E. W., Baldwin, J. A., & Ferland, G. J. 2011, ApJ, 738, 34

Pérez-Montero, E. 2014, MNRAS, 441, 2663

Pérez-Montero, E., & Contini, T. 2009, MNRAS, 398, 949

Pettini, M., & Pagel, B. E. J. 2004, MNRAS, 348, L59

Pettini, M., Rix, S. A., Steidel, C. C., Adelberger, K. L., Hunt, M. P., & Shapley, A. E. 2002, ApJ, 569, 742

Pilyugin, L. S., & Grebel, E. K. 2016, MNRAS, 457, 3678

Pilyugin, L. S., Grebel, E. K., & Mattsson, L. 2012a, MNRAS, 424, 2316

Pilyugin, L. S., & Thuan, T. X. 2005, ApJ, 631, 231

Pilyugin, L. S., Vílchez, J. M., Cedrés, B., & Thuan, T. X. 2010, MNRAS, 403, 896

Pilyugin, L. S., Vílchez, J. M., Mattsson, L., & Thuan, T. X. 2012b, MNRAS, 421, 1624

Price, S. H., Kriek, M., Brammer, G. B., Conroy, C., Förster Schreiber, N. M., Franx, M., Fumagalli, M., Lundgren, B., Momcheva, I., Nelson, E. J., Skelton, R. E., van Dokkum, P. G., Whitaker, K. E., & Wuyts, S. 2014, ApJ, 788, 86

Queyrel, J., Contini, T., Kissler-Patig, M., Epinat, B., Amram, P., Garilli, B., Le Fèvre, O., Moultaka, J., Paioro, L., Tasca, L., Tresse, L., Vergani, D., López-Sanjuan, C., & Perez-Montero, E. 2012, A&A, 539, A93

Reddy, N. A., Pettini, M., Steidel, C. C., Shapley, A. E., Erb, D. K., & Law, D. R. 2012, ApJ, 754, 25

Reddy, N. A., Kriek, M., Shapley, A. E., Freeman, W. R., Siana, B., Coil, A. L., Mobasher, B., Price, S. H., Sanders, R. L., & Shivaei, I. 2015, ApJ, 806, 259

Reines, A. E., Nidever, D. L., Whelan, D. G., & Johnson, K. E. 2010, ApJ, 708, 26

Reynolds, R. J. 1985, ApJ, 294, 256

Reynolds, R. J., Haffner, L. M., Madsen, G. J., Wood, K., & Hill, A. S. 2012, in EAS Publications Series, Vol. 56, EAS Publications Series, ed. M. A. de Avillez, 213–220

Reynolds, R. J., Haffner, L. M., & Tufte, S. L. 1999, ApJ, 525, L21

Reynolds, R. J., Scherb, F., & Roesler, F. L. 1973, ApJ, 185, 869

Reynolds, R. J., Sterling, N. C., Haffner, L. M., & Tufte, S. L. 2001, ApJ, 548, L221

Rigby, J. R., Wuyts, E., Gladders, M. D., Sharon, K., & Becker, G. D. 2011, ApJ, 732, 59

Rosolowsky, E., & Simon, J. D. 2008, ApJ, 675, 1213

Rupke, D. S., Veilleux, S., & Sanders, D. B. 2005, ApJS, 160, 115

Salim, S., Lee, J. C., Davé, R., & Dickinson, M. 2015, ApJ, 808, 25

Salim, S., Lee, J. C., Ly, C., Brinchmann, J., Davé, R., Dickinson, M., Salzer, J. J., & Charlot, S. 2014, ApJ, 797, 126

Salim, S., Rich, R. M., Charlot, S., Brinchmann, J., Johnson, B. D., Schiminovich, D., Seibert, M., Mallery, R., Heckman, T. M., Forster, K., Friedman, P. G., Martin, D. C., Morrissey, P., Neff, S. G., Small, T., Wyder, T. K., Bianchi, L., Donas, J., Lee, Y.-W., Madore, B. F., Milliard, B., Szalay, A. S., Welsh, B. Y., & Yi, S. K. 2007, ApJS, 173, 267

Salpeter, E. E. 1955, ApJ, 121, 161

Sánchez, S. F., Rosales-Ortega, F. F., Jungwiert, B., Iglesias-Páramo, J., Vílchez, J. M., Marino, R. A., Walcher, C. J., Husemann, B., Mast, D., Monreal-Ibero, A., Cid Fernandes, R., Pérez, E., González Delgado, R., García-Benito, R., Galbany, L., van de Ven, G., Jahnke, K., Flores, H., Bland-Hawthorn, J., López-Sánchez, A. R., Stanishev, V., Miralles-Caballero, D., Díaz, A. I., Sánchez-Blazquez, P., Mollá, M., Gallazzi, A., Papaderos, P., Gomes, J. M., Gruel, N., Pérez, I., Ruiz-Lara, T., Florido, E., de Lorenzo-Cáceres, A., Mendez-Abreu, J., Kehrig, C., Roth, M. M., Ziegler, B., Alves, J., Wisotzki, L., Kupko, D., Quirrenbach, A., Bomans, D., & Califa Collaboration. 2013, A&A, 554, A58

Sánchez, S. F., Rosales-Ortega, F. F., Iglesias-Páramo, J., Mollá, M., Barrera-Ballesteros, J., Marino, R. A., Pérez, E., Sánchez-Blazquez, P., González Delgado, R., Cid Fernandes, R., de Lorenzo-Cáceres, A., Mendez-Abreu, J., Galbany, L., Falcon-Barroso, J., Miralles-Caballero, D., Husemann, B., García-Benito, R., Mast, D., Walcher, C. J., Gil de Paz, A., García-Lorenzo, B., Jungwiert, B., Vílchez, J. M., Jílková, L., Lyubenova, M., Cortijo-Ferrero, C., Díaz, A. I., Wisotzki, L., Márquez, I., Bland-Hawthorn, J., Ellis, S., van de Ven, G., Jahnke, K., Papaderos, P., Gomes, J. M., Mendoza, M. A., & López-Sánchez, Á. R. 2014, A&A, 563, A49

Sánchez, S. F., Pérez, E., Rosales-Ortega, F. F., Miralles-Caballero, D., López-Sánchez, A. R., Iglesias-Páramo, J., Marino, R. A., Sánchez-Menguiano, L., García-Benito, R., Mast, D., Mendoza, M. A., Papaderos, P., Ellis, S., Galbany, L., Kehrig, C., Monreal-Ibero, A., González Delgado, R., Mollá, M., Ziegler, B., de Lorenzo-Cáceres, A., Mendez-Abreu, J., Bland-Hawthorn, J., Bekeraitė, S., Roth, M. M., Pasquali, A., Díaz, A., Bomans, D., van de Ven, G., & Wisotzki, L. 2015, A&A, 574, A47

Sanders, R. L., Shapley, A. E., Zhang, K., & Yan, R. 2017, ApJ, 850, 136

Sanders, R. L., Shapley, A. E., Kriek, M., Reddy, N. A., Freeman, W. R., Coil, A. L., Siana, B., Mobasher, B., Shivaei, I., Price, S. H., & de Groot, L. 2015, ApJ, 799, 138

—. 2016a, ApJ, 825, L23

—. 2016b, ApJ, 816, 23

Scoville, N., Sheth, K., Aussel, H., Vanden Bout, P., Capak, P., Bongiorno, A., Casey, C. M., Murchikova, L., Koda, J., Álvarez-Márquez, J., Lee, N., Laigle, C., McCracken, H. J., Ilbert, O., Pope, A., Sanders, D., Chu, J., Toft, S., Ivison, R. J., & Manohar, S. 2016, ApJ, 820, 83

Scoville, N., Lee, N., Vanden Bout, P., Diaz-Santos, T., Sanders, D., Darvish, B., Bongiorno, A., Casey, C. M., Murchikova, L., Koda, J., Capak, P., Vlahakis, C., Ilbert, O., Sheth, K., Morokuma-Matsui, K., Ivison, R. J., Aussel, H., Laigle, C., McCracken, H. J., Armus, L., Pope, A., Toft, S., & Masters, D. 2017, ApJ, 837, 150

Segers, M. C., Crain, R. A., Schaye, J., Bower, R. G., Furlong, M., Schaller, M., & Theuns, T. 2016, MNRAS, 456, 1235

Seon, K.-I., Witt, A., Kim, I.-J., Shinn, J.-H., Edelstein, J., Min, K.-W., & Han, W. 2011, ApJ, 743, 188

Shapley, A. E., Coil, A. L., Ma, C.-P., & Bundy, K. 2005, ApJ, 635, 1006

Shapley, A. E., Steidel, C. C., Pettini, M., & Adelberger, K. L. 2003, ApJ, 588, 65

Shapley, A. E., Reddy, N. A., Kriek, M., Freeman, W. R., Sanders, R. L., Siana, B., Coil, A. L., Mobasher, B., Shivaei, I., Price, S. H., & de Groot, L. 2015, ApJ, 801, 88

Shaw, R. A., & Dufour, R. J. 1994, in Astronomical Society of the Pacific Conference Series, Vol. 61, Astronomical Data Analysis Software and Systems III, ed. D. R. Crabtree, R. J. Hanisch, & J. Barnes, 327

Shimakawa, R., Kodama, T., Steidel, C. C., Tadaki, K.-i., Tanaka, I., Strom, A. L., Hayashi, M., Koyama, Y., Suzuki, T. L., & Yamamoto, M. 2015, MNRAS, 451, 1284

Shirazi, M., Brinchmann, J., & Rahmati, A. 2014, ApJ, 787, 120

Shivaei, I., Reddy, N. A., Shapley, A. E., Kriek, M., Siana, B., Mobasher, B., Coil, A. L., Freeman, W. R., Sanders, R., Price, S. H., de Groot, L., & Azadi, M. 2015, ApJ, 815, 98

Skelton, R. E., Whitaker, K. E., Momcheva, I. G., Brammer, G. B., van Dokkum, P. G., Labbé, I., Franx, M., van der Wel, A., Bezanson, R., Da Cunha, E., Fumagalli, M., Förster Schreiber, N., Kriek, M., Leja, J., Lundgren, B. F., Magee, D., Marchesini, D., Maseda, M. V., Nelson, E. J., Oesch, P., Pacifici, C., Patel, S. G., Price, S., Rix, H.-W., Tal, T., Wake, D. A., & Wuyts, S. 2014, ApJS, 214, 24

Smit, R., Bouwens, R. J., Labbé, I., Zheng, W., Bradley, L., Donahue, M., Lemze, D., Moustakas, J., Umetsu, K., Zitrin, A., Coe, D., Postman, M., Gonzalez, V., Bartelmann, M., Benítez, N., Broadhurst, T., Ford, H., Grillo, C., Infante, L., Jimenez-Teja, Y., Jouvel, S., Kelson, D. D., Lahav, O., Maoz, D., Medezinski, E., Melchior, P., Meneghetti, M., Merten, J., Molino, A., Moustakas, L. A., Nonino, M., Rosati, P., & Seitz, S. 2014, ApJ, 784, 58

Speagle, J. S., Steinhardt, C. L., Capak, P. L., & Silverman, J. D. 2014, ApJS, 214, 15

Springel, V., White, S. D. M., Jenkins, A., Frenk, C. S., Yoshida, N., Gao, L., Navarro, J., Thacker, R., Croton, D., Helly, J., Peacock, J. A., Cole, S., Thomas, P., Couchman, H., Evrard, A., Colberg, J., & Pearce, F. 2005, Nature, 435, 629

Stark, D. P., Auger, M., Belokurov, V., Jones, T., Robertson, B., Ellis, R. S., Sand, D. J., Moiseev, A., Eagle, W., & Myers, T. 2013, MNRAS, 436, 1040

Stasińska, G. 2005, A&A, 434, 507

Steidel, C. C., Erb, D. K., Shapley, A. E., Pettini, M., Reddy, N., Bogosavljević, M., Rudie, G. C., & Rakic, O. 2010, ApJ, 717, 289

Steidel, C. C., Strom, A. L., Pettini, M., Rudie, G. C., Reddy, N. A., & Trainor, R. F. 2016, ApJ, 826, 159

Steidel, C. C., Rudie, G. C., Strom, A. L., Pettini, M., Reddy, N. A., Shapley, A. E., Trainor, R. F., Erb, D. K., Turner, M. L., Konidaris, N. P., Kulas, K. R., Mace, G., Matthews, K., & McLean, I. S. 2014, ApJ, 795, 165

Storey, P. J., Sochi, T., & Badnell, N. R. 2014, MNRAS, 441, 3028

Storey, P. J., & Zeippen, C. J. 2000, MNRAS, 312, 813

Stott, J. P., Sobral, D., Bower, R., Smail, I., Best, P. N., Matsuda, Y., Hayashi, M., Geach, J. E., & Kodama, T. 2013, MNRAS, 436, 1130

Stott, J. P., Sobral, D., Swinbank, A. M., Smail, I., Bower, R., Best, P. N., Sharples, R. M., Geach, J. E., & Matthee, J. 2014, MNRAS, 443, 2695

Strom, A. L., Steidel, C. C., Rudie, G. C., Trainor, R. F., Pettini, M., & Reddy, N. A. 2017, ApJ, 836, 164

Tacconi, L. J., Genzel, R., Neri, R., Cox, P., Cooper, M. C., Shapiro, K., Bolatto, A., Bouché, N., Bournaud, F., Burkert, A., Combes, F., Comerford, J., Davis, M., Schreiber, N. M. F., Garcia-Burillo, S., Gracia-Carpio, J., Lutz, D., Naab, T., Omont, A., Shapley, A., Sternberg, A., & Weiner, B. 2010, Nature, 463, 781

Tacconi, L. J., Neri, R., Genzel, R., Combes, F., Bolatto, A., Cooper, M. C., Wuyts, S., Bournaud, F., Burkert, A., Comerford, J., Cox, P., Davis, M., Förster Schreiber, N. M., García-Burillo, S., Gracia-Carpio, J., Lutz, D., Naab, T., Newman, S., Omont, A., Saintonge, A., Shapiro Griffin, K., Shapley, A., Sternberg, A., & Weiner, B. 2013, ApJ, 768, 74

Tassis, K., Kravtsov, A. V., & Gnedin, N. Y. 2008, ApJ, 672, 888

Tayal, S. S. 2007, ApJS, 171, 331

Tayal, S. S., & Zatsarinny, O. 2010, ApJS, 188, 32

Toribio San Cipriano, L., García-Rojas, J., Esteban, C., Bresolin, F., & Peimbert, M. 2016, MNRAS, 458, 1866

Tremonti, C. A., Heckman, T. M., Kauffmann, G., Brinchmann, J., Charlot, S., White, S. D. M., Seibert, M., Peng, E. W., Schlegel, D. J., Uomoto, A., Fukugita, M., & Brinkmann, J. 2004, ApJ, 613, 898

Troncoso, P., Maiolino, R., Sommariva, V., Cresci, G., Mannucci, F., Marconi, A., Meneghetti, M., Grazian, A., Cimatti, A., Fontana, A., Nagao, T., & Pentericci, L. 2014, A&A, 563, A58

van der Wel, A., Franx, M., van Dokkum, P. G., Skelton, R. E., Momcheva, I. G., Whitaker, K. E., Brammer, G. B., Bell, E. F., Rix, H.-W., Wuyts, S., Ferguson, H. C., Holden, B. P., Barro, G., Koekemoer, A. M., Chang, Y.-Y., McGrath, E. J., Häussler, B., Dekel, A., Behroozi, P., Fumagalli, M., Leja, J., Lundgren, B. F., Maseda, M. V., Nelson, E. J., Wake, D. A., Patel, S. G., Labbé, I., Faber, S. M., Grogin, N. A., & Kocevski, D. D. 2014, ApJ, 788, 28

van Zee, L., & Haynes, M. P. 2006, ApJ, 636, 214

Veilleux, S., & Osterbrock, D. E. 1987, ApJS, 63, 295

Vila-Costas, M. B., & Edmunds, M. G. 1992, MNRAS, 259, 121

Villar-Martín, M., Cerviño, M., & González Delgado, R. M. 2004, MNRAS, 355, 1132

Voges, E. S., & Walterbos, R. A. M. 2006, ApJ, 644, L29

Wang, X., Jones, T. A., Treu, T., Morishita, T., Abramson, L. E., Brammer, G. B., Huang, K.-H., Malkan, M. A., Schmidt, K. B., Fontana, A., Grillo, C., Henry, A. L., Karman, W., Kelly, P. L., Mason, C. A., Mercurio, A., Rosati, P., Sharon, K., Trenti, M., & Vulcani, B. 2017, ApJ, 837, 89

Watson, C., Povich, M. S., Churchwell, E. B., Babler, B. L., Chunev, G., Hoare, M., Indebetouw, R., Meade, M. R., Robitaille, T. P., & Whitney, B. A. 2008, ApJ, 681, 1341

Weiner, B. J., Coil, A. L., Prochaska, J. X., Newman, J. A., Cooper, M. C., Bundy, K., Conselice, C. J., Dutton, A. A., Faber, S. M., Koo, D. C., Lotz, J. M., Rieke, G. H., & Rubin, K. H. R. 2009, ApJ, 692, 187

Whitaker, K. E., van Dokkum, P. G., Brammer, G., & Franx, M. 2012, ApJ, 754, L29

Whitaker, K. E., Franx, M., Leja, J., van Dokkum, P. G., Henry, A., Skelton, R. E., Fumagalli, M., Momcheva, I. G., Brammer, G. B., Labbé, I., Nelson, E. J., & Rigby, J. R. 2014, ApJ, 795, 104

Wright, S. A., Larkin, J. E., Graham, J. R., & Ma, C.-P. 2010, ApJ, 711, 1291

Wuyts, E., Rigby, J. R., Sharon, K., & Gladders, M. D. 2012, ApJ, 755, 73

Wuyts, E., Kurk, J., Förster Schreiber, N. M., Genzel, R., Wisnioski, E., Bandara, K., Wuyts, S., Beifiori, A., Bender, R., Brammer, G. B., Burkert, A., Buschkamp, P., Carollo, C. M., Chan, J., Davies, R., Eisenhauer, F., Fossati, M., Kulkarni, S. K., Lang, P., Lilly, S. J., Lutz, D., Mancini, C., Mendel, J. T., Momcheva, I. G., Naab, T., Nelson, E. J., Renzini, A., Rosario, D., Saglia, R. P., Seitz, S., Sharples, R. M., Sternberg, A., Tacchella, S., Tacconi, L. J., van Dokkum, P., & Wilman, D. J. 2014, ApJ, 789, L40

Wuyts, E., Wisnioski, E., Fossati, M., Förster Schreiber, N. M., Genzel, R., Davies, R., Mendel, J. T., Naab, T., Röttgers, B., Wilman, D. J., Wuyts, S., Bandara, K., Beifiori, A., Belli, S., Bender, R., Brammer, G. B., Burkert, A., Chan, J., Galametz, A., Kulkarni, S. K., Lang, P., Lutz, D., Momcheva, I. G., Nelson, E. J., Rosario, D., Saglia, R. P., Seitz, S., Tacconi, L. J., Tadaki, K.-i., Übler, H., & van Dokkum, P. 2016, ApJ, 827, 74

Yabe, K., Ohta, K., Iwamuro, F., Akiyama, M., Tamura, N., Yuma, S., Kimura, M., Takato, N., Moritani, Y., Sumiyoshi, M., Maihara, T., Silverman, J., Dalton, G., Lewis, I., Bonfield, D., Lee, H., Curtis-Lake, E., Macaulay, E., & Clarke, F. 2014, MNRAS, 437, 3647

Yabe, K., Ohta, K., Akiyama, M., Bunker, A., Dalton, G., Ellis, R., Glazebrook, K., Goto, T., Imanishi, M., Iwamuro, F., Okada, H., Shimizu, I., Takato, N., Tamura, N., Tonegawa, M., & Totani, T. 2015, PASJ, 67, 102

Yan, R., Bundy, K., Law, D. R., Bershady, M. A., Andrews, B., Cherinka, B., Diamond-Stanic, A. M., Drory, N., MacDonald, N., Sánchez-Gallego, J. R., Thomas, D., Wake, D. A., Weijmans, A.-M., Westfall, K. B., Zhang, K., Aragón-Salamanca, A., Belfiore, F., Bizyaev, D., Blanc, G. A., Blanton, M. R., Brownstein, J., Cappellari, M., D'Souza, R., Emsellem, E., Fu, H., Gaulme, P., Graham, M. T., Goddard, D., Gunn, J. E., Harding, P., Jones, A., Kinemuchi, K., Li, C., Li, H., Maiolino, R., Mao, S., Maraston, C., Masters, K., Merrifield, M. R., Oravetz, D., Pan, K., Parejko, J. K., Sanchez, S. F., Schlegel, D., Simmons, A., Thanjavur, K., Tinker, J., Tremonti, C., van den Bosch, R., & Zheng, Z. 2016, AJ, 152, 197

Yates, R. M., Kauffmann, G., & Guo, Q. 2012, MNRAS, 422, 215

York, D. G., Adelman, J., Anderson, Jr., J. E., Anderson, S. F., Annis, J., Bahcall, N. A., Bakken, J. A., Barkhouser, R., Bastian, S., Berman, E., Boroski, W. N., Bracker, S., Briegel, C., Briggs, J. W., Brinkmann, J., Brunner, R., Burles, S., Carey, L., Carr, M. A., Castander, F. J., Chen, B., Colestock, P. L., Connolly, A. J., Crocker, J. H., Csabai, I., Czarapata, P. C., Davis, J. E., Doi, M., Dombeck, T., Eisenstein, D., Ellman, N., Elms, B. R., Evans, M. L., Fan, X., Federwitz, G. R., Fiscelli, L., Friedman, S., Frieman, J. A., Fukugita, M., Gillespie, B., Gunn, J. E., Gurbani, V. K., de Haas, E., Haldeman, M., Harris, F. H., Hayes, J., Heckman, T. M., Hennessy, G. S., Hindsley, R. B., Holm, S., Holmgren, D. J., Huang, C.-h., Hull, C., Husby, D., Ichikawa, S.-I., Ichikawa, T., Ivezić, Ž., Kent, S., Kim, R. S. J., Kinney, E., Klaene, M., Kleinman, A. N., Kleinman, S., Knapp, G. R., Korienek, J., Kron, R. G., Kunszt, P. Z., Lamb, D. Q., Lee, B., Leger, R. F., Limmongkol, S., Lindenmeyer, C., Long, D. C., Loomis, C., Loveday, J., Lucinio, R., Lupton, R. H., MacKinnon, B., Mannery, E. J., Mantsch, P. M., Margon, B., McGehee, P., McKay, T. A., Meiksin, A., Merelli, A., Monet, D. G., Munn, J. A., Narayanan, V. K., Nash, T., Neilsen, E., Neswold, R., Newberg, H. J., Nichol, R. C., Nicinski, T., Nonino, M., Okada, N., Okamura, S., Ostriker, J. P., Owen, R., Pauls, A. G., Peoples, J., Peterson, R. L., Petravick, D., Pier, J. R., Pope, A., Pordes, R., Prosapio, A., Rechenmacher, R., Quinn, T. R., Richards, G. T., Richmond, M. W., Rivetta, C. H., Rockosi, C. M.,

Ruthmansdorfer, K., Sandford, D., Schlegel, D. J., Schneider, D. P., Sekiguchi, M., Sergey, G., Shimasaku, K., Siegmund, W. A., Smee, S., Smith, J. A., Snedden, S., Stone, R., Stoughton, C., Strauss, M. A., Stubbs, C., SubbaRao, M., Szalay, A. S., Szapudi, I., Szokoly, G. P., Thakar, A. R., Tremonti, C., Tucker, D. L., Uomoto, A., Vanden Berk, D., Vogeley, M. S., Waddell, P., Wang, S.-i., Watanabe, M., Weinberg, D. H., Yanny, B., Yasuda, N., & SDSS Collaboration. 2000, AJ, 120, 1579

Yuan, T.-T., & Kewley, L. J. 2009, ApJ, 699, L161

Yuan, T.-T., Kewley, L. J., Swinbank, A. M., Richard, J., & Livermore, R. C. 2011, ApJ, 732, L14

Zahid, H. J., Dima, G. I., Kudritzki, R.-P., Kewley, L. J., Geller, M. J., Hwang, H. S., Silverman, J. D., & Kashino, D. 2014a, ApJ, 791, 130

Zahid, H. J., Kashino, D., Silverman, J. D., Kewley, L. J., Daddi, E., Renzini, A., Rodighiero, G., Nagao, T., Arimoto, N., Sanders, D. B., Kartaltepe, J., Lilly, S. J., Maier, C., Geller, M. J., Capak, P., Carollo, C. M., Chu, J., Hasinger, G., Ilbert, O., Kajisawa, M., Koekemoer, A. M., Kovacs, K., Le Fèvre, O., Masters, D., McCracken, H. J., Onodera, M., Scoville, N., Strazzullo, V., Sugiyama, N., Taniguchi, Y., & COSMOS Team. 2014b, ApJ, 792, 75

Zaritsky, D., Kennicutt, Jr., R. C., & Huchra, J. P. 1994, ApJ, 420, 87

Zhang, K., Yan, R., Bundy, K., Bershady, M., Haffner, L. M., Walterbos, R., Maiolino, R., Tremonti, C., Thomas, D., Drory, N., Jones, A., Belfiore, F., Sánchez, S. F., Diamond-Stanic, A. M., Bizyaev, D., Nitschelm, C., Andrews, B., Brinkmann, J., Brownstein, J. R., Cheung, E., Li, C., Law, D. R., Roman Lopes, A., Oravetz, D., Pan, K., Storchi Bergmann, T., & Simmons, A. 2017, MNRAS, 466, 3217

Zurita, A., Rozas, M., & Beckman, J. E. 2000, A&A, 363, 9